Impact of Joining Dissimilar Steel and Aluminium for Future Automotive Structures

A thesis submitted for the degree of Doctor of Philosophy

by

André Oliveira

Supervisor team: Professor Hari Babu Nadendla (Academic Supervisor)
Sullivan Smith (Industrial Supervisor)

Abstract

The transport sector is the largest contributor of greenhouse gas emissions globally [1],[2], and new limits for greenhouse gas emission from new cars have been imposed. It was shown that a reduction in carbon dioxide emissions of about 9g/km can be achieved by reducing the weight of a car by 100kg [3]–[6]. The automotive industry is therefore adapting “new” materials with improved strength to weight ratio, like ultra-high strength steels and aluminium castings and extrusions in the body in white (BIW) to achieve this goal.

For dissimilar joining of steel to aluminium in car body applications, a range of mechanical joining technologies are becoming established as reliable solutions. These include; rivets (self-piercing and blind), flow drilling screws, friction welding elements, tacking elements and many more. The broad spectrum of technologies has different locking mechanisms, properties and weaknesses, however very little is known on the impact of the dissimilar properties on different joining mechanisms for comparison and selection purposes. This is due to the small handful of publications that discuss this impact.

This work successfully identifies the limitations for the individual joining technologies for different material combinations, provide the necessary guidelines for technology selection and can be used as a detailed manual for guidance in technology selection. Results show, from a lightweight and economical viewpoint, that the clinching process offers the best solution as there is no added weight or cost of an additional element at the expense of low joint performance. However, if joint access is a requirement then blind rivet technology is the only possible solution, although this will be at the expense of added weight from the element and the need to have a pre-formed hole that must be correctly matched in both components in order to form the joint. If the requirement is performance alone, then piercing technologies provide a better solution. Among these piercing technologies self-piercing rivets offer the best strength performance, however, there is a trade-off with added weight, requirement of dual sided access for joining sheets and the specific requirement of the sheets’ properties. This reinforces the main principal conclusion drawn from this work, which is, that there is currently no solution that is able to provide all the required needs.

Another available, but little unexplored technology is Resistance Spot Welding which offers the advantage of being a non-added weight process as it is an autogenous and it is potentially an extremely low-cost technology in addition to being a technology that is already established in nearly every high volume automotive production line for similar materials joining (particularly steel to steel joining). Since this is a fusion process, it is unavoidable to form different intermetallics of Fe-Al welding that will provide an increased challenge in obtaining structural high-quality welds.

The inherent problem for welding Fe-Al dissimilar materials is that the materials are different in nature; crystal structure, melting point, specific heat, and thermal conductivity. In welding process, these factors lead to local stresses and the formation of different intermetallic phases where very hard low ductility crystal structures predominate. In a weld the presence of intermetallics leads to poor fracture toughness [7]–[9] giving way to very weak joints. Therefore the aim of this work is to promote greater understanding of the mechanisms of steel to aluminium joining by resistance spot welding, with a view to developing an industrially applicable solution.

According to literature; in order to form a good weld between aluminium and steel it is critical to understand and control the morphology, volume and location of the Fe-Al intermetallics present [8]. Intermetallic layer thicknesses greater than 10 µm seriously deteriorate the mechanical properties of the joints [10]. The agreed consensus in the literature is that the main phases present are Fe_4Al_{13} and Fe_2Al_5 and the thickness of the intermetallic layer is governed by the temperature and time of the welding process.

In this sense, this work focused on the resistance spot welding of steel to aluminium by exploring the effect of parameters responsible for the heat input. In turn the effect of heating on intermetallic phase development and the resulting effect on mechanical properties was investigated and explained. The focus was in tailoring the fundamentals of the process by indirect control of the local contact resistance of the interface by controlling the pressure to increase heat generation and localization in the centre of joints and improve weld size and quality. Results show that the parameters that govern joule heating are shown to strongly influence the weld size and performance. Increased welding time either in single pulse or dual pulse increased the heat input and therefore increased the weld size. For a given pulse duration, multiple pulses produced a larger weld size compared to its single pulse counterpart. Under optimal system parameters this work has shown that the weld size can be larger (8.8 mm) than the size of the electrode tip (8 mm).

From this comprehensive piece of work, it was shown not only how to improve weld quality but also semi-empirical models were generated to predict weld size and performance.

Overall, this thesis has built on and improved the joining process knowledge associated with Fe-Al joining, by providing a comprehensive manual for technology selection with both impact of joint performance as well as economical implications. Additionally, this work provided a technological milestone by enabling Fe-Al resistance spot welding by providing a basis for the continuation of the understanding how to control the process in order to target the necessary properties and the development of preliminary semi-empirical models to achieve the targeted properties.

Acknowledgements

I would like to start by thanking TWI and BCAST from Brunel University London, for the PhD program in industry through the NSIRC program.

Secondly, I would like to thank my supervisor team Prof. Hari Babu Nadenla and Sullivan Smith for the support during my PhD study and related research, for their patience, inspiration, and knowledge. Their guidance was instrumental during this research work and writing of this thesis.

Besides my advisors, I would like to thank the rest of my thesis committee: Prof. Wamadeva Balachandran, Prof. Hamid Assadi, Prof. Dmitry Eskin and Dr Brian McKay, for their insightful comments and encouragement, but also for the series of hard questions which propelled me to expand my research from various perspectives.

Additionally, I would like to thank the Lasers And Sheets group (LAS) from TWI for welcoming me into the group during the course of the PhD, for the stimulating discussions and for all the fun we have had in the last four years. I would like to particularly thank mention Dr Chris Allen, and Frank Nolan. Also, I thank my friends in the following institutions GESIPA UK, Henrob – Atlas Copco, BTM for their fundamental contributions.

Last but not the least, I would like to thank my wife, as with her continued support has allowed to make this dream into reality.

Contents

Index of Abbreviations

AA	–	Aluminium Alloy
AHSS	–	Advanced High Strength Steels
AISI	–	American Iron and Steel Institute
BIW	–	Body in White
CFRP	–	Carbon Fibre Reinforced Plastic
CTS	–	Cross Tension Strength
DC	–	Direct Current
FDS	–	Flow Drill Screw
FEW	–	Friction element welding
FSSW	–	Friction Stir Spot Welding
GA	–	Galvanneal coating
GI	–	Galvanized coating
HSLA	–	High Strength Low Alloy
ISO	–	International Organization for Standardization
LVDT	–	Linear Variable Differential Transformer
MAG	–	Metal Active Gas Welding
MIG	–	Metal Inert Gas Welding
NI	–	National Instruments
REW	–	Resistance Element Welding
RSW	–	Resistance Spot Welding
RWMA	–	Resistance Welding Materials Alloy
SMDI	–	Steel Market Development Institute
SPR	–	Self-Piercing Riveting
SPSR	–	Self-Piercing Solid Rivet or Solid Punch Riveting
TIG	–	Tungsten Inert Gas Welding
TSS	–	Tensile Shear Strength
UHSS	–	Ultra High Strength Steels
ULSAB	–	Ultralight Steel Auto Body

Index of Figures

Index of tables

1. Introduction

Throughout the last two decades global warming has been a topic that has been gathering more and more momentum due to the undeniable climate changes that have been felt throughout the years. Observed global changes in the environment have been correlated to the increased greenhouse gas emissions. Society and governments have begun new measures to start evaluating and reducing greenhouse emissions. It is shown that CO_2 emission sources originate from: Transportation (26%), Energy supply (25%), Business (17%), Residential (14%), Agriculture (10%), Waste management (4%) and others [1],[2]. New laws and emission targets have been devised for every major industry sector to control and minimize emissions.

Studies performed by the European Council have shown that 12% of the overall greenhouse gas emissions originate from personal vehicles. Therefore, the focus is on finding a solution for minimising emissions in the transportation sector with a special interest on high volume manufacturing vehicles (as these make up the greatest majority of vehicles on the road). Since 2015 new laws have been devised to limit greenhouse gas emission on new cars to 95 g CO_2/km [11] by 2021. To comply with these new legislations car manufactures started with new developments to improve car efficiency and ecology, by improving and developing new powertrains, alternative energy sources (vehicle electrification), improved aerodynamics and targeted tyre rolling resistance [12]. However, these improvements are extremely time and resource consuming.

Alternatively, it was shown that lightweighting a vehicle is a cheaper and faster solution to reduce CO_2 emissions, as a reduction of 9g/km can be achieved by reducing the weight of a car by 100kg [3]–[6]. Light weighting a car is not so straight forward, because the car needs to be lighter but without losing structural integrity while considering the final price of the car and satisfying the growing customer demands.

To achieve lightweighting targets car manufactures are adopting new materials with improved strength to weight ratio: high strength steels, aluminium (sheet, extrusions and castings), magnesium, stainless steels, polymers and composites; into the manufacturing process while being sustainable and producing more efficient cars. However new materials require the development of new joining technologies or adaptation of unfamiliar joining methods to enable the usage of these materials. Therefore, when adopting a new material there is a significant increase in cost incurred not limited to the material cost but also the extra complexity of the production process required in many cases. This extra cost means that adoption of the new materials can often be economically unviable [13]. In order to be competitive with other fuel-economy actions, a general industry target for the cost of weight reduction has been proposed as $\leq$ 4.5 USD$/(kg saved) (~3.6 £/(kg saved)) [12].

1.1. Steels in the automotive industry

Mass production in the automotive industry started in the early 20th Century. Reliable high-volume automotive sheet metal components could be made extremely fast and the resistance spot welding technique is partly responsible for this scale of mass production, therefore the high volume car industry is mostly dominated by steel sheets joined with resistance spot welding.

The widespread usage of steels is related to its advantages over other materials: low cost; high modulus (stiffer); its formability; and the possibility of a wide range of ductility and strength through processing. Adding to these reasons, steels have been the key material in the automotive industry due to formability, consistency of supply, corrosion resistance with zinc coatings, ease of joining, recyclability and good crash energy absorption. However, some weaknesses of using steel are that heavier than other automotive materials and it can corrode if uncoated.

To comply with fuel economy requirements and more recent new CO_2 emission targets, the steel industry has been developing a new set of high-strength steels commonly denominated as High Strength Low Alloy (HSLA), Advanced High Strength Steels (AHSS), Ultra High Strength Steels (UHSS) and 3rd generation high strength steels. The Ultralight Steel Auto Body (ULSAB) promoted by the American Iron and Steel Institute (AISI) and the Steel Market Development Institute (SMDI) has been demonstrating how new steel development can lead to weight reduction in a body in white (BIW) with superior structural performance and strength along with a reduced parts count and net manufacturing cost savings compared to a conventional steel body[14]–[17]. A similar approach could also be applied for mass reduction of add-on components such as doors, hoods, among others, and similar mass reductions benefits could be achieved [18], [19]. According to another study new AHSS steels can offer up to a 25% weight reduction at a cost of less than 2 USD$/(kg saved) (~1.6 £/(kg saved)) [12]. Figure 1 presents the behaviour of different steel grades strength as a function of elongation. To give an overview of recent advances, in this figure, there are more grades displayed than the ones used in automobiles. In figure 1 it is evident that the increase of strength comes as a compromise of elongation, therefore the material selection is critical for each application. By implementing stronger steels, it is possible to achieve the same performance of a given structural component with a lighter and thinner material. Therefore, the implementation of higher strength steels helps to reduce the vehicle weight.

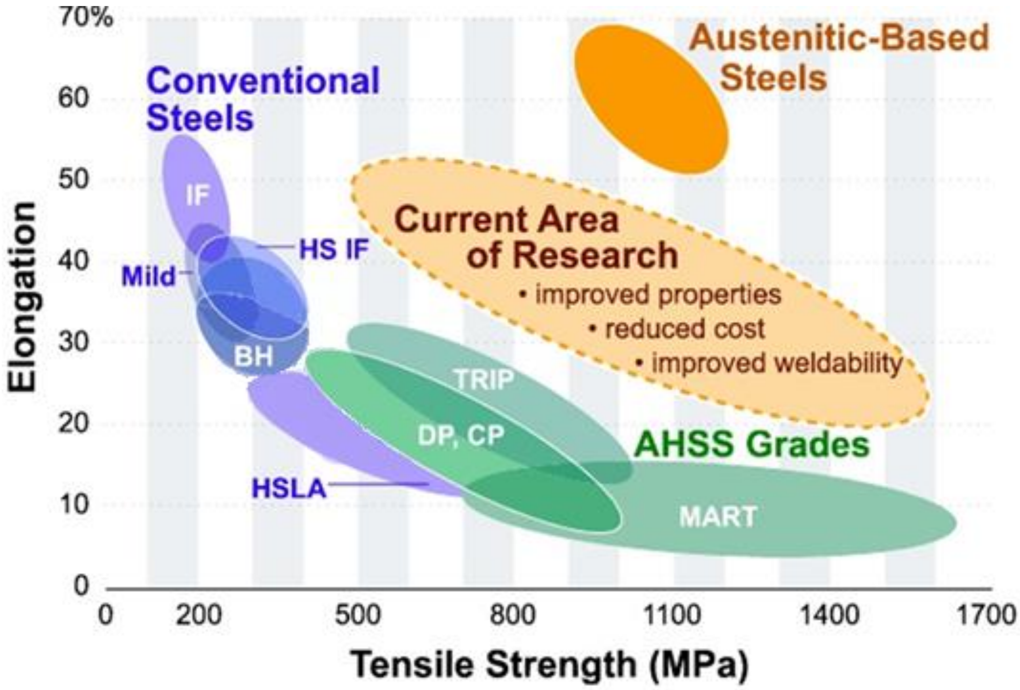

Figure 1- Steel grades behaviour of tensile strength as factor of elongation: IF – Interstitial Free Steel; HS –High Strength; BH – Bake Hardened; HSLA – High Strength Low Alloy; DP – Dual Phase; CP – Complex Phase; TRIP – Transformation-Induced Plasticity; MART – Martensitic (adapted from http://www.slideshare.net/katehickey/world-auto-steel-general-presentation-20090630 acceded 23/06/2020)

1.2. Aluminium in the automotive industry

Compared to steel, aluminium offers a weight reduction potential of 30-50% [20] considering the differences in density alone (steel density 7.9 g/cm^3, aluminium 2.7 g/cm^3, which is around 2.5 times lighter than steel). However, pure aluminium is very soft and ductile, therefore alloying with other elements allows tailoring the aluminium alloys (AA) to the desired physical properties. A downside of using aluminium is the high production cost associated with high energy consumption in aluminium extraction process and limited lifetime of the electrodes used in this process. So it is no wonder that at the present day several vehicles with fully aluminium body constructions are available and their production cost is extremely high. Therefore, aluminium is only available for cars that have limited production volumes and are sold at a premium price (Audi, Jaguar, various high-end sports cars), this elevated price covers the extra cost surrounding implementation of aluminium in the production line. Then, this implies that these high cost cars are not economically viable to the general public, and consequently do not have the intended impact on the greenhouse effect. The cost associated with replacing aluminium for steel on body structures is more than 5 USD$/(kg saved) (~ 4 £/(kg saved)) [12]. It is important to note that aluminium is a sustainable light-weighting solution due to is excellent recycling characteristics. Henriksson *et al* [21] and Tisza *et al* [22] have both reached same conclusion that piece-by-piece component substitution of steel to aluminium is not economically viable. It was demonstrated that the cost of an aluminium body-in-white exceeds the cost of steels considering only the cost of structures itself. The cost of Al body can be minimised through a redesign of the structure, which has been demonstrated in aluminium intensive Ford pickup F150.

1.3. Industrial Impact / Need for a dissimilar multi-material BIW

As previously mentioned, to make a proper impact on meeting CO_2 reduction goals, it is necessary to focus on high-volume manufacturing by adopting affordable lightweight design. For this the automotive industry is evolving in order to incorporate materials with improved strength to weight ratio into the manufacturing process while being sustainable and producing more efficient cars. However, current jointing technologies cannot be applied to mass production, either because of their high cost or because they are not suitable to join the full range of dissimilar materials found in an optimised car body.

To understand the industrial impact of the evolution of incorporating “new" materials in the body of a car, an example of a body-in-white is presented in Figure 2. Body-in-White (BIW) is the terminology used for the body's metal sheet components that have been joined together before applying the first primer. From a steel intense BIW shown in Figure 2, it can be seen that different steel grades are required to achieve BIW that meets stringent specifications. Although this is a prototype study of a Volvo XC90, it already shows the complexity that a BIW needs to have to meet the required properties for structural performance and crashworthiness. The required joining techniques, used to produce this BIW, will be based on several parameters such as properties of material being used, the geometry, location of a joint and strength needed. In this example it is possible to view the beginning of the implementation of aluminium in the BIW, however this component is bolted on which is a mainly manual process and as such not suitable for automated high volume manufacturing.

Figure 2 – Dissimilar material BIW of a prototype from Volvo XC90

There are numerous techniques available to solve some of the difficulties that have been already encountered. However, for the automotive industry the full scope is not available due to factors like geometries needed, swiftness of the process, and principally the cost.

Steel BIW	Aluminium BIW	Steel-Aluminium Hybrid BIW
•Resistance Spot Welding •Arc Welding / brazing •Metal Active Gas (MAG) •Laser Welding •Clinching •Hemming •Screws and Nuts •Adhesive bounding	•Resistance Spot Welding •Arc Welding / brazing •Metal Inert Gas (MIG) •Bling Riveting •Self- piercing Riveting •Clinching •Hemming •Scews and Nuts •Flow Drill Screws •Laser Welding •Adhesive bounding •Among others	•Resistance Spot welding •Arc welding / brazing •Metal Inert Gas (MIG) •Bling Riveting •Self- piercing Riveting •Clinching •Clinch-riveting •Solid punch riveting •Hemming •Scews and Nuts •Flow Drill Screws •Laser Welding •Friction Welding •Adhesive bounding •Among others

Figure 3 – Some joining techniques used in the different BIW

Figure 3 presents one of the great complications of a hybrid BIW which is that when more different materials are integrated, a greater range of joining solutions are required, so more joining processes types must be used. For the steel BIW, it is possible to see that the process has already been optimized to use the minimum amount of different techniques possible. This correlates cost/efficiency because fewer techniques required, less expenses with equipment and maintenance, also less supplies required, less time spent validating each joint combination and each geometry in the development phase, less factory space and the faster the car can be built. Therefore, there is a particular interest in reducing the number of technologies needed for joining a Steel-Aluminium hybrid BIW.

As stated by Meschut *et al* [23] “One prerequisite for multi-material structures in car bodies is the availability of material-capable and cost-efficient joining technologies”, however traditional high volume manufacturing technologies cannot be applied because they have reached their limitations. The limitations are wide and varies depending on the joining technology and will be explored subsequently, however, the main limiting factors are geometries needed, swiftness of the process and principally the cost.

1.4. **Challenges of Steel to Aluminium Joining**

As previously stated to make an impact on CO_2 emissions new BIW designs need to incorporate new dissimilar multi-material structures to provide the best lightweight structural performance while being economically viable. The development of a steel-aluminium hybrid BIW is a great leap in this direction, however joining these two dissimilar materials in a way to be applied in high volume manufacturing has not been achieved.

The inherent problem associated with joining dissimilar materials is that the materials are different in nature, with different thermal, mechanical and physical properties. In the particular case of steel to aluminium joining, the intention is to take advantage in their difference in specific modulus, as aluminium has around $1/3^{rd}$ the density of iron (Table 1), allowing a reduction in component weight. The low solubility of aluminium in iron follows from their different electronic configurations and crystal lattices. According to Ryabov [7], at room temperature the coefficients of thermal expansion are quite different for aluminium (23.9×10^{-6} / °C) and steel (11.9×10^{-6} /°C), and as temperature increases there is a corresponding increase in these coefficients, to 31.1×10^{-6} and 14.3×10^{-6} / °C, respectively, at 500°C. Added to this, the differences in thermal conductivity, coefficient of thermal expansion and specific heat capacity between aluminium and steel results in a joint with residual stresses, weld shrinkage, and distortion, all of which are detrimental to the joint. These challenges only take into account the thermophysical properties of these two materials. In the case of fusion welding, as can be inferred from the Fe-Al phase diagram shown in Figure 4, not only can there only be a small amount of Fe dissolved in Al and vice versa, there is the unavoidable formation of intermetallic phases many of which are extremely brittle [9], [24] leading to joints with poor mechanical properties. Intermetallics with higher Al content are associated with the most brittle phases [25]. An additional problem when fusion welding these two materials together is that the refractory oxide film on the aluminium, Al_2O_3, promotes the formation of oxide inclusions in the weld. Given its high melting point of around 2000 ± 30°C [26], the Al_2O_3 film does not melt and dissolve during weld formation, instead of forming Al_2O_3 inclusions in the weld, detrimental to weld quality and properties.

The binary Fe-Al phase diagram (Figure 4) proposed by Kattner and Burton [27] identifies various intermetallic phases that may be formed in a welding process. Table 2 summarises the binary Fe-Al intermetallics formed their properties according to Atabaki *et al* [8]. The brittleness of Fe-Al joints is down to the different crystal structures and hardnesses presented in Table 2. Alboom *et al* [28] concluded that the actual composition of more commonly reported phase of $FeAl_3$ is Fe_4Al_{13} and the Fe_3Al_5 phase is the partially disorganised Fe_3Al_{5+x}[28]. Under equilibrium conditions, the intermetallic phases FeAl, Fe_2Al, Fe_3Al, $FeAl_3$, $FeAl_2$ and Fe_2Al_5 are predicted to be mechanically stable, with the exception of Fe_2Al which is brittle and exhibits the lowest Poisson's ratio amongst these phases by Zhang *et al* [29]. Liu *et al* [30] calculated the mechanical and electronic properties of FeAl, Fe_3Al, $FeAl_3$, $FeAl_2$ and Fe_2Al_5 evidencing that these phases are all thermodynamically stable. This simulation work suggested that these phases exhibit anisotropy in Young's modulus in the following descending order Fe_3Al> FeAl> Fe_2Al_5> $FeAl_2$> $FeAl_3$. In contrast to Zhang *et al* [29], the Fe_2Al phase was not considered in this work.

Table 1 – Physical, mechanical and chemical properties of pure Aluminium and Iron at 20°C [31]

Properties	**Aluminium**	**Iron**
Crystal structure	FCC	BCC
Atomic electronic configuration	[Ne] $3s^2 3p^1$	[Ar] $3d^6 4s^2$
Density	2.7	7.85
Melting point (°C)	660	1536
Specific heat (J/kg K)	930	448
Thermal conductivity (W/m K)	235	79.6
Coefficient of Thermal expansion (Δl/l °C)	23.9×10^{-6}	11.9×10^{-6}
Electrical Resistivity (µΩcm)	2.65	9.7
Young's Modulus (N/mm^2)	6.7×10^4	21×10^4
Ultimate Tensile Strength (N/mm^2)	65	235

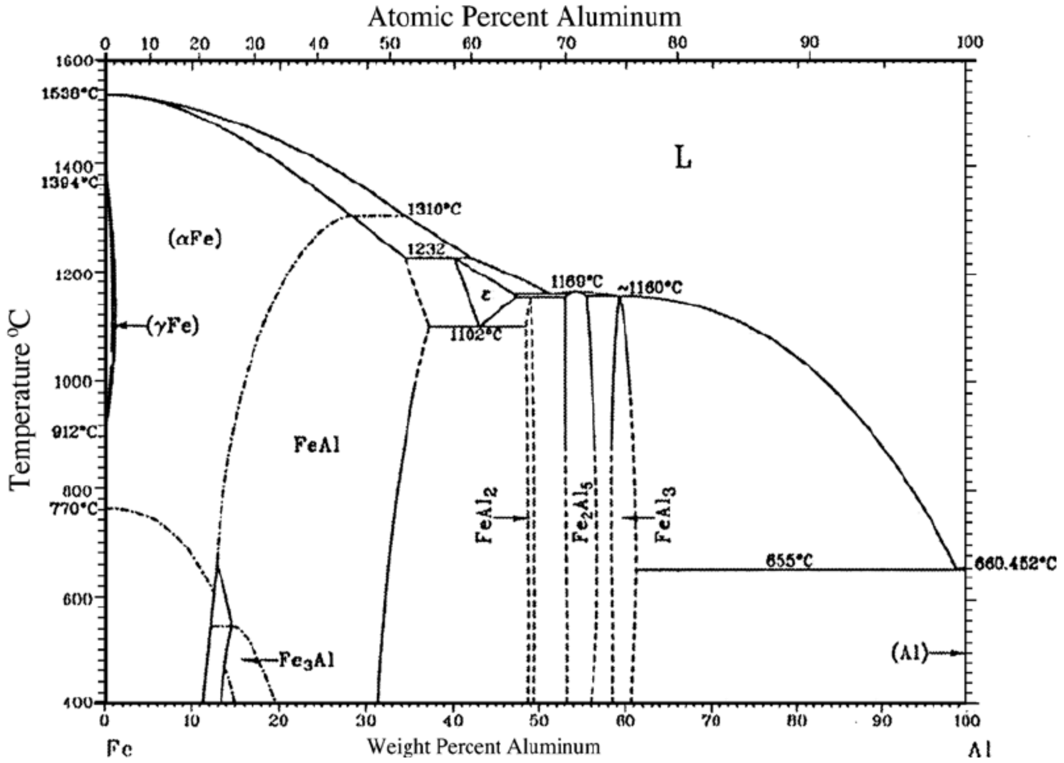

Figure 4 – Binary Phase Diagram Fe-Al [27]

Table 2 – Properties of Fe-Al intermetallics

Phase	**Stability range (at %)**	**Crystal Structure**	**Vickers Hardness**	**Activation Energy (eV)**	**Density (g cm^{-3})**
Fe solid solution	0 – 45	BCC	–	–	–
γ-Fe	0 – 1.3	FCC	–	–	–
FeAl	23 – 55	BCC	470 – 667	2.1	5.37
Fe_3Al	23 – 34	Ordered BCC	330 – 368	–	6.67
Fe_2Al_3	58 – 65	Complex cubic	–	–	–
$FeAl_2$	66 – 66.9	Triclinic	1058 – 1070	–	4.36
Fe_2Al_5 - η	70 – 73	BBC Orthorhombic	1000 – 1158	1.5	4.11
$FeAl_3$/Fe_4Al_{13}[28] - θ	74.5 – 76.5	Complex monoclinic BCC	772 – 1017	–	3.95
$FeAl_6$	–	-	–	1.2	–
Al Solid solution	99.998 – 100	FCC	–	–	–

Therefore in order to form a good weld between aluminium and steel it is critical to understand and control the size and quantity of the Fe-Al intermetallics present [8]. Intermetallic layer thickness greater than 10 µm seriously deteriorates the mechanical properties of the joints [10]. The agreed consensus in the literature is that the main phases are Fe_4Al_{13} and Fe_2Al_5 where the thickness of the intermetallic layer is associated with temperature.

According to Yang *et al* [10] the primary phase formed was Fe_2Al_5 due to its associated low Gibbs free energy, with a growth following an inter-diffusion mechanism, follow by $FeAl_3$ layer phase. In equilibrium conditions, the growth of these layers is followed by the growth of $FeAl_2$ and FeAl at the interface between the Fe_2Al_5 and the steel (Cheng *et al* [32]). This process controls the formation of the serrated morphology initially observed on the steel and for long temperature exposure times the full layer of Fe_2Al_5 is replaced by $FeAl_2$ and FeAl. Springer *et al* [33] observed that solid/solid interdiffusion in the Fe-Al system resulted in the formation of sub-micron sized thin bands of FeAl and Fe_3AlC, at the interface between steel and Fe_2Al_5. Rank *et al* [34] confirmed that the most stable Fe-Al intermetallic phases were $FeAl_2$, Fe_2Al_5 and Fe_4Al_{13}, by synthesising them and determining their heat capacities between 223K to 1370K. Haidara *et al* [35] studied the phase formation of thin Fe-Al films and concluded that the process starts with the formation of metastable phase $FeAl_6$ in the interval of 300 °C to 360°C, followed by the formation of Fe_2Al_5, except in the case of low Fe content, in which $FeAl_6$ remained stable until 600°C decomposing into $FeAl_3$. Ding *et al* [36] observed the interface of solid steel/liquid aluminium with temperature held at 850°C, showing that the reaction process started with the growth of finger-like Fe_2Al_5 into the steel and the melt without dissolving. When Fe_2Al_5 began melting the growth rate increased until the local Al depleted and the process became governed by the Al diffusion.

Due to the higher melting point of Fe, the welding interaction of the Fe-Al system will be between solid Fe and molten Al. Therefore, according to the literature the process for intermetallics formation will start with Fe diffusion into Al forming the Fe_2Al_5 (Eq1). The process is then followed between the interaction of the newly formed Fe_2Al_5 phase with the molten Al to form the Fe_4Al_{13} (Eq2). Both Fe and Al diffuse through the phases formed to continue the process. In this way 3 interfaces are formed Fe/ Fe_2Al_5; Fe_2Al_5 / Fe_4Al_{13}; Fe_4Al_{13}/Al [37] controlled by Fe diffusion. Based on the model proposed by Coulet [38] for simultaneous diffusive growths of several phases follow a parabolic growth rate, Bouche [37] verified that Fe_2Al_5 formation is governed by a parabolic law after an initial short ($0<t<30$s) transient period of faster kinetics. Primary kinetic growth starts without significant dissolution in the liquid. Fe_4Al_{13} follows a linear constant growth rate after equilibrium is reached ($t<1$ min) and is significantly smaller compared to the Fe_2Al_5 phase and therefore tends to be disregarded for growth kinetics prediction [39]. Rong *et al* [40] proposed that the finger-like formation of Fe_2Al_5 layer was associated with different governing growth kinetics, where the base of the finger (closer to the Fe) was governed by the interfacial reaction and diffusion, while the tip of the finger (closer to the Al) was only governed by the interfacial reaction.

$$2\,Fe\,(s) + Liq \rightarrow Fe_2Al_5 \qquad \text{Eq (1)}$$

$$Fe_2Al_5 + Liq \rightarrow Fe_4Al_{13} \qquad \text{Eq (2)}$$

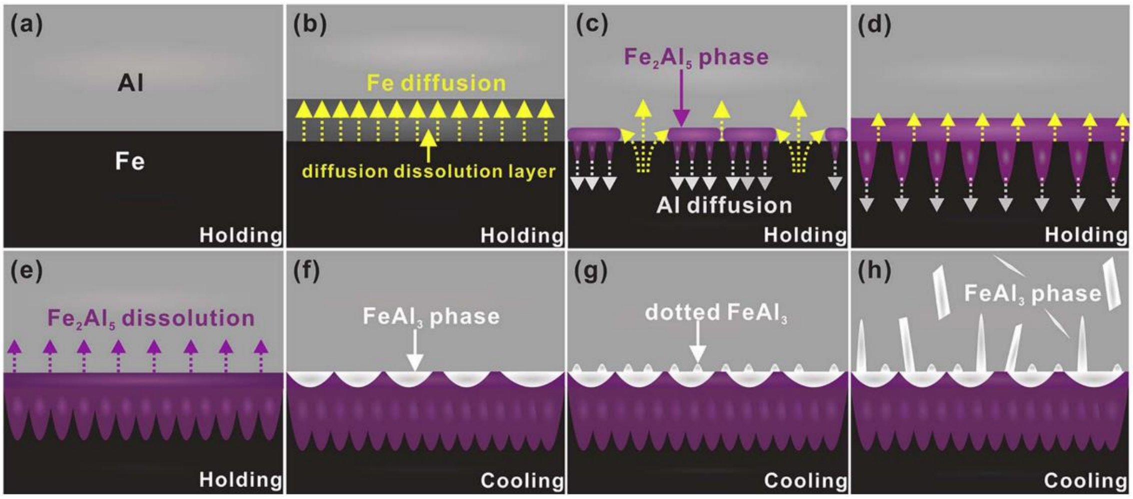

Figure 5 – Schematic representation of the intermetallic layer growth of Fe-Al system (Ding *et al* [36]). Process is characterized by Fe diffusion into liquid Al (a-b); followed by the formation Fe_2Al_5 (c-d); subsequently Fe_2Al_5 dissolved (e); followed by formation of Fe_4Al_{13} at the interface (f) and dispersion into the Al melt (g-h)

The growth kinetics equation for this system is:

$$Z_a = K\ (T)\ t^{\kappa} \tag{Eq (3)}$$

$$\log(Z_a) = \kappa \log(t) + Log(\ K\ (T)) \tag{Eq (4)}$$

where Z_a is the thickness of phase a (μm); K is the growth rate constant, T is the absolute temperature in Kelvin (K); t is the time (s) for reaction; κ is a constant; the growth is controlled by the interface when $\kappa = 1$, controlled by the diffusion process $\kappa = 0.5$ [40]. The rate constant is determined from the Arrhenius equation at various temperatures to determine dependence of growth rate constant *K(T)* from temperature *T*.

$$K\ (T) = K_0 e^{-\frac{Q}{RT}} \tag{Eq(5)}$$

$$\log(K\ (T)) = \log(K_0)\ - \frac{Q}{RT} \tag{Eq(6)}$$

Where Q is the activation energy (J mol^{-1}) for the growth of the layer, R the gas constant (8.314 $J{\cdot}K^{-1}\ mol^{-1}$), and K_0 is pre-exponential factor (constant). Combining both equations, it is possible to obtain the time dependence for the Arrhenius equation, and therefore the growth prediction phase can be used with the thermal history of the process [T(t)].

$$Z_a = K_0 e^{-\frac{Q}{RT}}\, t^{\kappa} \qquad \text{Eq(7)}$$

$$\log\,(Z_a) = \kappa \log(t) + Log(\,K_0) - \frac{Q}{RT} \qquad \text{Eq(8)}$$

Current literature focusses mainly on equilibrium based kinetics, where the bulk of intermetallic layer formation is associated with Fe_2Al_5 and the other phases can be negligible. Figure 6 shows a summary of the impact of short equilibrium growth kinetics and long equilibrium growth kinetics from different sources. Rong [40] proposed that initial stages exhibit a linear growth because the time exponent (κ) is 1, therefore growth is controlled by the interface, which is then converted into a parabolic growth are for longer times becoming a process driven by diffusion control.

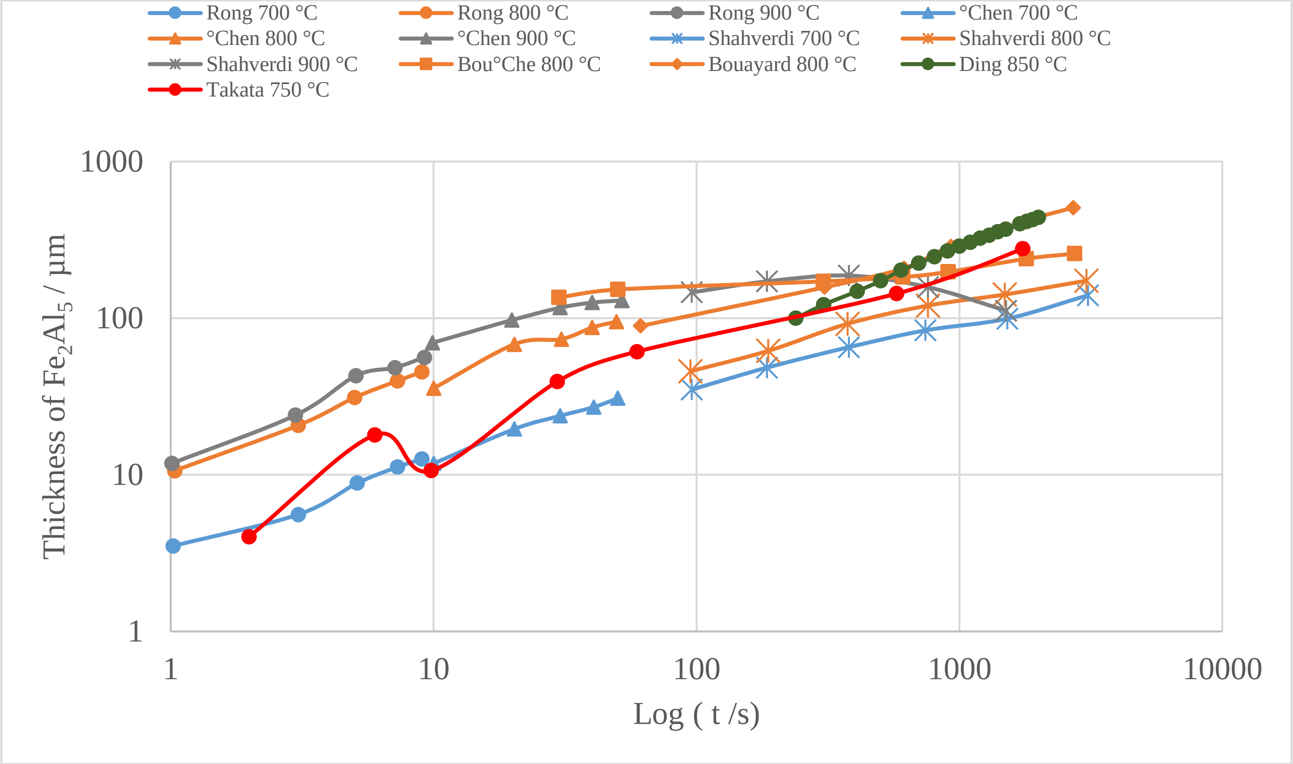

Figure 6 – Relationship between time at different temperatures and growth of Fe_2Al_5 layer based from [37], [39]–[43]

The described Fe-Al system did not consider the presence of other elements of significant importance that can be present in the practical alloys. These elements tend to be zinc in the case of zinc coated steel and 7xxx aluminium alloys and Si commonly from 5xxx and 6xxx series aluminium alloys.

1.5. Influence of Si on Fe-Al intermetallics

Springer *et al* [33] observed in the Fe-Al system that the solid/solid interdiffusion formation of sub-micron thin bands of FeAl and Fe_3AlC that are formed in the interface of steel and Fe_2Al_5, however with the addition of Si it was shown a reduction of the kinetic rate between solid/liquid interdiffusion and the main phases are Fe_2Al_5 , Fe_4Al_{13} and Al_8Fe_2Si. Lemmens *et al* [44] showed that a Si content of 0.3%wt led to Si enrichment at the interface between Fe_2Al_5/Fe_4Al_{13}, suggesting that this may then act as a diffusion barrier to Al, then controlling the growth of the intermetallic Fe-Al phases. If Si content is higher than 5%wt the formation of phases changes to $\tau_1(Fe_3Si_3Al_2)$ phase at the Fe_2Al_5 layer and the $\tau_5(Fe_2SiAl_8)$ phase between the Al and Fe_4Al_{13} layers[45]. Si influences the parabolic growth rate of Fe_2Al_5, reducing the overall thickness of that layer, despite suggesting that increasing Si content decreased the activation energy [45]. Yin *et al* [46] confirms that increasing the Si content decreased the growth rates of Fe_2Al_5 and $FeAl_3$. Furthermore, the ternary Al-Fe-Si phase $\tau_1(Fe_3Si_3Al_2)$ formed in the Fe_2Al_5 layer changing the normal finger-like growth morphology of Fe_2Al_5 into a coagulum form. The roughness at the Fe_2Al_5/steel interface is reduced due to the reduced thickness of the intermetallic Fe-Al layers but also by the ternary Fe-Si-Al phases (Cheng *et al* [47]). Jiang *et al* [48] proposes that Si addition restricts the propagation of Fe_2Al_5 due to its low solubility in the Fe_2Al_5, and impeding Al diffusion, instead then favouring the formation of Fe-Al-Si ternary phases. Takata *et al* [49] concluded that Fe_4Al_{13} changed from a discontinuous to a continuous layer when the Si content is increased by 5%wt blocking Fe diffusion.

In sum, Silicon additions will play an important role in the Fe-Al intermetallic formation system not only due to the formation of the ternary Fe-Si-Al phases but also for the apparent barrier effect. During the formation of the Fe-Al phases, Si content decreased the activation energy favouring their formation [45]. Si has low solubility in the Fe_2Al_5, therefore there is an increase in the local concentration of Si until the critical concentration for the formation of Fe-Si-Al phases. From the works [33], [44]–[46] it is evident that local Si concentration will influence the Fe-Si-Al phases $\tau_1(Fe_3Si_3Al_2)$ phase at the Fe_2Al_5/ Fe_4Al_{13} interface and $\tau_5(Fe_2SiAl_8)$ phase at the Fe_4Al_{13}/Al interface. Figure 7 shows the impact of a Si addition of 5%wt vs pure aluminium, where both thicknesses of the Fe_2Al_5

and Fe_4Al_{13} have decreased although the Fe_2Al_5 growth rate from 0.58 to 0.75, while the Fe_4Al_{13} growth rate decreases from 0.35 to 0.19. The change to a continuous Fe_4Al_{13} layer observed by Takata *et al* [49] reinforces the idea of the formation of a barrier that mitigates Fe diffusion controlling therefore the intermetallics growth and thicknesses (figure 8).

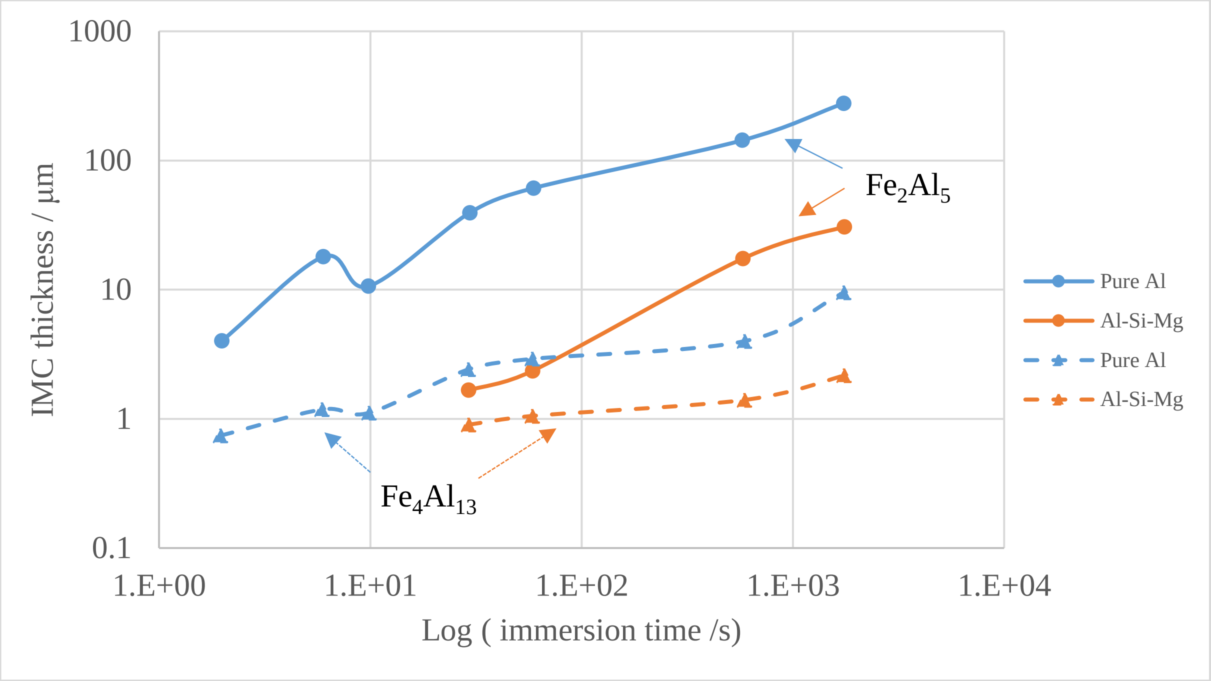

Figure 7 – Relationship between immersion time and growth of Fe_2Al_5 (line) and Fe_4Al_{13} (dash) layers based in pure Al and Al-Si-Mg alloy from Takata et al [49]

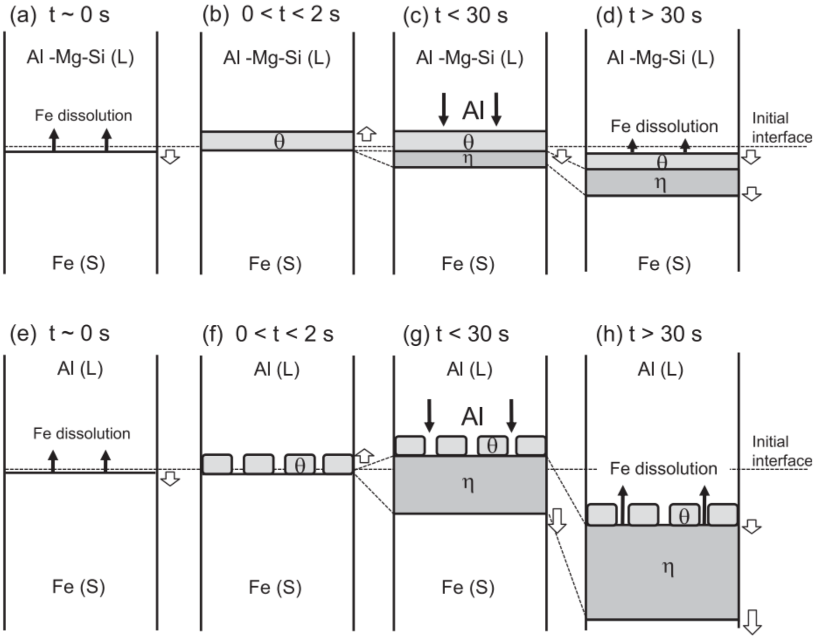

Figure 8 – Schematic illustrations of intermetallic growth at the interface of Al melt and steel. (a-d) formation of compact intermetallics in Si containing Al melt in which Si is believed to act as a barrier for free growth of intermetallic phases. (e-h) Free growth of intermetallics in pure Al melt illustrated by Takata *et al* [49]. η - Fe_2Al_5 ; θ- $FeAl_3$/Fe_4Al_{13}

1.6. Influence of other elements on Fe-Al intermetallics

The addition of Zn as in the case of galvanized Zn-coated steel in a solid-liquid interaction is proved to be beneficial due to rapid dissolution of zinc allowing a controlled formation of even and regular reaction layers [50]. The Fe-Al intermetallic growth exhibited an accelerated growth in this case, which may be caused by the interaction of Zn with the structural vacancies in Fe_2Al_5. However, if a higher content of Zn is added (e.g. the addition of Zn to a welding filler wire), it is possible to control the Fe_2Al_5 and $FeAl_3$ phases, by forming a $Fe_2Al_{5-x}Zn_x$ and dispersed $FeZn_{10}$ [51]. Improvements in joint shear performance can be achieved by improving bonding quality by the formation of $Fe_2Al_{5-x}Zn_x$ phase and the mitigation of crack propagation observed by $FeZn_{10}$ [51].

Other elements exhibit some control of Fe-Al intermetallic phases as in the case of Yousaf *el al* [52] proved that in a hot-dip aluminization process the addition of 11%wt Cu to Al resulted in the thickness reduction of the intermetallic layers of up to 75%, due to the formation of Al_2Cu and Al_7Cu_2 on the outer coating (Al side). This may be caused by these Al-Cu layers then blocking the diffusion of the Al, hindering the continued growth of Al-Fe intermetallics. Zheng *et al* [53] used density functional theory to study the properties of binary Fe-Al intermetallics modified by ternary additions. They concluded that additions of Cr, Ti and Co create the most stable FeAl-X intermetallics (X= Cr, Ti, Co), which have increased ductility with increased atomic mass.

2. Research question to be addressed:

The research question for this PhD has a direct link with industry and is “how to create high integrity multi-material joints in a way suitable for a low-cost high-volume car production line?”

In order to profit from a truly multi-material car body and achieve the goals of minimum weight with maximum performance, within an economical production line, car manufacturers require their structural car bodies to be manufactured from a range of materials, namely; formable grades of steel, high strength steels, press hardened (quenched) ultra-high strength steels, aluminium sheets of 5xxx, 6xxx and 7xxx, cast and extruded aluminium alloys. These materials are required to be joined in a very broad range of combinations and can be arranged in complex stack ups of up to 3 (and sometimes even 4) materials within one joint. At present, the technologies available for joining in car manufacture are only able to address a fraction of the spectrum of joint combinations required.

The technologies available for joining dissimilar materials for car body production use a range of mechanisms to create joints, from; heating via electric current or friction, to plastic deformation to create a lock or punching a hole and filling the gap with a metal element (rivet). All of these technologies work with materials of certain properties and are limited by other factors including; material tensile strength, plastic formability, surface properties, total joint thickness, number of sheet interfaces.

The key objective of this PhD is to develop a novel approach to allow the new generation of steel and aluminium materials to be joined. The process developed shall focus on the following factors:

- The mechanical performance of the joints
- The range of materials combinations that can be joined (in both 2 and 3 sheet stacks)
- The order in which materials are aligned within the joints (joint directionality requirements).
- The speed of the process
- The cost of applying the process

This document will therefore not focus on fatigue or corrosion resistance or ease of disassembly. To achieve this goal research question needs to be de-convoluted into intermediate steps:

- ❖ Evaluation of current mechanical fastening technologies for dissimilar material joining

The theme of dissimilar material joining is not new, especially in steel to aluminium joining. There are a number of mechanical fastening techniques already established, however they all have certain disadvantages. Aside from the comparatively high costs associated with the processes, they present huge limitations in terms of:

- Geometry and configuration of the place to be joined,
- The materials used and their thickness,
- The joining mechanism and application method

Evaluation of currently available techniques needs to be performed to determine what materials and thickness can be joined, what is the joint quality and performance. To make this evaluation, a selection of different steels (from formable to high strength steels) and a range of aluminium alloys are joined using the established techniques. This would take into account 2 sheet and 3 sheet material combinations. This will enable the identification of the current limitations in material stacks that can be joined but also what material grades can be joined with the current techniques. During these experiments, the mechanical performance will be assessed and analysed to understand and find factors where an improvement can be realised. Due to the links of this PhD to industry, the joint quality together with cost per joint and process time will also be analysed.

- ❖ Evaluation of current techniques for dissimilar material joining with a structural adhesive

All experiments performed in the previous step are analysed to check the effects of hybrid joining in combination with a structural adhesive. This will allow the evaluation of the effect of adding a structural adhesive to current techniques. Classification of joint quality together with cost per joint will also be addressed. In the case of dissimilar metal joining in a car body, a structural adhesive will almost always be used. This is because joints in dissimilar materials often have inferior strength when compared to joints in the same material. And, critically, dissimilar metals with greatly different electrode potential (such as steel and aluminium), pose a significant corrosion risk when in intimate contact and in the presence of an electrolyte. The addition of an adhesive to the joint is known to prevent water ingress into the joint (removing the electrolyte) and greatly reduces the risk of corrosion.

- ❖ Check the feasibility of adapting Resistance Spot Welding (RSW) for dissimilar material joining.

At the moment resistance welding is traditionally the technique of choice for thin metal joining in the automotive industry. Over the last century mass production of cars has been enabled as a result of high speed, reliable, easily automated joining of low carbon steels using the resistance spot welding process. Therefore, production plants already have the facilities for resistive spot welding in house to adapt this process for dissimilar material joints. During the course of this PhD, the feasibility of adapting RSW has been assessed in order to try and produce a novel approach for dissimilar material joining. The performance of joint strength as a function of current, electrode force and pulse duration is also assessed.

3. Dissimilar materials joining

There are several approaches for dissimilar materials joining; the three main families of techniques are; the Fusion State, the Solid State, Mechanical Joining. In the fusion joining processes, which are also known as liquid phase joining, in which at least one of the materials is melted using heat input. Solid State Joining, where there is a controlled minimum amount of heat input to soften and join the materials, there is no liquid phase in this process. In Mechanical Joining process, a mechanical interlock is created between the materials.

3.1. Fusion State Joining

Fusion welding represents a family of technologies that uses heat to join two or more materials by heating them to the melting point. This family of processes is normally defined in accordance with the heat source:

- Arc Welding: It is a welding process that creates an electric arc between an electrode and the base material to melt the metals at the point of contact. The electrode can be a non-consumable (tungsten) and consumable (filler). This branch includes the familiar technologies Metal Inert Gas Welding (MIG), Metal Active Gas Welding (MAG), Tungsten Inert Gas Welding (TIG), among others.
- Resistance Welding: It is a welding process that takes advantage of the electrical resistance of the materials to produce heat by passing high levels of current to produce heat. This branch includes Resistance spot, seam and projection welding.
- Power Beam Welding Processes: It is a branch of technology that uses high energy power beams such as lasers or electron beams to produce heat to melt and weld materials.

3.2. Solid State Joining

In this family of techniques, the metallic bond is formed without the transformation to the molten state; the joint is created by solid state diffusion. In this case, the energy added to the system is usually of thermal and mechanical nature, either by frictional forces or by pressure employing a separate heating source (contact heating, resistance heating, furnace heating etc.).

The pressure joints are created when two materials are pressed together in order to create an intimate contact between them, with sufficient local energy to achieve a joint. This contact energy needs to be of sufficient force in order to remove the oxide layers present in the materials being joined. These pressure induced joints are classified according to the method in which the force is applied, if it is just mechanical force without heat input is called Cold Welding; if an explosive is used to provide the pressure the process is called Explosion Welding; if the pressure applied is done by a magnetic field the process is called Magnetic Pulse Welding.

A friction induced joint is when two materials are rubbed to generate heat. The heating is localized and the material reaches a superplastic state. Depending on the technique, when the material is in its superplastic state, it can be pushed aside so that oxide films in the contacting surfaces can be displaced and can be mixed to form the metallic bond with the remaining material. Friction induced joints are classified according to the method of application of the frictional forces: when two materials are rubbed together in a linear way it is called linear friction welding, if one of the materials is rotating it is called rotating friction welding, if ultrasound is used to induce the friction then it is called ultrasonic welding, if a third (rotating) element is used to create the frictional heating and mix the two materials, before being retracted from the joint, it is called Friction Stir Welding.

3.3. Mechanical joining

For this family of joining techniques, the joint is created by achieving a mechanical interlock between the materials being joined. This interlock can be created by the addition of an external element to the joint or by plastic deformation of the materials to form a lock. The family of mechanical joining process is divided into two types by the mechanism of joining:

- Form fit joints, where deformation of material creates a mechanical lock, such as Self-Piercing Rivets (SPR) or Flow Drill Screws (FDS), or,
- Force fit joints, where a locking force is generated by a joining element, such as bolting or blind riveting.

The main advantage of using the material plastic deformation to form a lock is that it is element-free, therefore no addition of weight when the joint is formed and cost associated with consumable fasteners can be eliminated. The major downside is that the joint does not provide the same magnitude of joint quality and strength as with the addition of an external element. Some examples of the element-free joining and with the addition of an external element are presented in Figure 9.

Element-free processes

- Clinching
- Hemming
- Interference fit

Processes requiring a 3rd Element

- Blind riveting
- Blind rivet nuts
- Flow drill screws
- Flow drill riveting
- Friction element welding
- Tack high speed joining
- Self-piercing Riveting
- Self-piercing Solid Riveting
- Clinch riveting

Figure 9 – Examples of element less joining processes and the processes requiring 3rd element.

3.3.1. **Clinching**

This is a very simple process, requiring a punch and die and the steps in this process are displayed in Figure 10. The joining process is achieved by plastic deformation where the sheets are held together between the punch-holder and the die (Stage 1), and then the punch extrudes the materials into the die. This will force the materials to deform and form an interlock without the need of adding an element [54]. The sheet contacting the punch undergoes thinning (which can lead to fracture) due to the high deformation and localized strain.

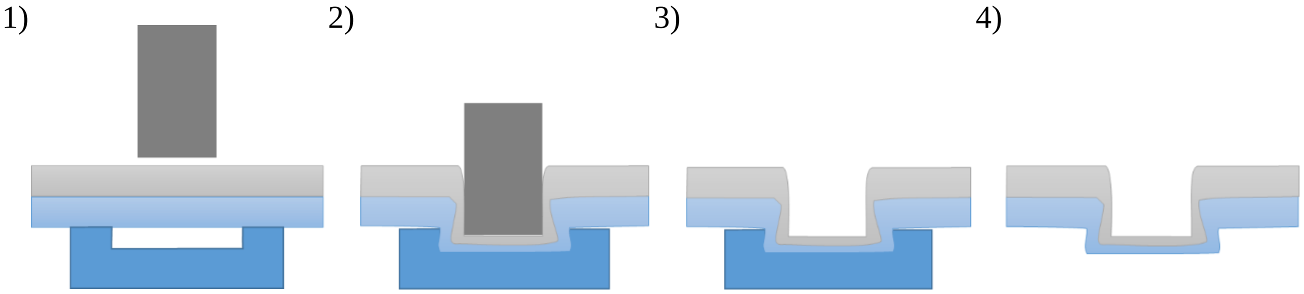

Figure 10 – Cross-sectional view of clinching tool setup which involves four Stages (1-4) from assembly to produce a joint.

Therefore, this technology is limited by the formability of materials and the material thinning from the resulting plastic deformation. The mechanical strength of clinched connections (joints) is dependent on the amount of interlock from the resulting neck thickness at the punch-sided sheet [55],

[56]. The joint strength depends on the punch-die geometry, the material properties, material thickness and the degree of friction between contact surfaces [57]. There is a wide selection of punch/die geometries and configuration that require validation to achieve the correct interlock shape and the joint. For the automotive industry a round clinch joint is the most used, which does not cut through the top material. In other industry sectors, a clinching process can be used that cuts through the upper sheet.

A large body of development work has been performed on optimisation of parameters such as die shape, punching depth, punch shape and simulation of the overall process for steel to steel and aluminium to aluminium joint configurations [55], [58]–[61]. Lambiase *et al* showed that extendable dies produce larger and therefore better interlocks compared to fixed dies for steel joining [62]. Chan-Joo Lee *et al* [63] showed that it was possible to join DP780 steel and AA5052 aluminium with poor interlocks and at the same time concluded that interlocking length increased with die length but also increased cracking in the lower sheets and the neck thickness increased with an increase of the punch radius. Therefore to predict joint quality, each sheet thickness, properties, material combination and a selection of fracture modes need to be taken into account. Clinching of materials with reduced ductility tends to lead to fracture of joint at the punch-sided sheet due to high strain or neck cracking due to high local stresses during plastic deformation [64]. One alternative to solve these issues is to apply the process with a hole in the material contacting the die [65], this way the interlock is created by plastic deformation of the top material through the hole of the bottom one to form the interlock in materials with low formability. Alternatively, another possibility to improve formability is to heat the sheet locally and therefore allow an interlock to be formed. Lambiase *et al* [66], Zhang *et al* [67] and Osten *et al* [68] have studied the impact of local heating with different sources (e.g. local heat gun, resistance heating and laser source) where it was concluded that it is possible to expand the limits of this technology and reduce joint local stresses. These results were achieved as a result of the increased ductility of metals at elevated temperatures.

3.3.2. **Blind Riveting**

Solid rivets were a very popular technology during the industrial revolution, enabling some iconic constructions such as the Eiffel Tower in Paris and Dao Luis Bridge in Porto, Portugal. This type of fastener was used to make a permanent joint, which was achieved by drilling a hole in the materials being joined, and then a cylindrical shaft with a head (rivet) is placed into the hole. Then the head is secured in place while the other side is hammered to form the second head and the rivet is fixed in place, as is represented in Figure 11.

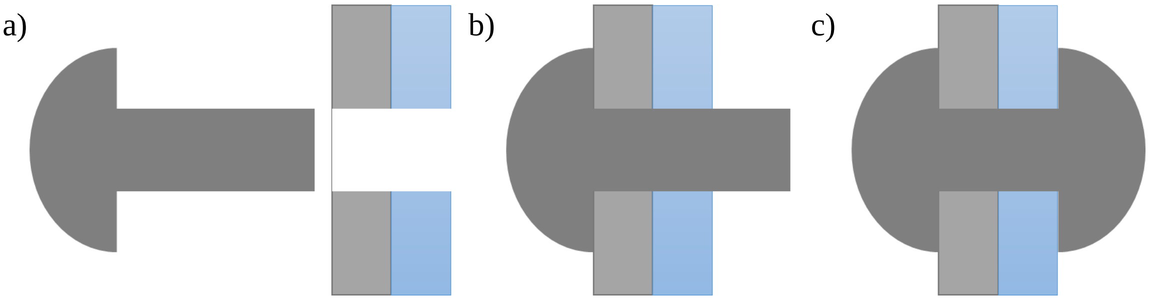

Figure 11 – Cross section schematic representation of the riveting process: a) shows a solid rivet with a pre-drilled sheets that will be joined; b) the rivet goes in the hole; c) the rivet is hammered to form the mechanical lock.

Blind rivets consist of a variation of the normal solid rivet that was adapted for single side application, e.g. "blind" from one side. The development of blind rivets started around 90 years ago and today blind rivets are common across the industry and importantly can be used to join dissimilar materials. Figure 12 is a schematic representation of this process. In this case, as shown in Figure 12.a, a hole is formed in the materials being joined, where the bottom material is not drilled through, then a steel ball is placed in the hole where afterwards a solid tubular pin with a hollow end is hammered. The applied force in the rivet forces the steel ball into the recess of the rivet to expand and lock it in place at the bottom of the rivet, with the top part expands to lock the top material. Depending on the application there are other locking mechanisms [69], [70].

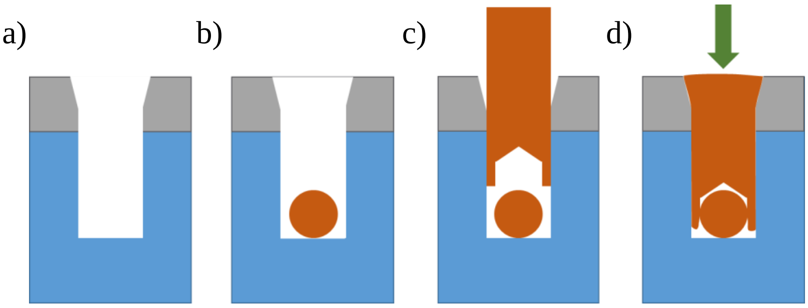

Figure 12 – Cross section schematic representation of riveting into a blind hole: a) a hole is formed in the materials to be joined with a recess on the top; b) a steel ball is put into the hole; c) the rivet is put into the hole; c) rivet is forced downwards crushing the steel ball and making the rivet expand and lock in place

This idea evolved into the commonly known as blind rivets. Blind rivets consist of a two-part component comprising of a rivet body and a mandrel as shown in Figure 13. The joint is made when the mandrel is driven through the rivet body expanding it and forming the locking mechanism. The mandrel has a grove where it will break when the applied force exceeds its rated force. The rated setting force is controlled by the grove size and is directly related to the breaking force.

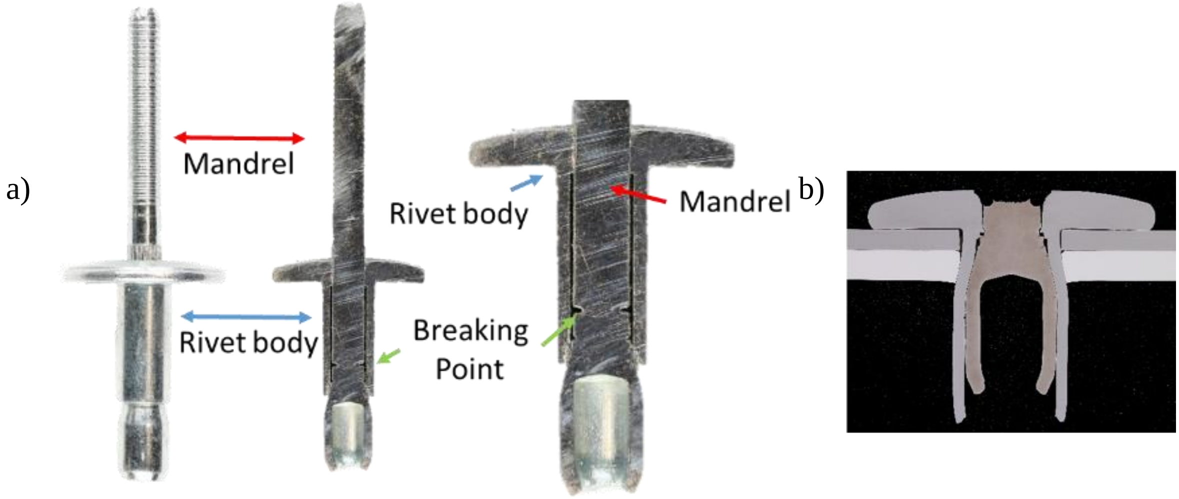

Figure 13 – Photographs of (a) blind rivet components and (b) dissimilar sheets joined with blind rivet process.

For the blind riveting process, the sheet materials to be joined need to have a pre-formed hole. Then the blind rivet is set in place, where the jaws of the blind riveting gun holds the rivet head down while the mechanism pulls the mandrel up to form the lock. When the rivet is set and there is a build-up of force, then mandrel will break leaving the joint in place [71], [72]. This process is illustrated in Figure 14. These improvements were made to blind rivet for faster deployment, nevertheless, the setting process can be automated, either by using manual hand tools [73] or automated columns for the aerospace industry [74]. Despite these improvements, this technology is not fast enough for the high-volume production in automotive industry.

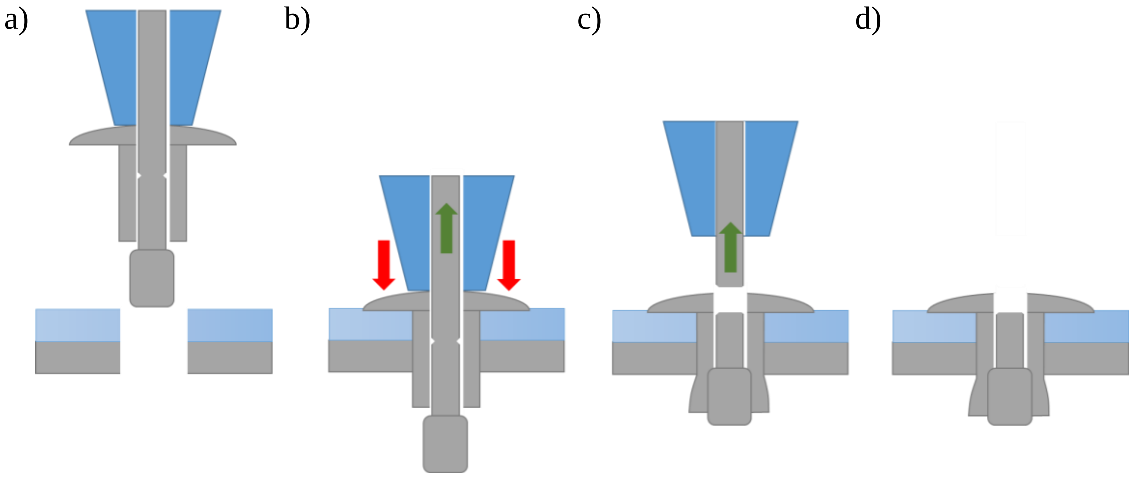

Figure 14 – Cross section schematic representation of blind riveting process: a) positioning; b) setting the rivet; c) breaking mandrel; d) joint finalised

Mucha and Witkowski [75], [76] have discussed the mechanical failure behaviour of dissimilar joints of soft steel and 5xxx series aluminium with various joints configuration and identified that, during loading, maximum load-bearing capacity is reached at the sheet material limit (from the rivet secondary head) and the tensile shear strength limit of the rivet tubular part of the blind rivet. The same evidence of local stresses were shown by Sanjaykumar and Mahesh [77] in their work that performed fatigue analysis based on simulation coupled experimental data. Mechanical performance of a single blind rivet joint is shown [78] to be strongly influenced by flatness and roughness of the sheets and they can cause loss of performance up to five times compared to a dual riveted symmetrical joint. This is caused by the resulting deformation around the rivet by the application process. Kelly and Costello [79] developed a model that predicts rivet shape deformation with the limitation of accurately predicting the forming forces and rivet failure. Depending on the ratio between the bottom (t_2) and top (t_1) sheet thicknesses, in tensile shear loading of blind rivet joints, three different failure modes are observed [11]. For $t_2/t_1 = 1$ there is the rivet pullout from the lower sheet, for $(t_2/t_1) \geq 1.5$ there is load bearing on the top sheet and rivet tensile shearing from the top sheet and for the case of $1<t_2/t_1 <1.5$ there is a mixed mode failure comprised of rivet tilting/rotation and partial tensile shearing of the rivet head.

In sum, blind rivets have the great advantage of being a one-sided process that in theory can join any material combination provided that a pre-formed hole can be made and the materials are inside the rivet griping range. However, drilling or punching the components will increase the processing time to an already slow process. In automotive production line the holes are performed at the same time as stamping occurs or punched prior to components assembly, this, in turn, causes misalignment of holes in an automated robotic system. Another limitation is the weight of the blind rivet because it has a huge impact for being too heavy, especially for lightweighting solutions. As for quality control the joining process can only be monitored by analysing the mandrel displacement vs measured load curve and this does not provide an efficient certification of joint quality, instead this assumes that the rivet has a greater probability of being set correctly if the measured curve follows the same consistent behaviour. Therefore, no non-destructive technology is available for joint quality monitoring.

3.3.3. Self-Piercing Riveting – SPR

As the name suggests this technique is a form of riveting with the main advantage being that there is no need for a pre-drilled hole. Semi-tubular rivets that are partially hollow with a cutting edge are used to pierce the material. The SPR rivets are forced into the material stack, forcing them into a die as is illustrated in Figure 15. During this process there is a material build-up in the hollow SPR rivet, which creates an opposing force causing the rivet to flare, which creates an interlock between the bottom sheet and the flared part of the rivet.

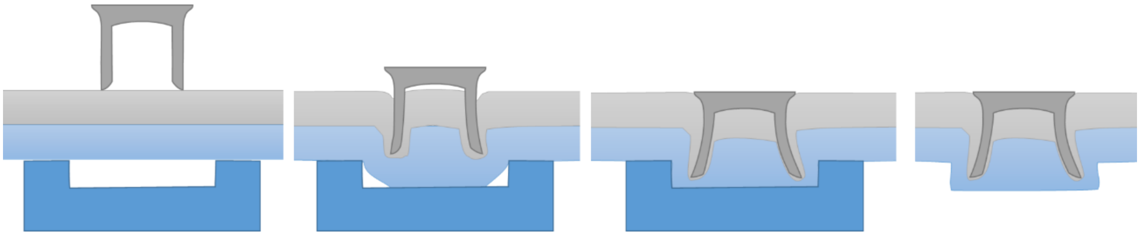

Figure 15 – Schematic representation of the SPR process

This technique must be tailored to the geometric and mechanical properties of the materials to be joined, therefore a combination of different rivets with different lengths, different internal and external diameters, materials and properties as well as die geometries are available. This means it is necessary to determine the suitable set of rivets dies and parameters for each individual application. To improve joint quality, Han *et al* [80] focused on geometric parameters, such as raised height of concave die, cone radius, cone angle, draft angle, fillet radius, depth and diameter of the concave die using finite element simulation to optimize the concave die. Neugebauer *et al* [81] focused on the effect of riveting velocity on dissimilar steel to aluminium joints and the penetration at non-uniform velocities. This technique is already well established for joining of mild and high strength steels with different aluminium alloys[81]–[87], however it was not found to work properly for advanced high strength stainless steels (AHSS). New developments to expand the limitations of materials that can be joined and improve the interlock are being explored. In the case of friction SPR where rivet rotates at high speeds and penetrates through frictional heated and softened materials and improves setting and interlock [88]. Similar approaches have been investigated but using a laser [89] and induction pre-heating conditions [90] verifying the possibility of expanding technology limits.

3.3.4. **Self-Piercing Solid Rivet – SPSR or Solid Punch Riveting**

Due to the challenges associated with joining low formable materials with a SPR process, a variation of SPR was developed but using a solid SPR[91]. In Self-Piercing Solid Rivet or Solid Punch Riveting a solid rivet is driven through the material stack, punching the material out into a die. The joint is formed by deformation of the bottom material (Figure 16), which locks into a ribbed profile on the rivet body. Therefore the lock is obtained by the axial force exerted by the material compression of the rivet and the axial tensile stress in the rivet [92].

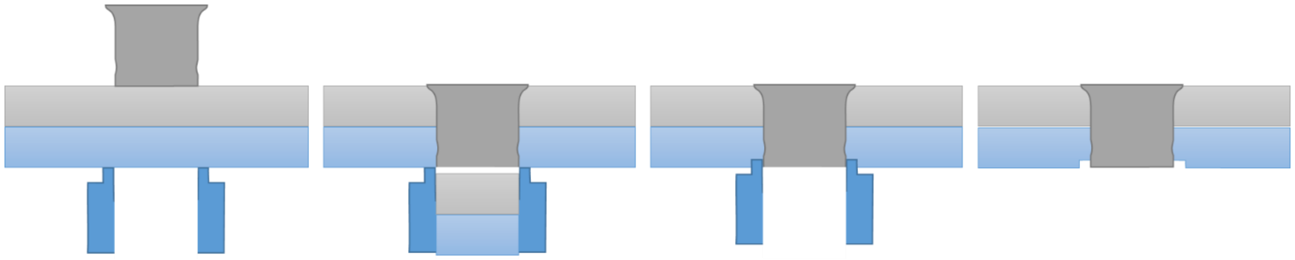

Figure 16 – Schematic representation of the Self-Piercing Solid Riveting Process

Mucha [93] showed that the setting (pressing) force is a critical part of the application and tool life, which directly correlate with rivet geometry. The grooving presented in the solid rivet is directly related to the filling of the groves by the bottom sheet. According to Jäckel *et al* [94], high setting speed can improve joint performance. Mucha [95] showed that increasing the pressing force induces the highest stress concentrations towards rivet grooves improving joint performance however it also increases the residual stresses in the rivet. It was also shown that the rivet shearing is associated with the combined contribution of elastic and plastic strain.

3.3.5. **Clinch Riveting**

A cross-developed technology based on self-piercing rivets and clinching has been developed to improve clinching performance. This technology comprises of a normal clinching process, where a solid cylindrical rivet is pressed-in into the material. The back face of the joint is opposed by a 4 bladed square die, the blades are mobile expanding outwards in order to give the necessary displacement to form a joint. In this case the solid rivet does not cut through the materials, instead it deforms and fills the cavity created by the clinching process (Figure 17). By adding the solid rivet it is possible to improve the joint performance by providing extra support to the necking effect created during the clinching process.

This process never gained much interest in academia however Mucha and Witkowski [96] and Kaščák and Spišák[97] proved the benefits that the clinch riveting can offer compared to clinching. Mucha has shown that the joint has an improved interlock compared to clinching alone because the rivet is set to an extreme that destroyed the clinching locking mechanism, but the rivet forms the necessary lock in its place.

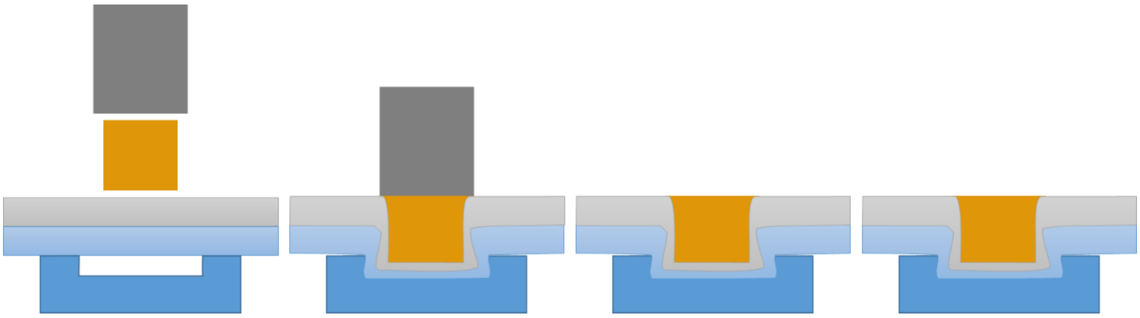

Figure 17 – Schematic representation of the clinch riveting process

More recent development of clinching rivet is seen in the work from Chen et al [98]–[101] which comprises of a reshaping behaviour on the clinch joint. Chen et al starts with the formation of a clinch joint followed by adding the clinch-rivet in a secondary stage with the usage of a flat die. This process, therefore, improves the locking mechanism by flattening the clinch protrusion and leaving the clinch rivet in place. However, being comprised of a two-step process this variation is not attractive for adaptation in industry.

3.3.6. **Flow Drill Screw (FDS)**

Flow drill screwing is a solid state technique that does not involve melting the material, instead, it uses the frictional energy to heat the material to reach a superplastic state in order to shape it to the required form. This technology is used for formable materials by applying a friction drilling mechanism to flow and pierce the material, so the joint can potentially be located wherever the screw tip is placed. Friction drilling, also known as thermal drilling consists of a conical tool that applies pressure and rotation to generate heat locally [102]. In this process, during drilling with a screw at first, the heat-affected zone (HAZ) softens, then when pressure is applied by the screw, the HAZ deforms and forms a hole and the screw penetrates into the weld material through this hole [102]. The deformed material forms a joint with the screw and the material. It is a clean process that does not produce chips or swarf, instead the displaced material is drawn out around the screw tip, which is favourable in certain industry processes, particularly automotive. The chip formation is unacceptable in an automotive production line because it creates contamination and these debris cause disturbances in the paint layer. Therefore, the tip of the screw is designed to allow friction drilling of the workpiece. In this sense the flow drill screw process consists of a screw with a sharp and unthreaded tip, as illustrated in Figure 18 a, which is pressed into the surface of the material and by applying high-speed rotations frictional heat is generated. The sheet material softens due to frictional heat and by applying downwards force the screw is able to flow (Figure 18 b, c) and form the thread locking the screw in place (Figure 18 d) [103]. However, some materials do not have the sufficient ductility or are too hard for the flow drilling process to work therefore a pre-formed hole is required for ease penetration of screw and the joint is made through the hole as is displayed in Figure 18.

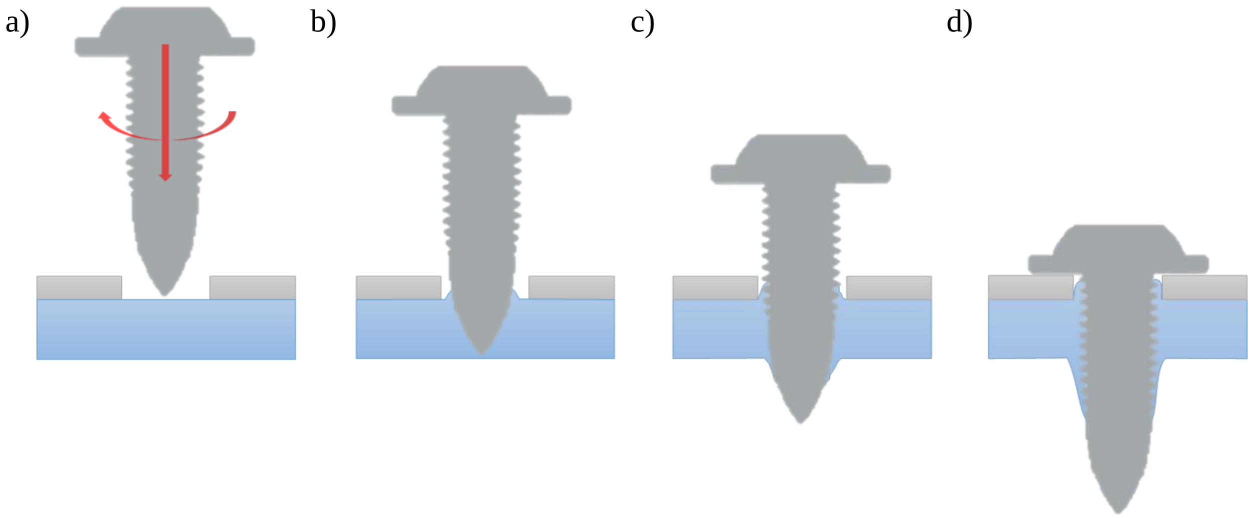

Figure 18 – Schematic representation of a flow drilling process: a) positioning and beginning of spin and downwards force (note: depending on ductility of sheets, either a hole is drilled or not. b) material flow in superplastic state; c) continuation of material flow; d) process end and the screw gets locked by the deformed material and an overall joints assembly forms between the sheets and the screw.

Szlosarek *et al* [104] made dissimilar material joints of a pre-drilled 1.2mm carbon fibre reinforced plastic (CFRP) and 2.5mm AA6060-T6 where damage sustained by the carbon fibres during loading was studied for different angles. This is a very limited study due to the nature of the components used, the conclusions obtained for CFRP are restrictive in a way that it cannot be transferred to other materials. Amundsen and Gustad [105] made advances in developing a macroscopic model of a flow drill screw joint, where a model has been validated through experimental work by making shear and tensile tests on 2 mm thick AA6063-T6 and 2 mm thick AA6016 T4 sheets. Failure mode for this 2 sheet material configuration is mainly associated with the de-threading of the joint. In the case of 3 sheet material configuration, in which an extra plate of AA6016 was added to the assembly, the failure mode is the breakage of the screw. No description on the material orientation is given, moreover, the joint was made with a pre-formed hole in the top sheet which is not needed for joining aluminium but simplifies the process. Sønstabø *et al* [106], [107] validated a macroscopic model of FDS by adapting and calibrating the model of Hansel [108] for self-piercing rivets. Hansel's model was successfully developed for general use with non-linear explicit finite element calculations and calibration based on an orthogonal, parallel scheme using experimental data from U-shaped specimens subjected to three different loading angles (0°, 45°, 90°) and a peeling test to improve the accuracy.

Sønstabø et al [109] studied the macroscopic strength and failure mode in sheets of 2mm thick AA6016-T4, giving evidence that the failure mode tended to be associated with removal of the thread (dethreading) of the bottom material (e.g. opposite to the FDS head). Hong et al [110] made joints of 2mm AA 6082-T6 with and without a pre-drilled hole for shear testing under cyclic conditions and showed that the failure mode was always the aluminium tear out and that the specimens with the pre-drilled hole had a better performance under the cyclic load conditions. It is important to note that in the case of a sample without the pre-drilled hole, the displaced material from the top sheet material gets trapped between sheets creating a gap, otherwise it is expected that joint performance should have improved.

Skovron *et al* [111] provided an extensive explanation of industrial quality and evaluation processes by joining sheets of 1.5mm thick AA5052-O under different forces and drilling speeds without a clearance hole. It was shown that the force applied has a direct effect on the material deflection which creates a gap between the sheets and is independent of the speed. High forces always created a downward deflection on the bottom sheet. Skovron *et al* [112], [113] show that pre-heating the sample can assist the FDS process as long as the material does not get too soft and over softening decreases the joint strength. Although this study is only focused on joining two AA 6063-T5 sheets, it points out the importance of considering that the change in properties of materials during the application process needs to be considered, because it can lead to performance improvement or deterioration.

In sum, the implementation of this technology requires that the assembly point has enough strength and structure to accommodate the distortional forces resulting from the application process in order to be applied as a one-sided application, otherwise a secondary support is needed turning the application a two-sided application. Also literature suggests that FDS was developed for soft materials like aluminium and CFRP. For the St-Al application FDS can only flow through a thin (<1mm) ductile steel however without proper reliability, therefore the joints with steel need to have a pre-drilled hole in order to make the joint for thicker sheets. Therefore, this technology is strongly orientation dependent since the aluminium sheet always has to be at the bottom due to the locking mechanism provided by the thread formation which is only possible with the ductile aluminium in this location. In a high volume automotive production line this technology has the advantage that it can be easily automated with joint assembly monitoring system but non-destructive testing assessment of joint quality poses challenges. The nature of locking mechanism for this joining technology is derived from the locking performed between the screw and the bottom aluminium sheet, therefore it is theorized and assumed that by using a top sheet with a pre-formed hole, any material combination can be joined. For this reason there is an absence of publications that focus on joints composed of dissimilar materials apart from CFRP and aluminium. From the literature it is evident the lack of publications taking into account the different materials used on the joint, this is due to the nature of the locking mechanism being derived mainly from the bottom aluminium sheet and assuming that the top material has a pre-drilled hole it is assumed and theorized that any material combination can be joint.

3.3.7. Tack high-speed joining

Tack high-speed technology, commercially known as RivTac by Bollhoff, takes advantage of the ballistic behaviour of materials to make the joint. A high strength grooved nail is driven into the sheets at high speed, the ogival arch on the tip displaces material and allows for penetration into the base sheet materials without needing a pre-existing hole [114]. The kinetic energy is converted into mechanical work or heat where the impact on material is minimal due to the processing speed [115]. The full cycle takes less than one second. During the process there is a momentary rise in temperature in the joint resulting in improved formability that causes the parent material to be displaced into the annular grooves on the shank of the nail. According to the supplier this is the only technology available to successfully join boron steels at high speeds. Boron steels are ultra-high strength steels (strength > 1500 MPa) which imposes added challenges to make joints with this material.

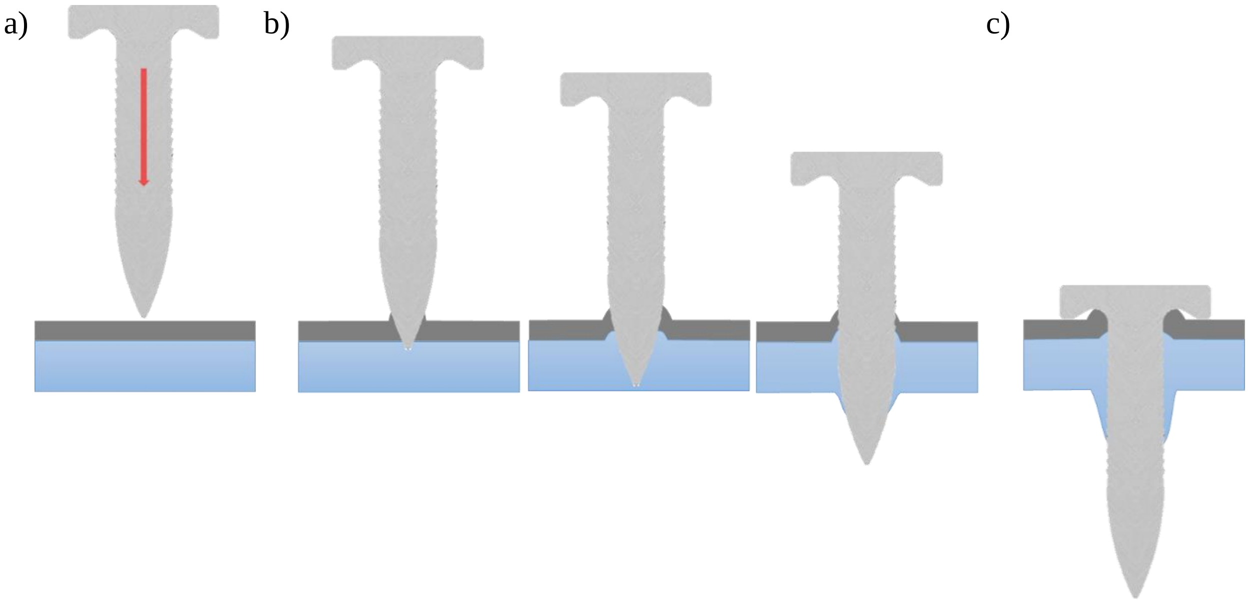

Figure 19 – Schematic representation of a Tack high speed joining process: a) positioning and beginning of downwards force, b) penetration sequences in sheets; c) process end and the nail gets locked by the deformed material locking on the material into the nail grooves.

The available literature on this technology is limited, recently Meschut *et al* [115] proposed a simulation to predict the geometric formation, joint processing parameters and joint load-bearing capacity. Meschut's work is only limited to 2D simulation with challenges in finding the remeshing frequency, as low frequency degenerates the mesh and high frequency leads to non-physical effects, such as a thickening of the sheet, generating errors and invalidating the matrix. Sankaran *et al* [116] proposed new improvements for the nail tip to improve workers safety by proposing a flat end nail. In aluminium-aluminium stack they observed a reduction of 5% in joint quality suggesting the trade-off between nail sharpness and joint strength to improve workers safety is acceptable.

3.3.8. **Adhesive Bonding**

Adhesive bonding is a joining process that involves the usage of an organic compound to form a bond between two surfaces. This bond is reliant on adhesive forces interacting between the adhesive and substrate surface as well as the cohesive forces holding the material together as displayed in Figure 20.

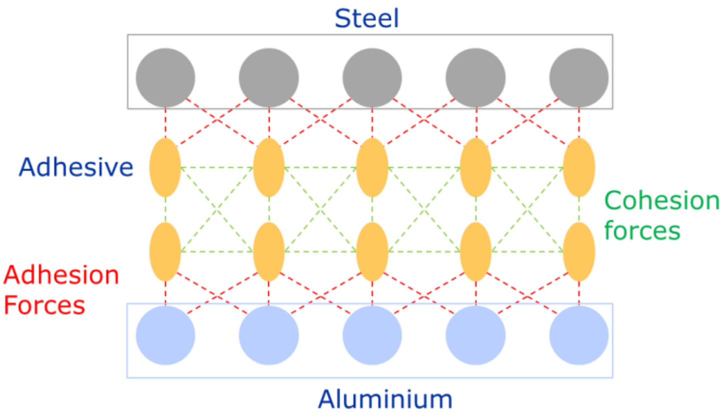

Figure 20 – Adhesive interaction between a steel and aluminium joint with representation of adhesion and cohesion forces

Adhesives can be classified by their chemical nature (e.g. epoxies, polyurethanes, polyimides), their form (e.g. paste, liquid, film, tape), their type (e.g. hot melt, reactive hot melt, thermosetting, pressure sensitive, contact, etc.), or their load carrying capability (structural, semi-structural, or non-structural). Small and Courtney [117] identified the main factors for adhesive joint performance (lifetime, robustness, etc.). To obtain a good joint it is needed to consider the physical and chemical properties of adhesives, the materials being joined (nature of adherents), surface preparation, surface wettability and joint design. Petherick [118] confirms that the joints need to be designed to reduce joint stress levels by considering the described factors and therefore create joints capable of taking structural loads. Martinsen *et al* [119] highlights some adhesive joint limitations by exposing the difficulty of disassembly, surface preparation requirements, extra time needed for polymerization, low thermal resistance, and influence from atmospheric agents, degradation and chemical agents. Therefore, joint failures are normally associated with poor design, unprepared surfaces, improper adhesive selection for the substrate or difficult operating environment. The automotive sector is mainly focused on structural adhesives which, as the name implies, adhesives that are specially designed for structural application which implies high load and stress carrying capabilities.

The main advantages of using an adhesive is associated with the increased joint area which supports higher loads therefore adhesives are normally applied in hybrid systems with another joining technology (riveting, clinching, etc)[118]. Although adhesive bonding improves load bearing performance of joint which can contribute to the safety performance of the joint, the key disadvantage is that there exists low amount of data on the effect of adhesive ageing on performance and reliability. Another advantage of the adhesive layer is the isolation and sealing the joint area, which is crucial for preventing accelerated corrosion in multi-material design due to the difference in electrochemical potential of the dissimilar materials [92].

Meschut *el al* [92] suggest that, in mass vehicle production, there is a significant potential for hybrid joining technology to achieve lightweighting through combining the established mechanical fastening technologies with adhesive bonding as the latter offers the main load carrier.

3.3.9. **Technology comparison**

As previously highlighted, the inherent problem associated with steel to aluminium joining is that the materials are different in nature, with different thermal, mechanical and structural properties. The broad spectrum of technologies with different locking mechanisms, properties and weaknesses, it is possible to understand the difficulties associated with technology selection for steel to aluminium dissimilar joining. In this particular case, very little is known on the impact of the dissimilar properties on different joining mechanisms for comparison and selection purposes. This is due to the small handful of publications that discuss this impact.

A technical report produced by Nippon steel by Sakiyama *et al* [120] composed a theoretical overview of a selection of joining technologies describing the methodologies of resistance spot welding, mechanical joining (clinching, SPR, FDS and blind rivets), adhesive bonding, Friction Stir Spot Welding (FSSW), and laser brazing as representative technologies for joining steel and aluminium alloy sheet. It was suggested that mechanical joining combined with adhesive bonding and FSSW had preference due to the minimization of the intermetallic layer and the perceived improvement of corrosion prevention. However, this study identifies the inadequate economical and reliability factors which further emphasizes the need for improvement in work efficiency, minimization of joint deformation, mitigate problems associated with dissimilar thermal expansion coefficients and cost reduction.

Mori *et al* [121] theoretically reviewed mechanical joining processes for aluminium to high strength steel sheets by plastic deformation. The disparity of the material properties of the aluminium and the steel with low ductility and high strength requires optimization of the joint to prevent material failure. As previously stated in section 3.3.3 in accordance with Mori *et al*, SPR die needs optimization to promote rivet flaring and interlock formation and to prevent material and joint failure. Contrastingly, the optimization in clinching process is obtained by controlling plastic deformation using a step punch to improve the clinch neck thickness. Authors assumed that joint performance of SPR is considerably higher than that of resistance spot welding, and the fatigue strength of clinching is similar to that of resistance spot welding.

Martinsen *et al* [119] reviewed joining processes suitable for the joining of dissimilar materials which covers selection criteria, modelling aspects and inspection/testing of joints. From this theoretical approach the authors flag the lack of collaboration between the manufacturing research and joining research communities, and there is a need for innovations in this area through the industry and academia collaboration. It was also evident that the lack of standardisation in dissimilar joints for both testing and characterization undermines the correct evaluation of joining technologies. Current methodologies follow standards for test specimens that do not characterise the most vulnerable microstructures, e.g. does not test the weakest element in the joint. In this sense structural assessment cannot be accurately determined due to disparity in material properties and localization of stresses caused by mixed mode failure. Both of these affect the crack formation and propagation.

Meschut et al [92] is the only report that performed a practical comparison of joining technologies used for joining 2mm AA 6016 to 1.5mm 22MnB5 steel sheets. The tensile strength of joints made with clinching, SPR, Tack High Speed joining, Solid Punch Riveting, Resistance Element Welding (REW) and Friction element welding (FEW) were compared both with and without a structural adhesive. The authors showed that the aluminium component is the weakest element in the joints and becomes the main limiting factor for joint properties under shear loading. Also, the introduction of the adhesive on the joint greatly improves the joint quality due to the delocalization of loading over a bigger surface area which is consistent with hybrid joining of the tested technologies. The clinch joint was shown to be impossible to apply with hybrid joining (clinch plus adhesive). The authors show that mechanical joining combined with local conditioning can have enough joint strength for dissimilar automotive applications. Authors justify the need to apply one or more joining technologies in a production line depending on the process limitations such as production, volume, joint strength, material properties and cost.

In sum, there is a big gap in understanding the joining capabilities and relative performance of the various available joining processes across the range of industrially interesting material combinations. The different joint configurations and materials push the limits of joining technology. The knowledge required to solve these issues and determine which process/processes are most suited to use in a volume production line is also not present in literature. Therefore, quantification of joint performance along with technology limitations for material properties and manufacturing requirements is desperately needed by industry. This knowledge would enable not only the correct deployment of lightweighting applications but also the improvement of manufacturing lines in terms of reduced costs through correct technology selection.

3.4. **Methodology**

As this thesis intends to bridge the gap between academia and industry all testing and materials here defined are based on industrial requirement. The selection of materials and their geometries were also based on industrial relevance.

3.4.1. **Materials**

The materials used in this work are of specific interest to the automotive industry and at the same time, due to their intrinsic properties, the selection allows the limits of the proposed joining techniques to be tested. Materials used are representative of what is being used in industry. The selected materials are presented in Table 3 with material properties and compositions presented in Table 4 and Table 5 respectively. The materials properties were verified in accordance with ISO 6892:1.

Table 3 – Selected materials

Selected materials	
Steel	**Aluminium**
0.8 mm DX56 GI	1 mm AA 6061
1.2 mm HSLA340 GI	2 mm AA 6061
1.4 mm DP 600 GA	2 mm AA 5754
1.5 mm DP 600 GI	

GI – Galvanized
GA – Galvanneal

Table 4 – Material properties (data from material supplier specifications)

Material	Reference	Coating	Thickness	Tensile Strength (MPa)	Yield Strength (MPa)	Total Elongation (%)
Steel	DX56	GI	0.8	270 – 330	140 – 180	
Steel	HSLA340	GI	1.2	410 – 510	340 – 420	21
Steel	DP 600	GA	1.4	620	365	27
Steel	DP 600	GI	1.5	635	370	24.5
Al	AA 6061	-	1	260	240	17
Al	AA 6061	-	2	260	240	17
Al	AA 5754	-	2	270	130	7

GI – Hot dip galvanized
GA – Galvanneal

Table 5 – Material chemical composition (data from material supplier specifications)

Material		DX56 GI	HSLA340 GI	DP 600 GA	DP 600 GI	AA 6061	AA 5754
Element (%)	**Al**					Balance	Balance
	C	0.08	0.06	0.09	0.1		
	Cr					0.04 – 0.35	0.10 – 0.60
	Cu					0.15 – 0.4	0.0 – 0.10
	Fe	Balance	Balance	Balance	Balance	< 0.7	0.0 – 0.40
	Mg					0.8 – 1.2	2.6 – 3.6
	Mn	0.6	0.35	1.6 – 1.9	1	< 0.15	0.10 – 0.60
	Si	0.04	0.1	0.2-0.3	0.3	0.4 – 0.8	0.0 – 0.40
	Ti					< 0.15	0.0 – 0.15
	Zn					< 0.25	0.0 – 0.20
	Others					< 0.15	0.15

Since this work is focused on dissimilar materials joining, these materials were mixed together in 2-sheet material combinations using 1 piece of steel and 1 piece of aluminium alloy (AA) and in 3-sheet material combinations of 1 piece of steel to 2 pieces of different aluminium grades. The 2-sheet material combinations used in this study are presented in Table 6.

Table 6 – 2 sheet material combination

Type of steel	Type of aluminium		
	1 mm AA 6061	2 mm AA 6061	2 mm AA 5754
0.8 mm DX56 GI		✓	
1.2 mm HSLA340 GI		✓	
1.4 mm DP 600 GA	✓	✓	✓
1.5 mm DP 600 GI		✓	

The 3-sheets joint configuration is designed to test the weakest joint possible; therefore the joint is designed by pulling the steel and 1mm AA together against the 2 mm AA. Examples of the 3-sheet material combinations were:

- 1.4 mm DP 600 GA – 1 mm AA 6061 – 2 mm AA 6061
- 1.4 mm DP 600 GA – 1 mm AA 6061 – 2 mm AA 5754

3.4.2. **Sample preparation**

3.4.2.1. **Samples for verification of parent material properties**

In accordance with ISO 6892:1 for samples of sheet metal between 0.1mm and 3mm require a dog bone shape specimen as shown in Figure 21. To produce 5 test coupons, sheets of 25 mm x 180 mm were machined into a flat dog bone shape where the gauge width of 12.5 mm with a tolerance of ± 0.05 mm, with a length of 75 mm after curvature and a radius of 20 mm. The ISO 6892:1 specification for a gauge length is 50mm, which is the parallel portion of the test piece where the mechanical properties are measured.

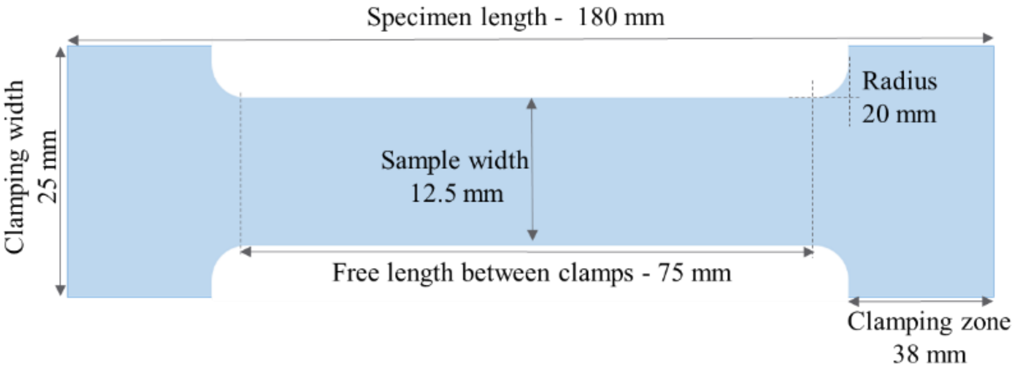

Figure 21 – Specimen for determination of material properties in accordance with ISO 6892:1 (example not up to size)

3.4.2.2. **Samples for joining**

Since this work is of high importance to the automotive industry, industry practices were followed. This meant that no surface treatment was applied to the materials prior to joining trials. This is because car companies process materials directly, without pre-cleaning or other preparation techniques. The received sheets were cut to size according to the tests to be performed. To validate the comparison across all the different techniques standard samples were prepared according to ISO 14273:2016 for the tensile shear strength and according to the ISO 14272:2016 for the cross-tension strength. Some joining technologies have specific requirements for joint orientation, therefore determining which material is required to be on top and bottom. For the joining technologies which are orientation independent the worse performing orientation was determined and the joint optimised for these trials. This follows the requirement of minimum joint performance for all trials.

3.4.2.3. **Tensile Shear Strength**

ISO 14273:2016 states that the normative parameters that need to be implemented for the sample preparation of the Tensile Shear Strength (TSS) specimens and execution of the testing. The metals need to be cut in the shape of rectangles of 45 mm by 105 mm with an accuracy of ±1mm. This is to keep a constant specimen positioning and geometry configuration as shown in Figure 22. This will lead to a full specimen length of 175 mm with a plate overlap of 30 mm. On both sides of the specimen there will be 40 mm for the clamping of the specimen leaving 95 mm of free length between the clamps. The joint has to be positioned in the centre of specimen with a tolerance of ± 1 mm.

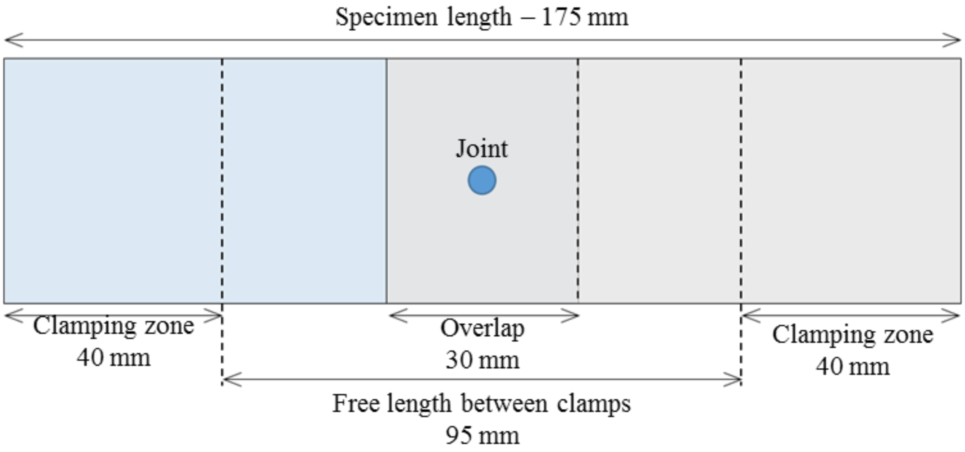

Figure 22 – Tensile Shear Strength specimen sizes and orientation according to ISO 14273:2016 (example not up to size)

An example of a tensile shear test is present in Figure 22 with representation of the shear forces and characteristic joint inclination associated with the dissipation of forces.

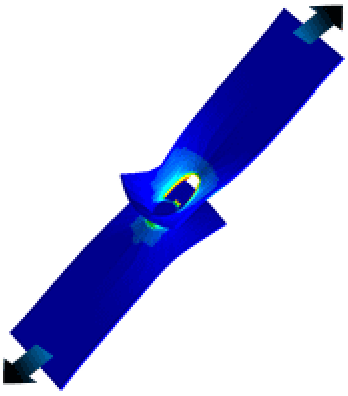

Figure 23 – Example of a tensile shear test with exemplification of shear forces (courtesy Swantec®)

3.4.2.4. **Cross Tension Strength**

ISO 14272:2016, like in the previous ISO norm, states that the normative parameters that need to be implemented for the sample preparation of the Cross Tension Strength (CTS) specimens, as well as experiment realization. The metals need to be cut in the shape of rectangles with a length of 50 mm with tolerance from 0 to +1 mm and width of 150 mm with tolerance from 0 to -0.5 mm. Since clamping bolts are used to fix the CTS specimen, clamping holes are required. The norm states that the clamping holes should be 100 mm apart from each other and centred in the sample, as is shown in Figure 24(a). For the CTS specimen a mounting jig is used to hold both pieces of the sample together in the correct angles (90 degrees from each other) and the joint should be positioned in the centre of the specimen with a tolerance of ± 1 mm, as shown in Figure 24(b).

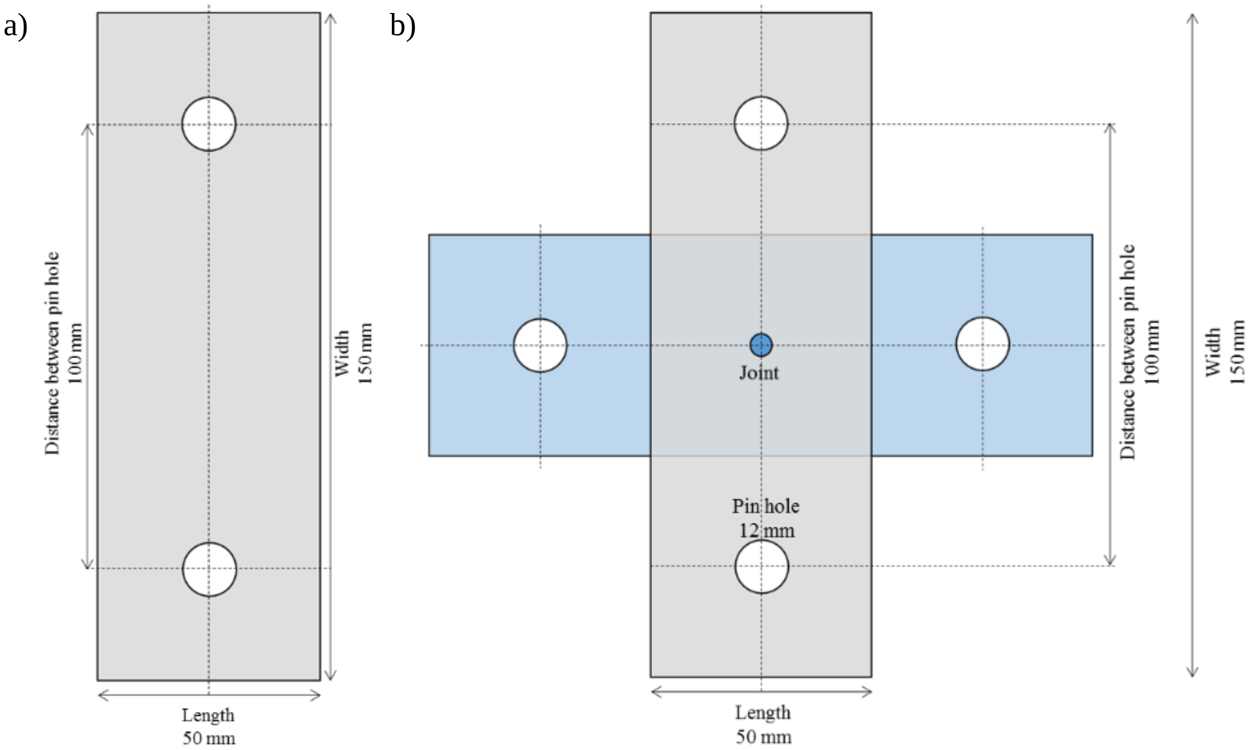

Figure 24 – Cross Tension Strength specimen sizes (a) and orientation (b) according to ISO 14272:2016 (example not up to size)

An example of a cross tension testing is present in Figure 24 with representation of the tension forces during loading.

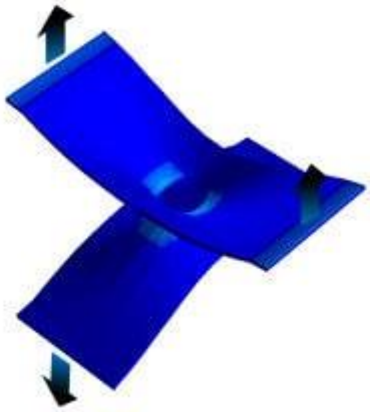

Figure 25 – Example of a cross tension test with exemplification of tension forces (courtesy Swantec®)

3.4.2.5. Samples for process exploration

The samples used for exploration of processes parameters and metallographic analysis consisted of small coupons of around 30 mm x 30 mm.

3.4.3. Equipment and experimental procedure

3.4.3.1. Adhesive bonding

The selected adhesive was for warm application, therefore prior to adhesive application the adhesive cartridge was heated up to 50°C in an oven for around 30 minutes. It is important to note that, to avoid undesired curing, the temperature of the oven was strictly maintained < 60°C.

The metal samples were cleaned with acetone and the overlap was marked in each sample as is shown in Figure 26(a). A thin (1-2 mm) line of adhesive was placed on the surface in a zig-zag pattern as represented in Figure 26(b). With the use of a lolly stick the adhesive was spread evenly to the whole overlaying surface as shown in Figure 26(c). Both halves of the sample were assembled and the excess outflow was cleaned with the lolly stick to ensure that the corners are well bonded. This process has been verified to form complete and uniform spreading without gaps across the overlap. The uncured sample is fixed with metal clips and left on a hot plate at 50°C for 10 min prior to secondary assembly or curing. This stage ensures that a uniform and even layer of adhesive is achieved between the sheets. The uncured samples need to be cured within 1 week after assembly. The curing process consists of 30 minutes in an oven at 180°C. The overlapping area is consistent in accordance with the ISO 14273:2016 for lap shear and ISO 14272:2016 for cross tension.

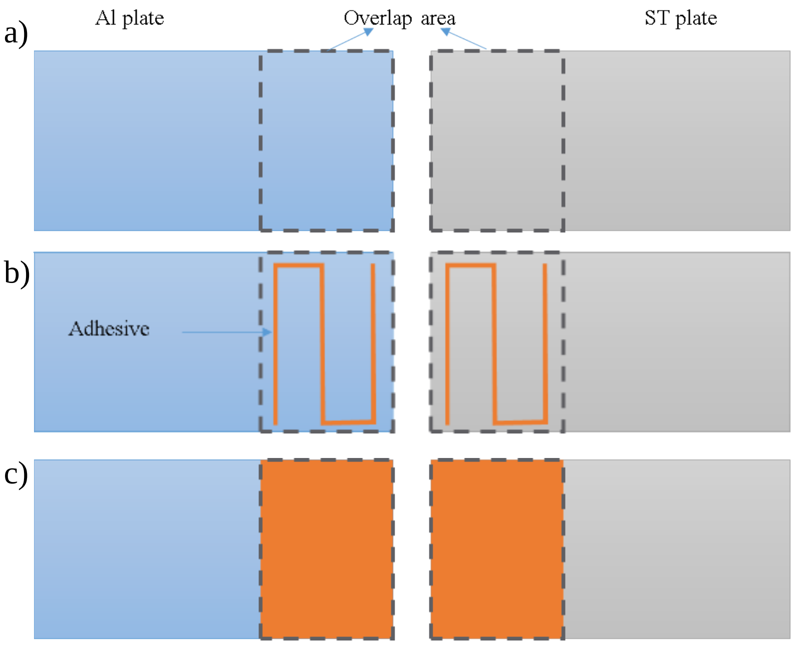

Figure 26 – Stages of preparation for adhesive bonding: a) defining overlap area; b) applying a strip of adhesive; c) evenly spreading of adhesive

3.4.3.2. **Blind Riveting**

For blind riveting, all sheets were pre-drilled before assembling. Taking into account the thickness of the material combinations, 2 rivets were selected; the 6.4 mm diameter rivet (fixing range 2.0 – 9.5mm) with a big clamping head and the 4.8 mm diameter rivet (fixing range 1.6 – 6.4mm) with a small clamping head. Therefore two different sizes of holes needed to be made in the samples, a hole of 6.7mm was made for the 6.4mm rivet and a hole of 5.0 mm was made for the 4.8 mm rivet.

The joint Al to St orientation, consisting of aluminium at the top contacting with the rivet head and the steel with the mandrel part, was produced by pulling the rivet through the predrilled holes. To guaranty alignment and reproducibility of samples they were assembled using bespoke designed and constructed jigs to obtain shear and tension joints.

For the samples joined with a structural adhesive the adhesive bonding procedure was used to prepare the samples prior to assemble. After assembling, samples were cured as specified on the adhesive bonding procedure, 30 minutes at 180°C.

The equipment used for blind riveting was the modular Gesipa Taurus PH 2000 with interchangeable nozzles for the different types of rivets, with a constant pull force of 11kN. These experiments were performed at Gesipa UK installations.

3.4.3.3. Clinching

For this technology a BTM clinch press with 80kN max force, with a custom fitted strain gauges for compression load measurements and a Linear Variable Differential Transformer (LVDT) for height positioning and displacement monitoring were used. A National Instrument Chassis cDAQ-9174 with a NI module 9237 was used to read the values of the custom fitted parts with a LabVIEW custom built software. The tooling used was a BTM Tog-L-Loc® punch of 5.5mm diameter and a set of different 5.5mm dies presented in Table 7 with different die depths.

Table 7 – BTM Tog-L-Loc® dies and respective depth

Die REF	Depth / mm
742100BE	0.635
742100CE	0.762
742100DE	0.889
742100EE	1.016
742100FE	1.143
742100GE	1.27
742100HE	1.397
742100JE	1.524
742100KE	1.651
742100LE	1.778

After the joint was made a set of non-destructive measurements was performed for each sample: cap thickness, cap depth and bottom diameter, as displayed in Figure 27(a), with a digital calliper and a point micrometer with carbide tips. For the samples that were cross-sectioned, using an optical microscope image, an average of the interlock and neck thickness were measured as displayed in Figure 27(b).

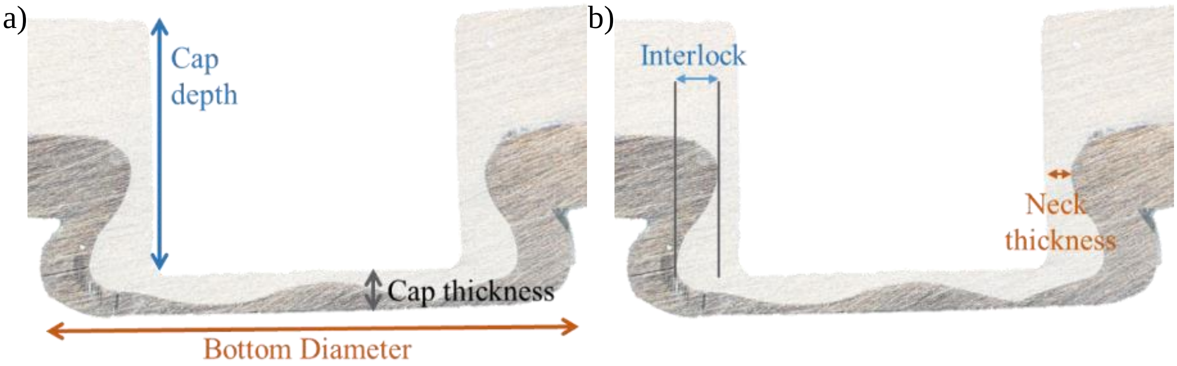

Figure 27 – Example of cross section of a clinch joint with illustration of: a) non-destructive measured parameters: Cap thickness, Cap depth and bottom diameter; b) destructive measured parameters: interlock and neck thickness

3.4.3.4. **Clinch-Rivet**

This technology employed a Tox press with 60kN max force with servopneumatic actuator for the trials and it does not require the piercing of the material in order to form the joint. Although the sheet materials with different lengths and properties are used, the same rivet was used for all the trials with the name RE 50.060.031 TOX-CN-A5x6-0 ZnN with rivet dimensions of a 5mm diameter and a length of 6mm.

3.4.3.5. **Self-piercing rivets (SPR)**

This technology employed an Alta Copco SPR equipment with 60kN max force with servopneumatic actuator for the trials which is capable of piercing the specimens studied. Two types of rivets were used for producing, one capable of performing 2 sheet material joints and another for the 3 sheet material combinations.

For the samples joined with a structural adhesive the adhesive bonding procedure was used to prepare the samples prior to assembly. After assembly, samples were cured for 30 minutes at 180°C.

3.4.3.6. **Solid Punch Rivets**

This technology employed a Tox press with 60kN max force with servopneumatic actuator for the trials. It is capable of piercing the specimens selected in this study in order to form the joint, however different material combinations required different rivets as shown in Table 8.

Table 8 – Joint configuration and rivet information of Solid Punch Rivet joints

Joint configuration	**Joint Thickness (mm)**	**Rivet Name**	**Rivet Length (mm)**
DP600 GA – 1AA6061	3.4	FPR 4,00x3,30XX K 492 100 005.900	3.3
DP600 GA – 2AA6061	4.4	FPR 4,00x3,90XX K 492 100 007.900	3.9
DP600 GA – 2AA5754	4.4		
DP600 GA – 1AA6061 – 2AA6061	5.4	FPR 4,00x4,80XX K 492 100 010.900	4.8
DP600 GA – 1AA6061 – 2AA5754	5.4		

For the samples joined with a structural adhesive the adhesive bonding procedure was used to prepare the samples prior to assembly. After assembly samples were cured for 30 minutes at 180°C.

3.4.3.7. **Flow drill screws**

This technology requires orientation preference in which the steel sheet is on top of aluminium sheet. The element is capable to flow through all the materials studied here. The screw used was a standard Bollhoff AFF_BLS-AFF-4,0X20,0-BAINITISIERT-10EP with a DELTA PROTEKT KL100+DELTASEAL SILBER. The equipment was a Deprag ADFS screw driving with a maximum rotation speed of 7000 rpm and maximum axial joining force of 3.5 kN.

For the samples joined with a structural adhesive the adhesive bonding procedure was used to prepare the samples prior to assembly. After assembly samples were cured for 30 minutes at 180°C.

3.4.3.8. **Tack high speed joining**

This technology employed a Bollhoff Rivtak press with an adjustable pneumatical drive for the trials. The same Zn/Ni coated FK 16-8-3 R07 H3 element was used for all the trials.

For the samples joined with a structural adhesive the adhesive bonding procedure was used to prepare the samples prior to assembly. After assembly samples were cured as specified on the adhesive bonding procedure, 30 minutes at 180°C.

3.4.4. Equipment for testing

Before any testing was performed on the samples, they were treated with a “simulated E-coat cycle” as is normal practice in a production line for the automotive industry. The E-coat cycle consists of a pre-treatment to clean and phosphatise the surface to allow better paint adhesion; an electro-coat bath which consists of the coating that is deposited by electrodeposition; a rinse cycle to clean undeposited particles; and finally a baking cycle to cure the paint. This is of special importance because all joints made during the production stage will undergo this thermal cycle. During this stage some grades of steel and aluminium harden and also due to thermal expansion and contraction some joints may loosen. Therefore, to account for all of these possibilities all samples (both with and without adhesive) will undergo a temperature cycle of 180ºC for 30min.

3.4.4.1. Mechanical Testing

Experiments were performed in an INSTRON 8801 with a load cell of 50 kN. Testing was performed at 10mm/min strain rate, which is common practice for strength testing in the automotive industry.

3.5. Comparison of dissimilar joining technologies

NOTE: Joint strength testing results will be presented in the form of load vs displacement curves, as is standard practice by automotive companies for welded or mechanically fastened joints. This is because the local loading conditions in the joint are very complex and cannot be monitored during a test that is continuously changing. For example, for the tensile shear test, although it is a shear test from the macroscopic point of view, as the joint deforms, the load stops being pure shear becoming a mixed mode between shear and pull. This is also consistent with the literature [105]–[107], [109] as well as the ISO norms and industrial standards (ISO 14272:2016, 14273:2016).

3.5.1. Material properties confirmation

Parent material properties were verified under the ISO 6892:1 and this information is presented in Table 9. Results are within the range of material suppliers with exception of the AA5754 which exhibit slightly higher yield point.

Table 9 – Material properties of parent materials measured in this study

Material	Yield Strength MPa	UTS MPa	Elongation %
DX56 GI	147 ± 1	252± 1	44 ± 3
H340 GI	344 ± 7	435 ± 2	28 ± 1
DP600 GI	357 ± 4	622 ± 4	31 ± 2
DP600 GA	415 ± 4	606 ± 4	27 ± 3
1AA6061	278 ± 1	321 ± 1	11 ± 1
2AA6061	282 ± 1	322 ± 1	13 ± 1
2AA5754	206 ± 2	261 ± 3	12 ± 1

3.5.2. Behaviour of individual technologies

3.5.2.1. Adhesive bonded samples (only adhesive)

To evaluate the performance of adhesive bond itself, samples were bonded using adhesive without an additional mechanical joining element. This was done to compare the properties of different adhesive types and to make a comparison with the performance of the various joining element types (previously referred to as ‘techniques’). In this sense a comparison of adhesives was also performed. The main adhesive used was Sika Power 492 and it was compared to the Dow Betamate 1600R which has similar properties, as represented in Table 10.

Table 10 – Properties for the Sika Power 492 and Dow Betamate 1600R adhesives

Property	**Sika Power 492**	**Dow Betamate 1600R**
Chemical Base	Epoxy	Epoxy
Density (g/ml)	1.30	1.31
Tensile Strength (ISO 527-1) / MPa	30	36
Elongation at break (ISO 527-1)/ %	8	7
Lap Shear Strength (EN 1465) / MPa	20	24
Oil Tolerance / g/m^2	3	5

The failure modes associated with adhesives are: (i) adhesion failure – the failure close to the substrate where it was not properly set; (ii) cohesion failure– it is associated with failure of the bulk of the adhesive layer. Another failure mode is associated with bond failure when the adhesive is not enough to contact both surfaces (e.g trapped air bubbles or lack of adhesive at corners). It is only observed in DP600GA material, in which delamination of the coating was observed. Examples of failure modes are presented in Figure 28.

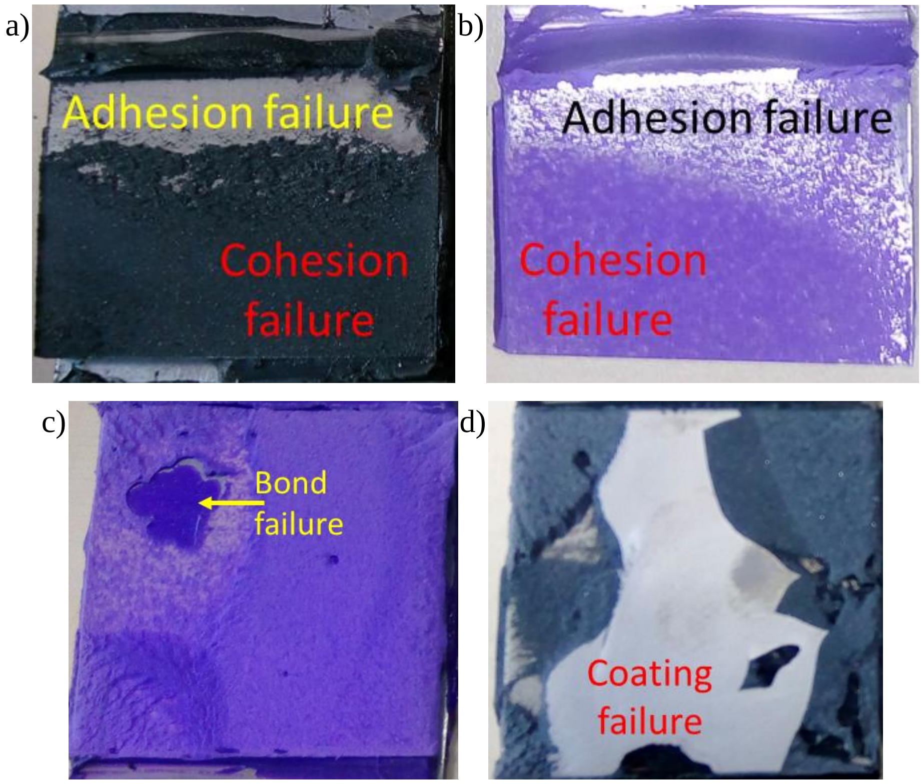

Figure 28 – Adhesive failure modes: Adhesion and Cohesion failure in Sika adhesive (a) and Dow (b); bond failure (c); coating failure (d)

For the comparison of the adhesives the primary phase of analysis consisted in the evaluation of the performance of the 2mm AA6061 joint with different steels as displayed in Figure 29. These results indicate that the yield strength of the parent material plays an important role in the joint properties. This is because the material starts to yield promoting the adhesive/cohesive failure. Since both adhesives exhibit very similar behaviour the huge gaps in the performance of both adhesives were not anticipated, as is evidenced by the results. There are some particularities associated with the DP600GI tensile shear strength results which are associated with the failure mode being associated with adhesive cohesion failure. In DP600GI joints, the fraction of cohesion failure area is measured to be 53% and 72% for the Sika adhesive and Dow adhesive, respectively.

In the case of DP600GA joints, the tension behaviour for the Dow is associated with the entrapment of air bubbles (bond failure) in the adhesive which therefore leads to the creation of stress points promoting the cohesion failure of the adhesive, whereas the failure in the Sika adhesive is associated with the delamination of the galvanneal coating on parent material.

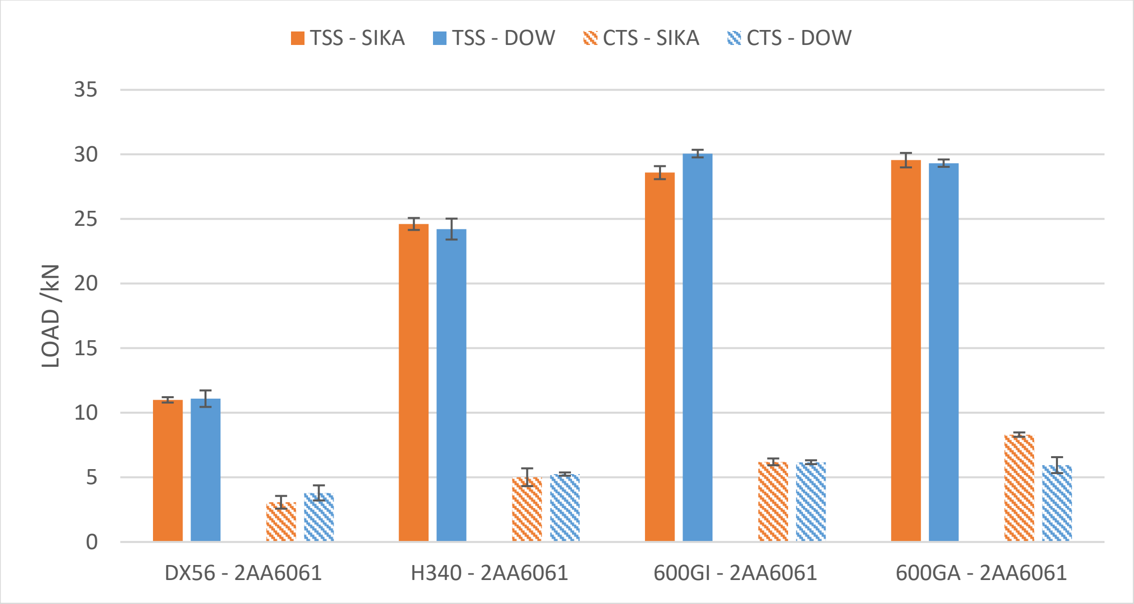

Figure 29 – TSS and CTS results for the adhesive bonded samples with Sika (orange) and Dow (blue) of joints made with 2AA6061 and different steels.

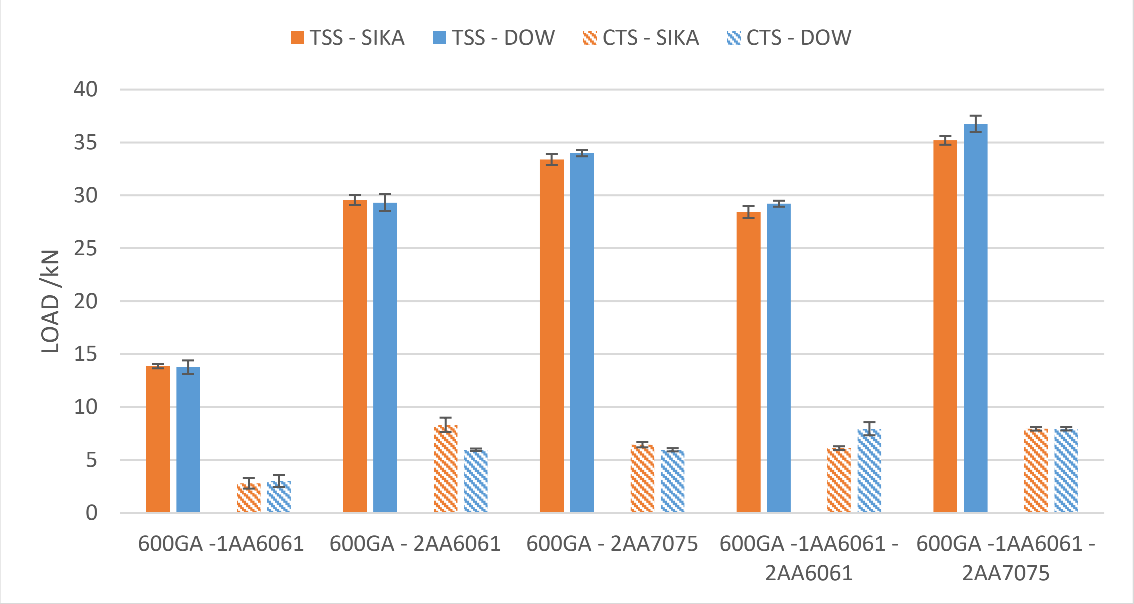

Figure 30 – TSS and CTS results for the adhesive bond samples with Sika (orange) and Dow (blue) of joints made with DP600GA steel and different AA and joint stack

In sum, there are no major differences observed between the two adhesives as both adhesives have similar properties and chemistries presenting a high affinity between the dissimilar substrates. For the purpose of the continuation of the present study the "Sika Power" adhesive was selected.

3.5.2.2. Blind rivets

For clarification of analysis the relevant modes of failure for this technology will be explained and presented prior to discussion of experimental results. The observed failure modes were classified into three basic failure mechanisms which are directly correlated to the mode of loading (cross tension or tensile shear) and to the selection of material. The three basic modes are (A) top sheet material failure (i.e., material close to the rivet head), (B) bottom sheet material failure (i.e., material close to the collapsible mandrel) and (C) rivet failure (rivet shearing). The nature of the dissimilar material joint and differences in thickness influences the loading behaviour. In the case of tensile shear testing, during testing the load will not remain in pure tensile shear loading, as the load increases a mixed mode between shear and peel takes place. The different sizes of the pilot hole and rivet also influence the mixed mode in tensile shear behaviour. These factors cause the rivet to tilt during the tensile shear loading and develop the mixed tensile shear and peel mode. Therefore, the modes of failure are associated with the modes B (bottom material failure) and C (rivet failure). In all the samples tested in cross tension, the failure mode was always associated with the failure mode B (bottom material failure). The loading behaviour in cross tension focuses the applied load directly on the interaction between bottom sheet and lock formed by the mandrel. The failure occurred when the material yielded and deformed enlarging the hole until the rivet slipped out as the example presented in Figure 31 (b2) with the deformed locking hole shown in the dashed box. Examples of failure modes are presented in Figure 31.

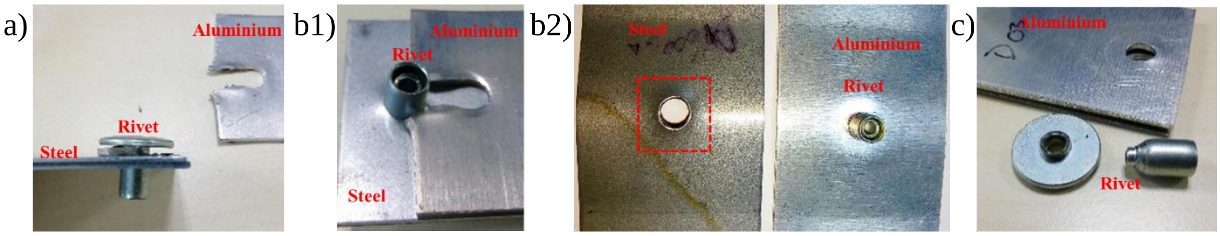

Figure 31– Observed failure modes: a) top sheet material failure; b1) bottom sheet material failure in tensile shear; b2) bottom sheet material failure in cross tension; c) rivet failure

Clarification of interpretation of the force vs displacement curves for the trials of a 2-sheet material configuration of 1.4 mm DP600 GA- 2 mm AA6061 are presented in Figure 32 for Tensile Shear Strength (TSS) and in Figure 33 for Cross Tension Strength. As previously described 3 different samples per joint are tested. This technology requires a pre-drilled hole bigger than the element used creating a clearance between the top material and the element as shown in Figure 34 between the aluminium and the rivet. This is evident on the load displacement curves by a shift in the load curve normally between 0.5 and 1.5 kN for the blind rivet technology in which there is a movement of the joint or slipping of the joint. Subsequently the most important information to be noted from these curves is the Ultimate Failure Load (UFL). It is also important to inspect associated failure mode. The associated failure mode for TSS samples shown in Figure 32 is the rivet failure, while the differences in the graph correlate with the way that the rivet is sheared. For the Sample 2 (red) the rivet became loaded in a way that it is partially pushed the mandrel out before the rivet shearing, while the other two joints samples did not present the same behaviour as it can be seen in Figure 35.

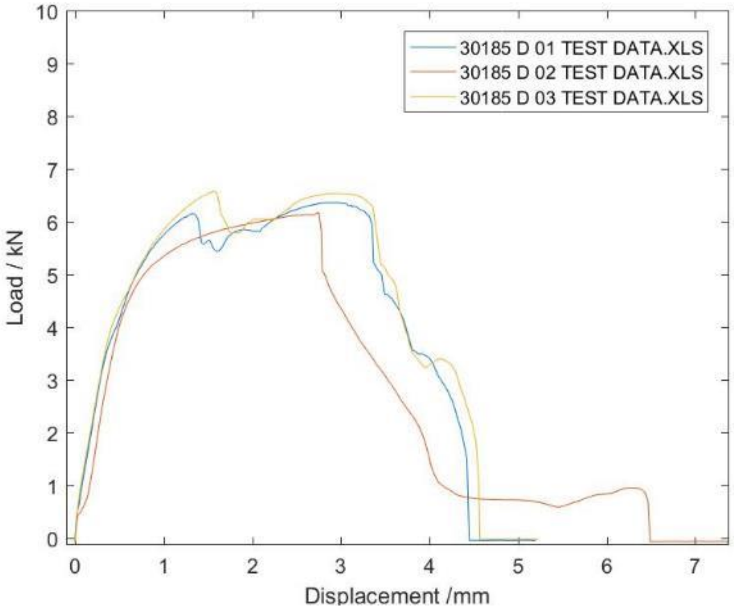

Figure 32 – Load versus displacement curves from Tensile Shear Strength tests performed for three joints of 1.4mm DP600 GA-2 mm AA6061

CTS results presented in Figure 33 are consistent in the behaviour of the failure mode which is associated with the material deformation of the bottom material followed by the release of the rivet. A CTS tested sample is presented on Figure 36 where it is possible to see that the rivet is intact and the failed mode is associated with the deformation of the steel around the hole.

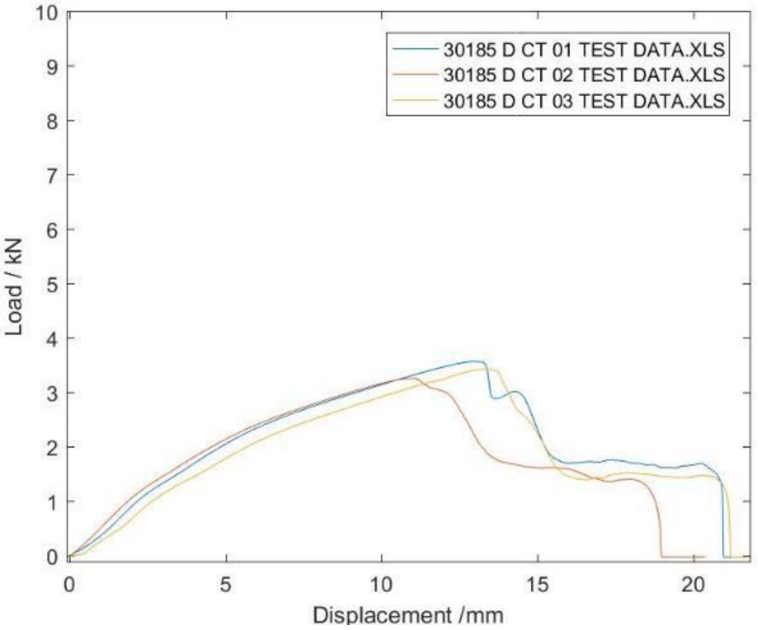

Figure 33 – Load versus displacement curves from Cross Tension Strength tests performed for three joints of 1.4mm DP600 GA-2 mm AA6061

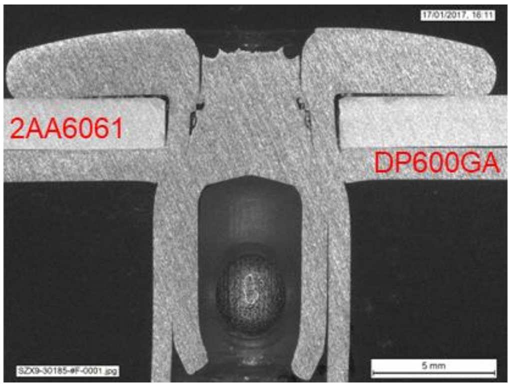

Figure 34 – Cross section of a blind rivet joint 1.4 mm DP600 GA- 2 mm AA6061

Figure 35 – Rivets from TSS with different shearing behaviour. In Samples 1 and 3, the mandrel did not retract while in Sample 2 it is retracted displaying a different loading behaviour in TSS curves.

Figure 36 – Tested cross tension specimen. Failure associated with material deformation around the centre hole in the steel

The summary of the full set of results is presented in Figure 38. Some of the specified joints do not allow same rivet to be used for all the joint configurations due to the gripping range of the rivets, therefore a smaller Gesipa MEGAGRIP ® rivet (4.8mm) with a clamping range of 1.5 to 4 mm was used for the joint consisting of 0.8mm DX56GI joined with 2mm AA6061. The overall thickness for the joint of 2.8 mm with a cross section is presented in Figure 37. From the cross section and additionally shown by the yellow arrows it is possible to identify that the steel presents a higher degree of interaction with the deformed rivet body, evidenced by the steel deformation due to compressive force exerted by the rivet. This can be interpreted by a small amount of buckling, which according to the literature [75], [76] improves the joint strength. Moreover, the cross section shows interaction between the aluminium and the deformed rivet body, which offers better support and higher slip resistance. Under shear loading, which means the application of horizontal opposing forces (aluminium from the right to the left and steel from the left to the right), Al sheet (Figure 15) interacts larger surface area with the rivet which creates smaller local stresses at this interface and therefore the joint can take higher loads before it fails. The tensile shear ultimate failure loads (UFL) is associated with the deformation of the material around the hole which enables the release of the rivet.

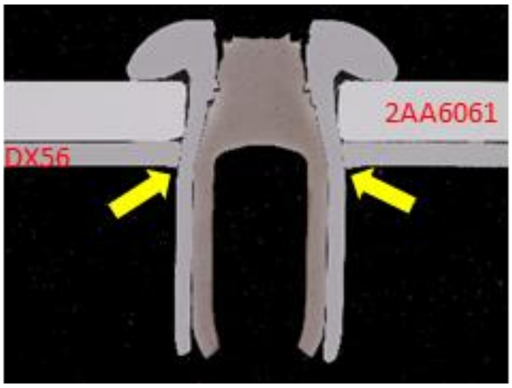

Figure 37 – Cross section of the joints made with the small rivet DX56 – 2AA6061

Another set of samples were prepared using the bigger Gesipa MEGAGRIP ® rivet (6.4mm) for the 2-sheet and 3-sheet material combinations. In the case of the HSLA340-2AA6061 the UFL is congruent with the yield point of the steel and it starts deforming until cracking starts. Combined with aluminium deformation the rivet is able to release from the material rather than getting sheared. In the case of DP600 steels, which have a higher yield point, the rivet is trapped between the deformed aluminium and the steel that does not deform. As a result rivet starts shearing and breaks. The failure mode in CTS is related with the slipping of the rivet through the deformed hole from the bottom material which is the steel. Values for UFL under cross-tension loading are congruent with the yield points of the different steels, therefore for these joints it is possible to conclude that the higher the yield the better CTS performance.

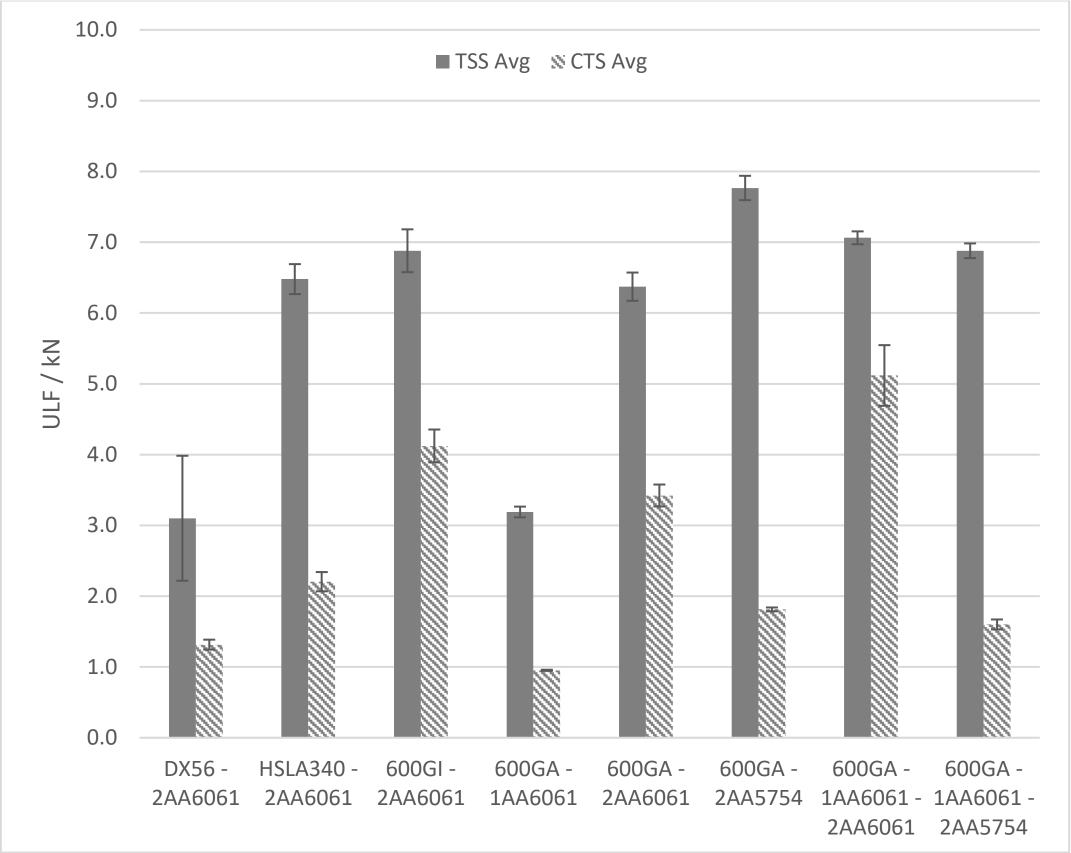

Figure 38 – Summary of Ultimate Failure Loads (UFL) from tensile shear and cross-tension from the different blind riveted samples

This blind riveting technology allows integration with adhesive bonding and could successfully achieve hybrid joining and a summary of achieved joint performance is presented in Figure 42. The results clearly show that adhesive provides significantly higher ultimate failure loads to the hybrid joint. Also, the associated failure modes differ as the thinnest materials leads to parent material failure as can be observed in Figure 39, which corresponds to the DX56 steel and the 1mm AA6061. The remaining observed failure modes are associated with the adhesive/cohesive failure of the joint followed by the interlock failure or rivet failure presented in Figure 40 and Figure 41 respectively.

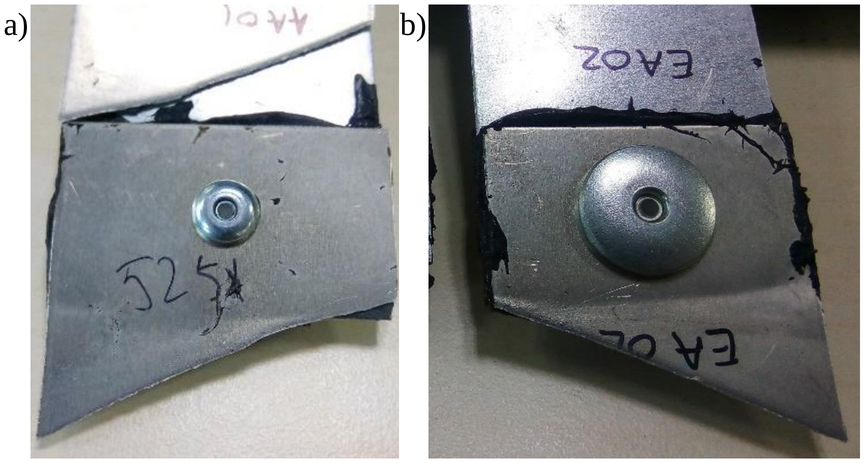

Figure 39 – Failure modes of parent materials of steel failure (a) and aluminium failure (b)

Figure 40 – Adhesive cohesion and adhesion failures followed by interlock failure

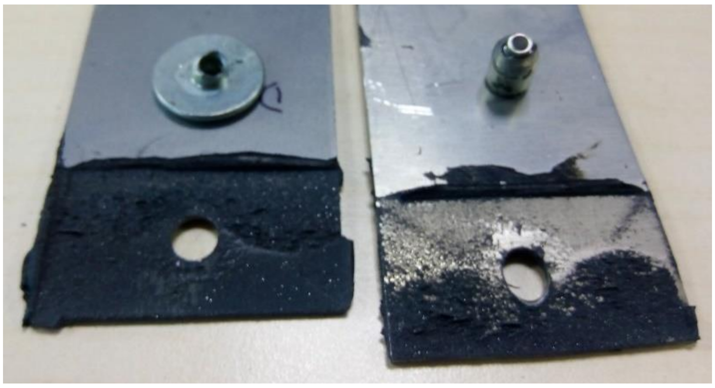

Figure 41 – Adhesive cohesion and adhesion failures followed by rivet failure

It is evident that the UFL behaviour for non-hybrid joint translates to the hybrid joints, as both the joints containing the DX56 and the 1mm AA6061 are the lowest performing joints. However, the failure modes are associated with failure on the parent material and not on the joint as shown in Figure 39. Although all joints have the same adhesive contact area the different material properties will dictate the joint performance. The different steels such as HSLA, DP600GI and DP600GA are all joined to the same 2mm AA6061 and their joint performance is very similar. However among this trio the lowest performing material is HSLA due to lower yield point for this material, which creates conditions for adhesive failure initiated by material deformation. The joints containing the DP600GI and DP600GA steels do not exhibit significant difference in UFL because the materials have very similar properties.

The use of distinctly different aluminium alloys with different strengths, allows us to evaluate the joint performance and the corresponding failure modes. In the case of using 2mm AA5754, the deformation of aluminium makes the adhesive fail followed by locking mechanism release, resulting in a lower joint performance. Tensile shear performance was lower in both 3-sheet combination and 2-sheet counter parts, this is because of the amount of deformation caused during riveting process partiality deforms the joint. This non-uniform joint undermines adhesive properties by creating stress nucleation points. Although the increased thicknesses of joint by 1mm from 2-sheet to 3-sheet combination promote the adhesive failure in shear performance, whilst, in cross-tension it has the opposite effect due to the need of locking mechanism in cross-tension being associated with the rivet pull through. The extra 1mm thick Al material imposes an improved contract between the rivet and the bottom steel increasing the clamping forces between steel and rivet.

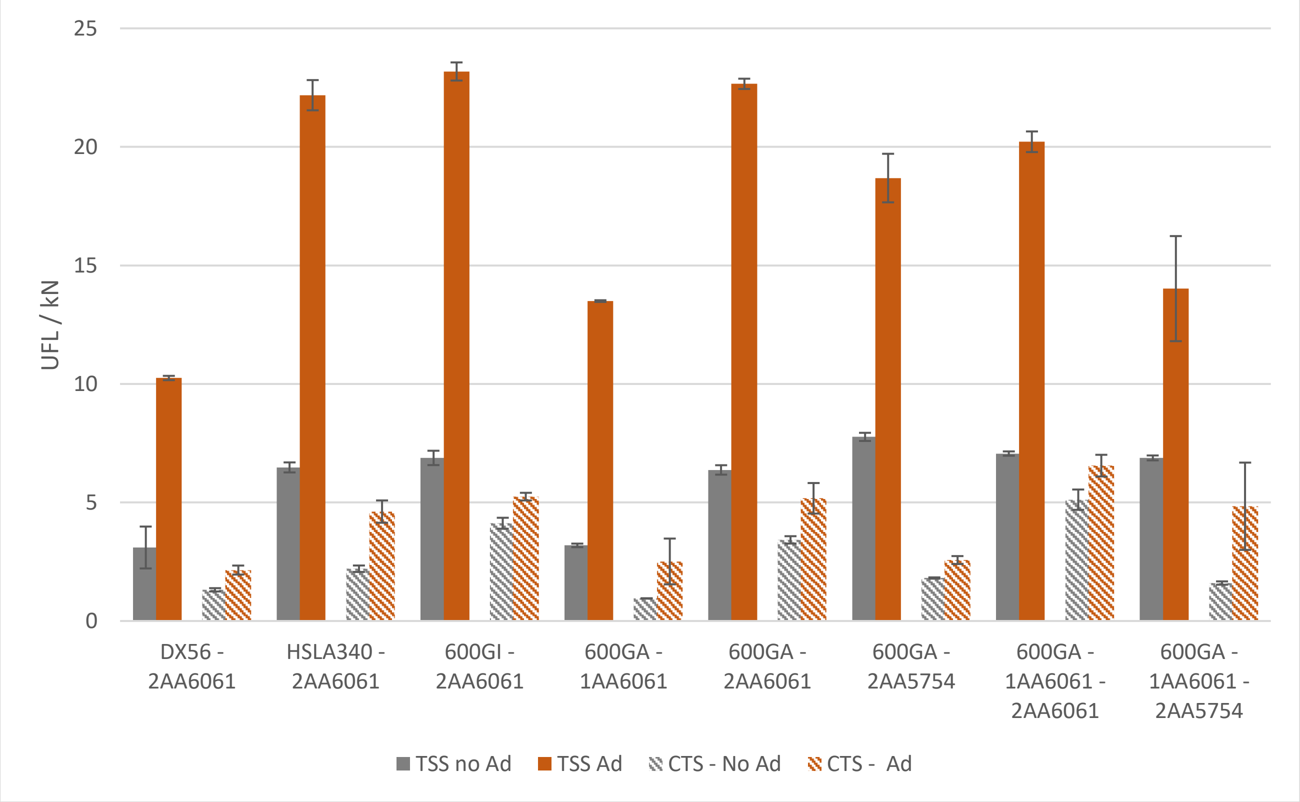

Figure 42 – Tensile and Cross tension results for the blind rivets for different material combinations with (orange) and without (grey) structural adhesive

In sum, this technology can be used to join any combination of material as long as they are within the clamping range of the rivet and there are pre-formed holes within the materials. However, this imposes the greatest challenge of this technology as the need for pre-formed holes creates an added layer of complexity in a BIW assembly due to the increased challenge in correctly aligning the components.

3.5.2.3. **Clinching**

Clinching is a straightforward technology which produces joints with a consistent failure mode. In this work, joints produced with this technology are observed to dominate with material failure at the neck of the joint as can be seen in Figure 43. This can be observed by the typical tensile load curve shown in Figure 44 where joints survive up to a maximum load before failing. When the load exceeds the yield stress of materials, it leads to shearing and cracking of the joint neck which is followed by joint movement as it can be observed by the displacement in Figure 44 that is further accompanied by sample tilting and inclination of the joint before the full cracking of the neck. Similar to the tensile shear loading, the cross tension loading the joints gets directly loaded until the neck cracks, however having another orientation of loading. The material failure as is evident in Figure 45, with exception of the Sample 1 (blue data curve) that had slipped into position on the fixture during the trial. Additionally it is possible to observe that this joint has higher joint movement as seen by the displacement in Figure 45.

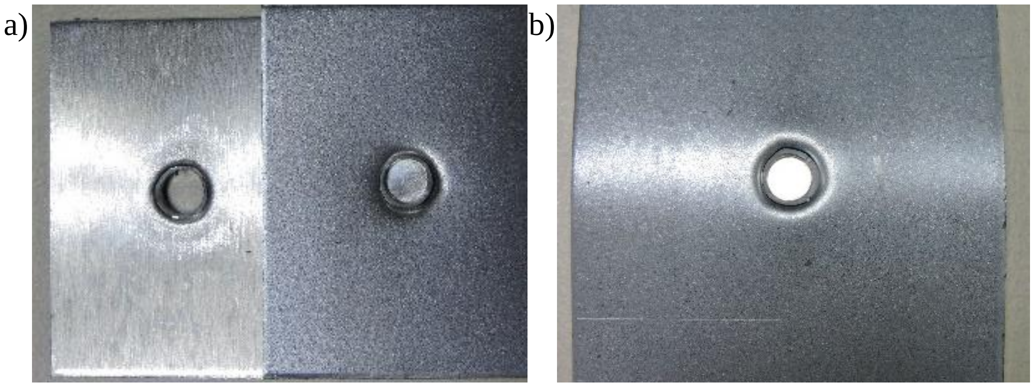

Figure 43 – Clinching material mode failure in joints tested under (a) tensile and (b) cross tension load conditions.

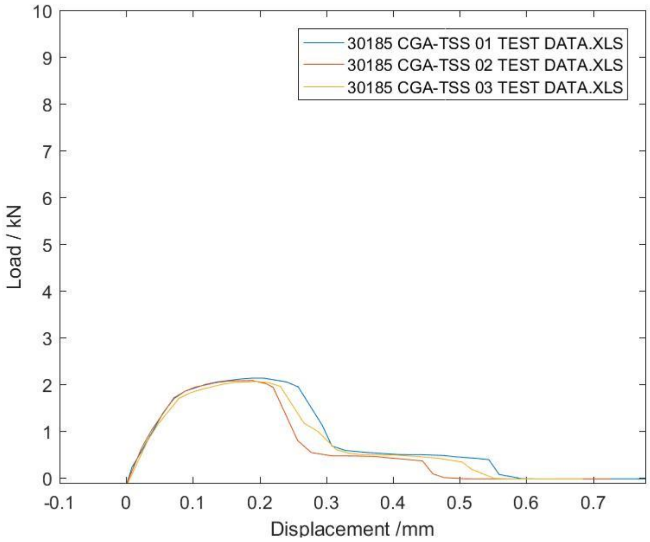

Figure 44 – Load versus displacement curves from Tensile Shear Strength tests performed for three joints of 1.4mm DP600 GA-2 mm AA6061

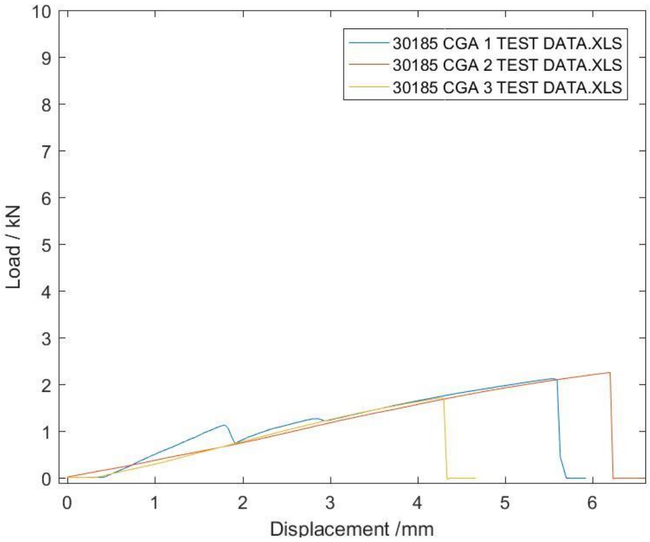

Figure 45 – Load versus displacement curves from Cross Tension Strength tests performed for three joints of 1.4mm DP600 GA-2 mm AA6061

A summary of all the different material combinations is presented in Figure 46. The most revealing results corresponds to the joint containing the 2mm AA6061sheet as it is possible to evidence the influence that the different steel properties and thicknesses have on the joint performance. As the material properties and thicknesses of the bottom material increases so does the joint performance. This is due to the combination of the improved interlock formed as well as the dissipation of forces during the loading behaviour. The lower performing material tends to bend earlier during loading leading to a higher localization of stresses in the joint neck leading to failure. The samples with the same DP600GA steel showcase the importance of the thickness and properties of the top material that forms the neck. The difference in performance of the 2-material joint, considering the transition from 1mm to 2mm AA6061 presents, an improvement of double the performance due to increase of neck thickness. Whilst the reduction of the material properties from the 2mm AA 6061 to the 2mm AA5754 also shows a small reduction on the joint performance. Note that the presence of additional 1mm AA6061 (3-sheet material combination) contributed to a very small improvement of the joint performance because there is a minimal contribution to the increase of neck thickness by adding this extra 1mm of AA6061.

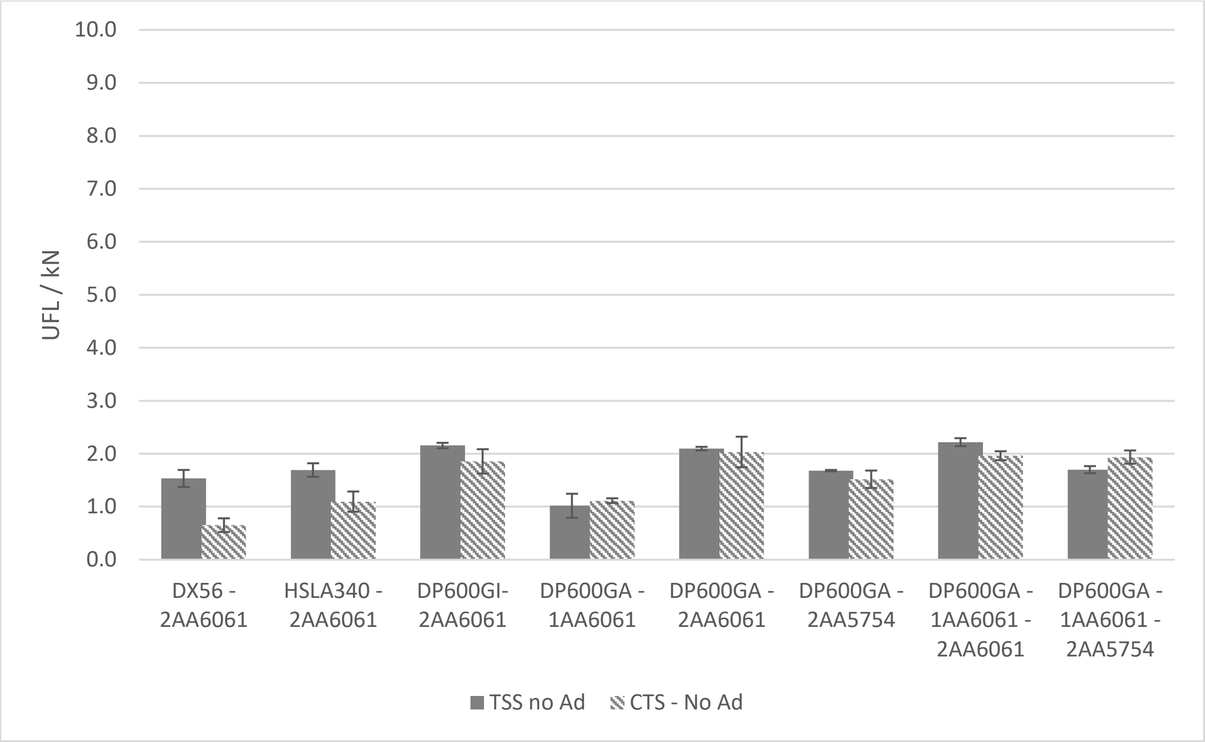

Figure 46 – Tensile and Cross tension results for the clinch joints with different material combinations

It was impossible to produce clinch joints with an adhesive because the localized stress induced in the neck of joint exceeds the yield point of the aluminium. This effect is associated with the entrapment of adhesive between the two sheets and the reduction of the friction coefficient between the materials as is observed in Figure 47. The trapped adhesive promotes inwards force making the aluminium shear instead of forming the neck and interlock during clinching. This finding contradicts the available information both in literature and technology suppliers. After careful investigation of this phenomenon it was possible to conclude that it is associated with the die used during the process, which are movable inducing a higher amount of stresses. Therefore, the associated stresses expressed by the trapped adhesive in combination of with the movable die provided the problems with this technology.

Figure 47 – Cross section of a clinch joint. Failure of neck can be seen.

In sum, this double-sided fast technology is able to form low performing joints in all material matrix. Not to be disregarded that this technology does not provide any added weight, this agrees with the lightweighting approach of this work. Regrettably the incompatibility of formation of the joint with adhesive, this technology was not provided an improved hybrid performance suggesting that it cannot be applied for high performing structural joints that require high joint quality.

3.5.2.4. **Clinch-Rivet**

Contrary to clinching technology, the clinch-rivet failure mode is dominated with material deformation followed by interlock failure of the joint as can be seen in Figure 48. Also evident from Figure 48(b) that this technology requires extra formality of the bottom material, due to the movable square die required to accommodate the rivet formability. The material deformation with interlock failure can exhibit various loading curves as is evident in Figure 49. During the loading of Sample 1 (blue) the joint failed under lower loads due to sample tilting which resulted in release of the interlock, while the other exhibited an inferior amount of tilting allowing for a higher amount of load dissipation through the joint. The use of Al as the bottom material induces the stable single failure mode of “interlock failure” for all samples during cross-tension loading condition. This behaviour is explicit for cross tension loading curves present in Figure 50.

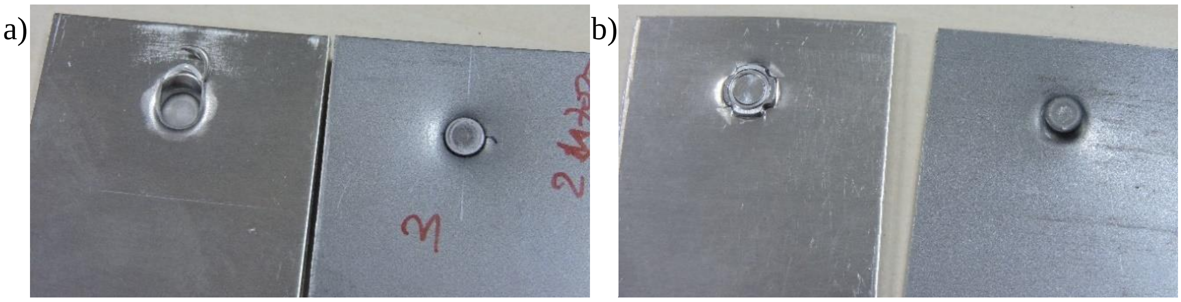

Figure 48 – Top (a) and bottom (b) view of material deformation followed by interlock failure

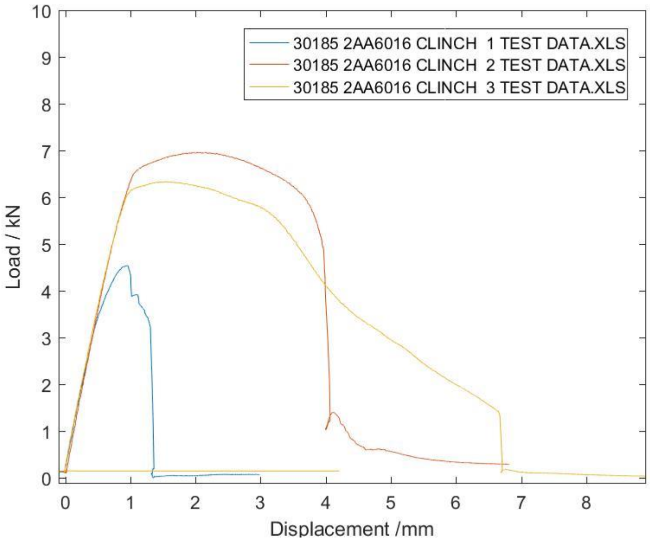

Figure 49 – Load versus displacement curves from Tensile Shear Strength tests performed for three joints of 1.4mm DP600 GA-2 mm AA6061

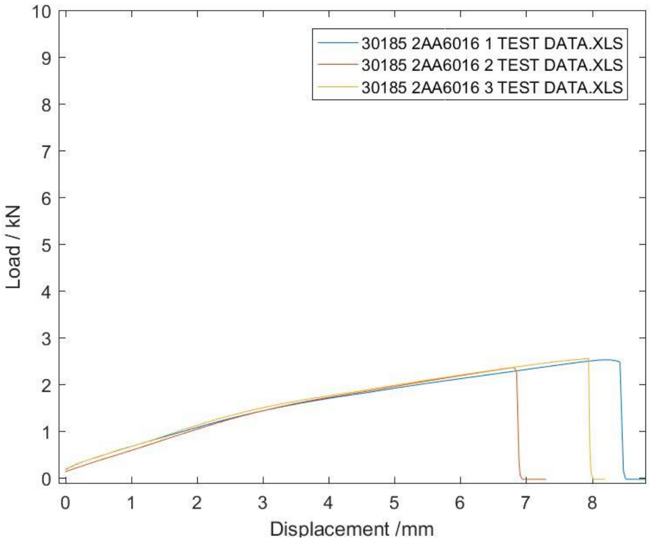

Figure 50 – Load versus displacement curves from Cross Tension Strength tests performed for three joints of 1.4mm DP600 GA-2 mm AA6061

Figure 51 summarises all the different material combinations and reveals how dependent this technology is from the material properties and various thicknesses of the bottom material. The joint containing 1mm AA6061 exhibits the lowest performing joint, under cross tension loading which was not able to achieve loads higher than 1kN and is associated with the low amount of interlock thickness material. By increase in thickness of Al sheet to 2mm from 1mm, an improvement of 270% has been observed in cross-tension behaviour due to the increase of material around the interlock, allowing for higher clamping forces in the interlock and therefore an improvement of the joint performance. Whilst the reduction of the material properties from the 2mm AA 6061 into the 2mm AA5754 also shows a small reduction on the joint performance. Interestingly the addition of the 1mm AA6061 for the 3-sheet material induces a small reduction of the joint quality, indicating a detrimental effect on the joint. This is shown in Figure 52(b) as it is possible to observe the reduction of the interlock induced by the additional 1mm AA 6061compared with Figure 52 (a).

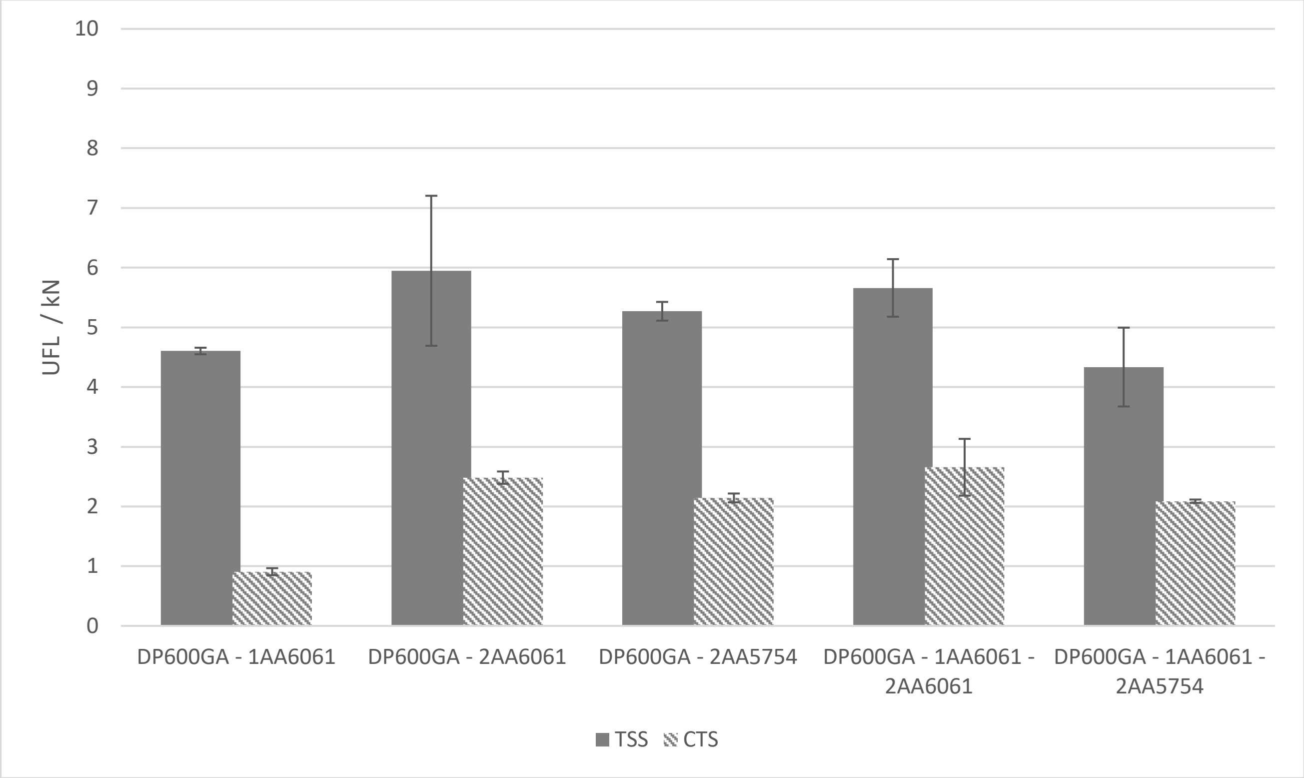

Figure 51 – Tensile and Cross tension results for the clinch rivet joints different material combinations

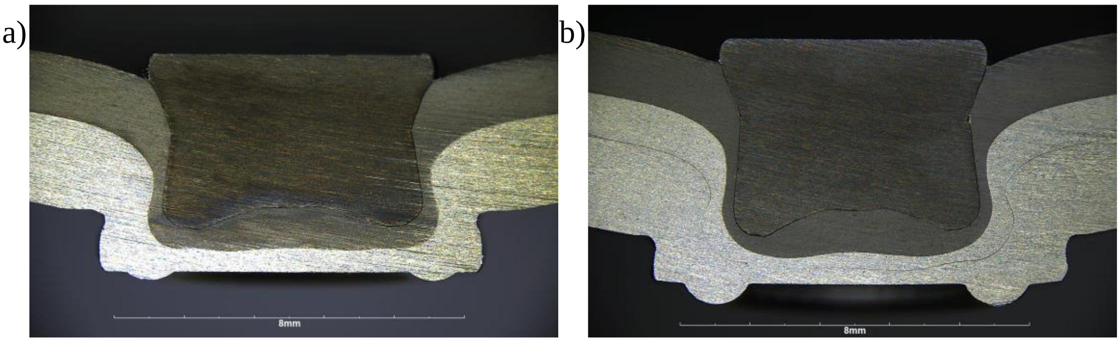

Figure 52 – Cross section of a joint of 2 sheet 1.4mm DP600GA – 2mm AA6061 (a) and 1.4mm DP600GA – 1mm AA6061 – 2mm AA6061(b)

Just like in clinching, it was impossible to produce clinch riveting joints with an adhesive because during clinch riveting process, the localized stress induced in the neck of joint exceeds the yield point of the steel and interlock formation has not been achievable without cracks due to adhesive entrapment. This supports the previous conclusion that a movable die generates a higher amount of stresses in the material leading it to fail as can be seen in Figure 53, the steel has been sheared in the joint during the riveting process.

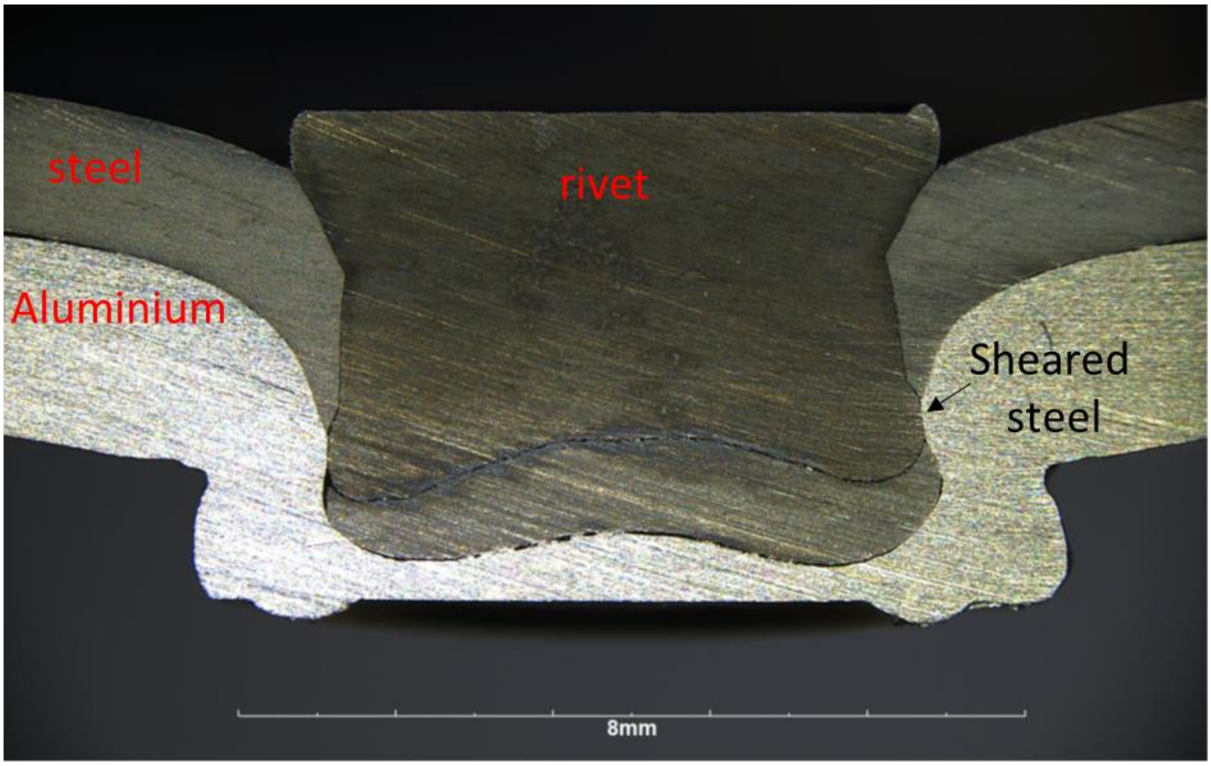

Figure 53 – Cross section of a clinch joint with adhesive

In sum, this double-sided fast clinch riveting technology provides an improvement compared to the clinching technology, however the use of element adds to cost and weight. The improved performance combined with cost and weight is not sufficient enough to be of industrial adaptation. There are other alternative technologies that can provide higher performing joints that allow hybrid adhesive and joining element technologies.

3.5.2.5. Flow drill Screws

According to the results observed the following failure modes have been identified;

- Lower sheet tear out – is normally associated with yielding and tearing of the aluminium around the joint element. This is evident in Figure 54 (a). Aluminium parent material has deformed and a small piece of the materials was snapped, while in the case of Figure 54 (b) the aluminium deformed but stayed in place.

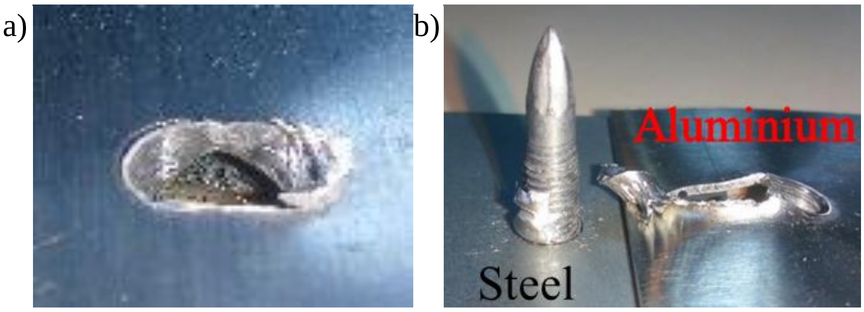

Figure 54 – Example of aluminium tear out

- Thread tear out – this is normally associated with the cross-tension testing. In this case there is the tear out of the aluminium parent material but is associated with failure of the threading on the aluminium. This is evident in Figure 55(a) where some aluminium debris can be seen in the screw grooves, whereas in the parent material (Figure 55 b) it is evident that the threads were torn out.

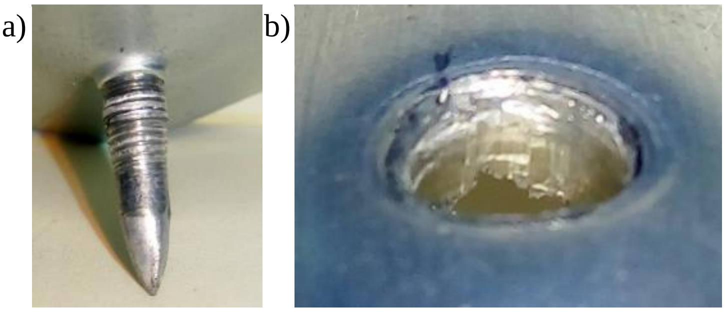

Figure 55 – Example of aluminium thread tear out

- Screw failure – as the name suggests the failure mode associated in this case is the screw breaking, as is evident in Figure 56 that the head of the screw is still intact on the steel part and the rest of the screw body in the aluminium.

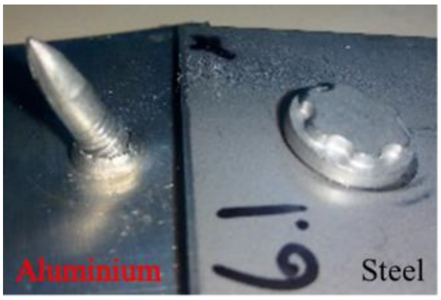

Figure 56 – Example of a screw failure

As shown in Figure 57 during loading there is a small amount of movement in the joint associated with the joint tilting due to the shear forces. When the joint reached the maximum loading the FDS screw experiences both shear and pull making the neck shear and break leading to the "screw failure" mode. The cross-tension loading shown in Figure 56 exhibits a loading that is purely tension leading to the failure mode of "thread tear out" due to the stress concentration in the screw thread making them fail.

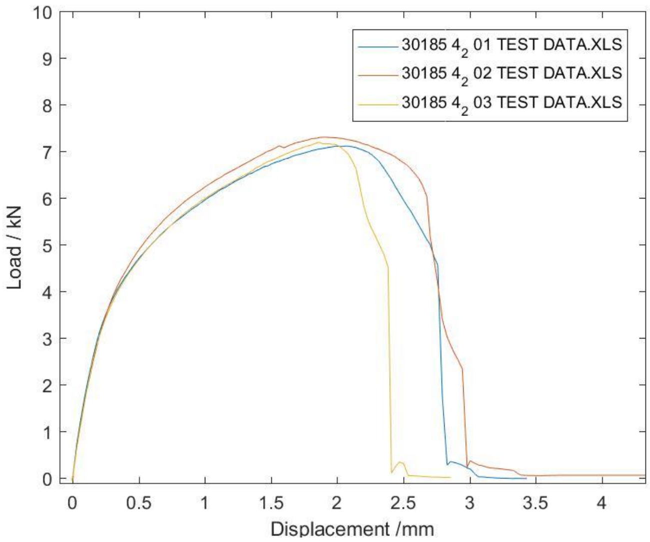

Figure 57 – Load versus displacement curves from Tensile Shear Strength tests performed for three joints of 1.4mm DP600 GA-2 mm AA6061

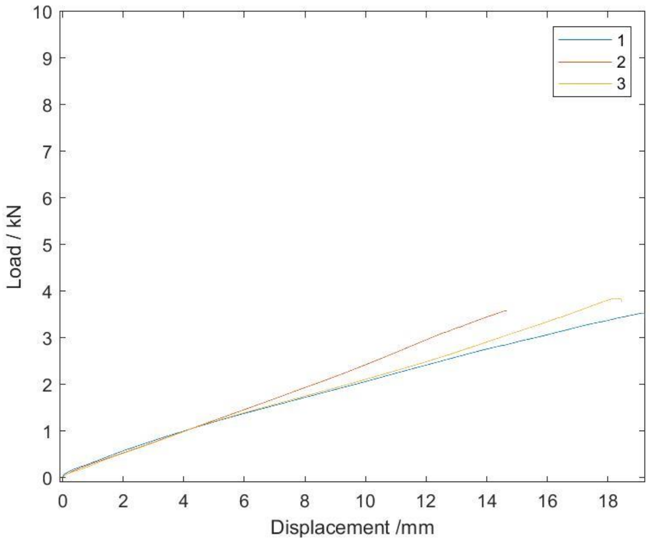

Figure 58 – Load versus displacement curves from Cross Tension Strength tests performed for three joints of 1.4mm DP600 GA-2 mm AA6061

Figure 59 summarises all the different material combinations and reveals how dependent this technology is from the material properties and thickness of the bottom material. This technology requires aluminium as the bottom material to form the threading and locking mechanism. Therefore, the joint containing 1mm AA6061 exhibits the lowest failure load in both CTS and TSS. In TSS, the failure mode is lower sheet tear out. However, for thicker 2mm AA6061, joint performance improves and failure changes in to the screw failure mode. Under both loading conditions, increased sheet thickness increases the failure load performance by double. The failure mode in cross-tension behaviour is consistent in all the different joints as is associated with failure of the thread, so doubling the thickness (transition from 1mm to 2mm AA6061) allows the depth of the locked region to be significantly higher in the joint. In 3-sheet combination a small decrease in performance has been observed which in turn is associated with change of equilibrium for force dissipation in the joints. As can be seen in Figure 60 the addition of another dissimilar layer of aluminium creates an additional gap that is undermining the joint performance. On closer inspection of Figure 60 (b) it is possible to see that the additional 1mm AA 6061 is protruding into the lower 2mm AA6061, thus reducing the area of locking thread of the bottom material, whilst in the Figure 60 (a) the 2mm AA6061 has the freedom to flow upwards which increases the thread locking area. Relatively small reduction in the joint performance has been observed by replacing high strength 2mm AA 6061 sheet with the lower strength 2mm AA5754 alloy.

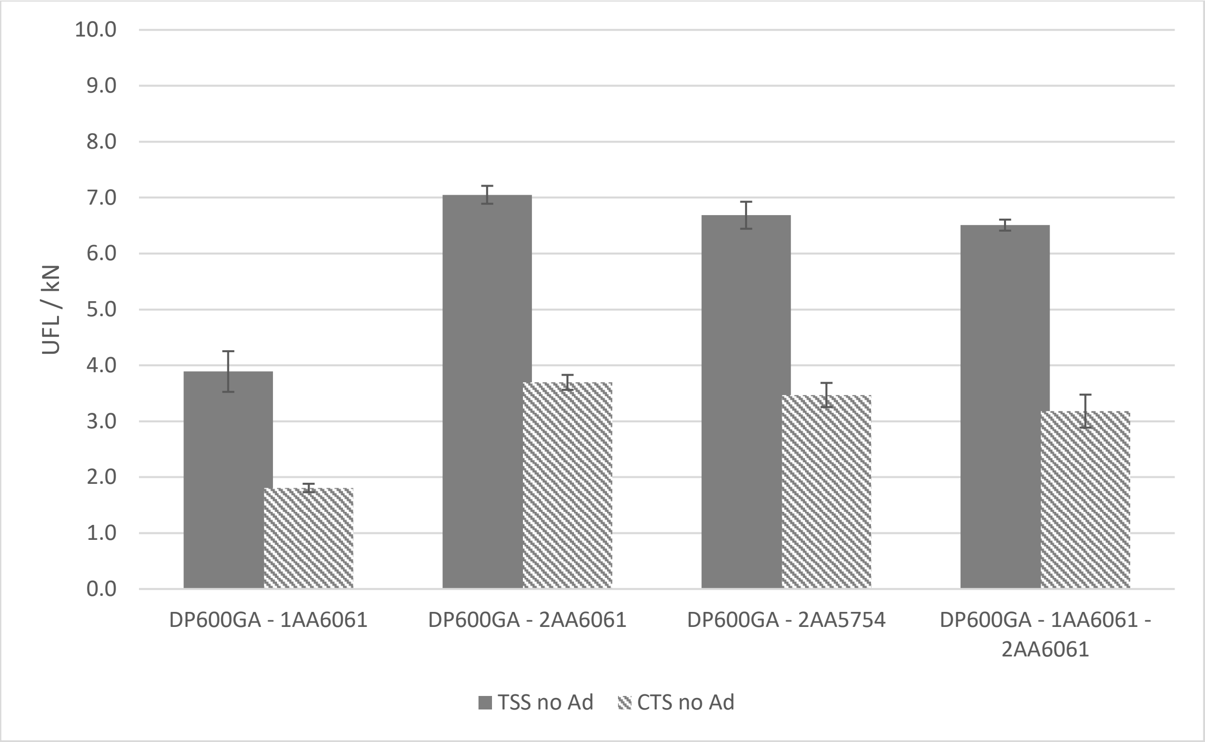

Figure 59 – Tensile and Cross tension results for the flow drill screw joints different material combinations

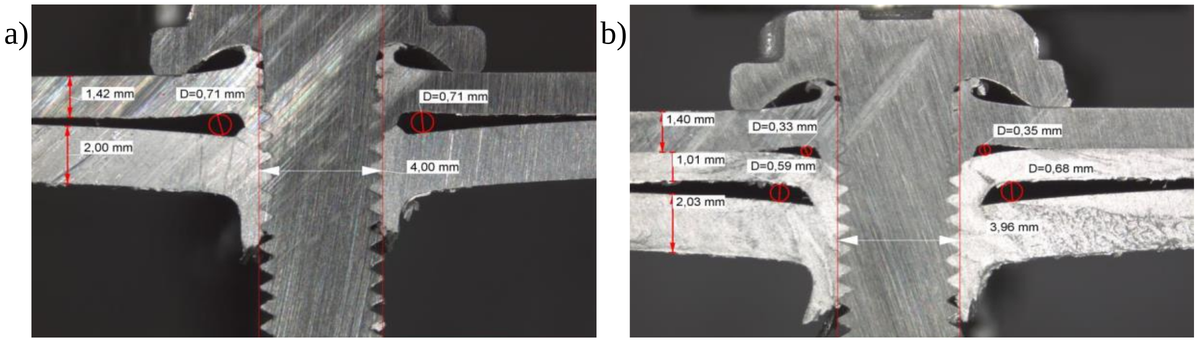

Figure 60 – Cross section of a joint of 2 sheet 1.4mm DP600GA – 2mm AA6061 (a) and 1.4mm DP600GA – 1mm AA6061 – 2mm AA6061(b)

This technology allowed us to successfully achieve hybrid joints with adhesive and a summary of joint performance is presented in Figure 61. The results evidently show significant improvement in joint performance with adhesive. In this particular case the conclusions observed from the non-hybrid joint translate to the hybrid joints, as the joint with 1mm AA6061 is still has lowest performance compared to the 2mm AA6061 because the failure mode is associated with parent material failure whilst the 2mm AA 6061 counterpart suffers from adhesive failure followed by screw failure or bottom material tear out. Similarly, the 3-sheet material combination suffers from the previously described additional gap that is present between the sheets and flow of aluminium creates stress nucleation point that promote the adhesive failure flowed by material failure. The particular case of the 2mm AA5754 is associated with adhesion failure due to the surface oxide layer associated with the fact this alloy is rich in Mg content. As expected from the adhesive, an improvement in performance has been observed not only in TSS but also in CTS condition.

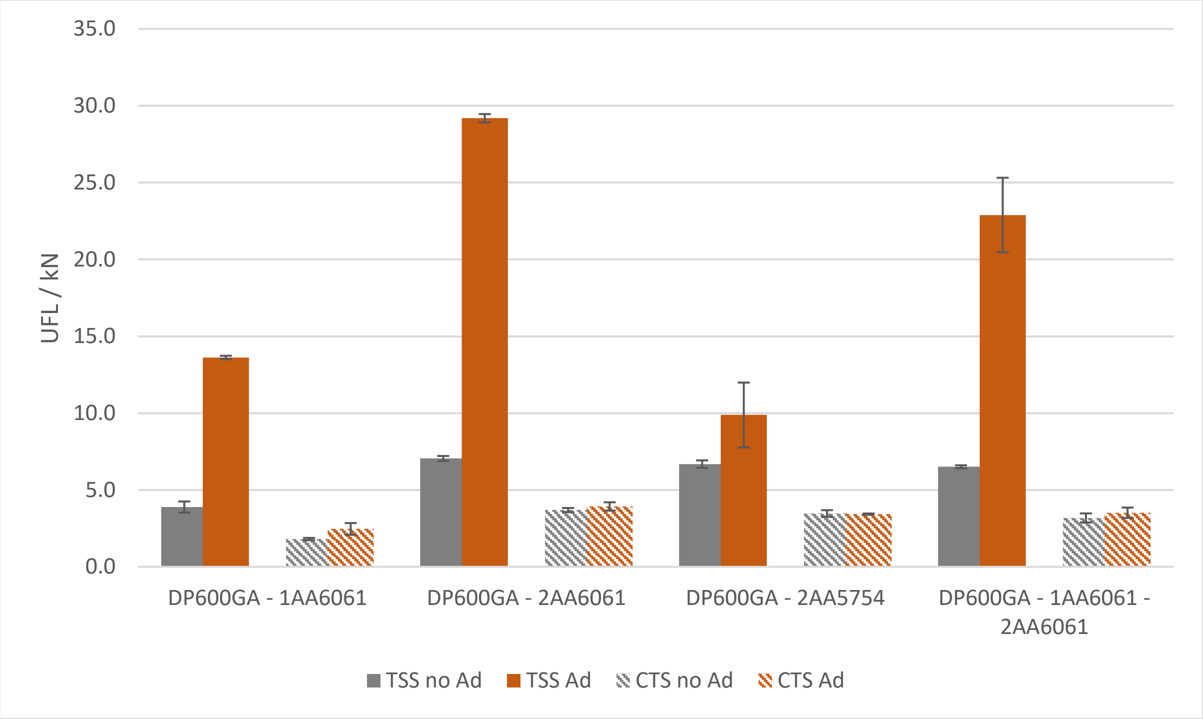

Figure 61 – Tensile and Cross tension results for the flow drill screw joints with different material combinations. Orange and grey represents data for with and without structural adhesives respectively.

In sum, this double-sided FDS technology requires high formable materials to be positioned at the bottom part of the joint but it has the potential to be used as single-sided. This technology can be categorised as high cost, high cycle time of 6 sec per joint and the protrusion of a long element restricts its application to where the element does not pose a safety threat during maintenance.

3.5.2.6. Self-piercing rivet

Self-piercing rivets is uncomplicated technology with a consistent failure mode associated with the loss of interlock by bottom material deformation in the joint which can be seen in Figure 62. The interlock formed by the rivet is achieved by piercing the top material and flaring to form the interlock between the rivet and the bottom material. Therefore, as shown in Figure 62 (b), this technology requires extra formability of the bottom material to form the interlock. The consistent failure mode of material deformation followed by interlock failure can be observed in the tensile shear load curves presented in Figure 63. As the load increases in the joint there is a small tilting of the samples creating a hybrid shear/peel mode. This creates the conditions for the joint interlock to fail as the material around the interlock deforms and releasing it. The use of Al at the bottom material induces the stable single failure mode of “interlock failure” for all samples during cross-tension loading condition. This behaviour is explicit for cross tension loading curves present in Figure 64.

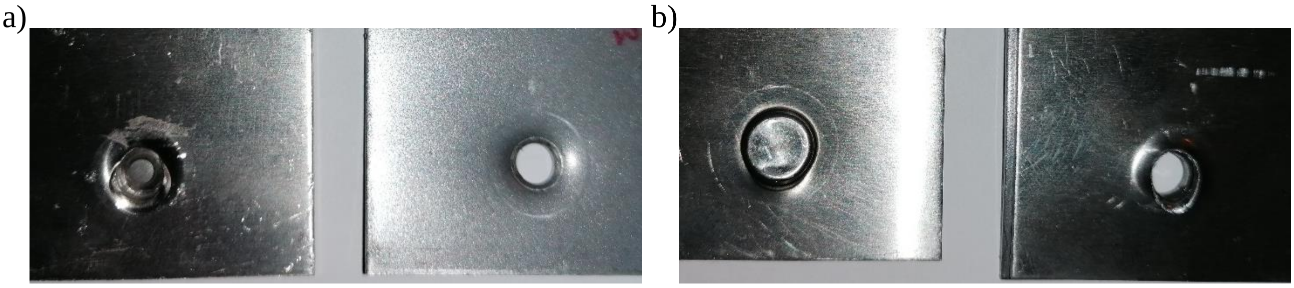

Figure 62 – SPR failure mode from top (a) and bottom (b) view

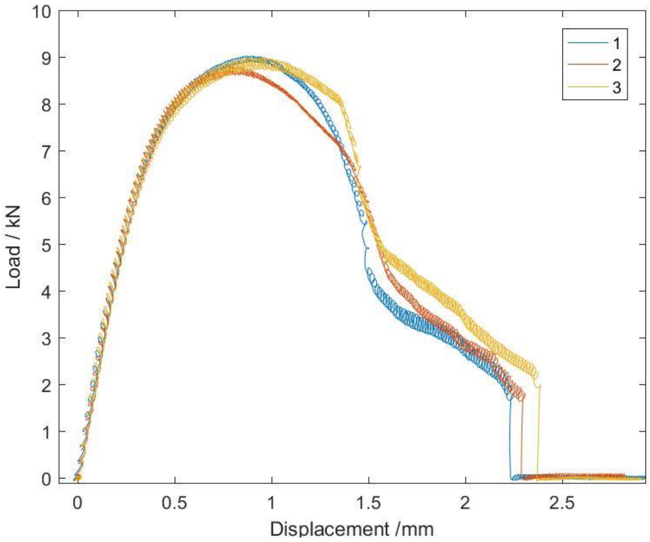

Figure 63 – Load versus displacement curves from Tensile Shear Strength tests performed for three joints of 1.4mm DP600 GA-2 mm AA6061

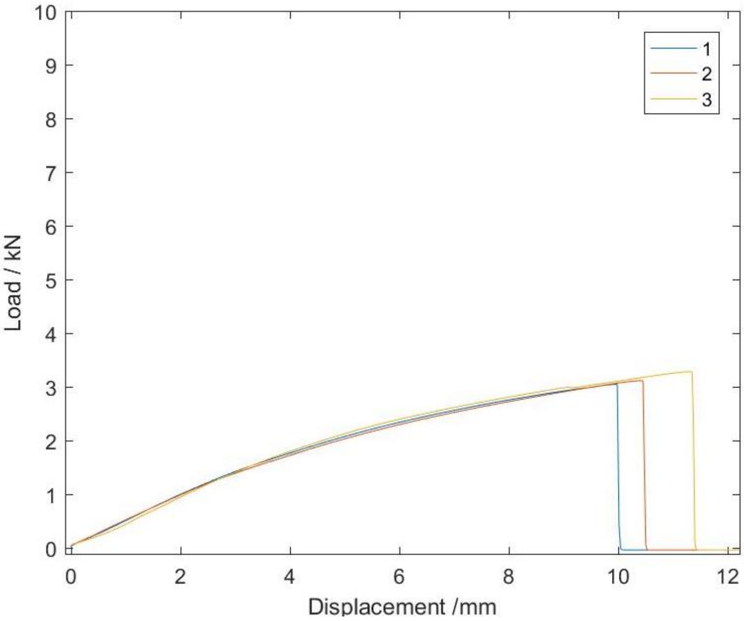

Figure 64 – Load versus displacement curves from Cross Tension Strength tests performed for three joints of 1.4mm DP600 GA-2 mm AA6061

Figure 65 summarises all the different material combinations and reveals how dependent this technology is on the material properties and thickness of the bottom material. Due to the rivet size limitation the joint containing the 1mm AA6061 was impossible to perform, showcasing that element size is crucial for joint assembly. The performed joint orientation is steel to Al, so all the joints with 2mm AA6061 sheets have the same material as the bottom and interlocking material. Therefore the observed improvement in the joint quality with the improvement of steel material properties does not correlate with an improvement of the interlock. This improvement is associated with the reduction of the joint bending as well as an increase in thickness of steel. Therefore the DX56, which has a lower yield point, induces joint tilting at lower loads compared with the DP600GA. This is a crucial factor because the joint failure is associated with the pull/shear motion induced in the joint during tensile shear loading. This is further evidenced in the cross tension loading tests that the joint strength is reliant primarily on the AA6061 locking mechanism during load and therefore all joints exhibited similar failure loads. To prevent cracking in the bottom material, the rivet selected for 3 sheet material joints and the joint containing the AA5754 was different from the other joint configurations. Compared to the standard rivet, this has restrictive flow properties, therefore not flaring as much and therefore slightly compromising the shear performance of the joint. Similar to TSS tests, for cross tension tests, joints with two different rivets were produced. One type of rivet is for 2-sheet geometry consisting of 2mm AA6061 sheet and the other rivet is for joint containing AA5754 and 3-sheet geometry.

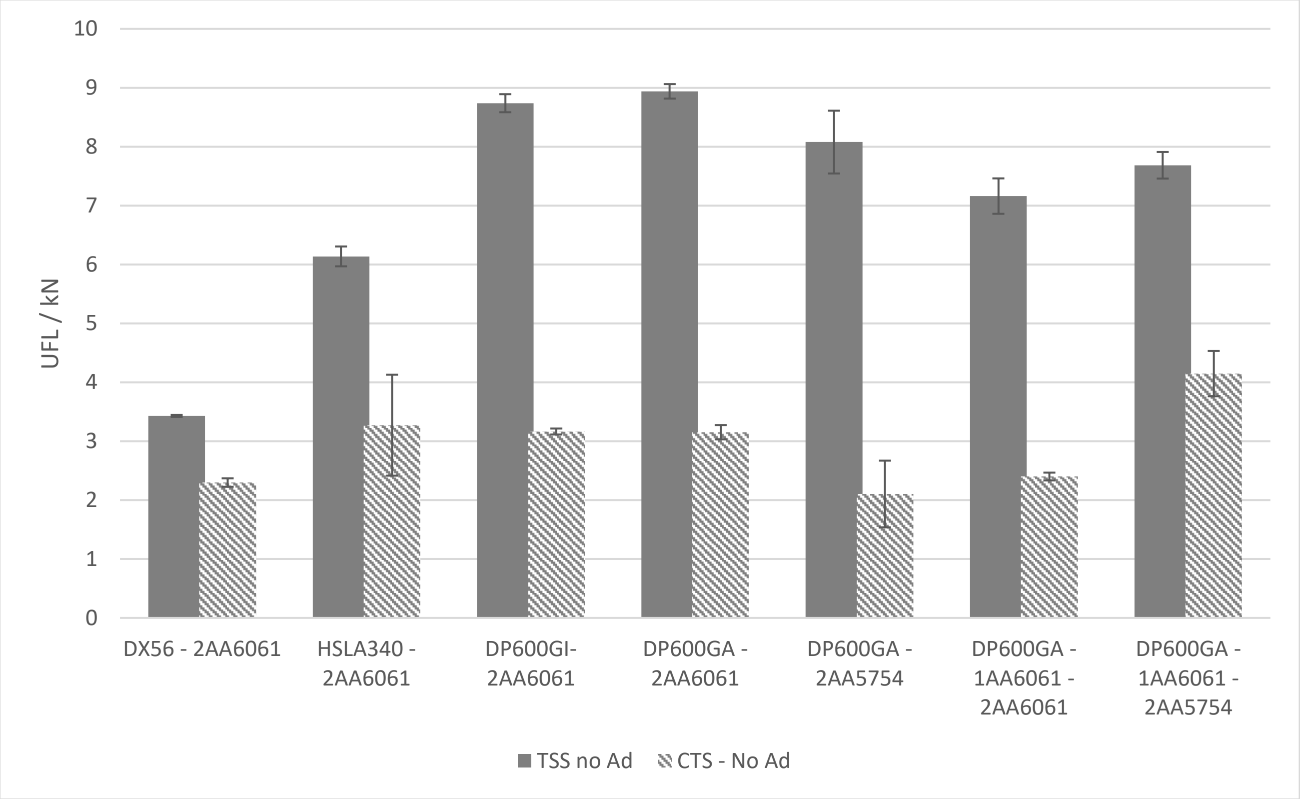

Figure 65 – Tensile and Cross tension results for the Self-Piercing Rivet joints different material combinations

Contrary to clinching and clinch-rivet this technology allowed us to successfully achieve hybrid joining with an adhesive and a summary of achieved joint performance is presented in Figure 66. Thus, similar to other technologies, the results clearly show that joints with adhesive performed significantly better. The observations from the non-hybrid joint translate to the hybrid joints especially as the failure mode is constant during all loading trials, where there is adhesive/cohesive failure followed by the loss of interlock. The observed improvement of the joint quality directly correlates with reduction of the material bending during the shear loading as well as an increase in material thickness. Therefore there was a reduction on the peal/shear loading on the joint thus improving the adhesive performance. The particular case of the 2mm AA5754 is associated with adhesion failure due to the oxide layer at the surface of the 2mm AA5754.

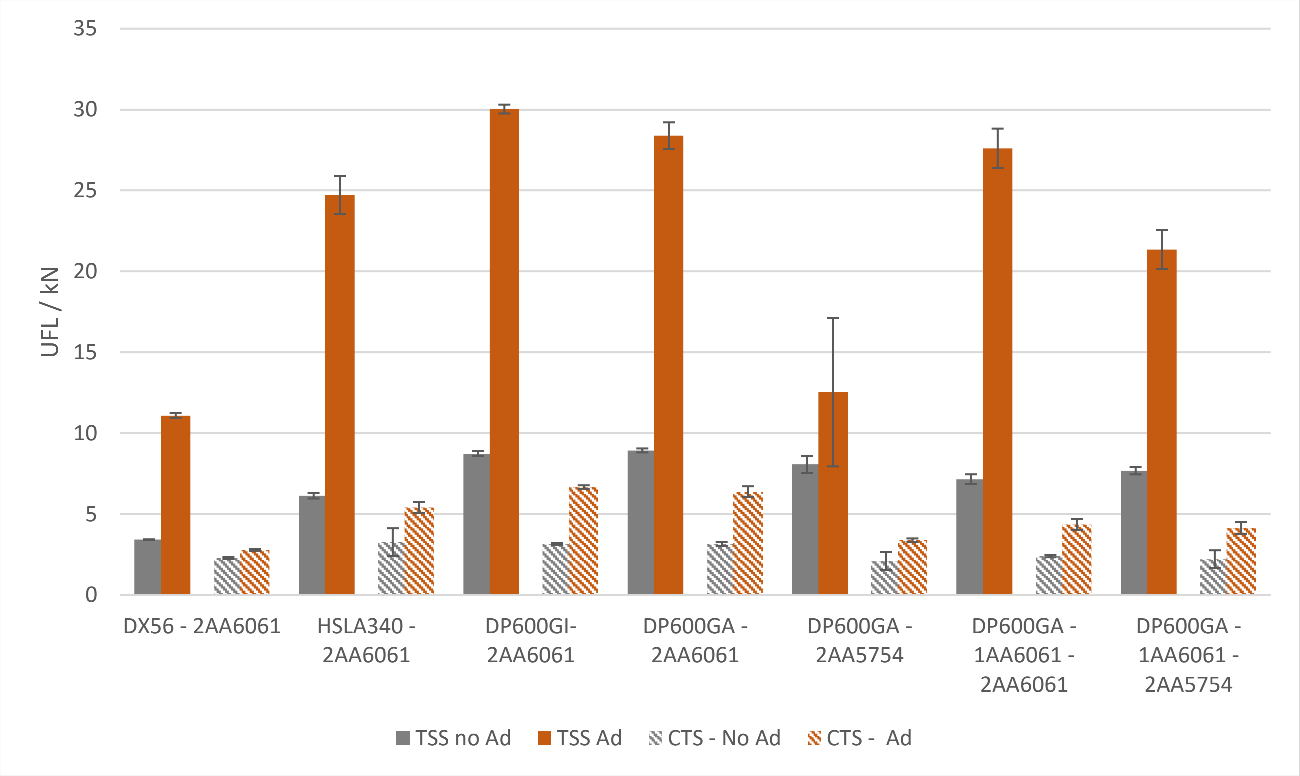

Figure 66 – Tensile and Cross tension results for the Self-Piercing Rivet with different material combinations with (orange) and without (grey) structural adhesive.

In sum, this double-sided technology offers selections of materials with wider range of formability characteristics as the self-piercing capability minimizes the formability requirements compared to other technologies. Also the high performing joints and easiness of application justifies being the technology with most application within the automotive industry for dissimilar joining, despite the added weight, cost and access. SPR joints combined with a structural adhesive exhibits great improvement of the performance.

3.5.2.7. **Solid Punch Rivet**

Solid punch rivet failure mode is dominated with material deformation followed by interlock failure of the joint as can be seen in Figure 67. This behaviour is seen explicitly in the tensile shear loading curves observed in Figure 68, where the joint sustains loading until the local stress exceeds the yield point of the aluminium making the material deform and the joint tilt until the interlock gets released. Like in all the previous technologies the joint performance in cross tension loading strongly depends on the bottom material interlock and the failure mode is associated with material deformation prior to interlock failure.

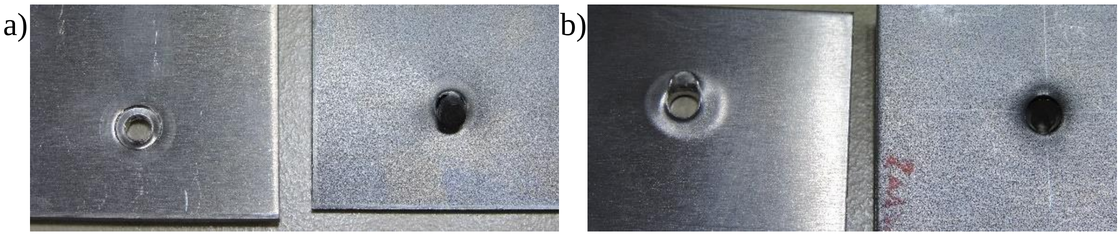

Figure 67 – Top (a) and bottom (b) view of material deformation followed by interlock failure

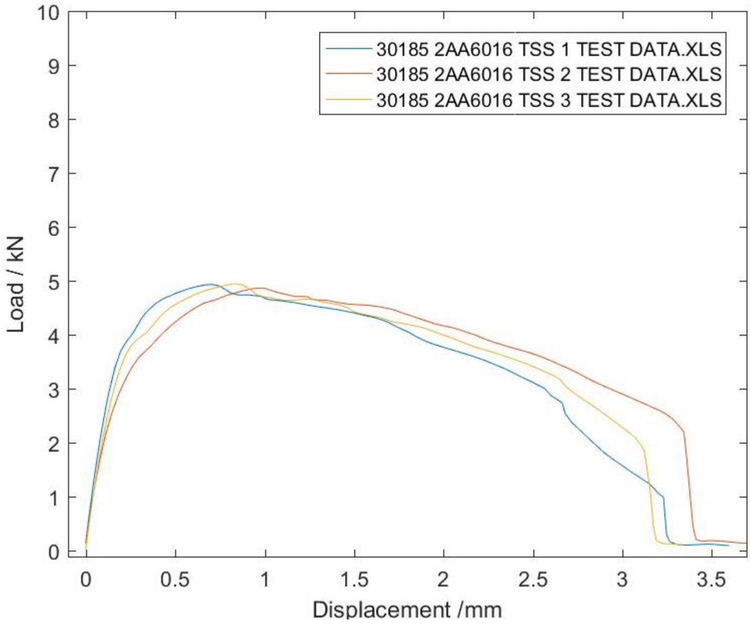

Figure 68 – Load versus displacement curves from Tensile Shear Strength tests performed for three joints of 1.4mm DP600 GA-2 mm AA6061

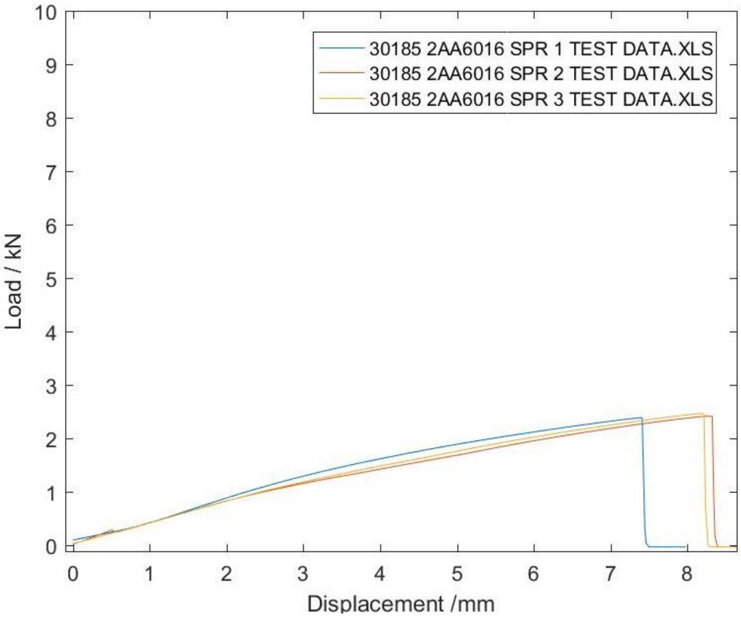

Figure 69 – Load versus displacement curves from Cross Tension Strength tests performed for three joints of 1.4mm DP600 GA-2 mm AA6061

Figure 70 summarises all the different material combinations and reveals how dependent this technology is on the material properties and thickness of the bottom material. This technology is reliant of the aluminium as the bottom material to form the interlock mechanism and the locking mechanism is independent of the thickness of the joint. During shear loading, in DP600GA joined with either 1mm AA6061 sheet or 2mm AA6061 sheet and the 3-sheet combinations containing the 1mm AA6061-2AA6061 sheets exhibits the same nature of failure mode and exhibit similar ultimate failure loads as shown in Figure 71. However, the same behaviour does not translate under cross- tension loading, due to the nature of the tension loading. The cross-tension loading is reliant on the interlock formed between the solid rivet and the bottom material, therefore the 1mm AA6061 exhibits the lowest performing joint due to thin interlock area as shown in Figure 71. The 2mm AA6061 joint provide the highest performing joint followed by the 3-sheet material joint with a small decrease of joint performance. This is associated with the presence of additional 1mm AA6061 which is reducing the interlock size as can be seen in Figure 71 (c). The joints containing AA5754 sheets present the same behaviour however with a decreased performance due the decrease in material tensile properties.

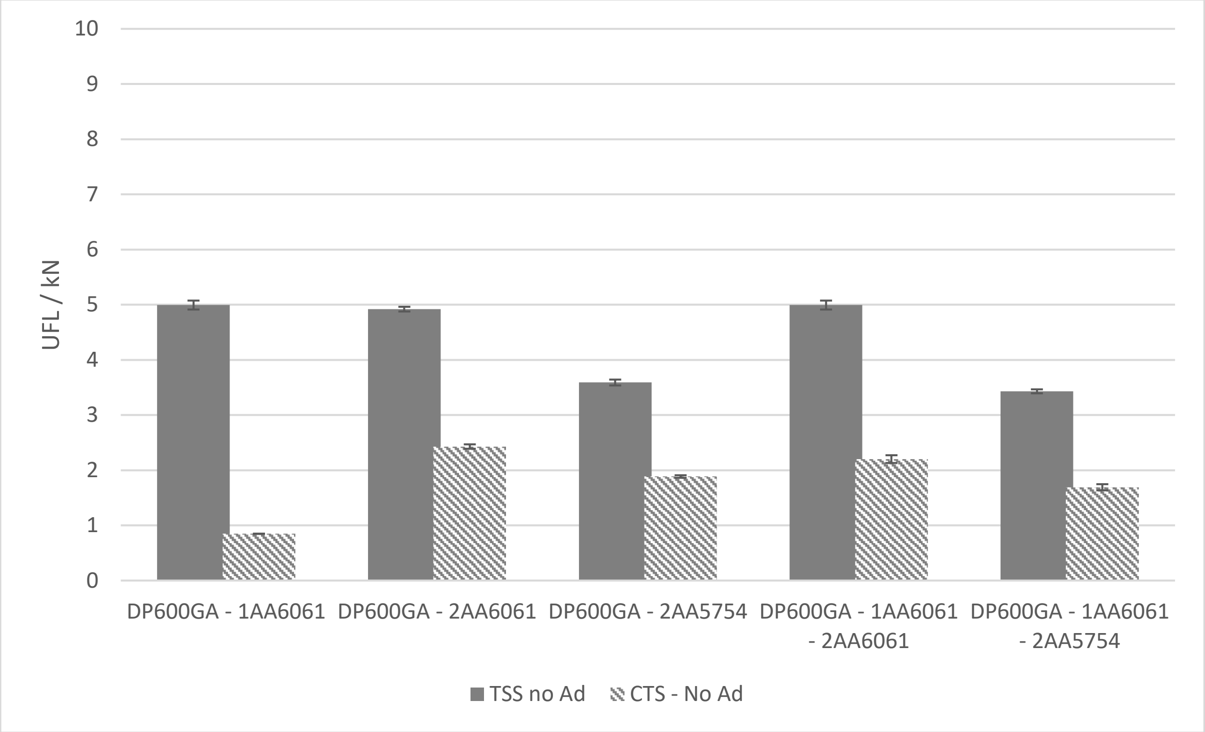

Figure 70 – Tensile and Cross tension results for the solid punch rivets joints different material combinations

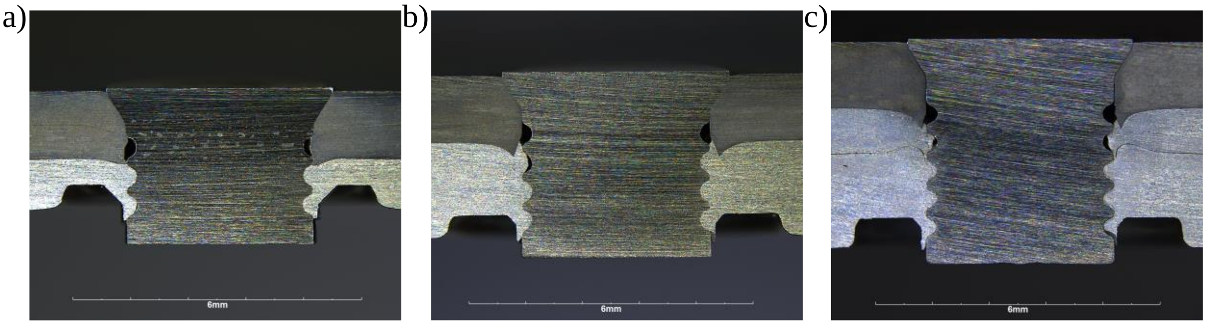

Figure 71 – Cross section of a joint of 1.4mm DP600GA – 1mm AA6061 (a); 1.4mm DP600GA – 2mm AA6061 (b) and 1.4mm DP600GA – 1mm AA6061 – 2mm AA6061(c)

This solid punch rivet technology can be combined with adhesive to successfully achieve hybrid joining and a summary of achieved joint performance is presented in Figure 72. Hybrid joints with adhesive are shown to perform significantly better to adhesive free joints. Similar to FDS technology the conclusions observed from the non-hybrid joint translate to the hybrid joints, as the joint with 1mm AA6061 is still has lower performance compared to the 2mm AA6061 because of the failure mode is associated with parent material failure whilst the 2mm AA6061 counterpart suffers from adhesive failure followed by interlock failure. The same behaviour was also translated into the 3-sheet material combination of 1mm AA6061 – 2mm AA6061. The particular case of the 2mm

AA5754 is as previously described suffers adhesion failure due to the oxide layer at the surface of the 2mm AA5754, exhibiting poorer performance in the 3-sheet 1mm AA6061 – 2mm AA5754 due to the nature of the adhesive bond layer between Al-Al. In this joint, on one side there is AA5754 sheet which has problems with the oxide layer followed by the 1mm AA 6061 which does not provide a stable interaction layer as the steel. The cross-tension load exhibits an improvement in performance as expected from the adhesive.

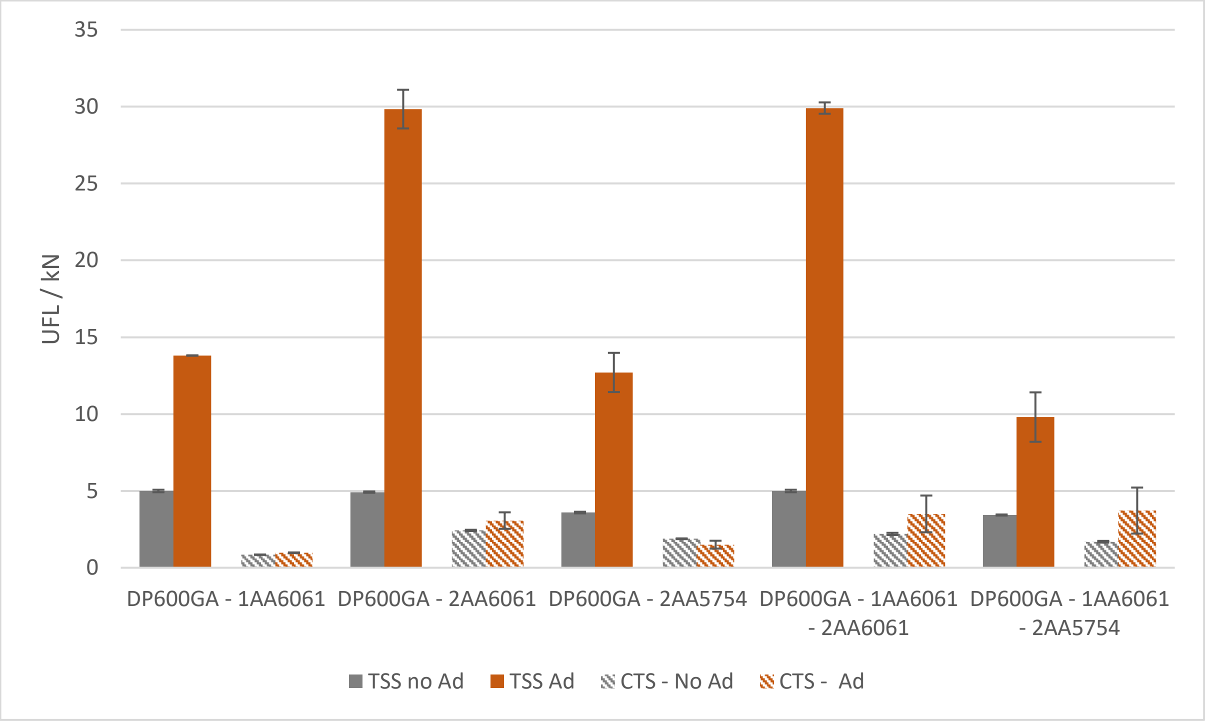

Figure 72 – Tensile and Cross tension results for the Solid Punch Rivets in different material combinations with (orange) and without (grey) structural adhesive

In sum, in this double-sided technology, part of the sheet material gets extruded by the screw in order to form the lock, making the net added weight is very small. Processing speeds are of around 1 second per joint, however the biggest limitation of this technology is the need to collect the extruded material. This will become incrementally difficult when if the material has an adhesive layer because this increases the complexity by becoming stuck and soiling the equipment.

3.5.2.8. Tack high speed joining

Tack high speed joining as previously described consist of a hardened nail fired at extreme speeds to form a tack joint. The failure modes observed were (i) the failure of the element due to shearing of the nail between the nail head and body as it can be seen in Figure 73, (ii) the failure mode that is associated with interlock loss due to material failure (sheet deformation) along with element failure as is evident in Figure 74; and finally (iii) the failure mode that is specific to cross-tension loading is the loss of interlock followed by the rivet slipping through the material (Figure 75). The tensile shear loading curve presented in Figure 76 reveals the evidence for the failure mode by the loss of interlock and element failure. As the load increases the sample begins to tilt which induces a mixed mode of shear/pull loading. The localization of stresses makes the sheet material yield and deforms the head of the nail until the interlock fails as the example presented in Figure 74. The cross tension exhibits a constant behaviour as presented in Figure 77 with the sheet material deforming during loading followed by the release of interlock.

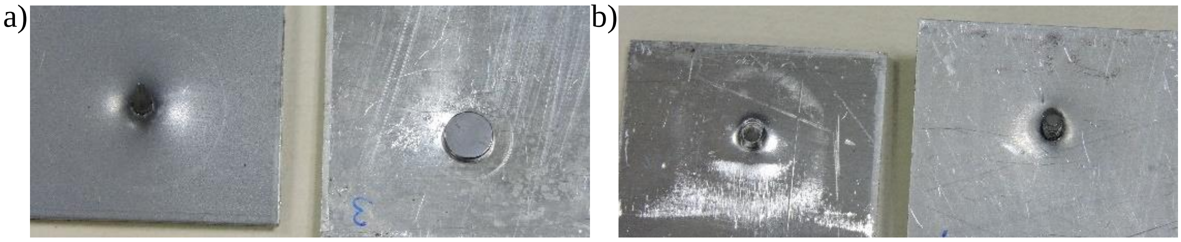

Figure 73 – Top (a) and bottom (b) view of failure of the joint element (sheared nail)

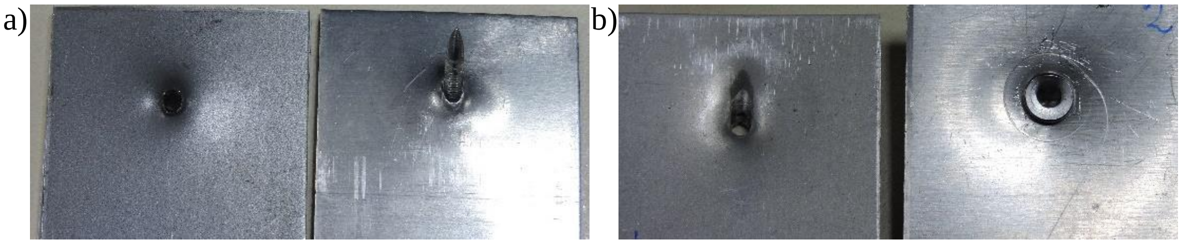

Figure 74 – Top (a) and bottom (b) view of material failure with loss of interlock and element failure (nail broken around the top).

Figure 75 – Bottom view of interlock failure without any damaged to the element

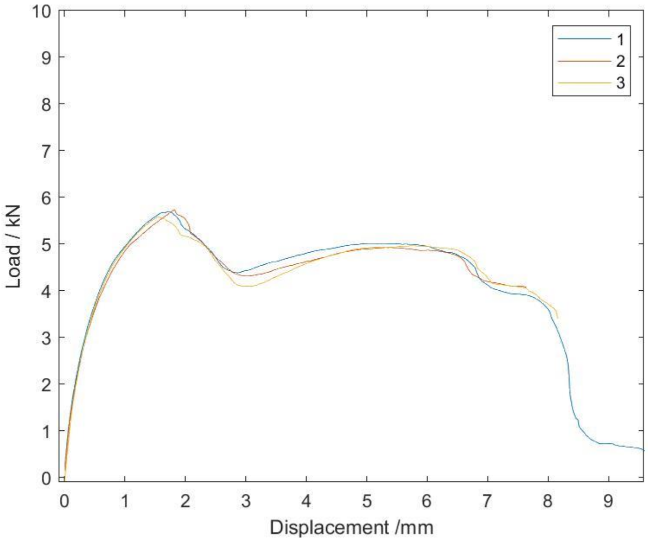

Figure 76 – Load versus displacement curves from Tensile Shear Strength tests performed for three joints of 1.4mm DP600 GA-2 mm AA6061

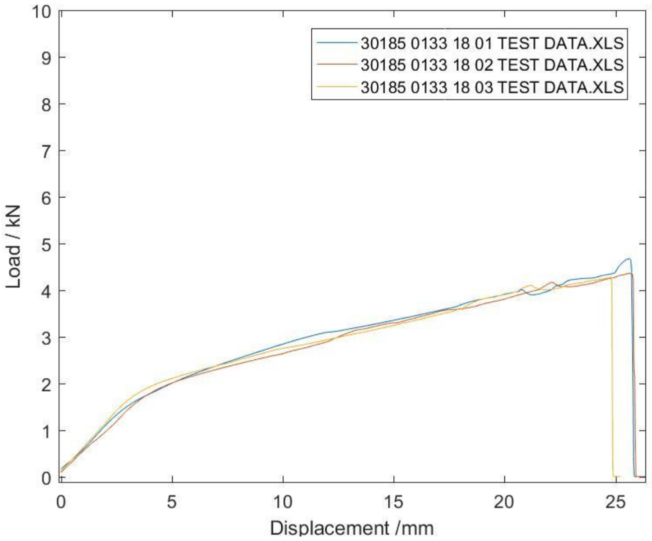

Figure 77 – Load versus displacement curves from Cross Tension Strength tests performed for three joints of 1.4mm DP600 GA-2 mm AA6061

Figure 78 summarises all the different material combinations. It can be seen that the joints produced with this technology is dependent on material properties that are able to take high loads during the setting. In the case of the joint containing the 1mm AA6061 the material is too thin not having the necessary properties for this joint to take the necessary loads, and therefore it was impossible to produce. Although this technology is reliant on the bottom material (steel) to produce the interlock, the interaction with the different top aluminium creates distinct joint with different aspects and behaviours. The material flow of the different aluminium exhibits very different properties, as shown in Figure 79a, the AA6061 does not exhibit a high amount of opposing flow to the nail and has a smooth interaction with the DP600. Contrarily the AA5754 exhibits higher flow material resistance during the nail application as well as the formation of a bulge in the steel as observed in Figure 79b, being translated in a failure mode that is associated with the failure of the rivet and therefore having the highest performing shear joint. However, the advantage seen in tensile shear loading compromises the performance in the cross tension due to the gap between the two materials undermining the clamping forces between the steel and the nail. On the contrary the joint with the AA6061 offers higher flowability of material and the failure mode in tensile shear is associated with the material failure with the loss of interlock and element failure. This joint offers the best performing cross tension joint due not only to the intimate contact between the joints but also the high amount of clamping force. It is possible to see also in Figure 79 that the behaviour observed in the 2-sheet material combination was transferred in to the 3-sheet material combination counterparts however resulting in a reduction in their joint performance.

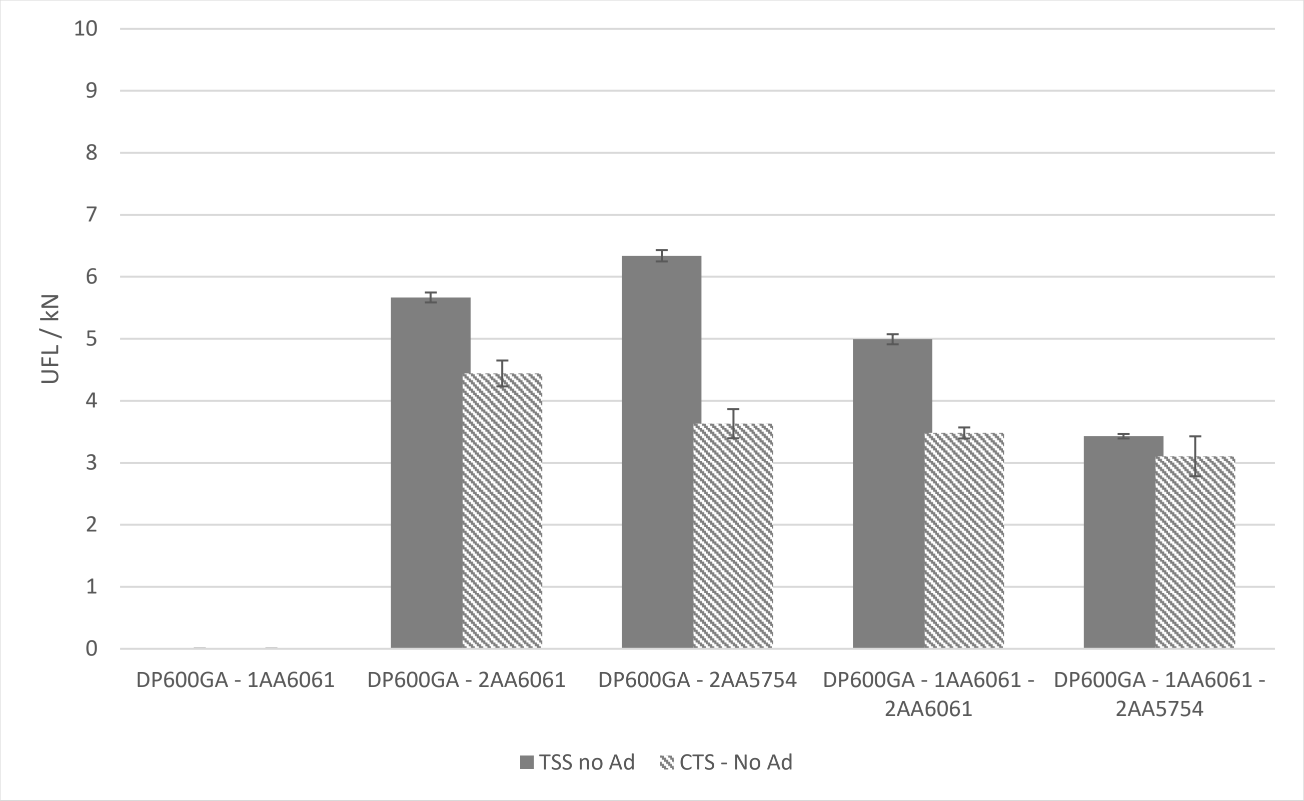

Figure 78 – Tensile and Cross tension results for the tack high speed joints different material combinations

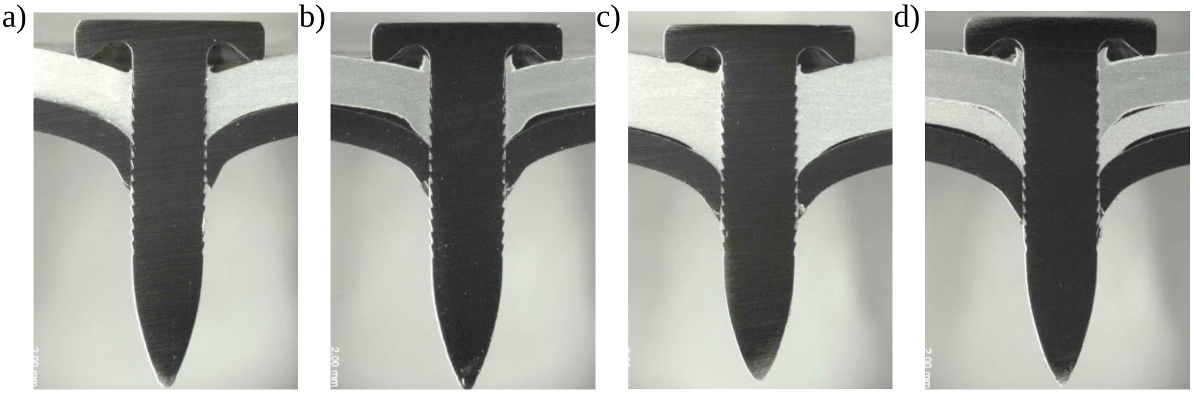

Figure 79 – Cross section of the tack high speed joints for the: DP600GA – 2AA6061 (a); DP600GA – 2AA5754 (b); DP600GA – 1AA6061 – 2AA6061 (c); DP600GA – 1AA6061 – 2AA5754 (d);

This technology allowed us to successfully achieve hybrid joining with an adhesive and a summary of joint performance is presented in Figure 80. In the case of the AA6061 the deformation during setting created an area of non-bonding between the adhesive and the AA6061 leading to a reduction of bonded area as well as localization of stresses over a non-uniform area which is observed in Figure 81 for tensile shear and Figure 82 for the cross tension joints. This accounts for the low tensile loads in the joints containing the AA6061 as well as in the cross tension testing. In previously discussed technologies, it is mentioned that AA5754 has oxide layers which causes lower strength, however for this technology the joints containing the AA5754 exhibit a dramatic improvement compared to other joining technologies as the joints managed to surpass the previously observed low performance of 10kN caused by the surface oxide. The high clamping forces associated with the local material deformation promote a higher affinity between the adhesive and substrate leading to such a dramatic increase in performance. This behaviour was observed not only in the tensile specimens but also in the cross tension specimens.

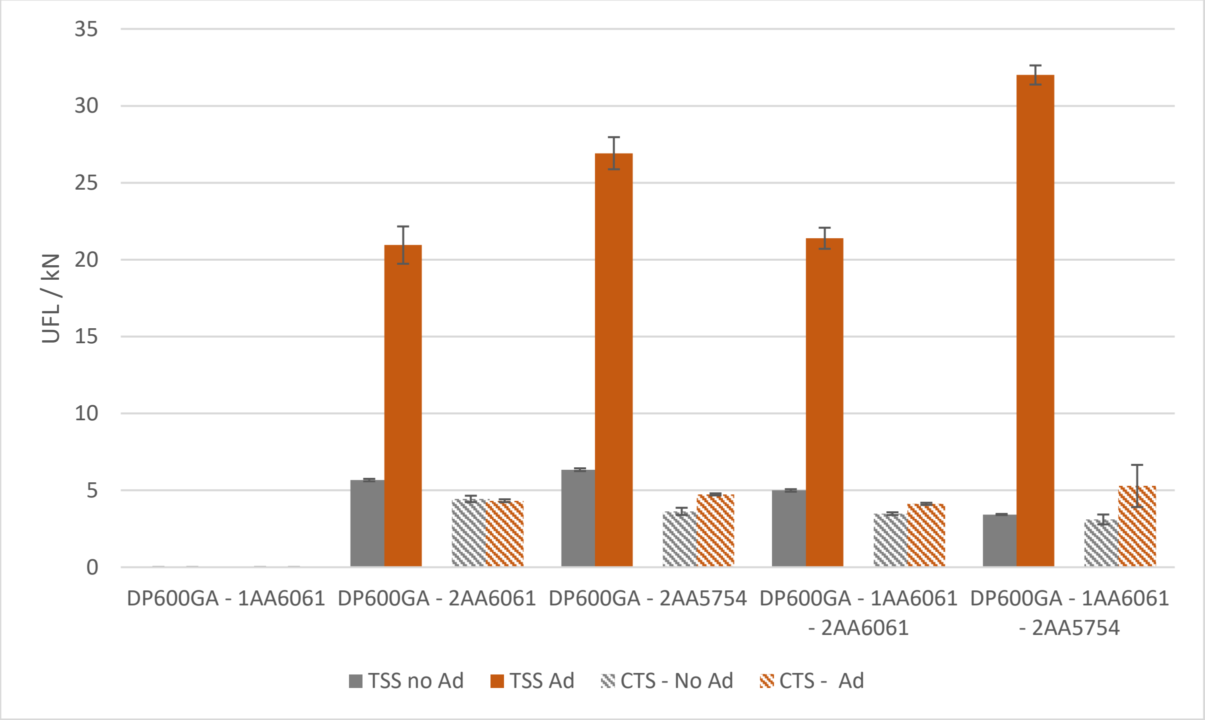

Figure 80 – Tensile and Cross tension results for the Tack high speed joining in different material combinations with (orange) and without (grey) structural adhesive

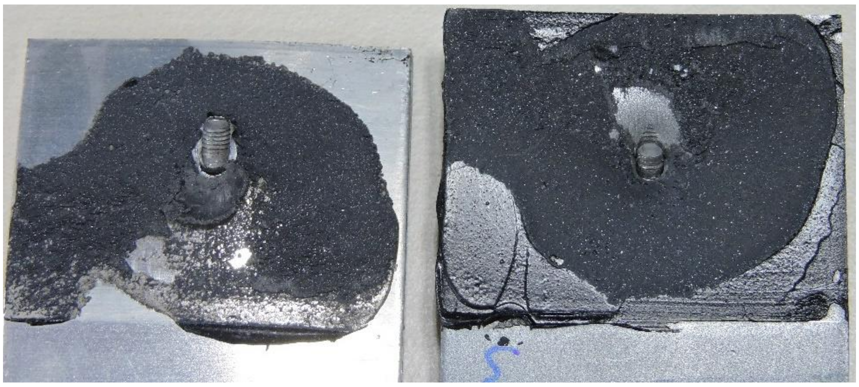

Figure 81 – Evidence of non-bonded are in a DP600GA-2AA6061 tensile shear joint with Cohesive failure followed by joining element failure

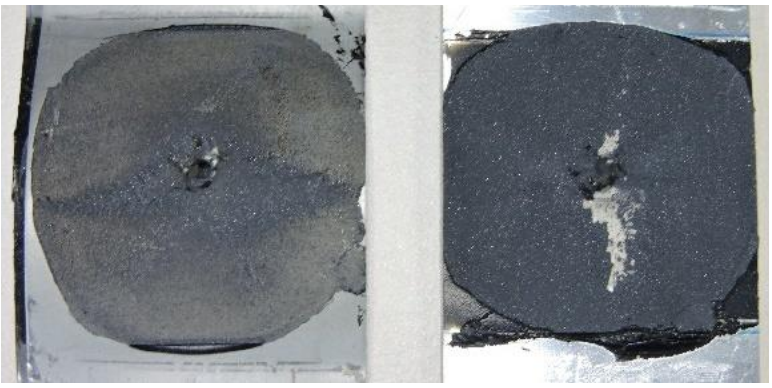

Figure 82 – Evidence of non-bonded are in a DP600GA-2AA6061 cross tension joint with Cohesive failure and no damage to the element

In sum, this one-sided technology requires a bottom material that can take the high loads associated with the forming process, making it ideal for high performance materials as boron steels. However, the major downside of this technology is the need for ballistic safeguards as the high forces during the application, because if the nail slips it can be fired as a bullet. Moreover, this technology can only be applied to components that are typically used in pre-defined confined spaces because of the exposed part of the element can create a piercing point. Additionally, if an adhesive is being used the material flow and bending of the top material can provide inconsistencies in joint performance because of non-uniform bonding.

3.5.2.9. Comparison of joining technologies

A comprehensive range of joining technologies was presented and characterized with an aim to compare technologies for application purposes. Due to limited access to facilities, as they were located at various manufacturing sites in different countries, some of technologies presented here could only be used to produce joints with DP600GA steel with various combinations of aluminium sheets. For some technologies, joints with greater range of steels were also produced. In all joining technologies, a test matrix comprised of joints made of DP600GA to the different aluminium alloys of 1mmAA6061, 2mm AA6061, 2mm AA5754 and the 3 sheet. This enables to compare different techniques under same materials combinations. All tensile shear and cross tension performance of the different joining technologies is summarised in Figure 83 and Figure 84 respectively. For tensile shear it is possible to observe that clinching exhibits the worst performing joints however this is the only technology that does not use an external element. Among remaining technologies in which an external element penetrate both sides of the joints (e.g. Blind rivets, flow drill screws and tack high speed joining) the joints have exhibited similar performance. The highest performance is observed in the case of blind rivets joint having 3-sheet combinations. This is caused by the nature of the joining technology, in which a blind rivet is set in a pre-formed hole, the rivet keeps all three sheets together with a high clamping force. Both flow drill screws and tack high speed joining techniques have similar elements but require opposing material orientation as flow drill screws require the aluminium at the bottom whilst tack high speed joining requires the steel at the bottom. Nevertheless the shear forces experienced at the joint are similar in nature and therefore the joints performances are similar in behaviour. Solid punch riveting does not have a protruding element therefore leading to lower shear performance because there is less dissipation of forces thought the element, moreover the shorter element size allows the release of the interlock at lower loads. Ultimately the partially penetrated joints, in clinch rivet and self-piercing rivet process, provide similar interlock because the joints have similar application methods with a crucial element difference. In the clinch-rivet, non-hollow element only forms into place having an improved interlock compared to clinching, whilst the semi-hollow self-piercing rivet allows the rivet to flare thus improving the interlock with an expanded steel element that created the strongest shear joints. Therefore a characteristic of high strength joints in this mode of loading is associated with the mechanism of force dissipation by specimen tilting combined with the parent material properties for resistance to joint tilting.

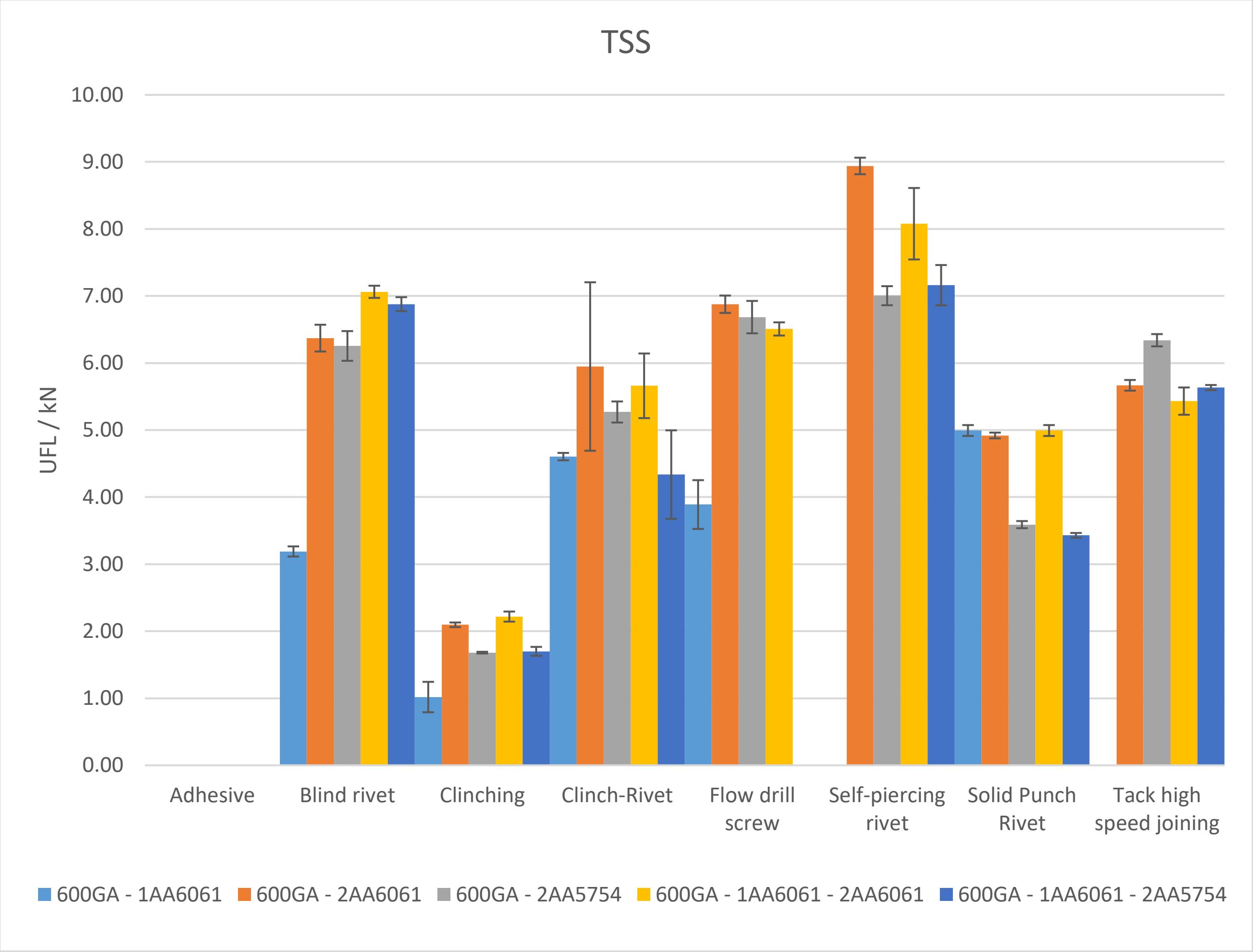

Figure 83 – Summary of all tensile results for all the different technologies without adhesive.

These conclusions from tensile shear studies do not translate into the cross-tension loading due to the change in the nature of the loading on joints as it can be perceived in Figure 84. This difference is not only associated with the lower performance values but also with a change of behaviour of the joining technologies. The poorest performance continues to be clinching, however the difference in performance to the other joining technologies has been reduced. The improved interlock obtained by the clinch-rivet is not able to offer a statistically different results compared to clinching, demonstrating how critical the mode of loading is governing the joint performance. Nevertheless, these joints are exhibiting stable values between the 2-sheet and the 3-sheet material combinations. This behaviour is analogous to Self Piercing Rivet (SPR) technology in which the joint is formed by piercing the top material. For 3-sheet material joint, the SPR rivet only pierces the top sheet whist the other 2 remain intact. This leads to a joint performance and cross section appearance very similar to clinching and clinch-rivet. The 2-sheet SPR joint has an improved performance compared to 3-sheet joint. The remaining technologies in which elements penetrate both sides of the joints such as blind rivets, flow drill screws and tack high speed joining exhibit highest performing joints under tension loading, with having similar values between them with some minor difference. Tack high speed joining exhibits higher values for the dual sheet combination containing the 2mm AA6061 due to combination of steel sheet being at the bottom and different locking mechanism as previously described. This superior performance is present neither in the blind rivets nor in the flow drill screws which have the aluminium at the bottom which has lower yield point compared to steel thus leading to lower performance of lock.

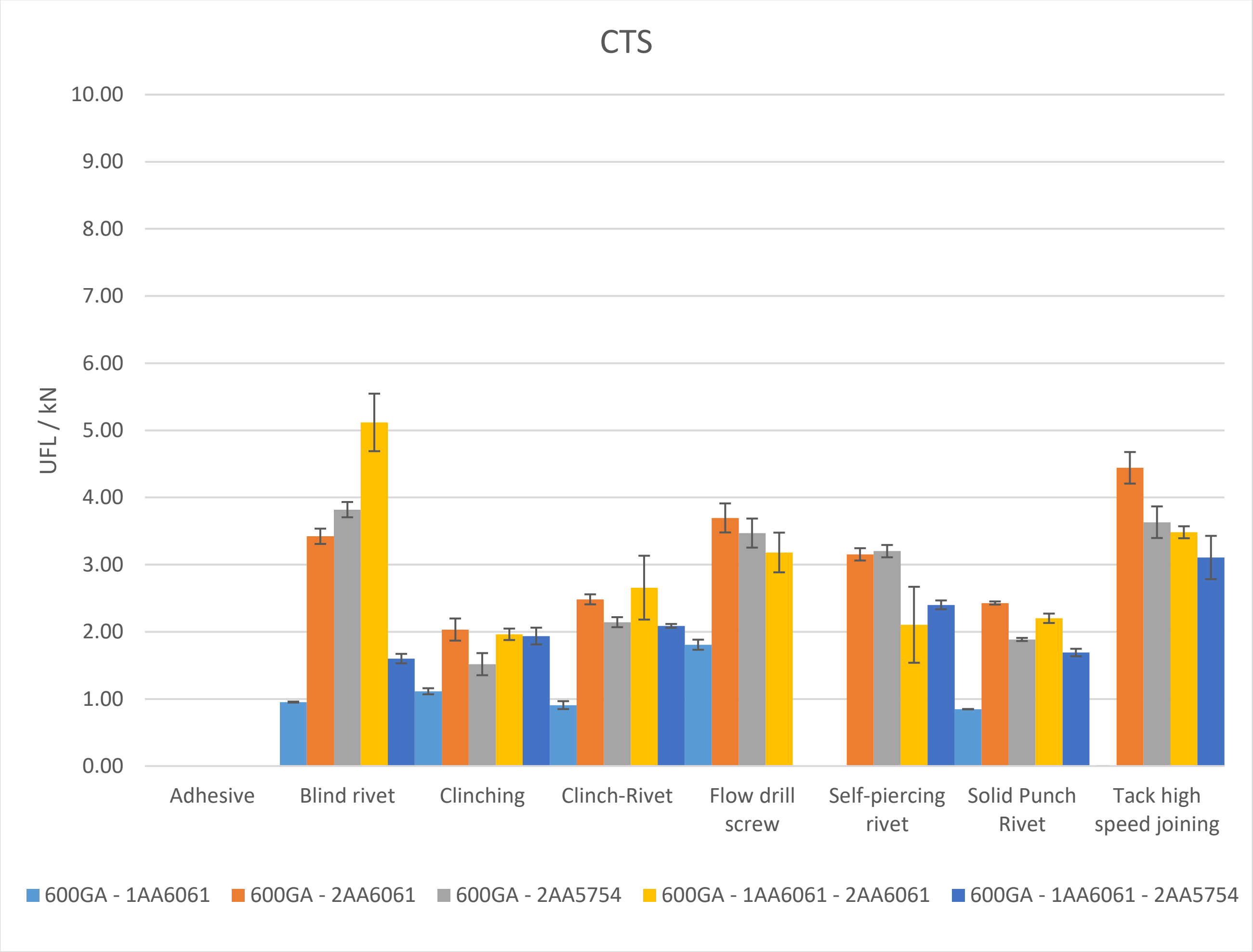

Figure 84 – Summary of all tension results for all the different technologies without adhesive.

Focusing this comparison on mechanical performance alone would generate both incomplete and restrictive analysis due to the differences in the locking mechanisms, material orientation and access. Additionally, the lightweighting implication requires another level of analysis by taking into account the element weight. Table 11 summarizes the technology characteristics for requirements, added weight and cost. From a manufacturing and design perspective, selection of a suitable joining process depends on several factors such as (i) required minimum joint strength (ii) satisfying the requirement of material orientations (iii) requirement of equipment access to a single or both sides of the joint, (iv) manufacturing speed/cost (v) restriction on element size and its protrusion and (vi) weight saving that a technology can offer whilst meeting the strength specification requirements.

Table 11 – Joining technology characteristics

	Orientation	Access	Process speed / s	Element cost per joint	Element weight /g	Additional requirements / comments
Blind rivet	Independent	Single	2	£ 0.087	5.00	Pre-formed hole in all materials being joined.
Clinching	Thin into thick	Double	1	£ 0	0.00	Requires that the thickest material being on top
Clinch-riveting	Aluminium at the bottom	Double	1	£ 0.003	0.54	Requires that the bottom material with high formability
Flow drill screw	Aluminium at the bottom	Double / Single	6	£ 0.030	4.40	May require pre-formed hole on the top material
Self-piercing rivet	Independent	Double	2	£ 0.010	0.80	None
Solid punch riveting	Aluminium at the bottom	Double	2	£ 0.050	0.26	The thickest and most formable at the bottom
Tack high speed joining	Steel at the bottom	Double / Single	1	£ 0.080	1.17	Cannot joint thin materials

DP600GA-2AA6061 joint has been selected to aid the process analysis and interpretation data is normalized in percentage of maximum values for the characteristics analysed and presented in a spider diagram (Figure 85). The spider diagrams were obtained by normalizing the performance of the given field with the maximum value obtained for that field, e.g.: the normalized value for tensile strength of blind rivet was obtained by dividing the tensile performance obtained from blind rivet by the maximum value obtained for tensile performance. In the case of speed and economy fields the scales are reversed to correspond to the correct analysis of the field. In the case of added weight, the higher percentages indicate the larger the added weight. It allows a comprehensive analysis for the different technologies from a holistic methodology. The principal evidence is that there is a trade-off between added weight, element cost and mechanical properties as the most economical and lightweight joint but compromise the joint mechanical performance, as in the case of clinching. This analysis brings evidence that the most economical and lightweight technology with acceptable mechanical performance is the clinch-rivet. However, clinch rivet is pretty much extinct in BIW applications, being only applied in white goods productions, due to the limited applicability in a very narrow range of formable material combinations. Contrastingly the joining technology with highest performance for this material combination with the best set of economical and lightweighting competence is SPR.

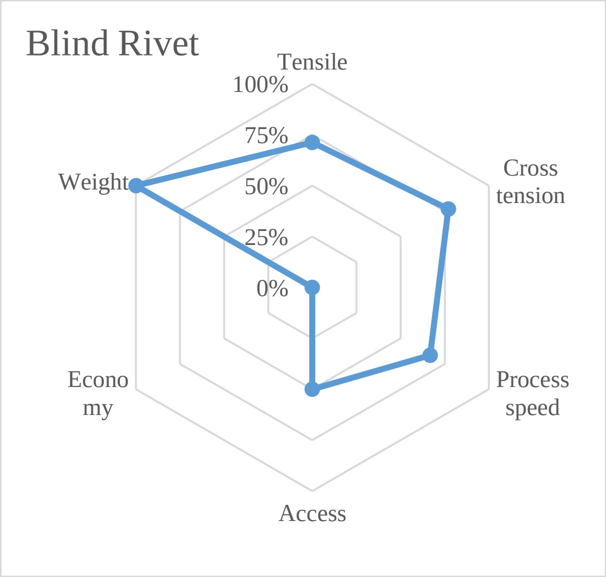
Blind Rivet
Tensile
100%
75%
50%
25%
0%
Cross tension
Process speed
Access
Econo my
Weight

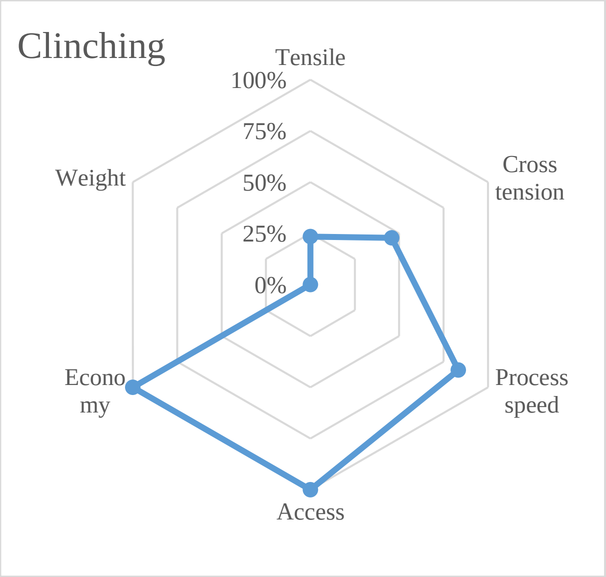
Clinching
Tensile
100%
75%
50%
25%
0%
Cross tension
Process speed
Access
Econo my
Weight

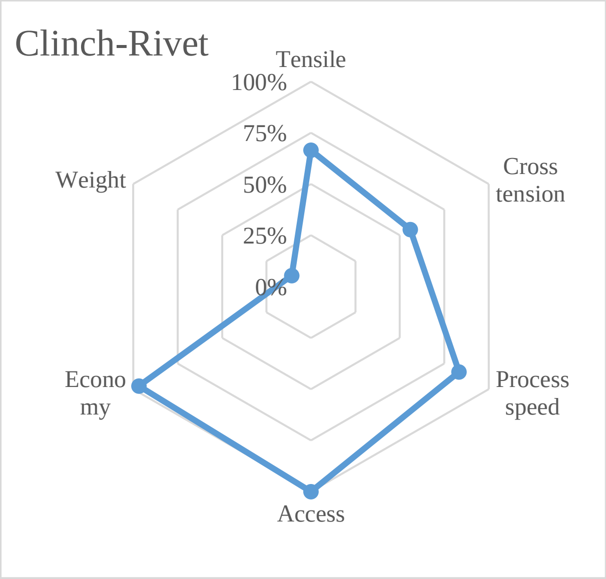
Clinch-Rivet
Tensile
100%
75%
50%
25%
0%
Cross tension
Process speed
Access
Econo my
Weight

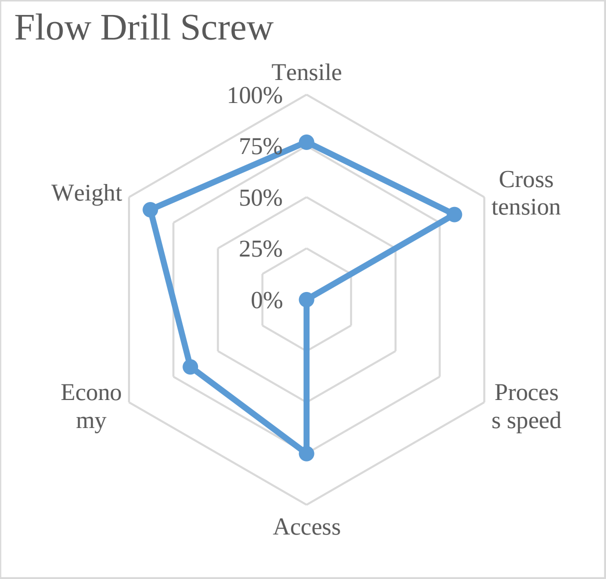
Flow Drill Screw
Tensile
100%
75%
50%
25%
0%
Cross tension
Proces s speed
Access
Econo my
Weight

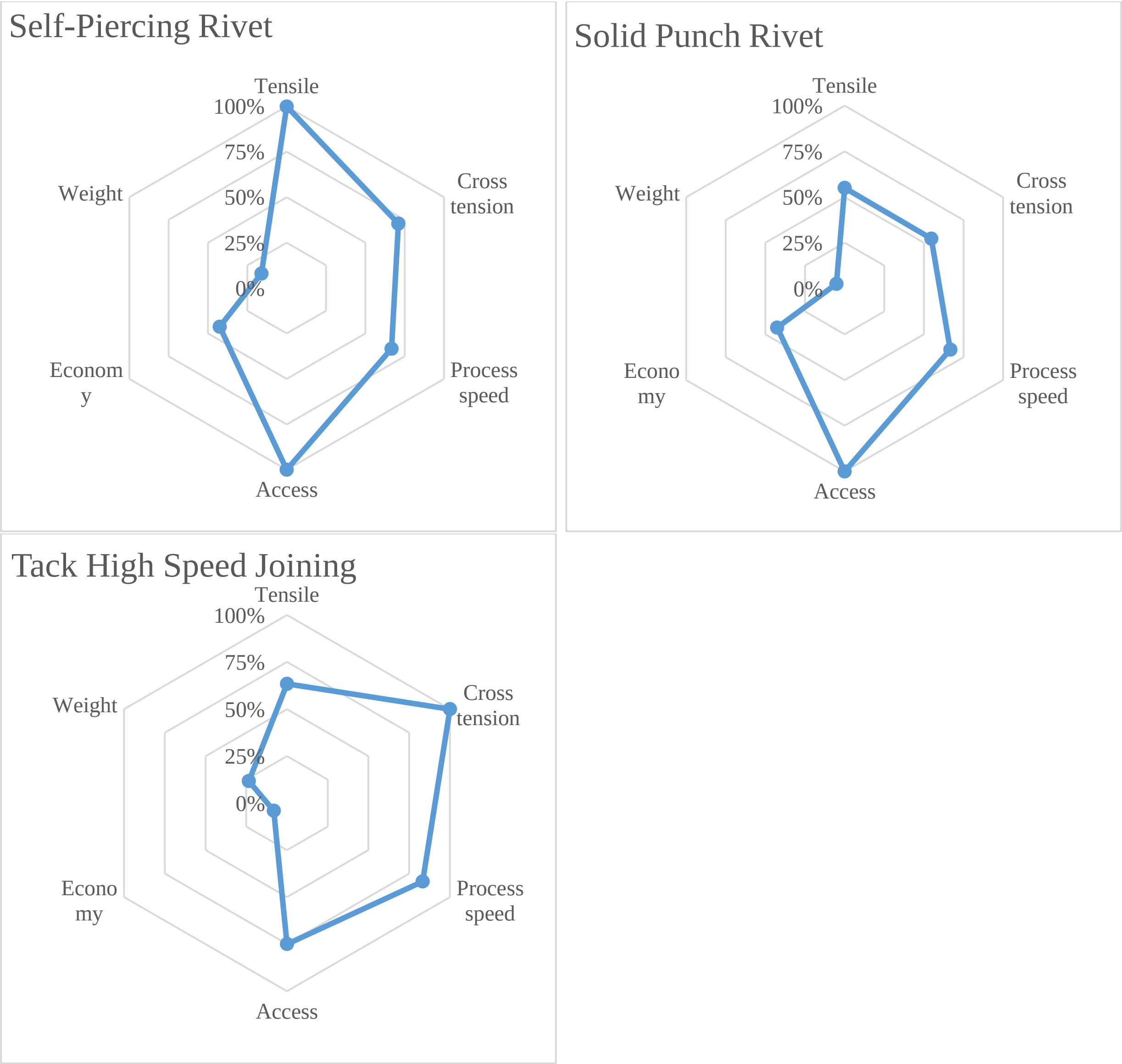

Figure 85 – Joining technologies normalized characteristics for a DP600GA-2AA6061 joint

However, this conclusion is material specific as it can be seen that in the 3-material joint of DP600GA-1AA6061-2AA6061 presented in Figure 86. In 3-sheet material combination, the best performing joint becomes the blind rivets and the most economical and lightweight technology with acceptable mechanical performance continues to be the clinch-rivet.

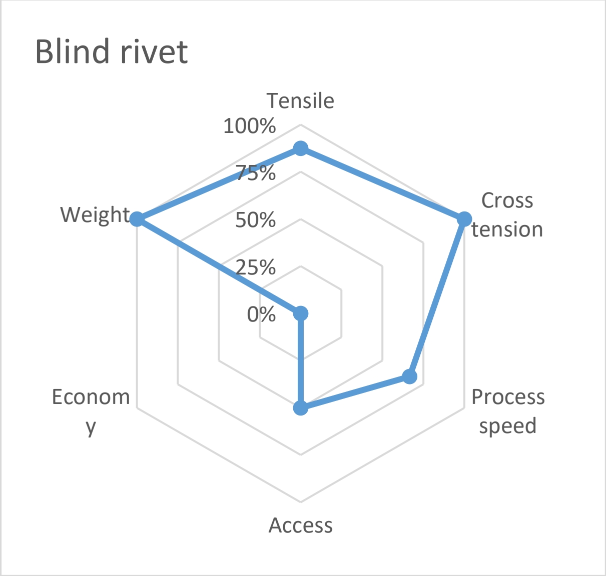
Blind rivet

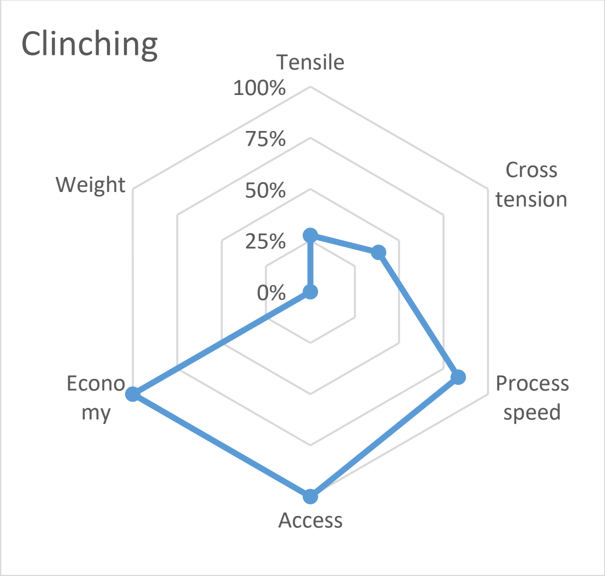
Clinching

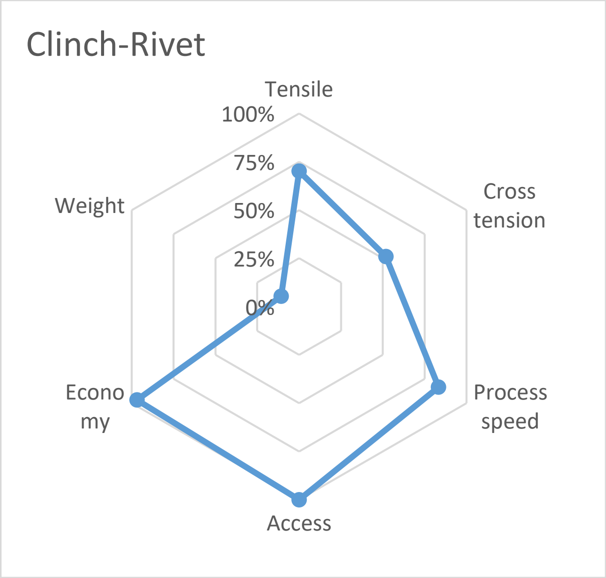
Clinch-Rivet

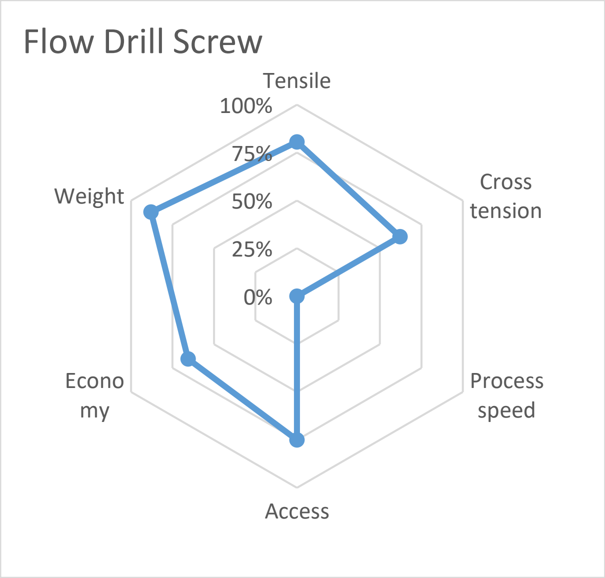
Flow Drill Screw

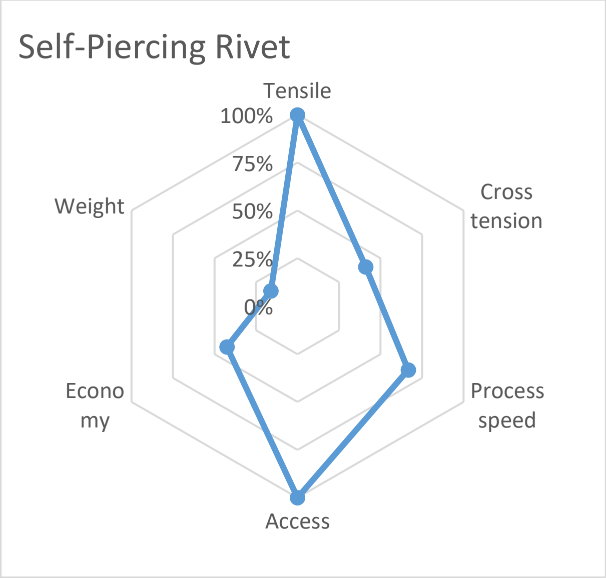
Self-Piercing Rivet

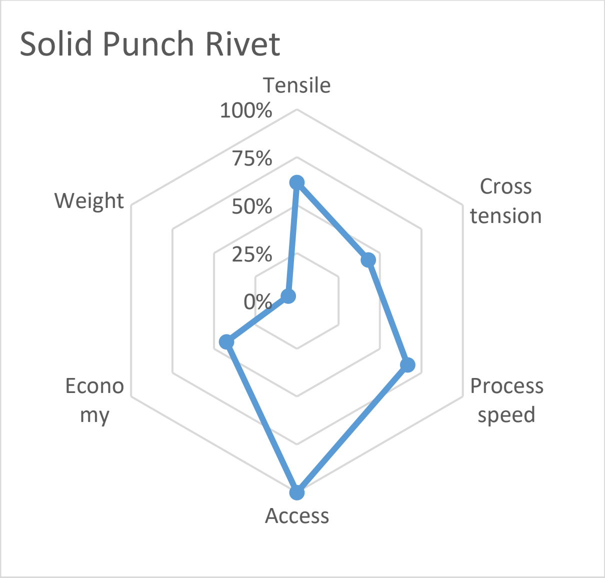
Solid Punch Rivet

Figure 86 – Joining technologies normalized characteristics for a 3 sheet DP600GA- 1AA6061 – 2AA6061 joint

In sum, performing these multivariable analysis shows that it is possible to understand the joining capabilities and relative performance of the various available joining processes across the range of industrially interesting material combinations. This work rightly addresses the Martinsen *et al* [119] comments about lack of comprehensive knowledge due to insufficient collaboration activity between the manufacturing research and joining research. This work bridges the identified gap between manufacturing requirement and joining technology limitations and identifies the boundaries of various joining technologies. Additionally, this study shows that the most restrictive structural assessment is congruent with the tension loading, which is relevant to the mode of failure. Additionally, non-pure loading mode associated with the tensile shear mode, due to the natural transition created by material deformation and joint tilting, creates intrinsic challenges to the comparison. Nevertheless, this behaviour is representative of an in service application of the different joints and only becomes limiting for application in simulation packages. As previously stated by Meschut *et al* [92] technology selection cannot be limited to one technology as the decision needs to be driven by the correlation of service requirements, accessibility and cost.

This work provides additional novel knowledge that enables not only the correct deployment of lightweighting applications, but improvement of manufacturing lines by reducing costs through selection of appropriate technology.

3.5.2.10. Comparison of joining technologies with adhesive (Hybrid joints)

As previously discussed in the section 5.3.8, joint performance greatly improves due to the delocalization of loading over a bigger surface area, effectively reducing local stresses and therefore this implication was also investigated in the present study. Therefore, the same comprehensive range of joining technologies with adhesive was investigated and characterized.

The same matrix comprised of joints made of DP600GA to the different aluminium alloy sheets of 1mmAA6061, 2mm AA6061, 2mm AA5754 and the 3-sheet material combinations 1mmAA6061 – 2mm AA6061 and 1mmAA6061 – 2mm AA5754. All tensile shear and cross tension performance of the different joining technologies is summarised in Figure 87 and Figure 88 respectively where solid fill data point corresponds to the stand-alone joining technology and the striped fill corresponds to the hybrid (joining technology with adhesive). The primary obvious result obtained in tensile shear for joints made of hybrid technologies with an adhesive is superior to those of standalone technologies. Maximum obtained values were for the standalone adhesive joints, as the joint area is larger because (i) there is no joining element to accommodate, (ii) possibly non-uniform adhesive area due to deformation of sheets during setting of element in each joining technology and (iii) non-uniform stress distribution around the element. Secondly it is observed that it was impossible to perform hybrid joining in clinching and clinch-riveting processes as previously discussed the entrapped fluid adhesive experience compression in a confined area which exerts pressure outwards that exceeds the material strength thus forming a crack at the weakest point, which for this joints is consistent of the deformed sheet on joint neck leading it to shear. And finally, all the successful hybrid joints exhibit an improved mechanical performance compared to the stand-alone technology. Additionally, it is possible to observe that all hybrid joints containing the DP600GA-1AA6061 fail at the same value of around 13.5kN, with a consistent mode of failure for all joints which is the shearing of the aluminium sheet which is the weakest part of the joint. The hybrid joints containing the AA5754 have some of the lowest ultimate failure loads due to the presence of oxide layer on AA5754 undermining the adhesion to the substrate as well as local deformation of the joint as previously discussed. The exceptions to these findings correspond to the joint of the hybrid – tack high speed joining and the 3-sheet material combination joint using hybrid-SPR, because the joining technology forces an intimate contact between the sheets allowing the adhesive properly set on the surface as in the case of the purely adhesive joints.

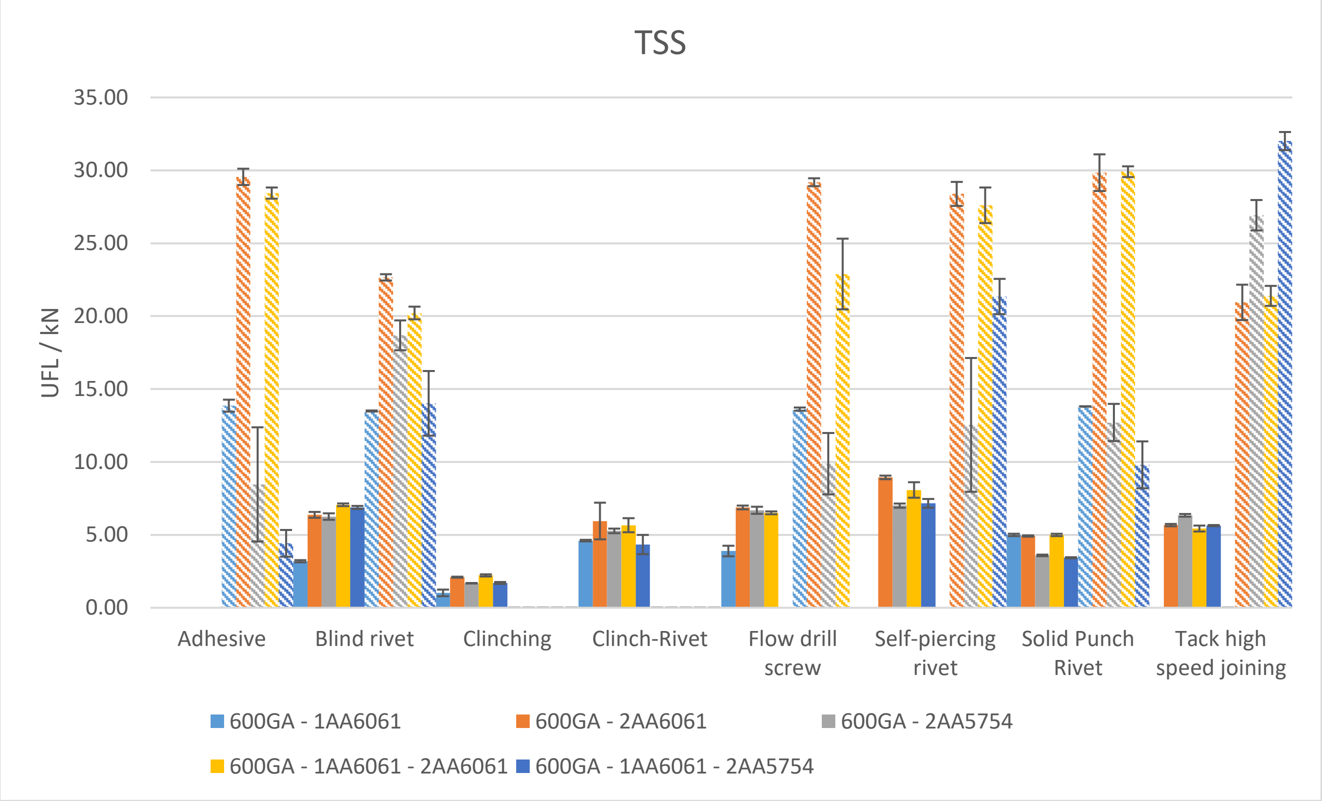

Figure 87 – Summary of all tensile results for all the different technologies without (bulk) and with adhesive (stripes).

Just like in the stand-alone technologies the conclusions obtained in tensile shear do not translate into the cross tension loading due to the change in the nature of the joint loading as it can be perceived in Figure 88. Cross tension loading forces the joints in the weakest mode of the joint, where the joints are dependent from the vertical interlock of joints and there is no dissipation of forces by joint tilting. Results show that the technology that offers the marginal improvement with adhesive is the flow drill screw. This is due to highest amount of perturbation to the joint during FDS process undermining the adhesive advantage that normally provides to the joint, requiring areas with increased overlay in order to minimize adhesive damage by providing increased adhesive coverage beyond the damaged area. This requires therefore both additional material and adhesive, which increases the weight of the joint. All other remaining technologies improved the joint performance significantly compared to the stand-alone technologies, where the biggest notable differences correspond to the SPR and solid punch technologies. However, just like in the tensile loading the effect of the oxide layer on the AA5754 is also evident in this loading mode.

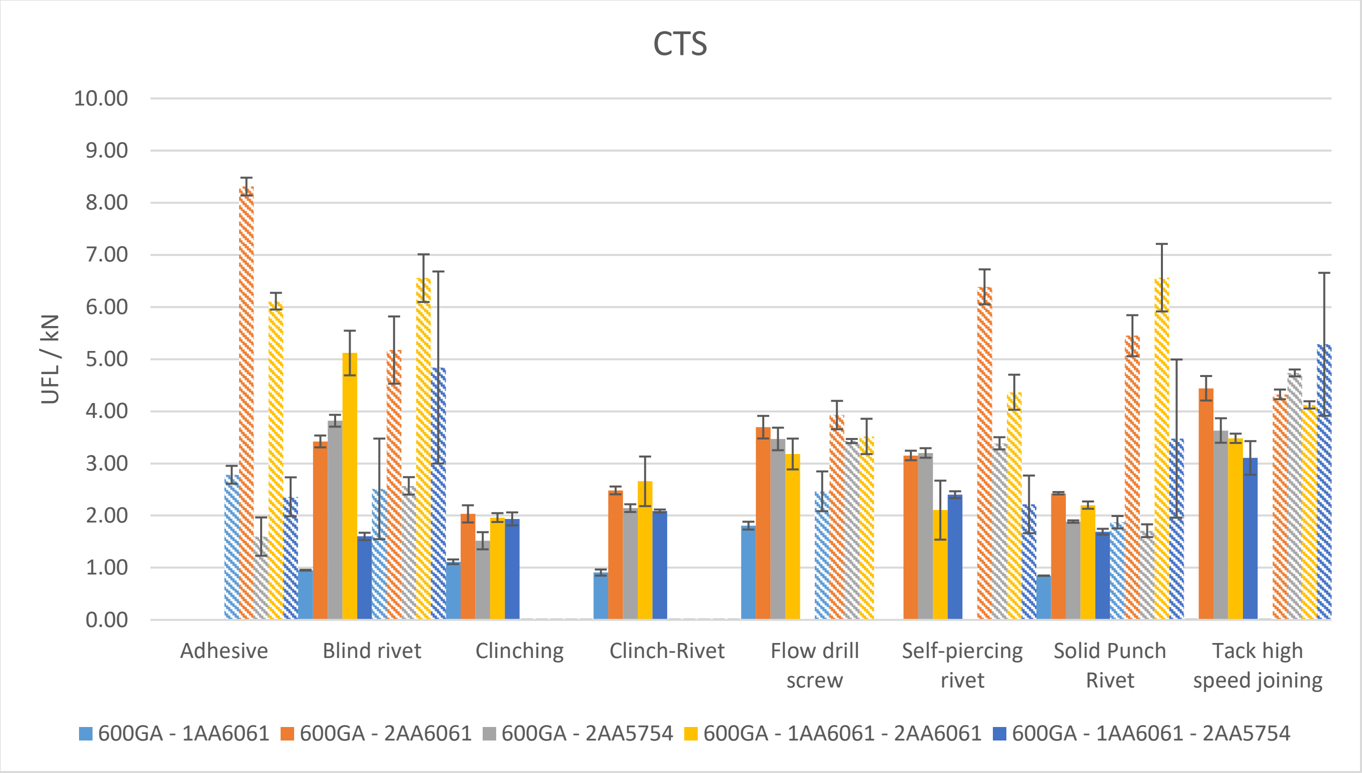

Figure 88 – Summary of all tension results for all the different technologies without adhesive.

Again only giving focus on mechanical performance alone would generate both incomplete and restrictive analysis due to the differences in the locking mechanisms, material orientation and access. Therefore additional data that could be useful in selection of appropriate joining processes has been summarized in Table 12. From a manufacturing and design perspective selection of a suitable joining process depends on several factors discussed in previous section.

Table 12 – Hybrid joining technology characteristics

	Orientation	**Access**	**Process speed / joint (s)**	**Element cost / joint**	**Element weight / joint (g)**	**Additional requirements / comments**
Adhesive	Independent	Single	n/A	£0.16	1.82	Performance only achieved after curing and does not hold sheets together uncured
Blind rivet	Independent	Single	2	£0.247	6.82	Pre-formed hole in all materials being joined.
Clinching	Thin into thick	Double	1	£0.16	1.82	Requires that the thickest material being on top
Clinch-riveting	Aluminium at the bottom	Double	1	£0.162	2.36	Requires that the bottom material with high formability
Flow drill screw	Aluminium at the bottom	Double / Single	6	£0.19	6.22	May require pre-formed hole on the top material
Self-piercing rivet	Independent	Double	2	£0.21	2.62	None
Solid punch riveting	Aluminium at the bottom	Double	2	£0.21	2.08	The thickest and most formable at the bottom
Tack high speed joining	Steel at the bottom	Double / Single	1	£0.24	2.99	Cannot join thin materials

Again for the simplification of the comparison, DP600GA-2AA6061 has been selected to aid the process analysis, for ease of interpretation, the data has been normalized with maximum values for the characteristics analysed and presented in a spider diagram in Figure 89 for the stand-alone (blue) and hybrid technologies (orange). As previously discussed, the biggest difference is the significant improvement on the joint performance obtained for all hybrid technologies. The optimum performing joint that offers the most economical and lightweight technology is the adhesive bonding alone, however a major drawback in adhesively bonded joints is that high performance joints can only be obtained after the adhesive cures. Therefore, this conclusion gets nullified as in a high-volume automotive application it would be impossible to have this adhesive joint because the adhesive needs additional support prior to curing. In addition, standalone adhesive joining method is undesirable for structural components due to stringent requirement of avoiding catastrophic failures, as adhesive have poor performance when loaded in peel/cleavage mode, so for any crash critical area a mechanical fastener joint is required to provide a crack arrest point. Consequently, purely adhesive joints are for indicative purposes only. In the case of hybrid joining processes external elements provides firm support to the sheet and keeps them together during curing process. Solid punch riveting emerges as the ideal candidate for this material combination, as the stand-alone technology offers sufficient joining strength to hold the components together prior to adhesive curing, and after curing the adhesive becomes the main load carrier.

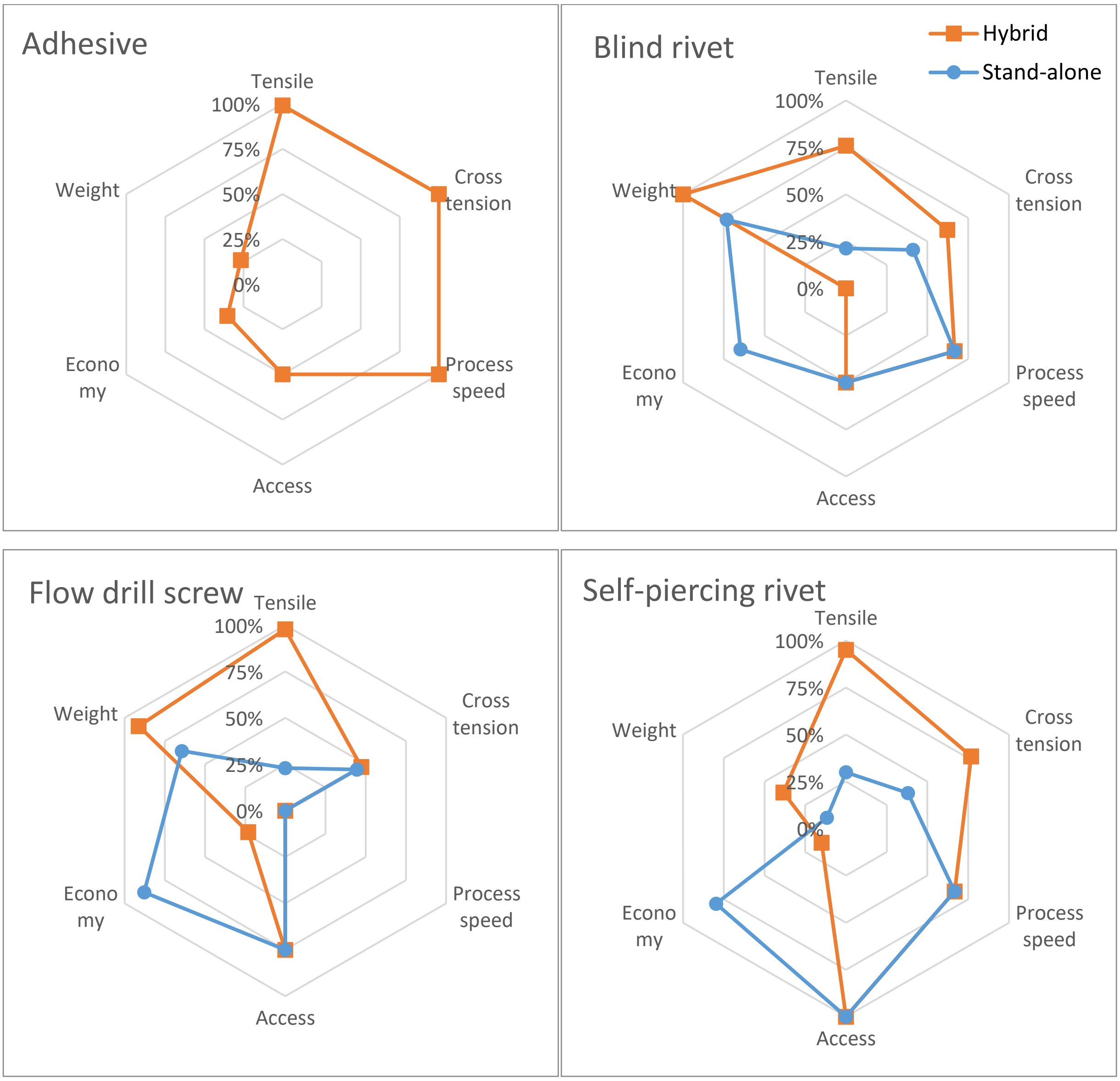

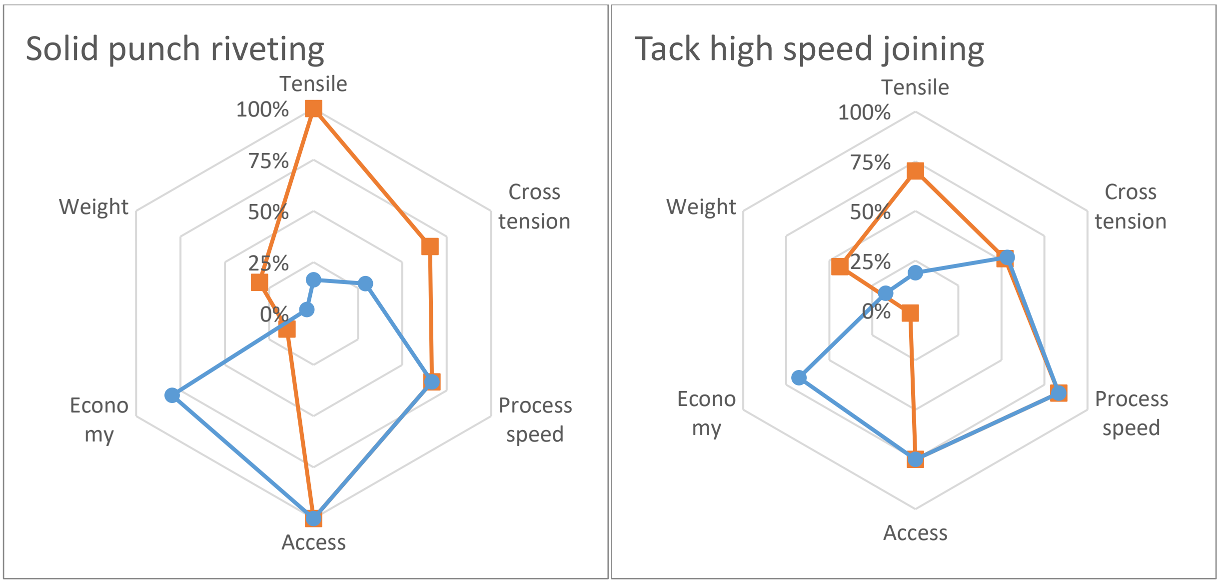

Figure 89 – Joining technologies normalized characteristics for a DP600GA-2AA6061 joint without (blue) and with adhesive (orange)

However, the conclusions are material specific. The key conclusions obtained for the 2 – sheet material combination are transferrable to the 3-material joint DP600GA-1AA6061-2AA6061 configuration as presented in Figure 86. Therefore, the best performing joint continues to be the solid punch riveting.

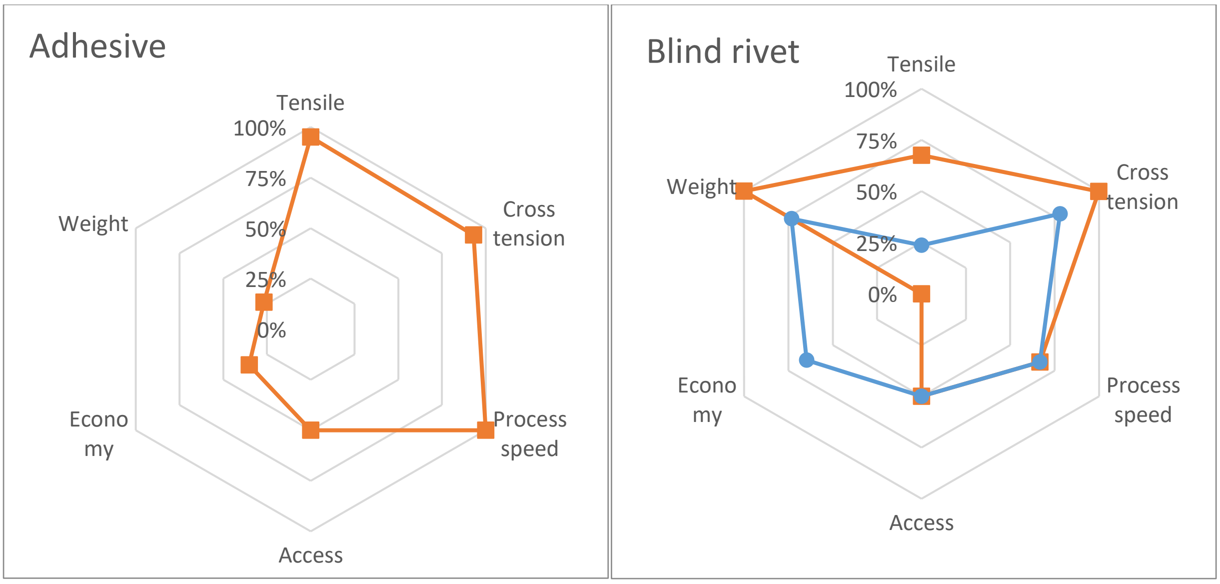

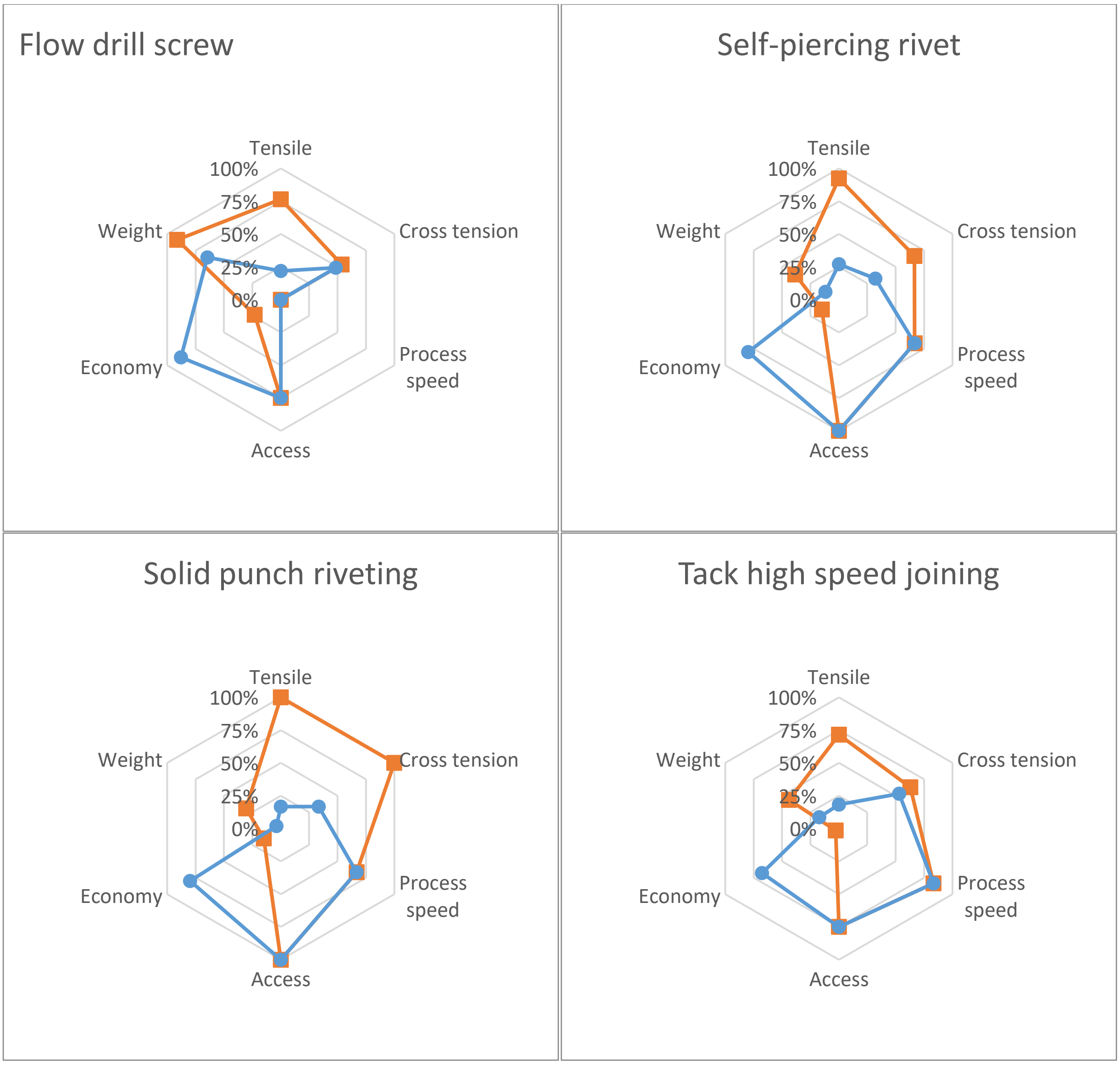

Figure 90 – Joining technologies normalized characteristics for a 3-material joint DP600GA-1AA6061-2AA6061joint without (blue) and with adhesive (orange)

In sum, performing this multivariable analysis not only remains valid but provides an additional layer of information to the understanding of hybridisation of joining capabilities. Additionally, relative performance of the various available joining processes across the range of industrially interesting material combinations could form fundamental basis for selection of joining technology for dissimilar materials.

3.6. **Conclusions**

This work successfully identifies the limitations for the individual joining technologies for different material combinations, establishing the necessary guidelines for technology selection culminating in a detailed manual for guidance in technology selection.

The principal conclusion is that there is currently no single joining process solution that is able to provide all the requirements to cover all joints in a car body. As highlighted there is a significant trade-off between joint properties, lightweighting, application and cost that need to be considered to secure a decision. Nevertheless, if an application needs to be most lightweight and economical possible then clinching is the solution as there is no added weight or cost on the element at an expense of low joint performance. If there is a specific requirement for single sided access for the technology then blind rivet is the only possible solution, however this will be at the expense of the added weight from the element and the material need to have a pre-formed hole that needs to be correctly matched in both components in order to form the joint. If the requirement is performance alone, then piercing technologies provides better solution. Among these piercing technologies self-piercing rivet offers best strength performance, however, there is a trade- off with added weight, requirement dual sided access for joining sheets and specific requirement of sheets properties.

In the case of hybrid joining the most lightweight technology is the adhesive alone with the huge concern that of the adhesive properties are only valid after curing, creating an impracticality on the high-volume manufacturing scenario (as the structure would simply fall apart without mechanical joints hold parts in place until the adhesive cures). One promising technology derived from this multivariable approach is the solid punch riveting, but this technique is widely overlooked in BIW applications. Nevertheless, the dual sided access of this technology and the material extraction by punching create a problem due to the adhesive application as the extruded material can block the extraction system creating manufacturing complications. In addition to that there is belief in the auto sector that creating a hole through the full sheet stack thickness will undermine the corrosion performance as well as the fatigue performance. However fatigue performance was not considered for the present study.

Another existing available technology, but not unexplored technology is Resistance Spot Welding, which offers the advantage of non-added weight as it is an autogenous low-cost welding technology in addition to being a technology that is already being applied in high volume manufacturing of steel-steel or Al-Al similar materials joining. Since this is a fusion process, it is unavoidable to form different intermetallics that will provide an increased challenge in obtaining structural high-quality welds. If the nature of interface is controlled, it could be possible to produce higher performance joints and is the subject of next chapter.

4. Development of Resistance Spot Welding

Resistance spot welding is the main technique used in car body manufacturing due to the low cost, high speed, reliability and ease of process automatization. Combined with the usage of low carbon steel, resistance spot welding enabled the mass production of cars in the early 20th Century. Consequently, automotive production facilities are already adapted for this technology evidencing the need and desire to reduce cost and reuse production lines for new and exotic material combinations within the same facilities as discussed in the introduction of this thesis. This potentially enables automotive industry to adapt this technology in existing manufacturing lines as it is cost effective and provides opportunity to achieve further lightweighting by implementing dissimilar joints.

This technology uses the natural electrical resistance of materials and the principles of joule heating to melt the material. As it can be seen in Figure 91 this is achieved by using copper alloy electrodes to clamp components prior to the passage of a high current. This current leads to intense localized heat that melts the material in a very small and confined area. The melted material cools down and the weld nugget is formed between the materials.

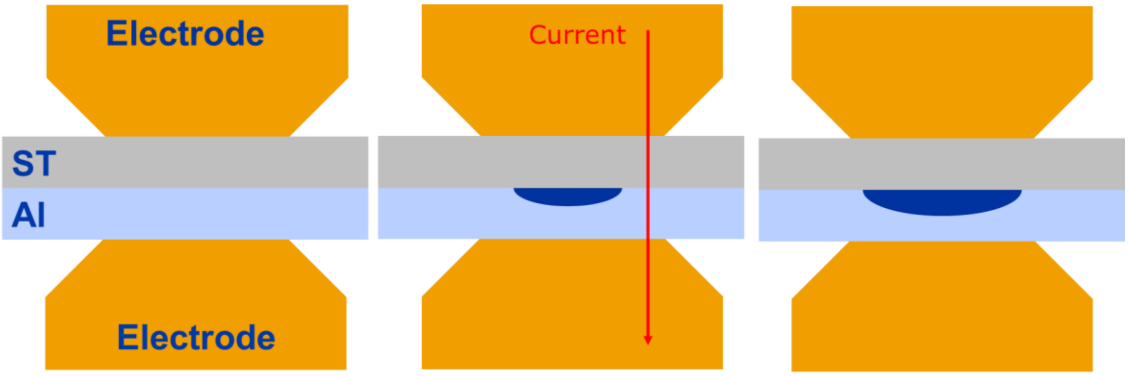

Figure 91 – Schematic representation of resistance welding process in a dissimilar steel to aluminium joint

As previously stated this process follows the principle of Joule heating and can be simply expressed as

$$H = I^2Rt \qquad \text{Eq(8)}$$

Where H is the heat generated, I is the current, R the system resistance and t the cycle time. The system resistance comprises of the sum of the resistances involved in the joint as shown in Figure 92, where R1, R3 and R5 correspond to electrode-steel, steel-Al and Al-electrode interface contact resistances respectively. The different interface resistances and R2 and R4 correspond to the dissimilar material resistances for steel and aluminium respectively. From the equation it is possible to predict that the location of peak heat generation will be associated with the region having highest resistance. Therefore for these dissimilar joints, heating will be associated with the interface between steel and aluminium. As previously described the melting point of aluminium is much lower than steel creating a joint similar to a brazed joint.

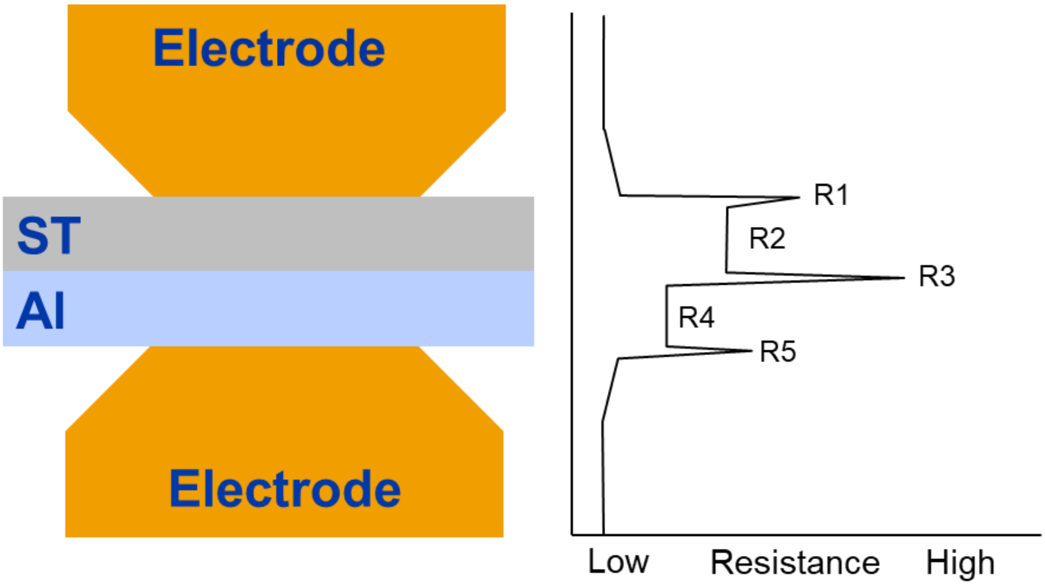

Figure 92 – Schematic representation of resistances in a dissimilar steel to aluminium joint

As previously described in chapter 1.4, adopting this technology to join steel to aluminium presents a complex challenge. The disparity of material properties with different thermal, mechanical and structural properties such as thermal conductivity and specific heat capacity between aluminium and steel results in a joint with residual stresses, weld shrinkage, and distortion, all of which are detrimental to the joint.

Additionally there is the unavoidable formation of intermetallic phases many of which are extremely brittle [9], [24] leading to joints with poor mechanical properties. Nevertheless according to the literature presented previously, in order to form a good weld between aluminium and steel it is critical to understand and control the morphology, volume and location of the Fe-Al intermetallics present [8]. Intermetallic layer thicknesses greater than 10 µm seriously deteriorate the mechanical properties of the joints [10]. The agreed consensus in the literature is that the main phases are Fe_4Al_{13} and Fe_2Al_5 in which the thickness of the intermetallic layer governed by temperature.

Martinsen *et al* [119] expands the previous points by adding that from RSW current knowledge of aluminium to aluminium it is predicted that the oxide layer will impact on the contact resistance, requiring the breaking of the oxide layer to reduce the contact resistance. Miyamoto *et al* [122] proposes to take advantage of Zn-Al eutectic reaction as a solution to remove the oxide film on the Al alloy surface at low temperature in idealized conditions of pre-polished Al and degreased steel. It is possible to remove oxide layer on Al by dissolution and expulsion during the RSW process. Miyamoto have demonstrated higher strength for joint with a IMC thickness < 2 µm and a granular morphology with grains < 500 nm in diameter.

In order to control the intermetallic formation, as shown by Chen *et al* [123], one of the adopted solutions was to adopt an interlayer that could be used as a transition material between steel and aluminium. In section 3 of the first chapter, the impact of using alloying elements for control of the intermetallics phases has been discussed. Si plays an important role in the Fe-Al intermetallic formation system not only due to the formation of the ternary Fe-Si-Al phases but also for the apparent barrier effect slowing the diffusion of species thought it. Zhang et al. [124] proposed the employment of $AlSi_{12}$ interlayer to block the diffusion paths forming predominantly $Fe_2Al_5Si_5$ and $Fe_4Al_{13}Si_{13}$. Addition of Zn to a filler wire, is shown to control the Fe_2Al_5 and $FeAl_3$ phases by forming a $Fe_2Al_{5-x}Zn_x$ and dispersed $FeZn_{10}$ phases[51]. Chen *et al* [123] have suggested the usage of a Zn interlayer of 50 µm to change both growth kinetics and morphology of the intermetallic layer which can improve joint performance. In sum, according to Martinsen *et al* [119] the challenge is to prevent interface failure of the joint, by promoting crack propagation along the aluminium heat affected zone. This promotes therefore the preferential plug failure, where the aluminium cracks along the heat affected region leaving a plug behind. Plug failure consists of parent material failure in one component, leaving the weld intact and attached to another component. It is an established norm in industry that plug failure is seen as an indication that the weld is stronger than the surrounding parent material.

Jianbin Chen *et al* [125] present the microstructure and mechanical properties of RSW 1.5mm AA5052 and uncoated 1.2mm DP 600. The process consists of the dual pulse pre-heating cycle followed by a welding pulse, although no explanation is offered for the benefits of this pre-heating cycle. The only identified intermetallic layers were: Fe_2Al_5 with thickness of 3.3 µm from the steel side, and the needle shaped Fe_4Al_{13} phase with a varied layer between 0.67 to 15.8 µm from the aluminium side. The overall thickness is very high as according to the previous literature the lack of Zn coating[126], the lack of Si in the aluminium alloy combined with the high welding times induce these thicker IMC layers. Despite this the authors managed to obtain a maximum tensile shear load of 5.5 kN for a nugget size of 6.3mm and welding current of 12.5 kA.

Jin Wang *et al* [127] presented one of the first publication on the simulation model of Fe-Al. The model was developed for studying the joints of 2mm AA6022-T4 with 2mm of low carbon steel. The author uses the proposed parabolic growth from Bouche *et al* [37] however disregarded the non-parabolic initial transient period prior to the equilibrium parabolic growth. It is proposed that the dominating phase is Fe_2Al_5 and other IMC thicknesses can be negligible. Therefore, combining the proposed Fe_2Al_5 parabolic growth Eq. 1 with the Arrhenius equation Eq. 2 it is possible to obtain the temperature dependent equation of Fe_2Al_5 thickness prediction Eq. 3

$$Z_{Fe_2Al_5} = \sqrt{2kt} \qquad \text{Eq(9)}$$

$$k = k_0 e^{-\frac{Q}{RT}} \qquad \text{Eq(10)}$$

$$dZ_{Fe_2Al_5} = \sqrt{\left(\frac{k_0 e^{-\frac{Q}{RT}}}{2t}\right)} \mathrm{dt} \qquad \text{Eq(11)}$$

where Z_{Fe2Al5} is the thickness of Fe_2Al_5, t is the reaction time and k the growth coefficient of Fe_2Al_5, k_0 is the pre-exponential factor, Q is the activation energy, R the gas constant and T the absolute temperature. Both the activation energy (Q) and the pre-exponential factor (K_0) are related to the iron diffusion rate in the aluminium. Although claiming that the calculated IMC thickness is in agreement with experimental data, the high difference (1-2µm) in thickness can be accounted for by the fact that the highest welding cycle of 300ms which is governed by the non-equilibrium non-parabolic initial transient as described by Bouche *et al* [37]. Jin Wang *et al* [127] work became the basis of most exploration of resistance spot welding of Fe-Al [128]–[133].

Zixuan Wan *et al* [128] proposed a new model, by calculating electrical contact resistance and thermal constant resistance for the interfaces of 1.2mm AA6022-T4 with 2mm of galvanised mild steel (60G) joints generated by RSW. This model includes the mechanical, electrical and thermal contacts changes during the welding process, especially the faying interface which is strongly affected by the mechanical contact pressure and temperature at the interface in addition to material composition and surface conditions. The model presents accurately the predictions of voltage, nugget growth and joint deformation. This work was used by Zixuan Wan *et al* [129] and characterized the interfaces of 1.2mm AA6022-T4 with 2mm of galvanised mild steel (60G) joints generated by RSW. Like Chen[125] this study used a dual pulse composed of a pre-heat followed by the welding pulse. The study characterized two zones of intermetallic layers at the interface. The first located in central area of the interface composed of tongue-like Fe_2Al_5 adjacent to the steel and serrated-like $FeAl_3$ adjacent to the Al. The second zone is located at the periphery of the joint interface composed of a mixture of $FeAl_3$ and Al which is formed by the solid-state diffusion of Fe into molten Al. The authors considered only the Fe_2Al_5 phase in the growth kinetics, following the work of Wang *et al* [127] which used thermodynamic based model using the dynamic interfacial thermal history and a parabolic growth rate to obtain reasonably accurate predictions.

Chen *et al* [130] discussed the different failure modes, mechanical strength and fracture mechanism in dissimilar resistance spot welding for a of 1.2mm AA6022-T4 with 2mm of galvanised mild steel. In conventional resistance spot welding for similar materials the main factors affecting the weld mechanical properties are porosity, sheet thickness, fusion zone dimensions and differences in hardness in the weld, heat affect zone and base metal. Chen concluded that additional factors in dissimilar RSW are to be considered such as defects on the Fe-Al interface, bulging of Fe into the Al and the thickness and morphology of the intermetallic compounds. The three major fracture mechanisms and failure modes observed are presented in Figure 93, where: brittle or semi-brittle fracture in the intermetallic layer which led to interfacial failure, ductile fracture in the aluminium fusion zone which led to thickness failure, and ductile fracture in the aluminium heat affected zone which led to the industrially preferred button pull-out failure.

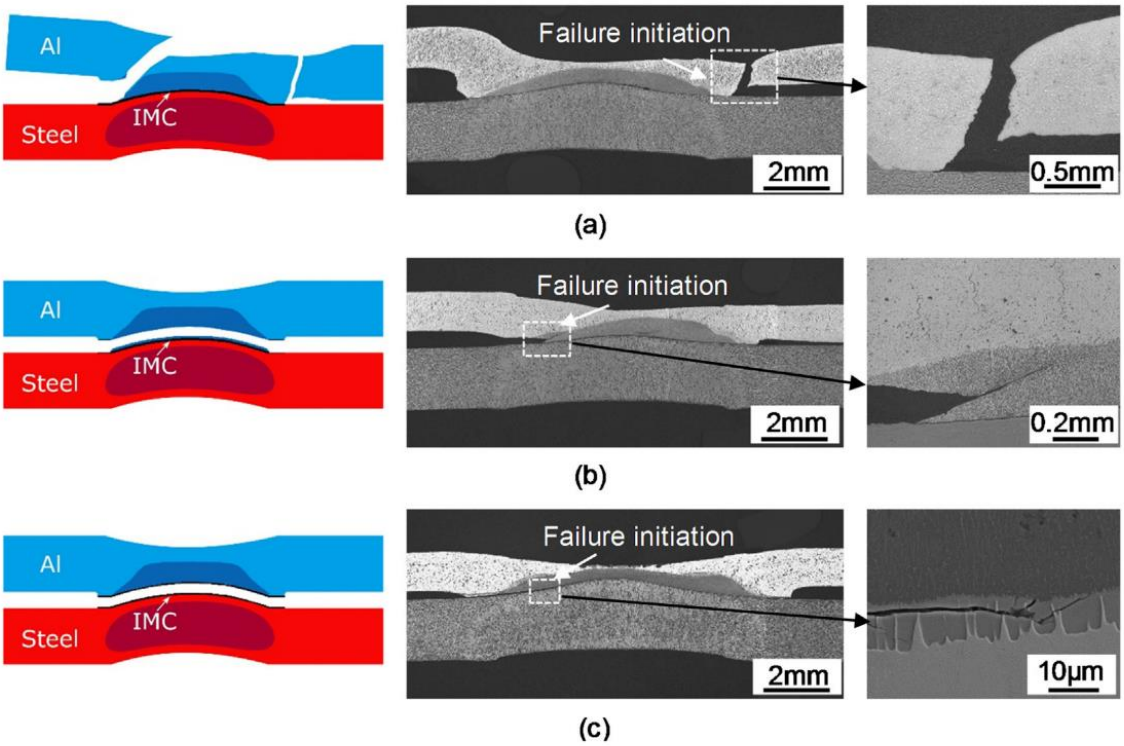

Figure 93 – Representation of three typical lap shear failure modes observed by Chen[130]: (a) button pull-out failure; (b) thickness failure; (c) interfacial failure.

Chen *et al* proved that an intermetallic layer thicker than 3 µm was prone to interfacial failure despite of large aluminium nugget and steel bulging. It was shown that pull-out and thickness failure produced better mechanical performance and therefore increasing the Al nugget or steel bulging height promoted higher tensile failure load. It is emphasised that high welding current in short welding time helped to grow Al nugget while minimizing intermetallic thickness, which improved mechanical performance significantly.

Chen *et al* [131] continued with their study to evaluate the facture mechanism of Fe-Al RSW in coach peel and cross tension loading. One of principal findings is associated with presence of Fe phase dispersions within the Fe_2Al_5 which promotes a quasi-cleavage fracture as opposed to full cleavage fracture. However, as the intermetallic thickness increases the Fe phase dispersions diminish. The main factors affecting cross tension failure mode and performance were dependent upon the intermetallic thickness, dendrites and Al shrinkage, Al nugget size and weld thinning. It was observed that cracks always initiated in the intermetallic layer and promoted three facture modes: interfacial fracture in the intermetallic layer, partial thickness fracture in the Al nugget close to intermetallic layer and partial button pull-out fracture. Contrastingly, the crack initiation on the coach peel test started in the Al fusion zone leading to a partial button pull-out fracture mode with Al deformation, which induces two characteristic peaks in the load-displacement curves. The main factors affecting coach peel fracture mode were dependent on the intermetallic thickness, Al shrinkage, Al nugget size and weld thinning.

Chen accentuated previous conclusions with the study of the relation between mechanical properties and the microstructural evolution of Al/steel interface [132]. This study suggests that Fe_2Al_5 layer nucleated in a random orientation with fine, discontinuous and equiaxed grains which evolved into coarse, continuous and columnar grains with a preferred orientation along [001] direction. These columnar grains are susceptible to cracking and generate cleavage fracture surfaces, leading to the formation of primary cracks propagating along the interface and secondary cracks orientated to the steel. Therefore thicker Fe_2Al_5 reduced the joint strength due to the interfacial fracture. The impact of the importance of the intermetallic thickness was justified by the estimation of fracture toughness via the indent crack extension method. It was shown that fracture toughness decreased with increased IMC thickness, a thickness of 3 µm corresponded to fracture toughness of 1.07 $MPam^{1/2}$ while 4 µm had a dramatic drop to 0.56 $MPam^{1/2}$. As observed in Ref [131] the reduced iron phase dispersions within the increasing Fe_2Al_5 phase increases susceptibility to crack propagation along the interface, undermining the weld strength.

Zhang *et al* [134] explored microstructures and mechanical properties of resistance welds of 1mm H220YD Zn galvanized steel and 1.5mm AA6088-T66. The morphology of the Fe_2Al_5 and

Fe_4Al_{13} was identified as a tongue like and needle like morphology respectively. This study shows that, as expected, with higher heat input, increasing the current and higher welding times is translated into thicker intermetallic layers. It was also shown that the interfacial intermetallic layer has higher nanohardness compared with the aluminium alloy nugget and galvanised steel. The continuation of this work lead to Zhang *et al* [135] where the interfacial characteristics and growth kinetics for resistance welds of 1mm H220YD-Z100 and 1.5mm AA6088-T66 was investigated. As in previous studies, the main IMC phases formed are Fe_2Al_5 and Fe_4Al_{13} which are formed by diffusion between solid steel and molten aluminium with thicknesses of 3.6 and 2 µm respectively. Through the usage of simulation, the authors suggest that the Arrhenius equation (Eq. 2) can be used for the growth coefficient of Fe_2Al_5 with an initial constant k_0 of $132m^2/s$ and activation energy Q_0 of 239 kJ/mol. Whilst the diffusion of Al through the Fe_2Al_5 phase is also governed by the Arrhenius equation with initial diffusion contact D_0 of 2.55 m^2/s and activation energy Q_0 of 259 kJ/mol. No correlation between welding parameters and growth kinetics is offered in this work. Maximum joint performance in this study was of 3.3kN with an interfacial failure in the intermetallic layers where cracks originated and propagated.

In sum, this work intends to progress on the elusive topic of resistance spot welding of steel to aluminium by tailoring the process to improve the weld quality. The main focus will be tailoring the fundamentals of the process by indirect control of the local contact resistance of the interface by controlling the pressure to increase heat generation and localization in the centre of joints and improve weld size and quality.

4.1. Methodology

4.1.1. Materials

The materials used in this work are of specific interest to the automotive industry and the adopted aluminium alloy for these trials was the 2 mm AA 6061 and the adopted steels were the DP600 steels with galvanized (GI) and galvanneal (GA) coatings. The differences in the coatings consist of the process variations. Zinc Hot-Dip Galvanized coatings, commonly known as Z or GI coating, consist of dipping the steel in a hot molten bath of Zn. The high temperature dissolves some iron creating a thin Zn-Fe intermetallic layer sandwiched between Zn and steel. To obtain the Galvanneal (GA) coating, the galvanised (GI) steel is annealed at elevated temperature. This facilitates the migration of some Fe to flow into the zinc coating creating a thick layer of Zn-Fe coating. Therefore, the GA coatings contains layers Zn-Fe intermetallics, making the coating brittle leading to powdering and flaking in pressing operations. However, these layers provide improved corrosion performance in comparison to the GI coatings. The stable intermetallic layer in the GA coating makes this material more suitable for resistance spot welding, due to lower availability of metallic Zn to react with Cu electrode forming Brass. The absence of reaction with Cu electrode justifies the reason for being favoured by several car producers, particularly in Asia.

Table 13 – Material properties (data from material supplier specifications)

Material	**Reference**	**Coating**	**Thickness (mm)**	**Tensile Strength (MPa)**	**Yield Strength (MPa)**	**Total Elongation (%)**
Steel	DP 600	GA	1.2	620	365	27
Steel	DP 600	GI	1.2	635	370	24.5
Al	AA 6061	-	2	322 ± 1	282 ± 1	13 ± 1

GI – Hot dip galvanized

GA – Galvanneal

Table 14 – Material chemical composition (data from material supplier specifications)

Material		**DP600 GA**	**DP600 GI**	**AA 6061**
,Element (%)	Al			95.8 – 98.6
	C	0.09	0.1	
	Cr			0.04 – 0.35
	Cu			0.15 – 0.4
	Fe	bal	bal	< 0.7
	Mg			0.8 – 1.2
	Mn	1.6 – 1.9	1	< 0.15
	Si	0.2-0.3	0.3	0.4 – 0.8
	Ti			< 0.15
	Zn			< 0.25
	Others			< 0.15

4.1.2. **Sample preparation**

4.1.2.1. **Metallographic samples**

There is no norm that currently covers the resistance spot welding of dissimilar materials therefore this work follows the automotive standard ISO 10447 for the development of welded specimens and preliminary evaluation method. The weld size is obtained by performing a chisel or peel test according to ISO 10447. In order to measure the weld size, spot weld joint is separated by applying a peel force around the weld. This leads to either interfacial failure or weld plug failure as the example provided in Figure 94. The formation of weld plug is an indication that the weld region is stronger than the parent Al material. In both cases, the weld size (diameter) is measured using Vernier callipers. The samples used for exploration of process parameters and metallographic analysis consisted of small coupons with the dimension of 30 mm by 30 mm.

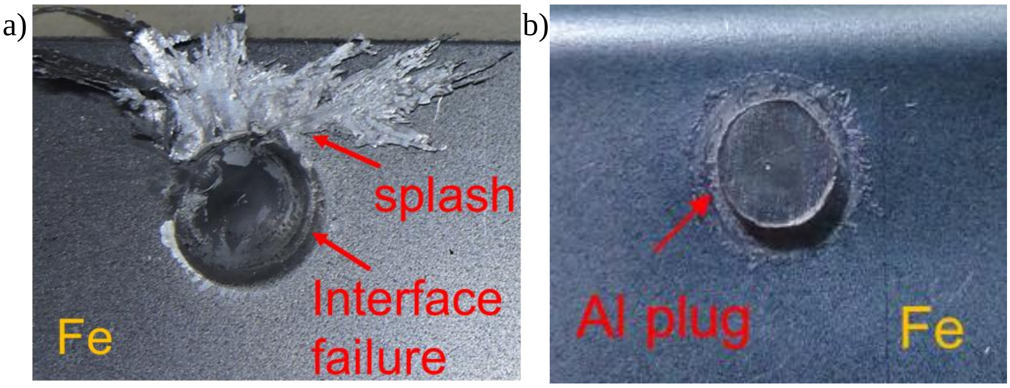

Figure 94 – Examples of interface failure (a) and weld plug failure

Additional measurements of joint assembly thicknesses within and outside the weld region were also obtained by using a point micrometer as represented in Figure 95. This was used to measure the "loss thickness" or "electrode indentation" by taking the difference of the two values.

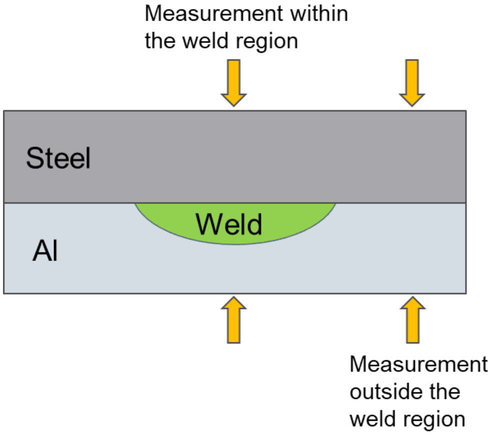

Figure 95 – Schematic representation of the point micrometer measurements

TSS and CTS testing methodology and geometry of the assembly for testing are described in section 4.

4.1.3. **Equipment and experimental procedure**

Resistance spot welding was performed using a Matuschek ServoSPATZ in a custom build ARO C frame gun of 1 kHz Direct Current (DC) 250kVA with 8 kN maximum force mounted on a Kawasaki ZX165U Robot. The electrode tips used were made from Luvata A-trode® material which consists of a copper alloy C18150 (CuCr1Zr) in accordance with EN ISO 5182 A2/2 and belongs to Resistance Welding Materials Alloy (RWMA) Class II. The electrode chemical composition provided by the supplier was: Cr 0.7% to 1.2%; Zr 0.06% to 0.15%; others max. 0.2%. The electrode properties provided by the supplier at 20°C are:

- Mass density - 8.9g/cm^3
- Specific heat - 376 J/kg.K
- Thermal conductivity - 320 W/m.K
- Expansion coefficient - 17.0 x 10^{-6}
- Electric conductivity - min. 43 S/m
- Softening temperature - min. 500°C
- Tensile strength - ≥ 490 N/mm^2
- 0.2% Yield Strength - ≥ 430 N/mm^2
- Elongation - ≥ 15 %
- Hardness - ≥ 172 HV

Electrode shape and cleaning was performed with Sinterleghe Ravitex tip dresser with a profile of 8mm flat surface, which ensures constant contact area with sheet for all welding experiments. Control parameters and welding schedules were programmed by the Matuschek SPATZStudio software which allows for easy manipulation of the welding schedule and provides information on welding such as actual electrode force, actual current and average system resistance which were registered for every trial. To calculate heat input measured values of current, time and resistance were considered rather than set parameters. There is small difference (±5) between measured and set values for current and force. However the disparity between set and observed data is taken into account during the data analysis.

4.1.3.1. **Metallographic analysis**

Metallographic analysis was performed in a Zeiss Σigma FEGSEM in combination with EDX detector. Composition analysis was performed by making 10 line scan with multiple passes per line in order to have representative data of each sample

4.1.4. **Approach**

As previously described this technology is based on the joule heating equation:

$$H = I^2Rt$$

Where H is the heat generated, I is the current, R is the system resistance and t is the cycle time. For joining similar materials, the process includes a fixed time and varying the current or vice versa with high electrode force to minimize interface resistance and it is pre-programmed in the system as per the standards. For dissimilar materials this information is not available and therefore no constraints exist to explore the impact of system variables on weld characteristics.

This work will explore all the 3 factors (Resistance, current and time) of the system simultaneously. As the individual material's resistance is constant, the system interface resistance has been varied by varying the electrode force. The parameters and their variations investigated here are presented in Figure 96.

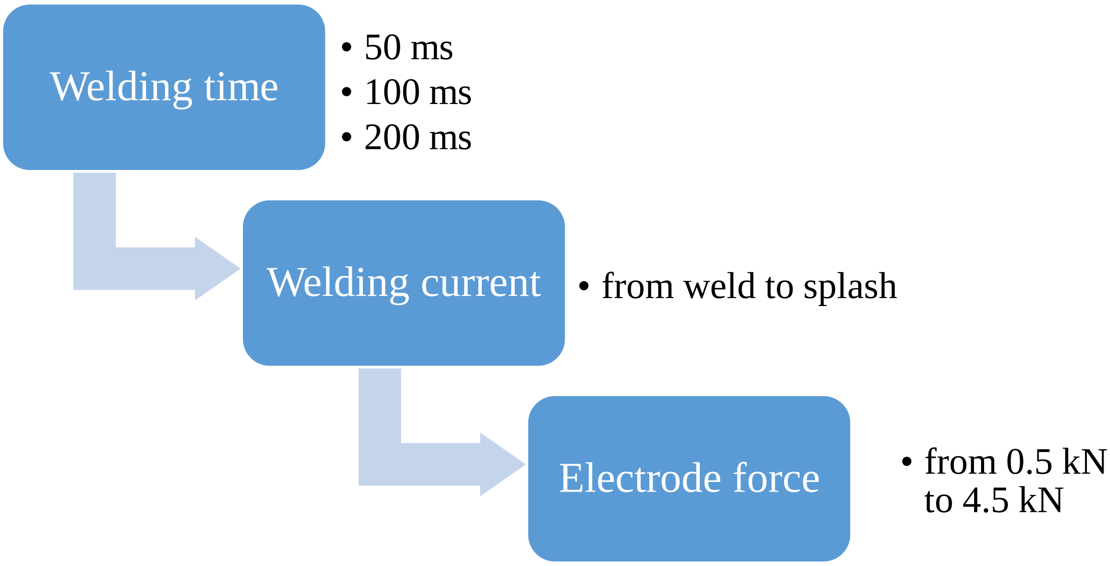

Figure 96 – Exploration of welding parameters.

4.2. Results and discussion

4.2.1. Impact on the weld size

Traditionally in resistance welding the information is presented in the form of weld growth curve, where the weld size is plotted as a function of current at a fixed electrode force. Such example is presented in Figure 97 for a weld of DP600GI-2AA6061 with a fixed welding time of 100ms and a fixed electrode force of 2 kN. The impact of changing the current on the growth of the weld nugget can be observed. The measured average resistance during the welding process can also be plotted to assist the results interpretation as shown in Figure 98. The joule heating equation can be used to calculate the heat in the system from the current and average resistance as presented in Figure 99. From this information it is possible to see that the average resistance decreases with welding current while the heat input increases. This fact is associated with the generated heat, which promotes material expansion within the weld region, thus improving contact between two metals and therefore promoting reduction of the contact resistance. It was confirmed in Figure 99 that the square function of the current in the joule equation, the current is one of the dominant factor for the joule heating. Although joule heating increases with the increased current, this does not translate into increased weld size. In spite of increased volume of melt associated with increased joule heating, loss of liquid metal takes place through liquid migration or splash as the interface is not completely sealed, due to uneven surfaces of sheets at microscopic level, which in turn reduces the weld size.

This can be cross validated by the loss of metal thickness (also referred as electrode indentation) presented in Figure 100, where it can be seen that the indentation increases with the increased heat and becomes especially high in the last two welds. Electrode indentation is an indication of both increased weld shrinkage and volume loss by expulsion.

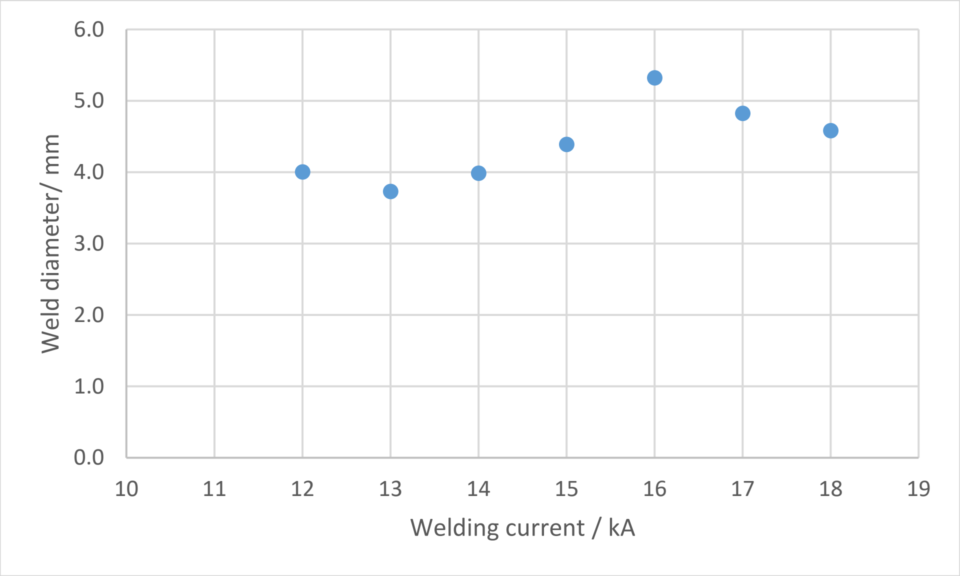

Figure 97 – Weld diameter growth curve for a fixed pulse of 100ms and fixed electrode force of 2 kN for a DP600GI – 2AA6061 joint.

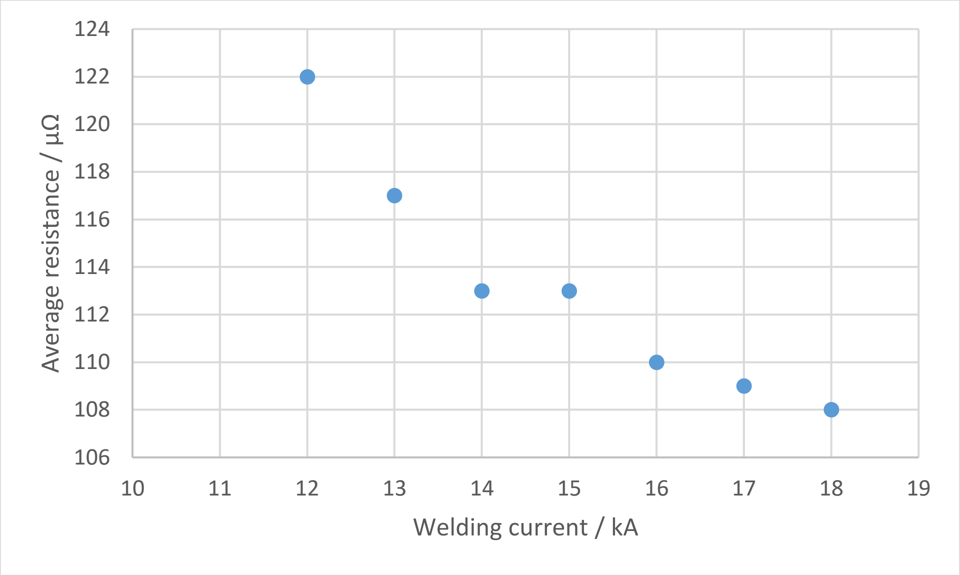

Figure 98 – Average resistance curve for a fixed pulse of 100ms and fixed electrode force of 2 kN for a DP600GI – 2AA6061 joint.

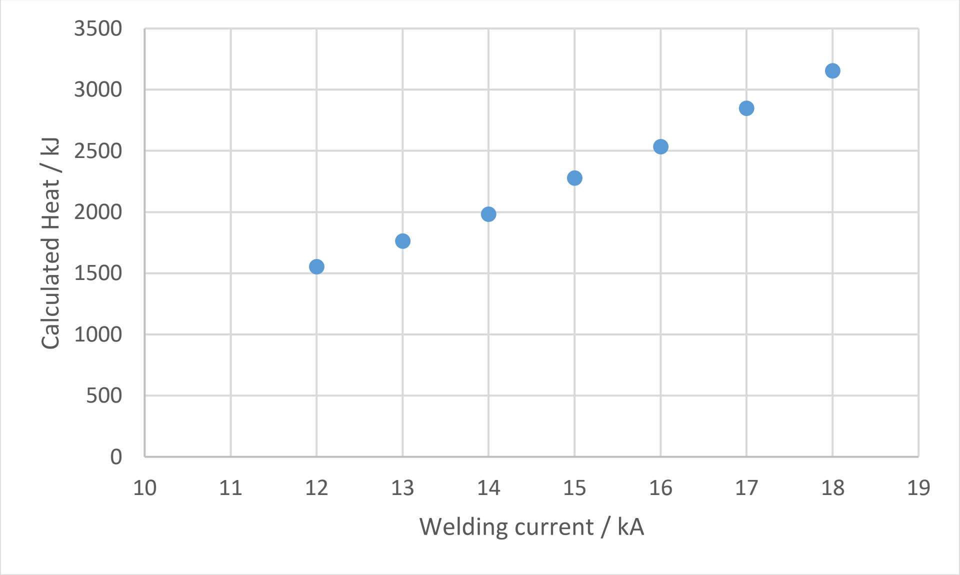

Figure 99 – Growth curve for a fixed pulse of 100ms and fixed electrode force of 2 kN for a DP600GI – 2AA6061 joint.

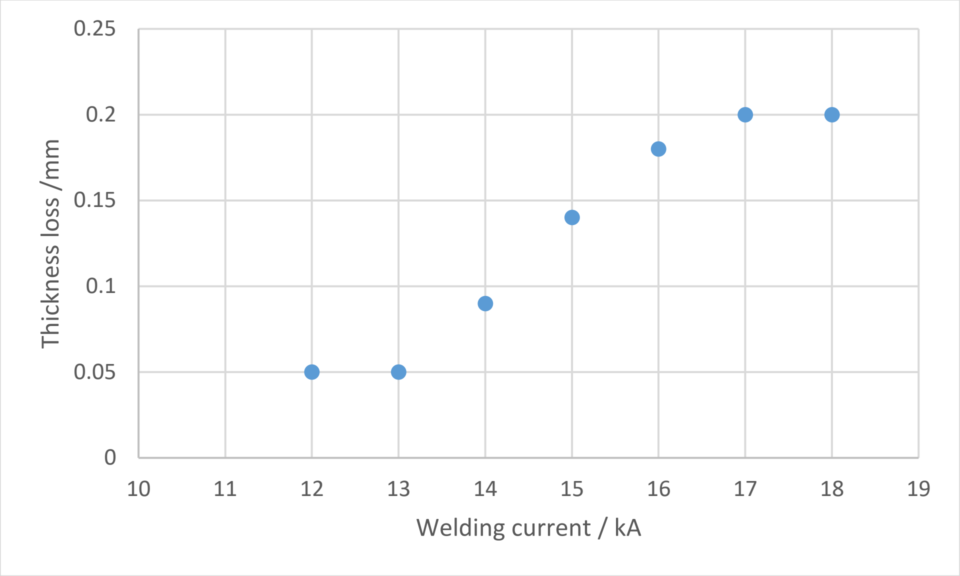

Figure 100 – Weld indentation for a fixed pulse of 100ms and fixed electrode force of 2 kN for a DP600GI – 2AA6061 joint.

The data shown in

Figure 101, Figure 102, Figure 103 and Figure 104 are conventional way of understanding the influence of changing one variable, however, in order to understand the effect when multiple variables are present the 3D plots provides comprehensive picture. A new 3D approach for data presentation and improved interpretation as a holistic view of all three dimensions simultaneously is explored by plotting the current vs electrode force vs a targeted variable. The contour plots have been made based on these three variables. The number of data points varied depending on data, with fixed intervals of 1kA and 250 N.

Figure 101 presents the impact of both welding current and electrode force has on the weld diameter for a pulse of 100ms. Evidently it is possible to see that low forces promote bigger welds which are caused by the increased interface resistance between materials due to less intimate contact between steel and aluminium surfaces which restricts current over smaller areas. This can be observed in Figure 102, where the impact on the average resistance is shown by the higher resistance at lower forces, which generates higher heat at the weld, evidenced in Figure 103 where the calculated heat for the system is presented. At lower electrode force, the average resistance decreases with the increased welding current, due to thermal expansion caused by local joule heating, which decreases the contact resistance between the two sheets. Furthermore, for a fixed current it is evident that the increased electrode force reduces the resistance, through improved interface contact, creating a region of increased indentation as can be seen in Figure 104. The region of increased indentation can be observed for high currents but at medium force. In this region, the electrode forces are not sufficient enough to accommodate gaps caused by thermal expansion. Therefore, the liquid metal is not contained within the weld region leading into small amount of expulsion by weld splash. Preliminarily results indicate that welds at low electrode force exhibit large weld size with low amount of electrode indentation which tends to be associated with low amount of material expulsion.

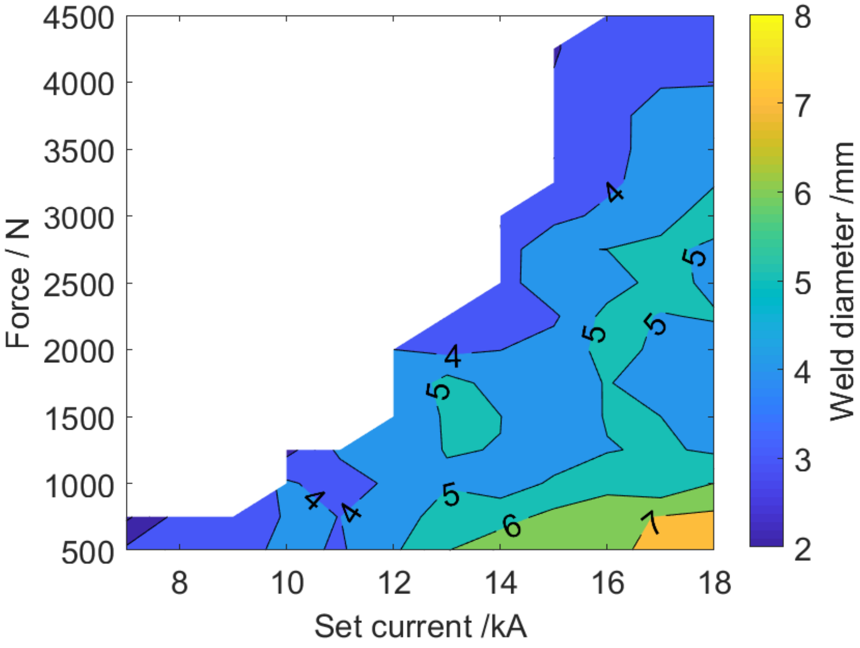

Figure 101 – Weld diameter in function of Current vs Force for welding pulse 100 ms. The contour region is referred as weldability lobe and the empty space represents lack of weld formation.

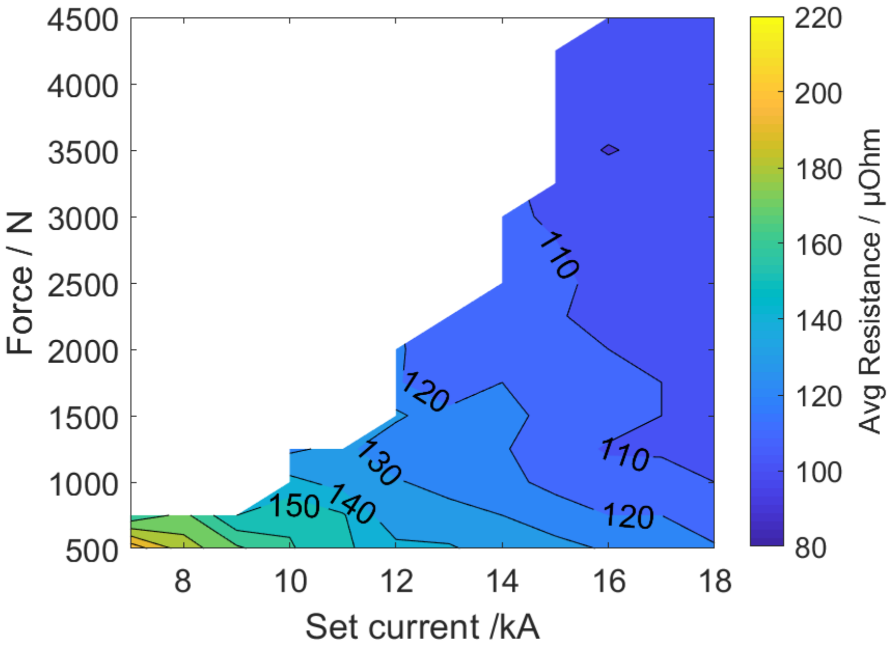

Figure 102 – Average resistance in function of Current vs Force for welding pulse 100 ms

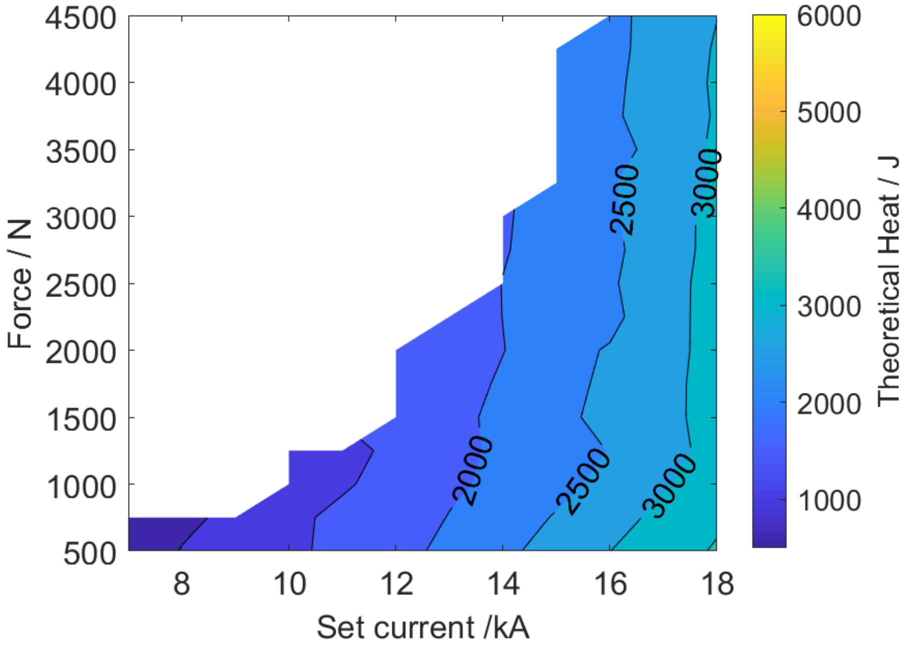

Figure 103 – Calculated Heat in function of Current vs Force for welding pulse 100 ms

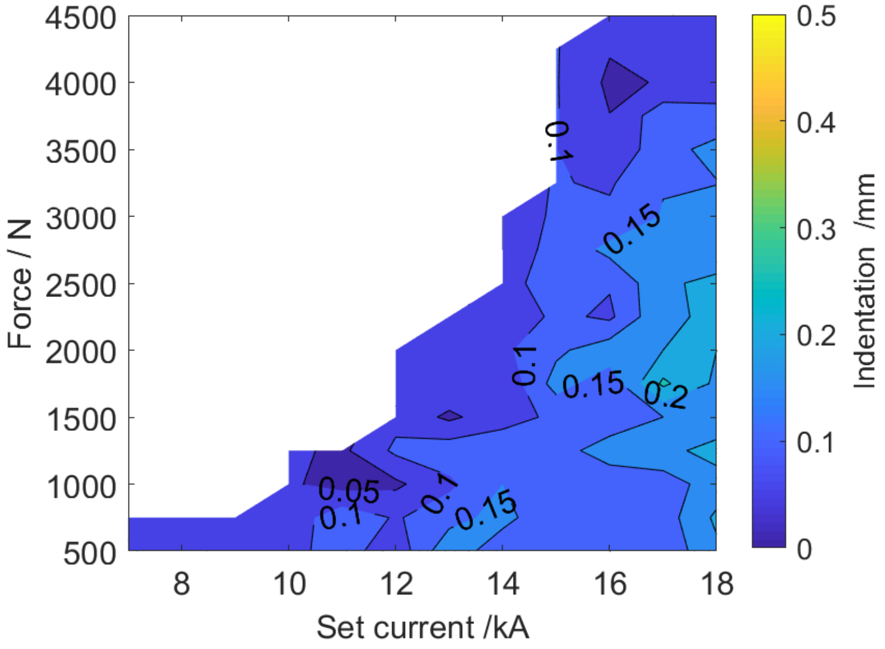

Figure 104 – Electrode indentation in function of Current vs Force for welding pulse 100 ms

The electrode force controls the heat in the system, which in turn affects the weld size. Based on joule heating, one can influence the weld nugget growth with the pulse duration. To analyse the influence on the weld nugget growth with time system variation included the variation of the welding time. The time parameter (pulse duration) is varied between 50 ms and 200 ms for the same current ranges and electrode forces.

Figure 105 – 108 presents results for the weld diameter, average resistance, theoretical heat and electrode indentation as a function of current and electrode force for a welding time of 50ms. Compared to the 100ms pulse, there is a clear difference in reduction on the weldability lobe and weld size, which is associated with a reduction of the heat input by the smaller pulse time. Results show a higher average resistance at higher currents, which is related with the lower heat input which promotes lower material expansion minimizing the resistance. It is also evident that it results in lower amount of indentation for 50ms compared to 100ms. Additionally the points with highest indentation are directly correlated with the points of highest heat input, e.g. lower electrode forces.

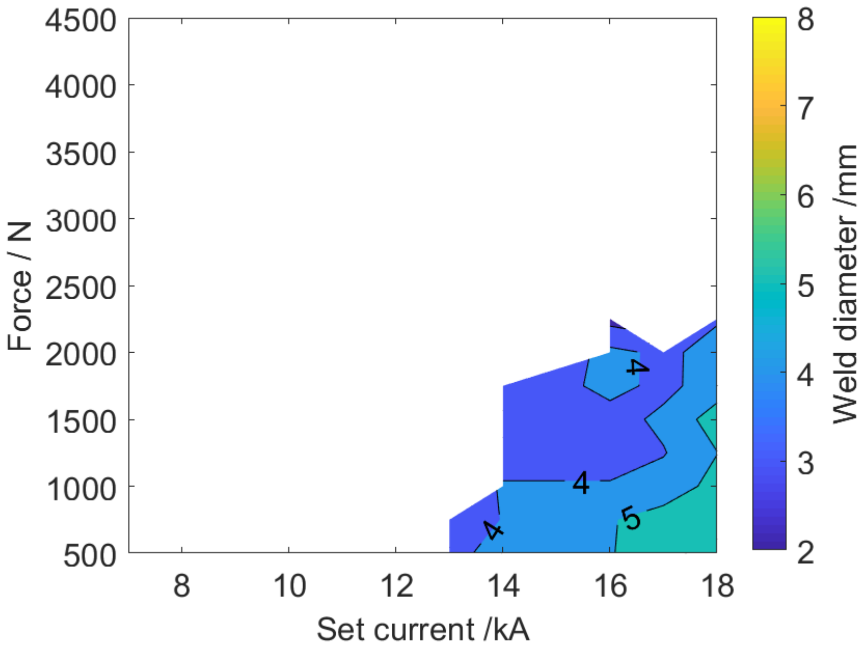

Figure 105 – Weld diameter in function of Current vs Force for welding pulse 50 ms

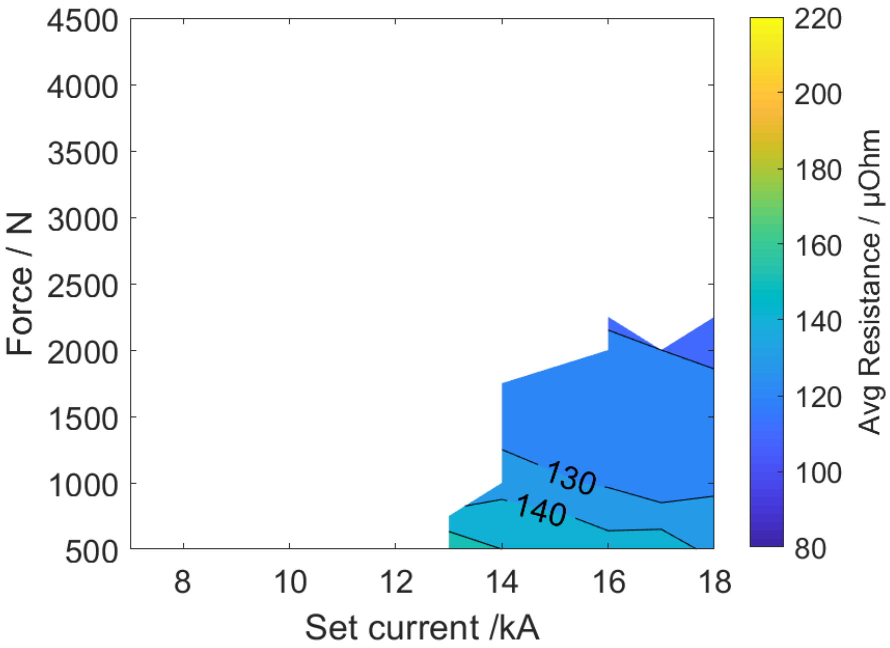

Figure 106 – Average resistance in function of Current vs Force for welding pulse 50 ms

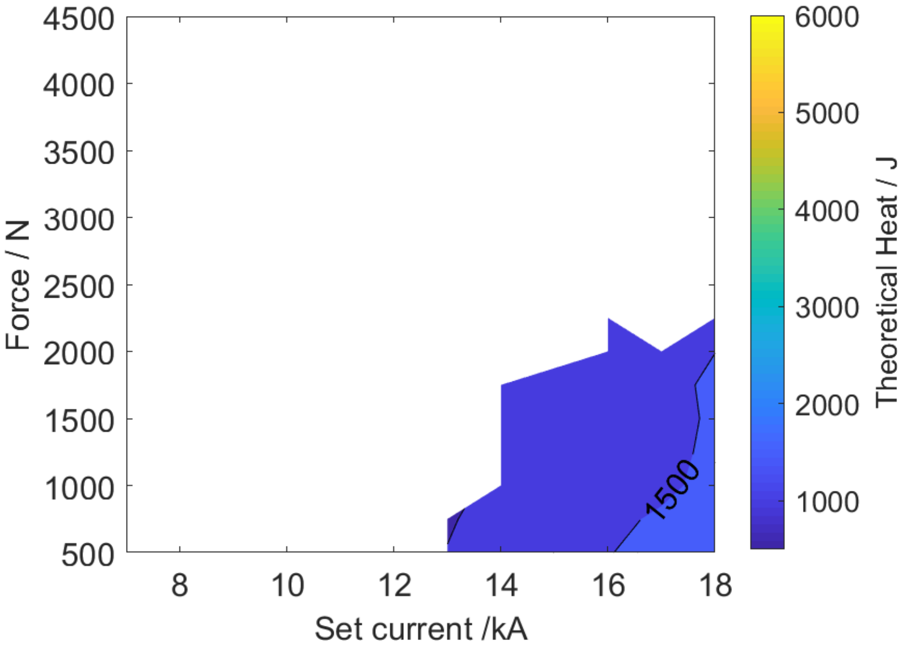

Figure 107 – Calculated Heat in function of Current vs Force for welding pulse 50 ms

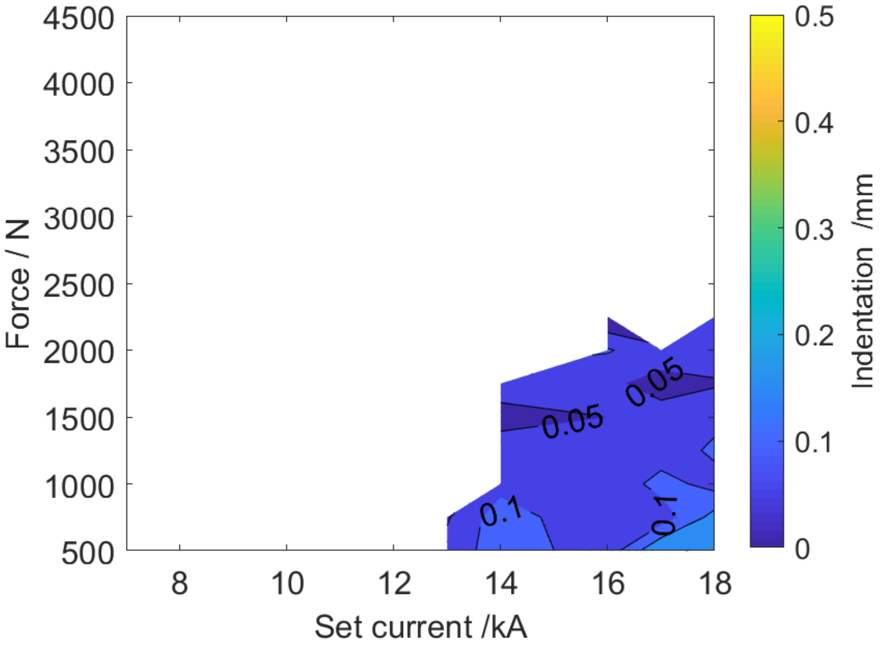

Figure 108 – Electrode indentation in function of Current vs Force for welding pulse 50 ms

The results of the 200ms pulse are presented in Figures Figure 109, Figure 110, Figure 111 and Figure 112 for weld diameter, average resistance, theoretical heat and electrode indentation as a function of current. There is an obvious increase in weldability lobe which is apparent in Figure 109, additionally it is possible to also observe an increase of weld diameter compared with the 100ms pulse welding schedule, longer pulse promotes an increase in heat input that induces therefore a bigger growth of the weld size. Discordant to previous results, an increase in weld size was also observed for high electrode forces and high currents that is accompanied by a high indentation. This metal loss is associated with the effect of weld splash which is consistent with the limits of the weld growth. However, the combination of the high electrode forces and pressure associated with local thermal expansion leads to liquid metal expulsion allowing solidification of melt in wider region and therefore contributing to the increased weld size. In addition to this effect the high electrode forces reduces porosity by expelling part of zinc vapour along with the melt expulsion.

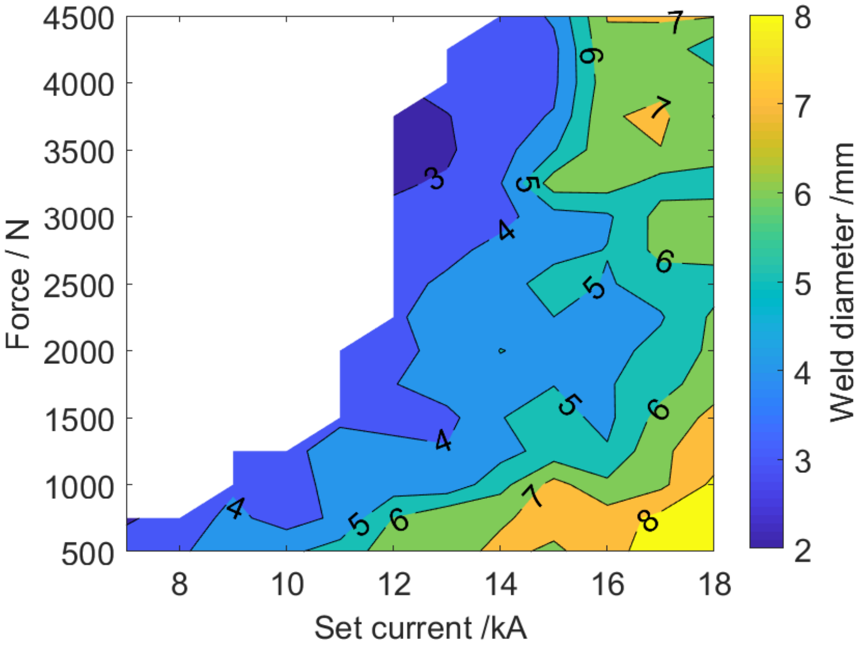

Figure 109 – Weld diameter in function of Current vs Force for welding pulse 200 ms

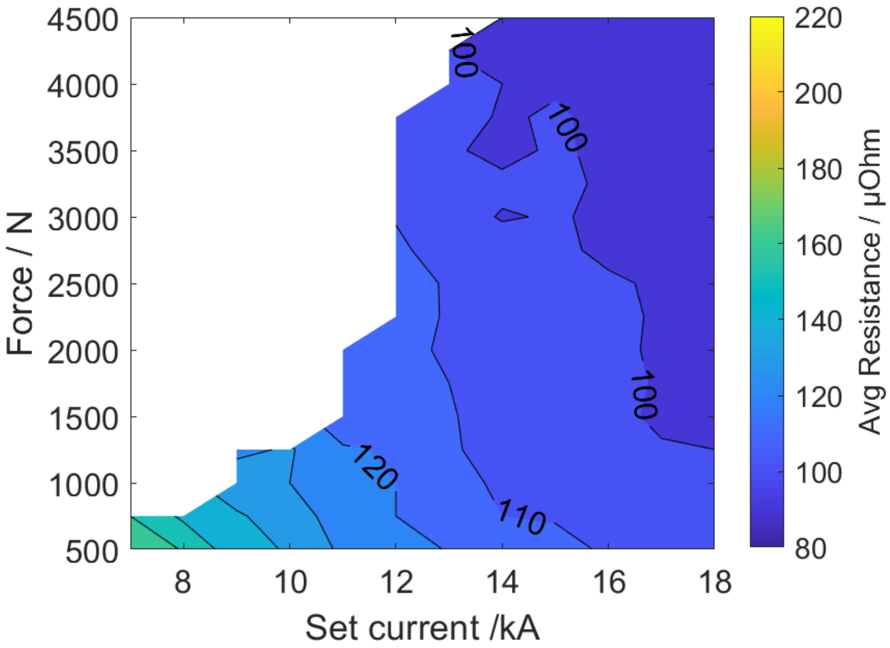

Figure 110 – Average resistance in function of Current vs Force for welding pulse 200 ms

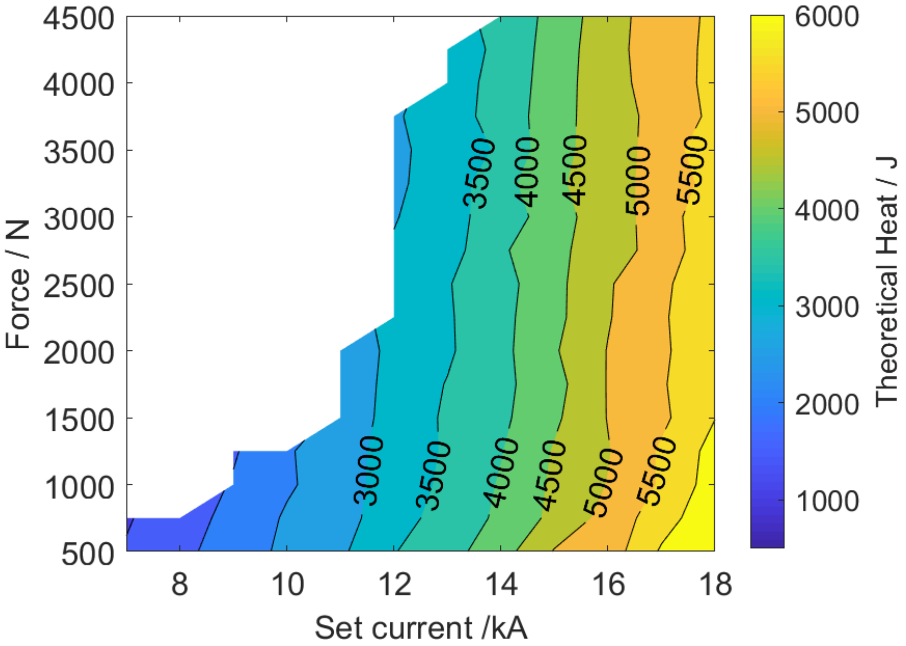

Figure 111 – Calculated Heat in function of Current vs Force for welding pulse 200 ms

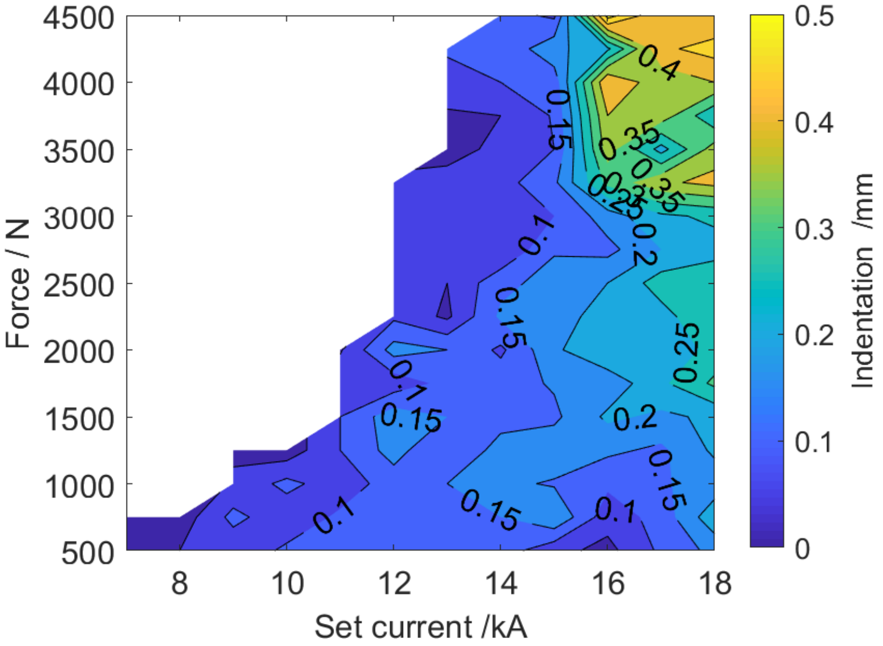

Figure 112 – Electrode indentation in function of Current vs Force for welding pulse 200 ms

The comparison of the measured data at various welding times of 50, 100 and 200 ms represents a direct interpretation of the Joule heating equation, as the welding time increases the higher heat input which leads to bigger welds. This is shown in Figure 113. In addition, the manipulation of the system resistance by controlling the electrode forces is shown to improve the weld size, especially at lower electrode forces. However, a high amount of porosity is evident within the weld zones. As a mean to reduce the observed weld porosity, a subsequent pulse was added creating dual stage process. The first pulse would initiate the weld and the second would promote minimisation of porosity. The rational is associated with the subsequent pulse which can re-melt the material minimizing porosity formation. Therefore the additional new welding schedules are two pulses of 50ms or 100ms with an interval of 20ms which allows at least a partial solidification to occur for the melt associated with the first pulse. Therefore the total heating time will be of 100ms for the double pulse of 50ms and 200ms for the double pulse of 100ms. Pulsed current profile also allows us to compare the weld characteristics for a given duration of pulse but with and without intermittent local solidification.

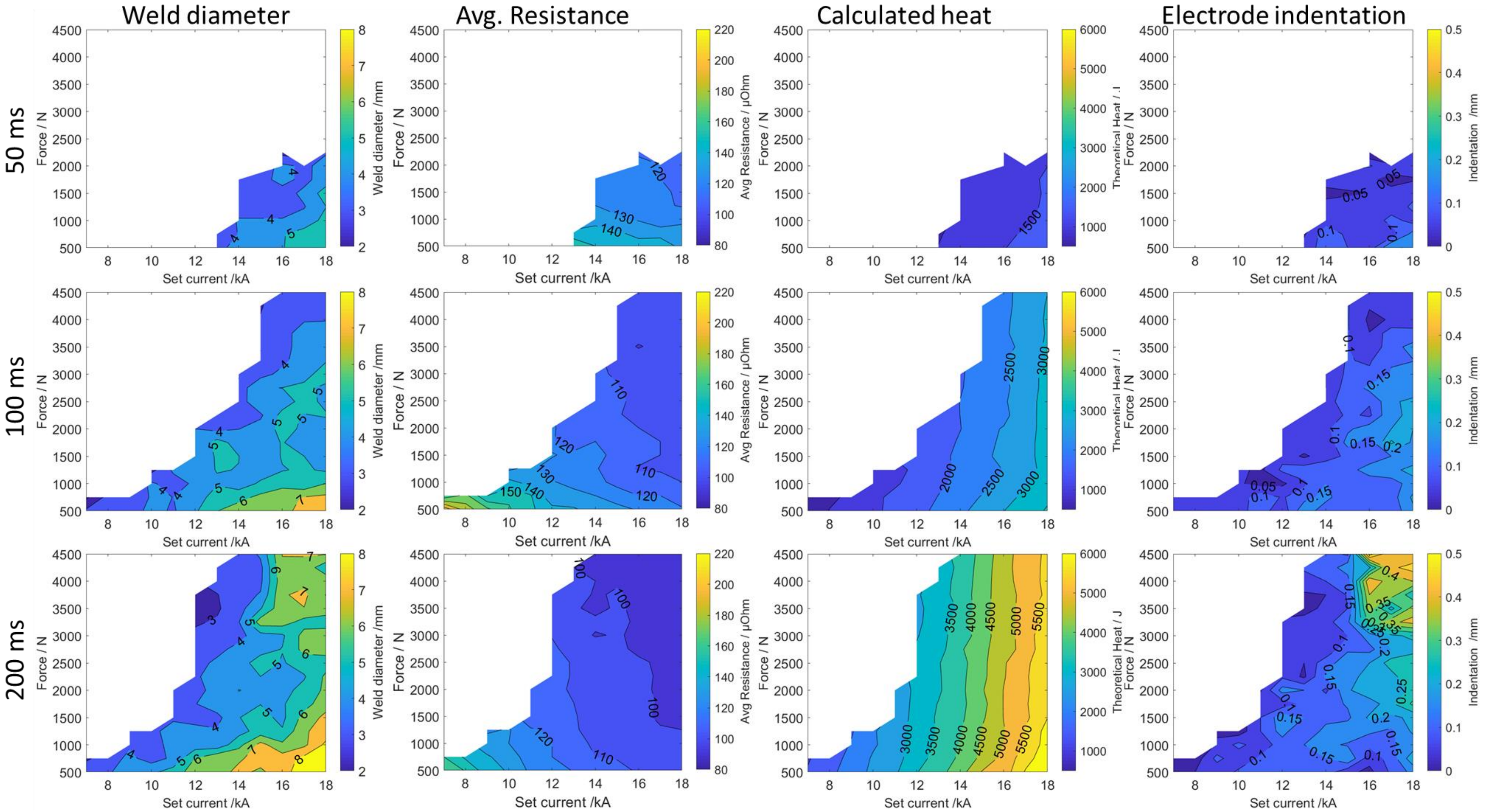

Figure 113 – Comparison of weld diameter, average resistance, calculated heat and electrode indentation for a single pulse of 50ms, 100ms and 200ms.

The results for the 2x50ms dual pulse cycle are presented in Figure 114, Figure 115, Figure 116 and Figure 117 for the weld diameter, average resistance, theoretical heat and electrode indentation as a function of current and electrode force respectively. Results for the multiple pulse welding schedules of 2x50ms lie between the single pulses of 50ms and 100ms as seen in Figure 118. Similar to previous observations, the increased time causes a higher heat input and lower average resistance, additionally the higher the heat input is the larger the weld size; however the weld size is inferior to the single pulse of 200ms. The most significant result is reduced electrode indentation compared to the 100ms along with the reduced porosity.

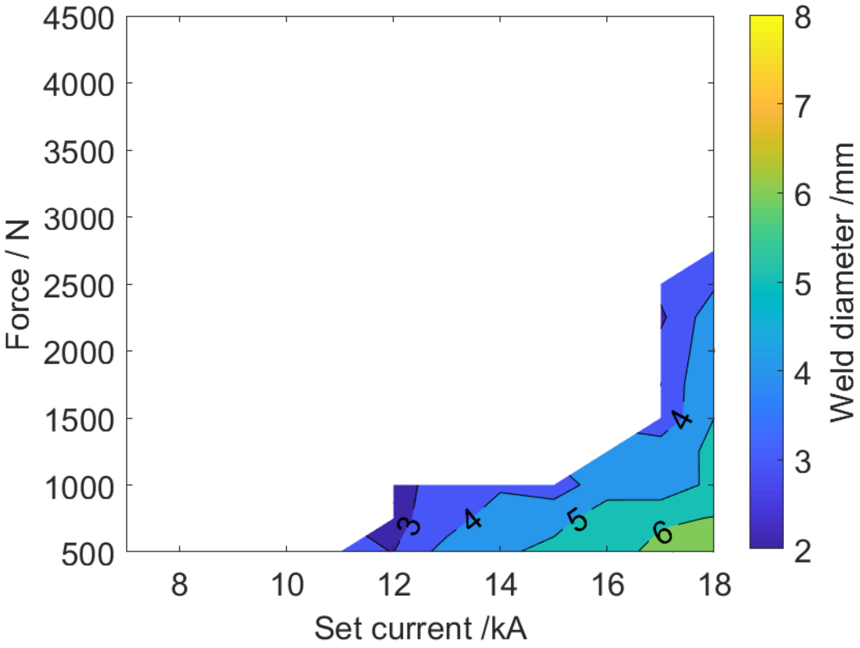

Figure 114 – Weld diameter in function of Current vs Force for welding pulse 2x50 ms

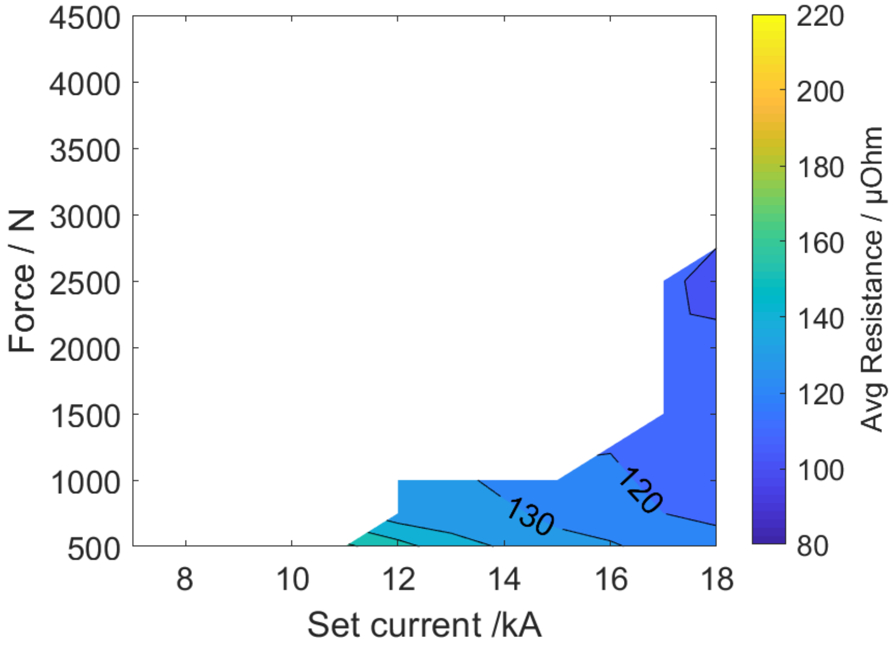

Figure 115 – Average resistance in function of Current vs Force for welding pulse 2x50 ms

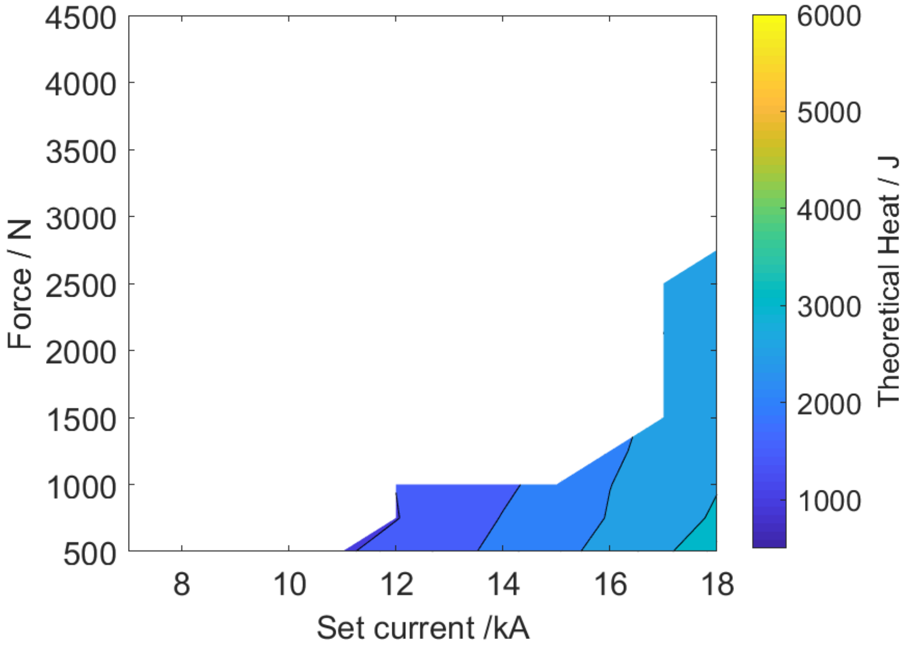

Figure 116 – Calculated Heat in function of Current vs Force for welding pulse 2x50 ms

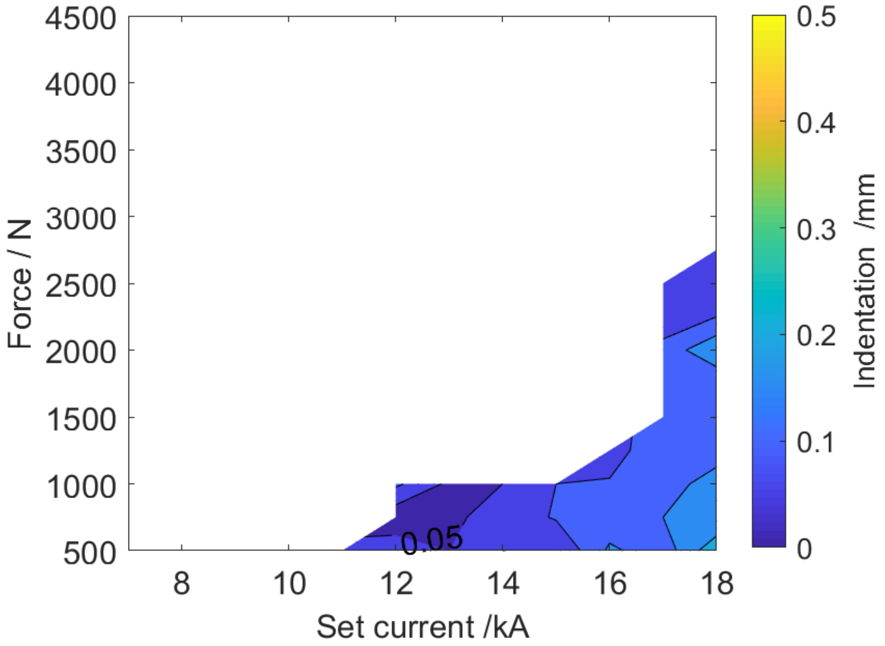

Figure 117 – Electrode indentation in function of Current vs Force for welding pulse 2x50 ms

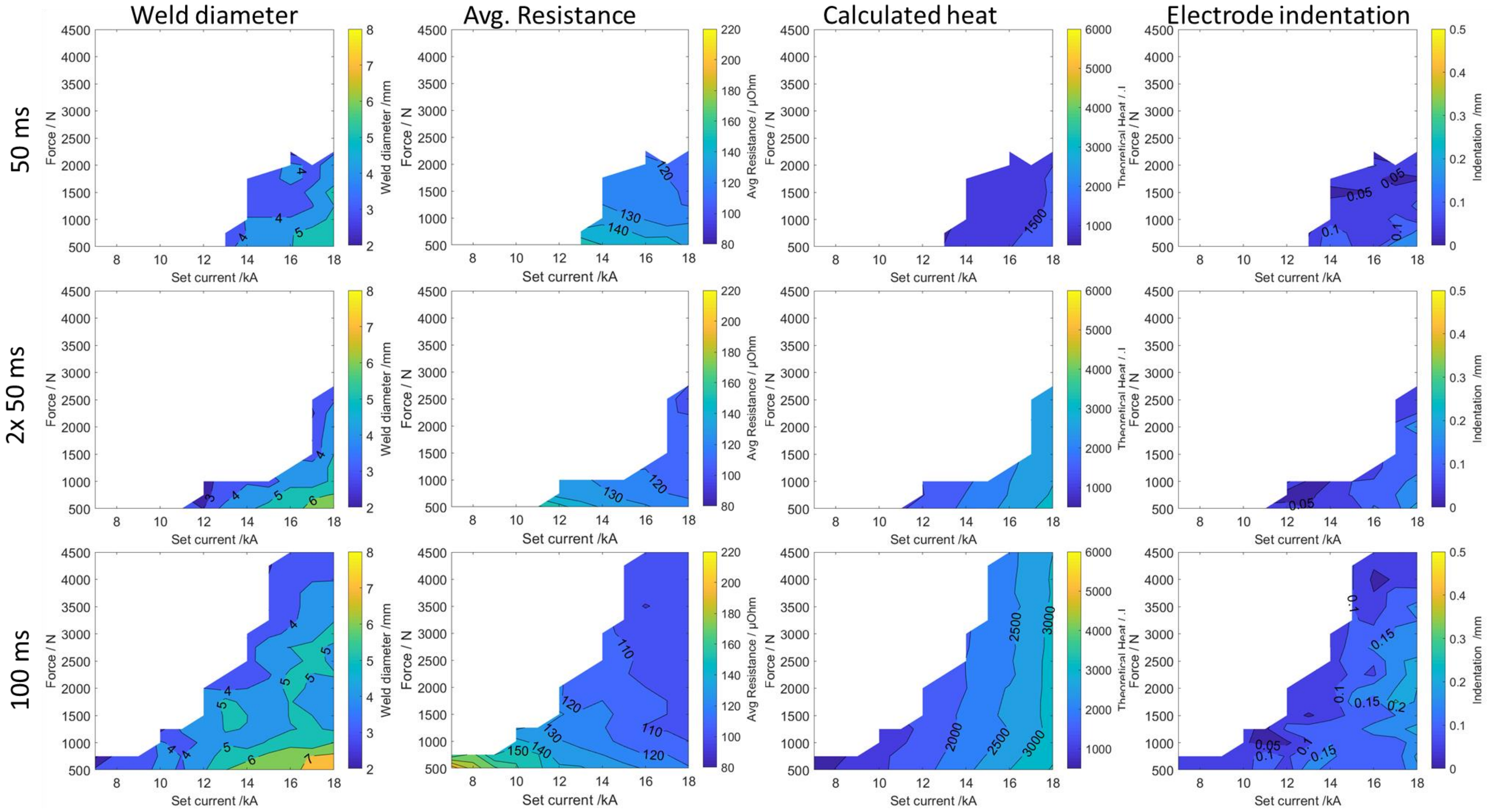

Figure 118 – comparison of weld diameter, average resistance, calculated heat and electrode indentation for a single pulse of 50ms, a double pulse of 50ms (2x50ms) and single pulse of 100ms

The results for the 2x100ms dual pulse cycle are presented in Figure 119, Figure 120, Figure 121 and Figure 122 for the weld diameter, average resistance, theoretical heat and electrode indentation as a function of current and electrode force respectively. Similar to the dual pulse of 50ms the dual pulse of 100ms (2x100ms), the size of the welds lie between the single pulse values of 100ms and 200ms. As previously observed in the single pulse, the increased time allows for a higher heat input which is inversely proportional to the average resistance. Again the most significant result is reduction in electrode indentation compared to the 200ms.

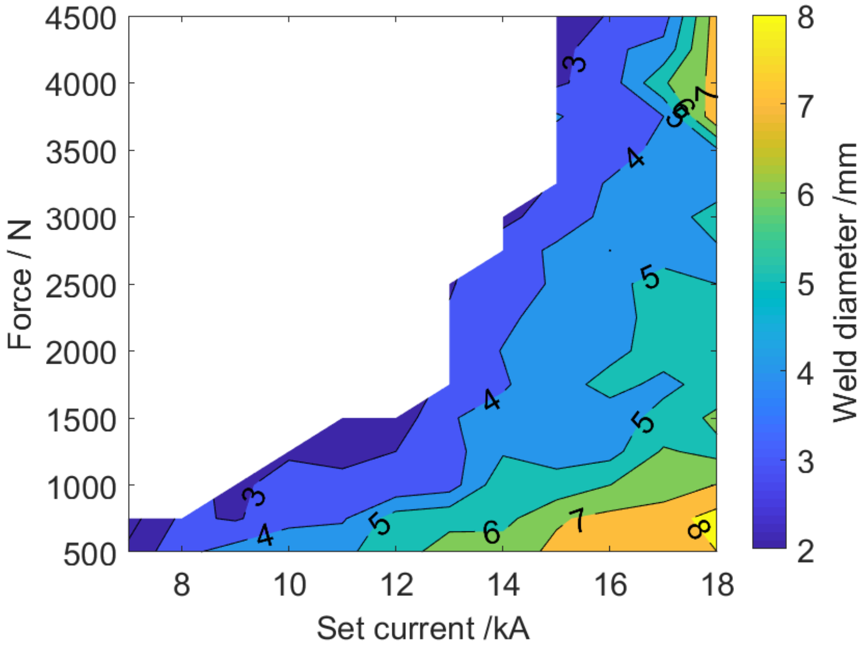

Figure 119 – Weld diameter in function of Current vs Force for welding pulse 2x100 ms

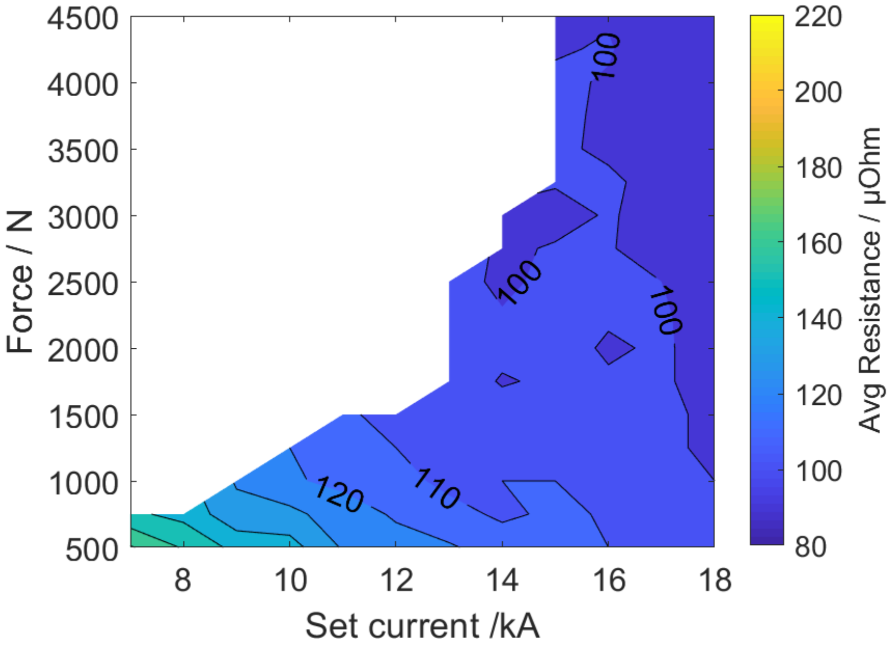

Figure 120 – Average resistance in function of Current vs Force for welding pulse 2x100 ms

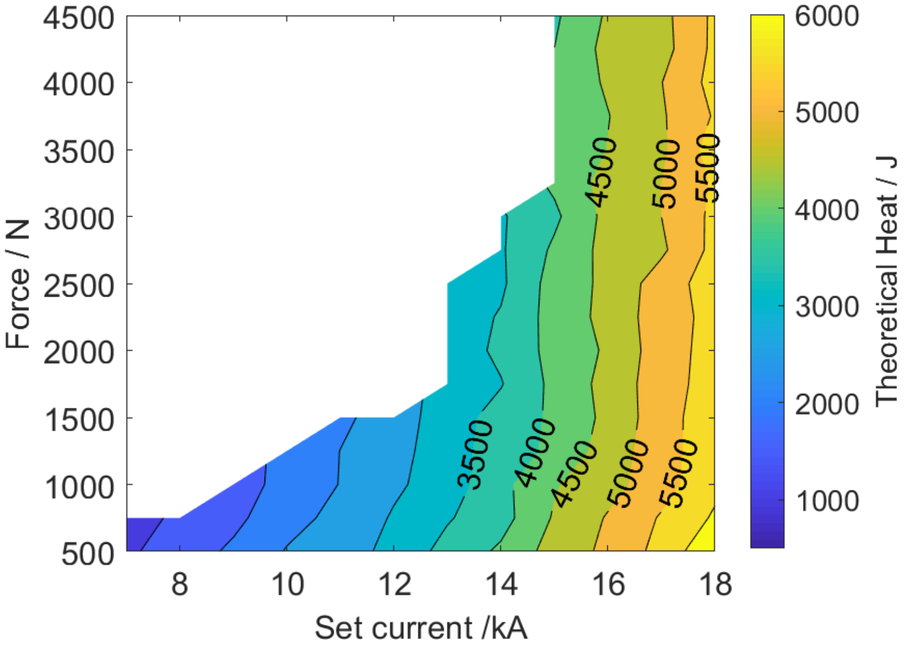

Figure 121 – Calculated Heat in function of Current vs Force for welding pulse 2x100 ms

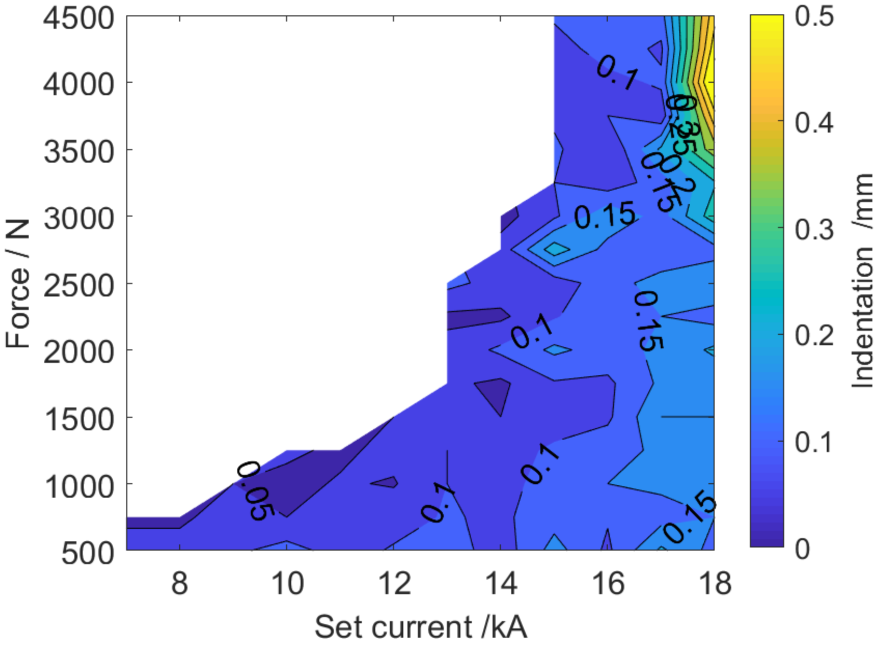

Figure 122 – Electrode indentation in function of Current vs Force for welding pulse 2x100 m

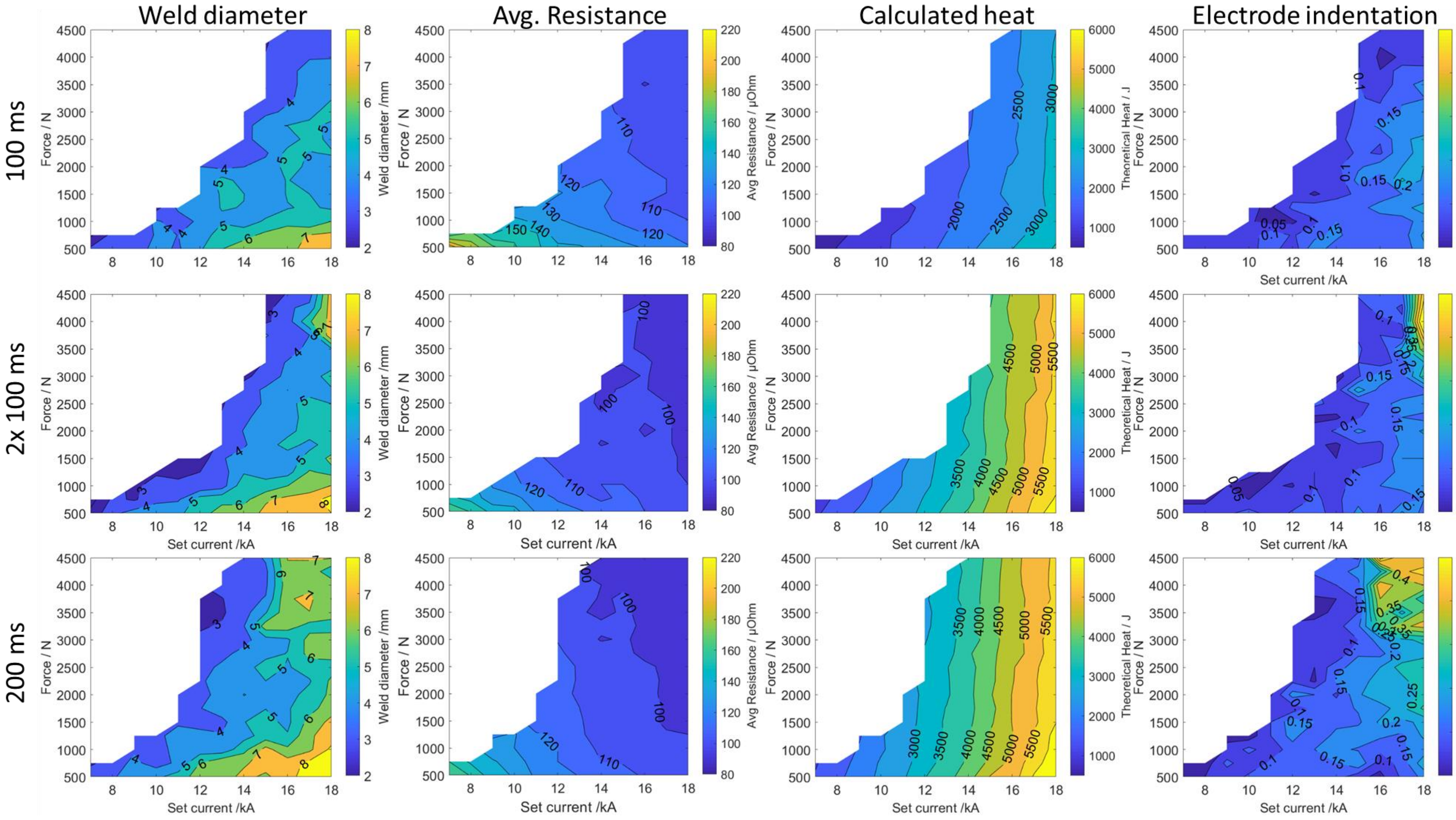

Figure 123 – comparison of weld diameter, average resistance, calculated heat and electrode indentation for a single pulse of 100ms, a double pulse of 100ms (2x100ms) and single pulse of 200ms

These results allow to unravel the impact of controlling the heat formation on weld. The direct interpretation of the Joule heating equation allowed to control the system to increase weld size. However, in order to characterise joint performance, additional information for the joint under loading conditions is needed. Therefore selective welds were tested under tensile shear and cross tension loading to evaluate their joint performance. Since welds with smaller size performs poorly compared to their larger counter parts, testing was performed preferentially for larger welds for the applied current ranging between 12 kA and 18 kA in 2 kA intervals. At each condition, the reported failure loads are the average value of 3 specimens along the standard deviation. The standard deviation allows to predict the volatility of joint production due to porosity effects. An example of a TSS loading curve is presented in Figure 124. It is evident on the load-displacement that this constitutes a solid joint, as the displacement is minimal. As the load start to be applied directly on the joint, the joint bears the applied load until interface failure occurs.

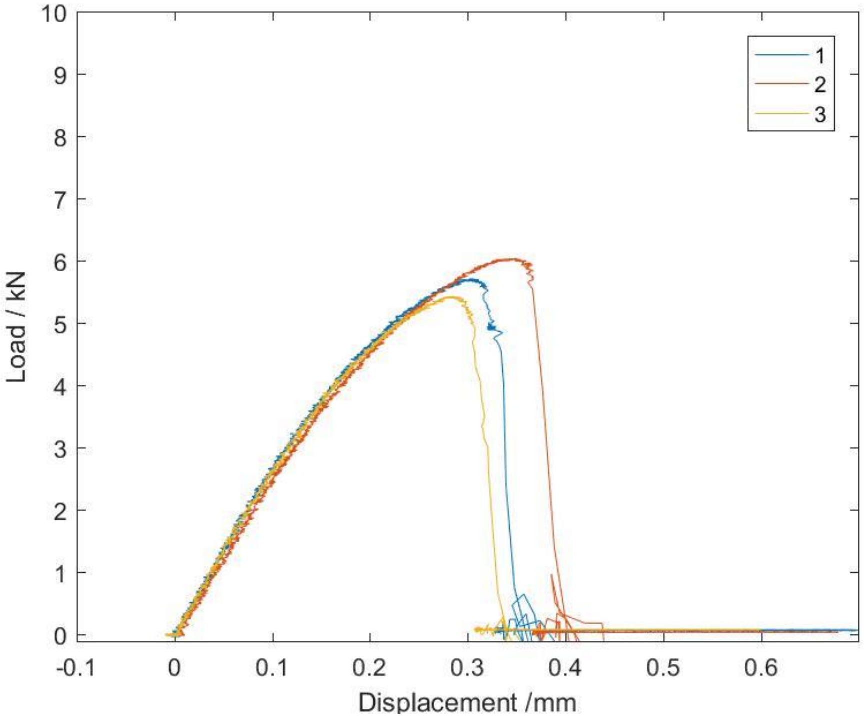

Figure 124 – Load displacement curve for a joint of 200ms at 18 kA and 2kN

The tensile data for all welding schedules is presented in Figure 125. In tensile shear tests, the welds with smaller weld size failed at lower loads, due to stress concentration over small area. Welds produced under single pulse of 100 ms duration exhibited higher performance compared to welds produced under dual pulse condition. This is correlated with the larger weld size as previously observed in Figure 118. Nevertheless, the analysis of the standard error deviation show that a multi-pulse approach exhibits higher weld cohesion and stability by exhibiting a lower error, especially for the process windows of high heat inputs. The zones of high heat input correlate with higher amount of porosity, evidencing the hypothesis that the second pulse would redistribute the melt locally leading to reduced porosity as a result of uniform shrinkage of melt which in turn leading to a more stable weld performance. The welding schedules totalling the welding time of 200 ms further confirm this, as at lower electrode forces the process is consistent with the higher heat input and therefore associated with greater amount of porosity and the error is much higher for the single pulse schedule. For the dual pulse of 200 ms (2x100ms) it is possible to observe a lower error combined with a better performing joint bringing evidence of lower porosity which reinforces the previous conclusions.

The results allow to identify the areas of process window that allow the creation of joints with low amount of joint performance variation. High reliability of joint manufacturing is of paramount importance as it will attest the applicability on critical components such as BIW structures.

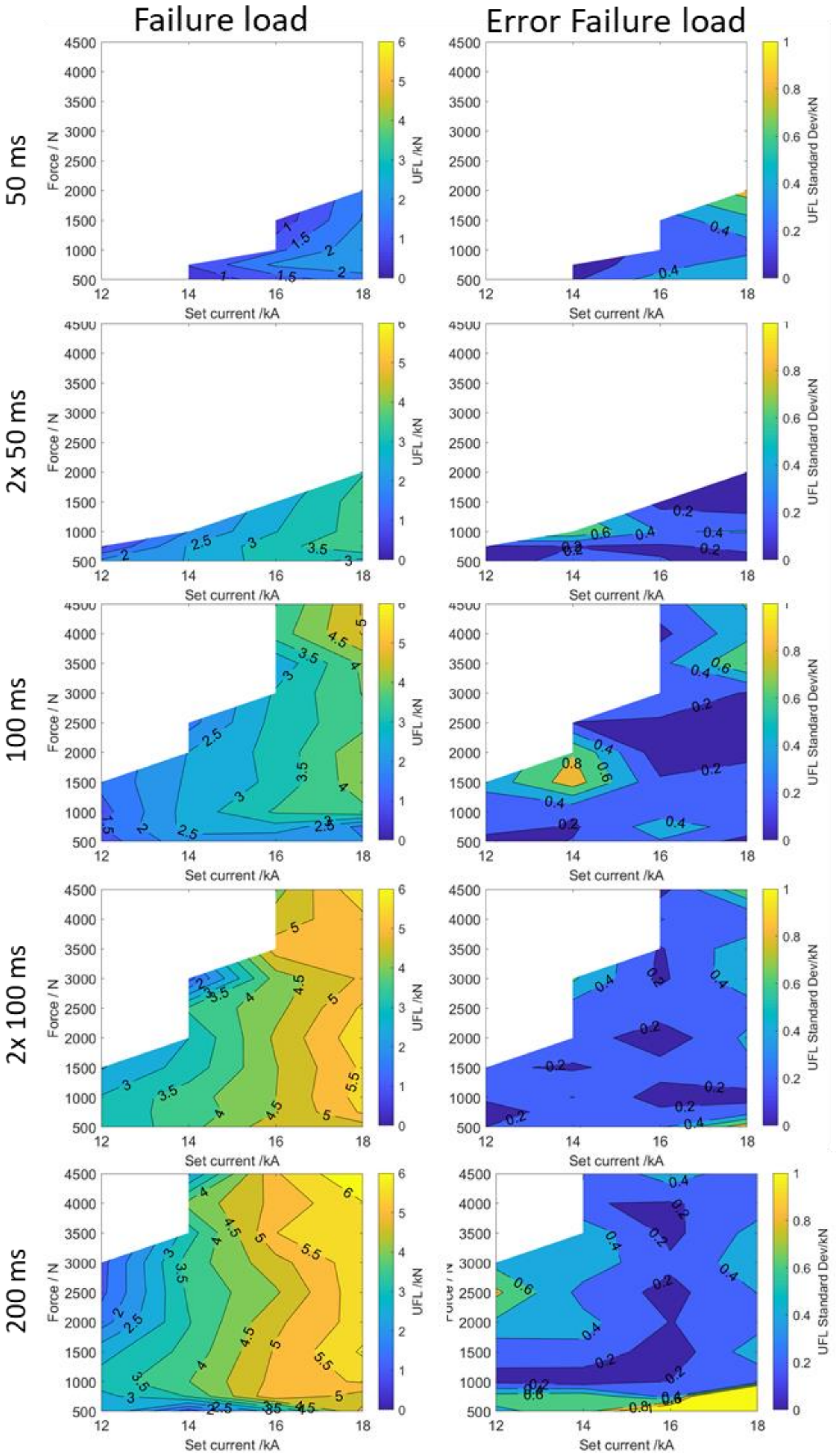

Figure 125 – Tensile shear failure loads and associated error

The cross tension results for all welds obtained at various conditions are presented in. Figure 126 Evidently as observed in the previous chapter of this thesis, the strength in cross tension loading is different due to change in the nature of loading in the joint. The RSW joint is no different, however during this work none of the joints exceeded more than 1.5 kN in max failure load. Similar to conclusions obtained for tensile testing, bigger welds are associated with better performing joints where the load can be distributed over a larger area. Again, areas of higher porosity are associated with the higher error deviation. Also as observed in tensile data, error deviation for joints with dual pulses is lower, evidencing higher amount of reproducibility of results. The observed highest performing joints are associated with the 200ms single pulse, however the 200ms dual pulse (2x100ms) show similar performance but with improved reproducibility which is of a practical importance for obtaining a BIW structure with uniform weld performance.

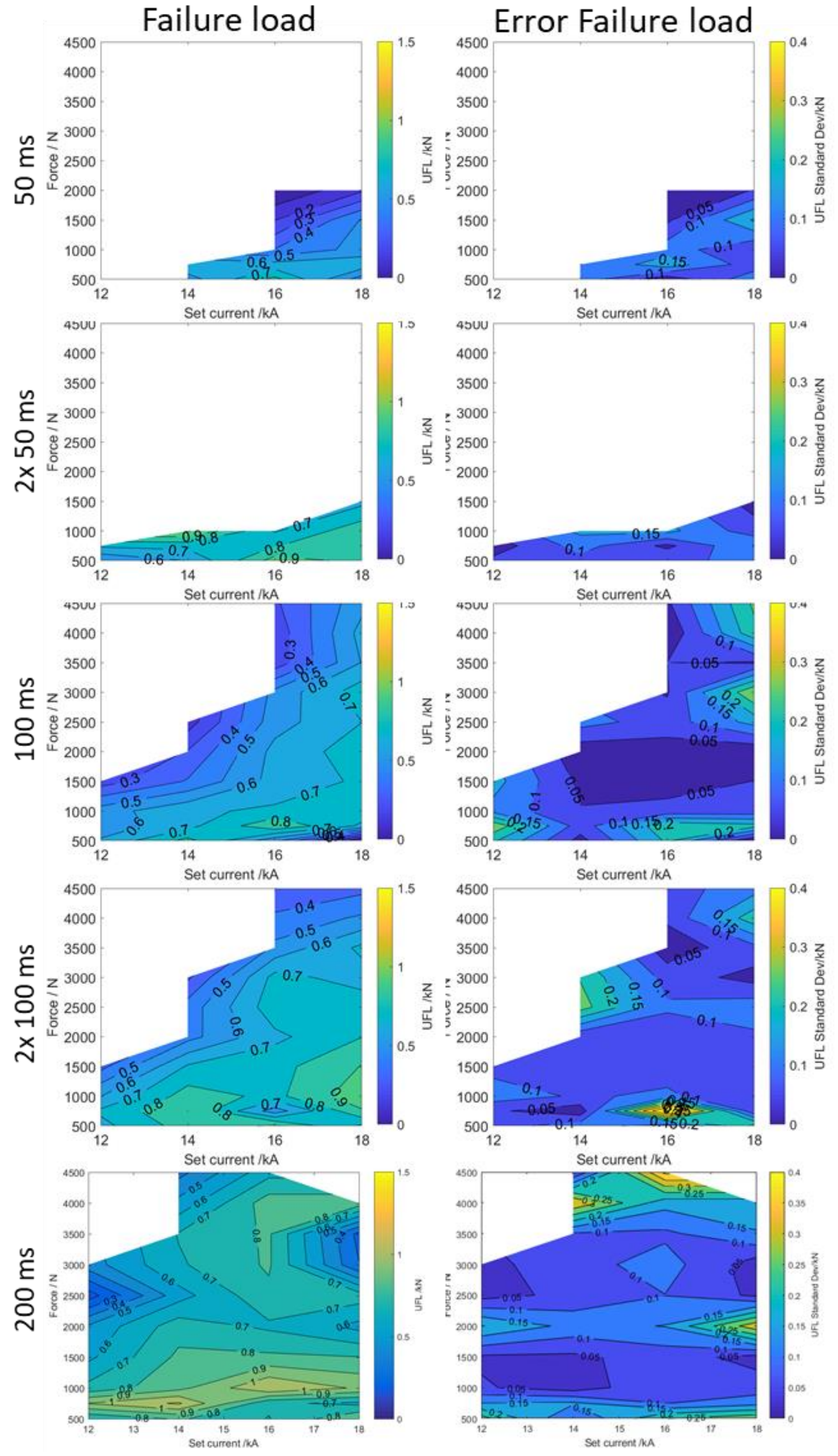

Figure 126 – Cross tension failure loads and associated error

This work generated a large amount of data from both parameters setting and the relevant effects, such as the weld diameter and joint performance, which permit subsequent study and interpretation. In order to analyse the impact of the control parameters a regression analysis of the system can be performed to generate a predictor model from the obtained data. This promotes both the analysis of the quality of the data input for a relative output (weld diameter, tensile shear performance or cross tension performance) but also generates a semi-empirical model for this particular system. Due to various predictor variables (numbers of pulses; welding time; welding current; electrode force) a Multivariate Polynomial Regression analysis has been performed. The data fitting has been performed in order to improve the system predictor accuracy and therefore different polynomials regressions were considered in order to predict different outcomes (weld diameter (WD), Tensile Shear Strength (TSS) and Cross Tension Strength (CTS)). Multiple regressions were performed for all data in order to achieve optimised regression variables considering the different polynomial orders as it can be observed in Table 15. Selection was performed by analysing the obtained R^2 for model accuracy and the associated Mean Average Error (MAE) for the respective regression. Therefore the improved scenario would be the R^2 closest to 1 with the minimal MAE. From the data in the table it is possible to see that the optimal regression for the WD, TSS and CTS are 3rd, 4th and 6th order polynomials respectively.

Table 15 – Evaluation of model regression for the different polynomial orders by the value of R^2 and Mean Absolute Error (MAE) for the WD, TSS and CTS regressions

Regression	WD		TSS		CTS	
	R^2	**MAE**	**R^2**	**MAE**	**R^2**	**MAE**
Polynomial order 2	**0.787**	**0.111**	**0.807**	**0.221**	**0.462**	**0.471**
Polynomial order 3	**0.848**	**0.097**	**0.839**	**0.197**	**0.547**	**0.379**
Polynomial order 4	**0.843**	**0.100**	**0.852**	**0.190**	**0.578**	**0.374**
Polynomial order 5	**-**	**-**	**0.853**	**0.191**	**0.594**	**0.361**
Polynomial order 6	**-**	**-**	**-**	**-**	**0.610**	**0.372**
Polynomial order 7	**-**	**-**	**-**	**-**	**0.602**	**0.387**

The simplified version of the 3rd order polynomial predictor equation to estimate the weld diameter size (WD) is presented below.

$$WD = 6.15 \times 10^{-3} \times F - 8.70 \times 10^{-7} \times F^{2} - 3.07 \times 10^{-4} \times I - 3.78 \times 10^{-7} \times I \times F + 1.05 \times 10^{-10} \times I \times F^{2} + 3.13 \times 10^{-8} \times I^{2} - 1.16 \times 10^{-11} \times I^{2} \times F - 4.95 \times 10^{-2} \times t \times F + 3.57 \times 10^{-6} \times t \times F^{2} + 7.02 \times 10^{-3} \times t \times I + 9.54 \times 10^{-7} \times t \times I \times F - 1.35 \times 10^{-7} \times t \times I^{2} + 4.94 \times 10^{-2} \times t^{2} \times F - 1.15 \times 10^{-2} \times t^{2} \times I + 2.39 \times 10^{-7} \times p \times F^{2} + 1.70 \times 10^{-7} \times p \times I \times F - 7.09 \times 10^{-9} \times p \times I^{2} + 5.64 \times 10^{-3} \times p \times t \times F - 2.10 \times 10^{-4} \times p \times t \times I - 1.49 \times 10^{-3} \times p^{2} \times F + 5.97 \times 10^{-5} \times p^{2} \times I + 8.46 \times 10^{-2} \times p^{3} + 1.37 \times 10^{-13} \times I^{3} - 1.79 \times 10^{-10} \times F^{3}$$

where p is the number of pulses, t is the welding time, I is the current and F is the electrode force. For weld diameter prediction, this semi-empirical model was obtained with an $R^2 = 0.848$ and a Mean Absolute Error (MAE) of 0.097 mm indicating that there is some undiscovered/unaddressed factor that has not been considered. Further evidence is observed in the goodness fit scatter plot (Figure 127) where a variation between predicted and observed values can be observed. This equation allowed achieving 85% accuracy for the prediction of the weld diameter despite not following the behaviour of the Joule heating equation since it does not account for the system resistance.

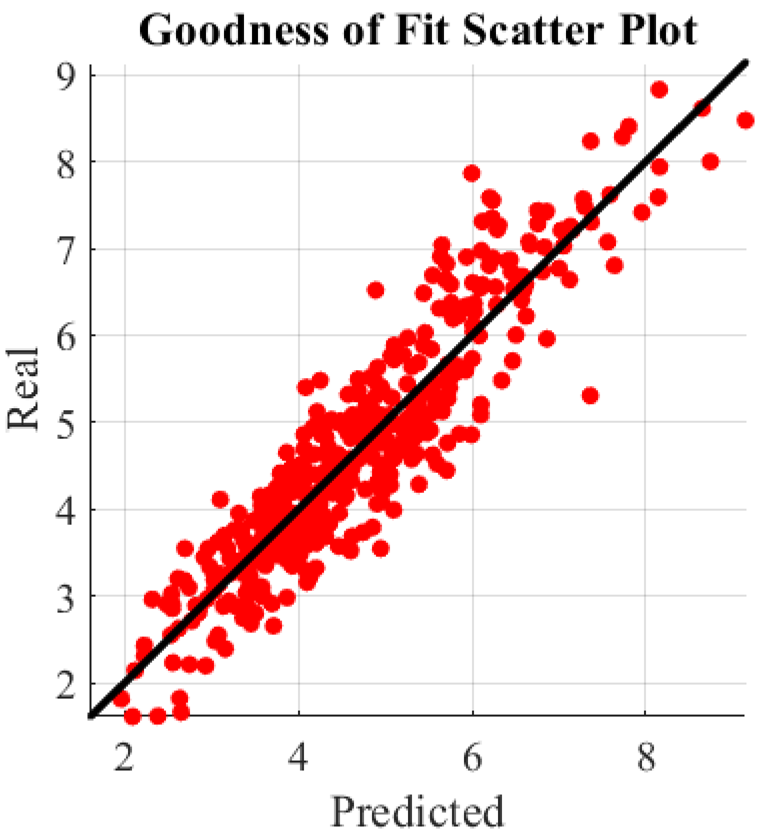

Figure 127 – Goodness of Fit Scatter Plot between Real and Predicted data for the weld diameter.

The system resistance is not an independent variable, therefore not being able to be used on the model prediction. In order to ascertain if the system resistance is being accounted for WD model regression, the same system external variables (*F*, *I*, *P* and t) were used to determine if system resistance is accounted for. The regression analysis for the system resistance (*R*) is presented below

$$R = -2.69 \times 10^{-8} \times F - 2.19 \times 10^{-8} \times I + 4.75 \times 10^{-13} \times I \times F - 6.31 \times 10^{-4} \times t + 2.43 \times 10^{-8} \times t \times F + 1.24 \times 10^{-8} \times t \times I + 2.28 \times 10^{-9} \times p \times F + 1.36 \times 10^{-9} \times p \times I - 5.75 \times 10^{-5} \times p \times t - 1.05 \times 10^{-5} \times p^2 + 1.12 \times 10^{-3} \times t^2 + 4.99 \times 10^{-13} \times I^2 + 1.99 \times 10^{-12} \times F^2 + 3.79 \times 10^{-4}$$

Where the obtained R^2 was of 0.9485 with a MAE of 0.0281 x 10^{-4} and the predicted values against measured average resistance is presented in Figure 128. This results show that the intendent variables not only exhibit a great affinity for the average resistance prediction, but also is evident that variables are inserted in the model prediction for the weld diameter. Therefore it is possible to conclude that the WD model is accounting the system resistance indirectly through external variables (such as force, current and time) and has direct correlation with the joule heating. It is revealed therefore that additional factors, other than average resistance, are influencing the model WD.

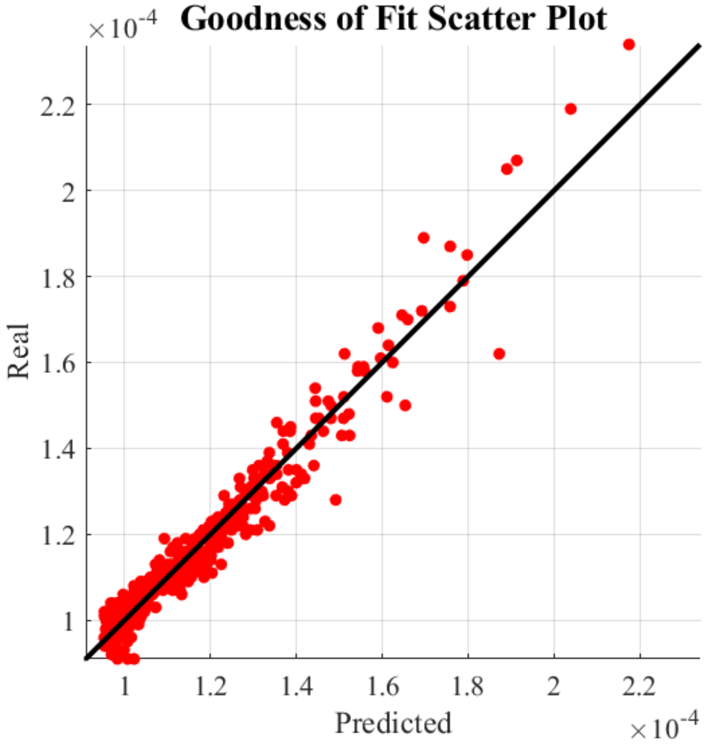

Figure 128 – Goodness of Fit Scatter Plot between Real and Predicted data for the prediction of system average resistance

Additional data for the characterization of weld performance, as the tensile and cross tension performance, can also be analysed with the previous methodology. The same variables are used in multivariable polynomial regression for tensile and cross tension data separately. The semi-empirical predictor equation for tensile performance characterization is below:

$$TSS = -6.00 \times 10^{-6} \times F^2 + 7.13 \times 10^{-10} \times F^3 + 2.01 \times 10^{-7} \times I \times F + 3.35 \times 10^{-10} \times I \times F^2 + 4.08 \times 10^{-14} \times I \times F^3 - 2.38 \times 10^{-9} \times I^2 - 1.68 \times 10^{-11} \times I^2 \times F - 1.99 \times 10^{-14} \times I^2 \times F^2 + 8.50 \times 10^{-13} \times I^3 + 1.29 \times 10^{-15} \times I^3 \times F + 1.22 \times 10^{-5} \times t \times F^2 - 2.20 \times 10^{-11} \times t \times F^3 + 4.64 \times 10^{-6} \times t \times I \times F + 7.97 \times 10^{-11} \times t \times I \times F^2 - 1.78 \times 10^{-7} \times t \times I^2 - 1.01 \times 10^{-10} \times t \times I^2 \times F + 2.79 \times 10^{-12} \times t \times I^3 - 1.22 \times 10^{-5} \times t^2 \times I \times F + 4.95 \times 10^{-7} \times t^2 \times I^2 - 9.75 \times 10^{-11} \times p \times F^3 + 2.04 \times 10^{-12} \times p \times I \times F^2 + 5.08 \times 10^{-12} \times p \times I^2 \times F - 8.14 \times 10^{-13} \times p \times I^3 - 1.29 \times 10^{-5} \times p \times t \times F^2 + 5.57 \times 10^{-7} \times p \times t \times I \times F + 5.19 \times 10^{-8} \times p \times t \times I^2 + 7.04 \times 10^{-7} \times p^2 \times F^2 - 9.65 \times 10^{-8} \times p^2 \times I \times F + 7.10 \times 10^{-9} \times p^2 \times I^2 - 2.17 \times 10^{-17} \times I^4 - 1.12 \times 10^{-13} \times F^4$$

Where the obtained R^2 was of 0. 852 with a MAE of 0.190 and the prediction plot presented in Figure 129.

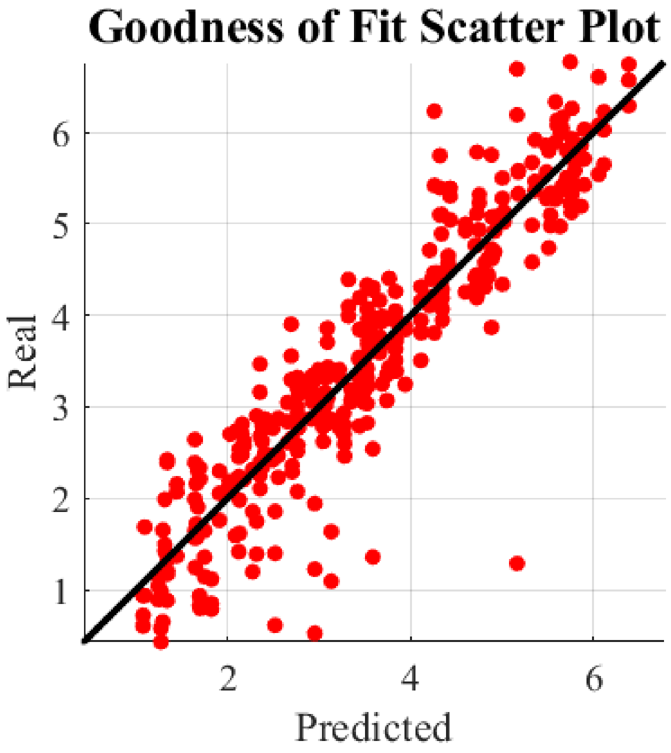

Figure 129 – Goodness of Fit Scatter Plot between Real and Predicted data for the prediction of tensile shear performance

For the cross tension data the prediction equation has been summarized below.

CTS = 2.82 x 10^{-16} x F^5 – 2.06 x 10^{-16} x I x F^4 – 7.10 x 10^{-21} x I x F^5 + 2.02 x 10^{-15} x I^2 x F^2 + 5.60 x 10^{-17} x I^2 x F^3 + 7.77 x 10^{-21} x I^2 x F^4 – 2.82 x 10^{-15} x I^3 x F – 7.18 x 10^{-18} x I^3 x F^2 – 2.35 x 10^{-21} x I^3 x F^3 + 2.87 x 10^{-16} x I^4 + 6.48 x 10^{-19} x I^4 x F + 3.05 x 10^{-22} x I^4 x F^2 – 3.58 x 10^{-20} x I^5 – 2.21 x 10^{-23} x I^5 x F- 3.48 x 10^{-16} x t x F^5 + 2.36 x 10^{-16} x t x F x F^4 – 5.67 x 10^{-17} x t x I^2 x F^3 + 8.78 x 10^{-15} x t x I^3 x F + 6.61 x 10^{-18} x t x I^3 x F^2 – 2.39 x 10^{-16} x t x I^4 – 6.34 x 10^{-19} x t x I^4 x F + 1.24 x 10^{-20} x t x I^5 – 1.10 x 10^{-14} x t^2 x I^3 x F + 4.84 x 10^{-16} x t^2 x I^4 – 3.22 x 10^{-18} x p x F^5 + 1.47 x 10^{-18} x p x I x F^4 – 1.06 x 10^{-18} x p x I^2 x F^3 + 3.92 x 10^{-19} x p x I^3 x F^2 – 5.98 x 10^{-20} x p x I^4 x F + 1.82 x 10^{-21} x p x I^5 – 1.17 x 10^{-14} x p x t x I^2 x F^2 + 7.19 x 10^{-16} x p x t x I^3 x F – 2.38 x 10^{-17} x p x t x I^4 + 4.95 x 10^{-15} x p^2 x I x F^3 – 1.81 x 10^{-15} x p^2 x I^2 x F^2 + 3.15 x 10^{-16} x p^2 x I^3 x F – 8.82 x 10^{-18} x p^2 x I^4 + 1.01 x 10^{-24} x I^6 – 7.26 x 10^{-21} x F^6

Where the obtained R^2 was of 0.610 with a MAE of 0.372 and the prediction plot presented in Figure 130.

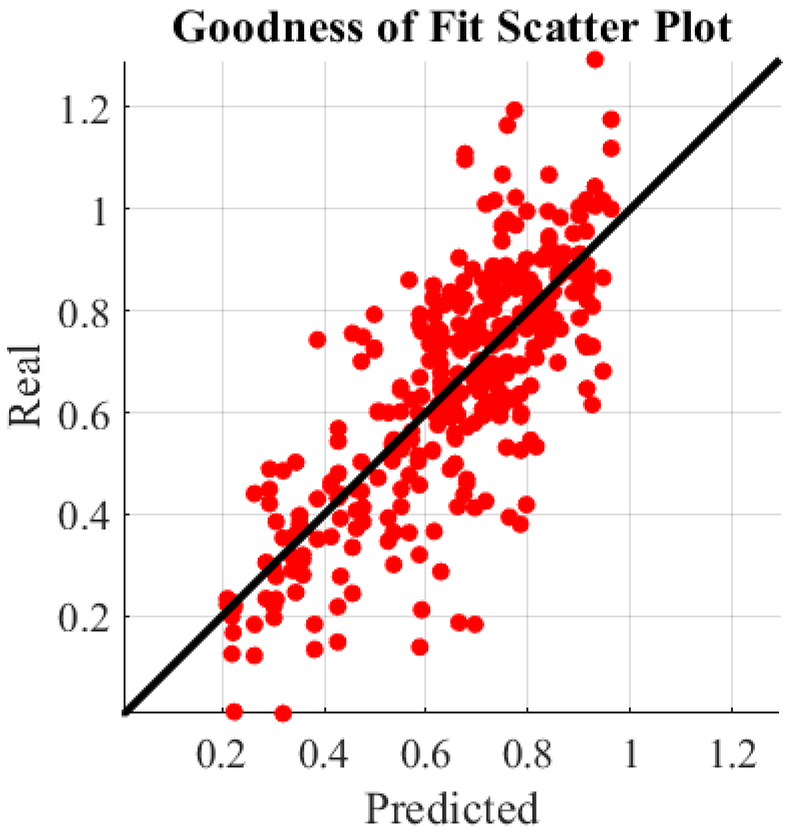

Figure 130 – Goodness of Fit Scatter Plot between Real and Predicted data for the prediction of cross tension performance

The regression analysis reveals that the variables can be used to predict the relevant outcomes with different grades of accuracy due to the different R^2 obtained. This is especially evident in the case of CTS data, there is only a reliability of 61% for the predicted data indicating that introducing additional factors are fundamental to the predictor model. The TSS, like the weld diameter exhibits a higher reliability in excess of 80% indicating that there is an intimate correlation between the independent variables (*p*, *I*, *F* and *t*) and the outcome variable (WD, TSS and CTS). This multi-variant polynomial predictor allows us to estimate the joint performance from a given experimental system investigated without needing to manufacture and destructively test the joints. From the regression of the system resistance, it was proven that the independent variables (P, I, F and t) are able to account for the average resistance and therefore the Joule Heating effect. This brings evidence to additional phenomenon that is not considered, such as effects of weld porosity and thickness of intermetallic layer between two dissimilar metals. It is important to note that we have minimised the influence of other variables, such as material surface condition (cleanliness and surface oil) and electrode condition, by pre-cleaning of surfaces of sheets and electrode as described in methodology.

Nevertheless, the multivariate regression analysis is focussed only to macroscopic impact in both weld size and strength performance without considering the chemical nature of weld and the porosity distribution across the weld. The nature of the observed porosity is associated with the volatilization of the Zn layer of the galvanized steel. However according to the available literature the main problem of these dissimilar joints is the thickness of intermetallic layer. Miyamoto *et al* [122] showed that joints with IMC thickness < 2 µm have yielded higher strength. In this current study, as in can be seen in Figure 131 and Figure 132 the thickness of intermetallic layer is found be between 1.744 µm to a maximum of 2.271 µm. Since the intermetallic thickness is small in this study, the current results are therefore discordant with the observed failure mode referenced by Chen *et al* [130] where the failure is associated with cracking along the intermetallic layer thickness. Chen *et al* observed that an intermetallic layer thicker than 3 µm is prone to interfacial failure independent of aluminium nugget size and steel bulging. The observed failure mode here is interface failure, which is similar to Chen *et al,* but the failure is initiated by the porosity and shrinkage rather than crack propagation through the intermetallics observed by Chen *et al*. Figure 133 shows the porosity in the vicinity of the joint which severely affects the weld performance by acting as crack initiation and propagation paths and not by cracking along the intermetallics as evidenced in Figure 134.

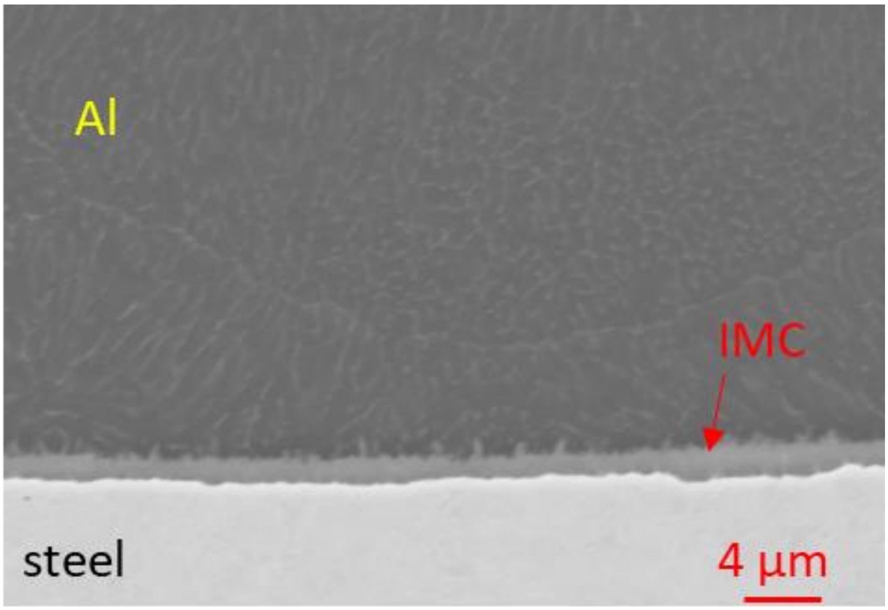

Figure 131 – Cross section of a DP600 – 2AA6061 joint for 200ms pulse 1 kN electrode force and 12 kA

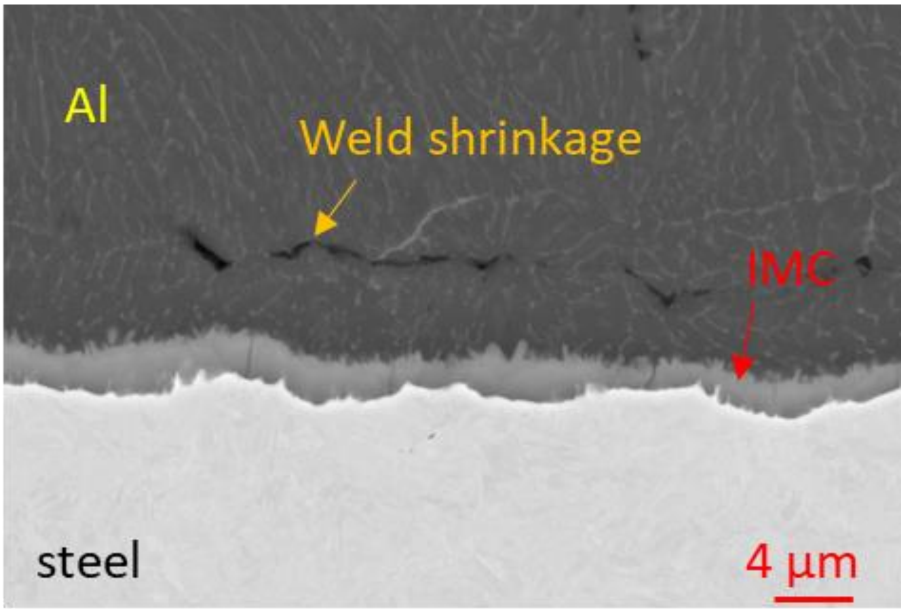

Figure 132 – Cross section of a DP600 – 2AA6061 joint for 200ms pulse 2 kN electrode force and 14 kA with evidence of weld shrinkage

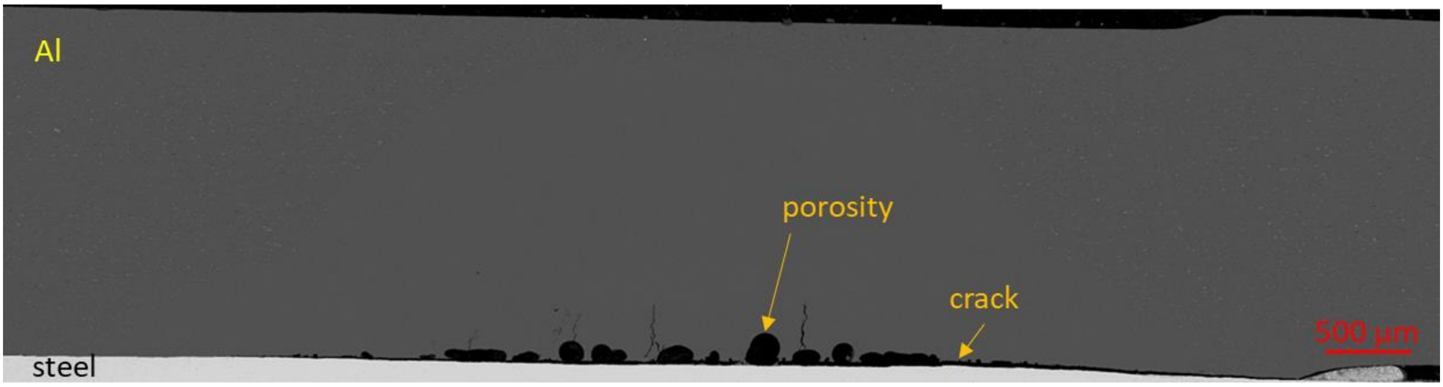

Figure 133 – Cross section of a DP600 – 2AA6061 joint for 200ms pulse 4 kN electrode force and 14 kA with porosity and weld porosity induced cracks

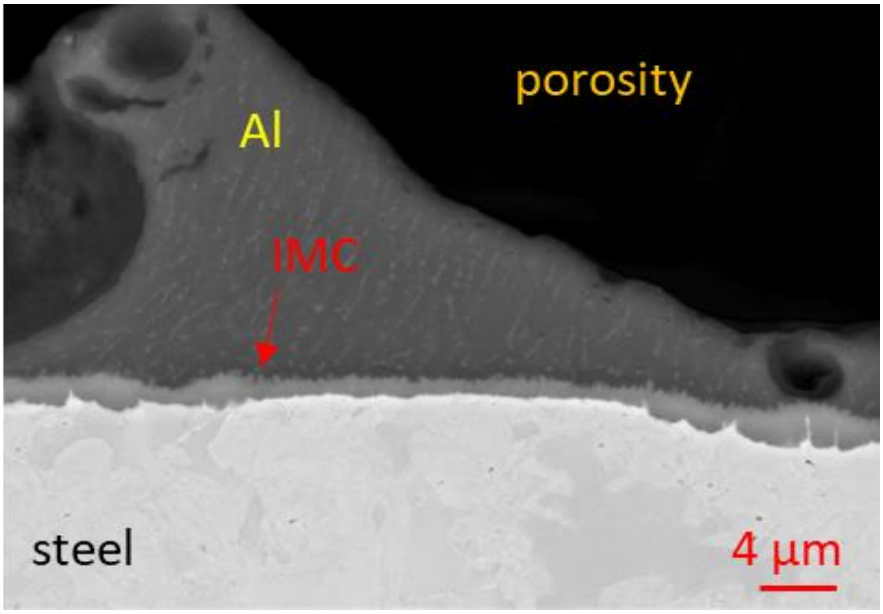

Figure 134 – Close up of cross section of a DP600 – 2AA6061 joint for 200ms pulse 4 kN electrode force and 14 kA with intact intermetallic layer

This predictive model could play a key role in selecting input parameters for RSW system and programme the welding equipment to result in joints with a desirable weld size and targeted strength in a serial production of dissimilar joints.

When conducting regression analysis for developing semi-empirical predictor equation, another factor that needs to be considered is the difference between programmed parameters in the SPATZStudio controller and the real measured values for each point. An example of the difference between set and observed data is presented in Figure 135 for the 200ms pulse. A small variation between the measured and set current with a constant off-set value of 0.4 kA can be noticed. Most obvious between the two data sets shown in Figure 135 is the difference between programmed force value and the measured force value which tends to exhibit slightly higher variation for the extremes of the force range.

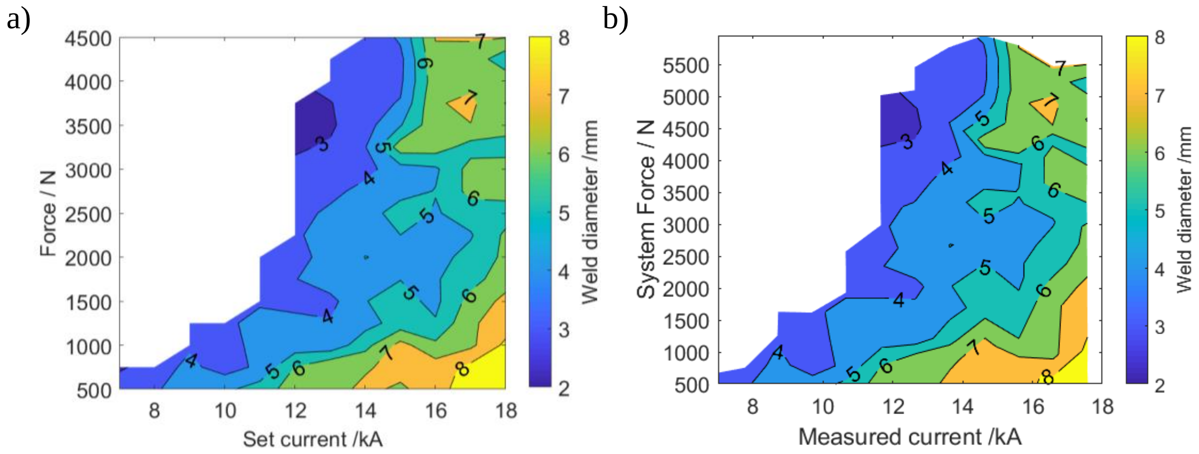

Figure 135 – Differences between set (a) and measured (b) data for a welding pulse of 200ms

Although the overall variation is minimal a regression analysis has been performed to evaluate the impact of the measured data. The new fittings do not exhibit a big variation in both R^2 and MAE as it can be seen in Table 16. Therefore, evidencing that the discrepancies between programmed and measured data are not relevant for the improvement of the model. This brings additional support that porosity and intermetallic thicknesses will have a higher impact on predicted semi-empirical equation.

Table 16 – Comparison of fitting between set and measured data

Fit		Set data	Measured data
Weld size	R^2	0.848	0.854
	MAE	0.097	0.095
TSS	R^2	0.852	0.848
	MAE	0.190	0.191
CTS	R^2	0.610	0.619
	MAE	0.372	0.386

This work has shown and proven that by proper control of input parameters, it is possible to have a rough prediction of both weld size and tensile performance, without the need to perform additional destructive analysis (e.g cross-sections inspection and weld porosity). This is however would be only valid as an approximate guidance to predict expected performance requiring additional validation by introducing additional parameters such as porosity and intermetallic thickness.

Here we show that semi-empirical models can be used to predict the system behaviour as a function of multiple variables. The expected WD, TSS and CTS properties, for a single pulse with welding time of 100ms, as a function of both the welding current and electrode force and results are shown in Figure 136, Figure 137, Figure 138 respectively. Although a small amount of disparity between real data and simulated data can be seen in Figure 136, the model can still reliably provide an accurate description of the system. This is also evident in the TSS model prediction. In CTS mode, since regression factor is low and the reliability of predicted values is only 60% and the predicted values only provide a qualitative guidance. This is evidenced by the predicted performance is much higher which is unphysical and is an artefact from the model as these superior joint strength values are non-existent due the weld size being below 0.5mm. Small sized welds aren’t capable of achieving high failure loads due to the high concentration of stresses over a small area. For 100 ms pulse cycle, the predictor model allowed us to predict weld size and tensile strength with high accuracy.

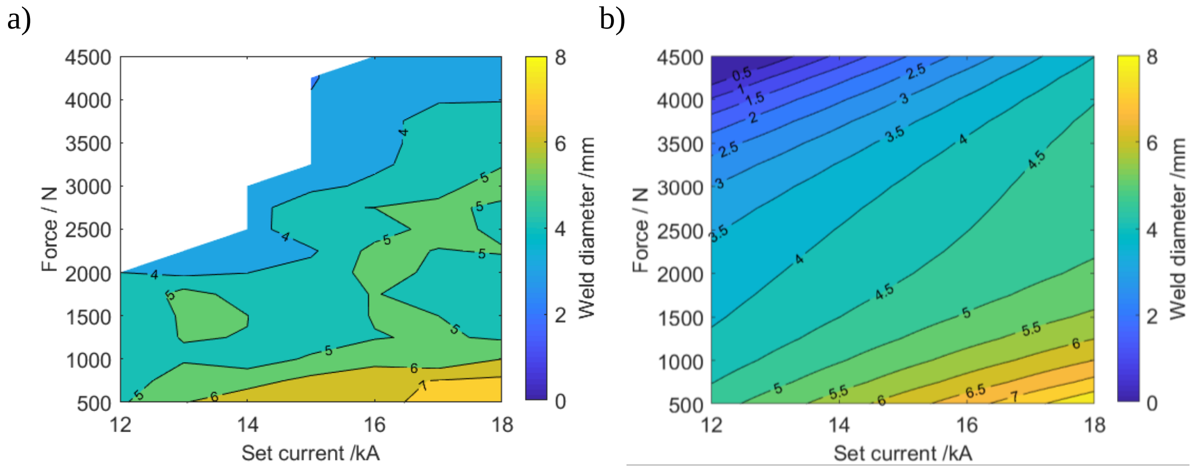

Figure 136 – Difference between real data (a) and simulation (b) of weld diameter size for a single pulse welding of 100 ms

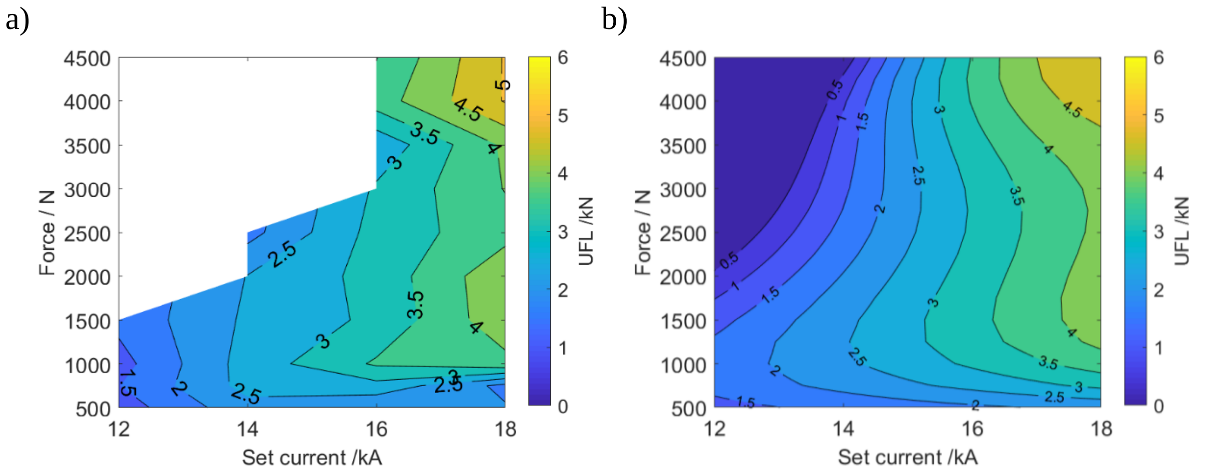

Figure 137 – Difference between real data (a) and simulation (b) of tensile shear strength for a single pulse welding of 100 ms.

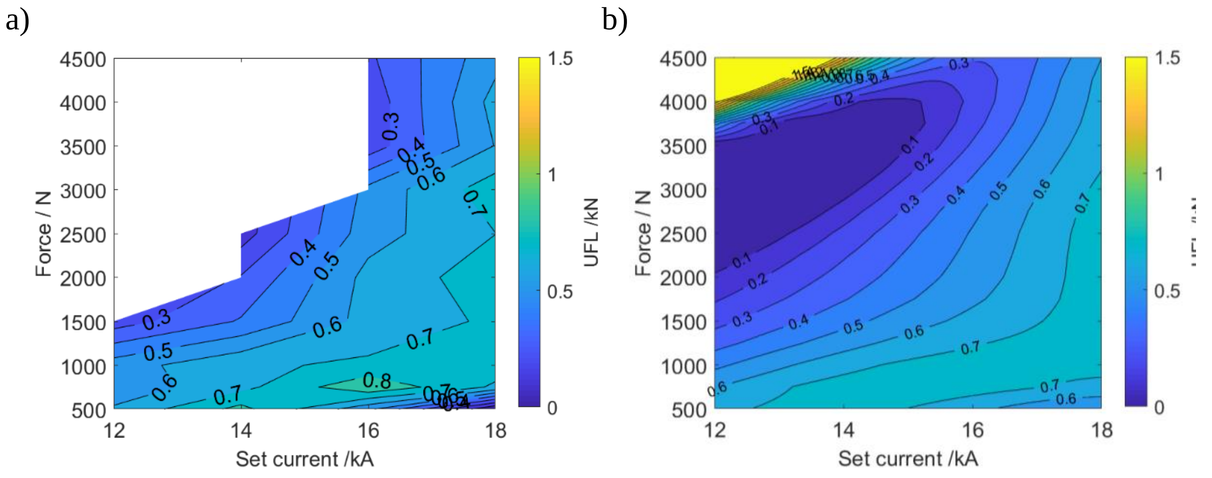

Figure 138 – Difference between real data (a) and simulation (b) of cross tension strength for a single pulse welding of 100 ms

The usefulness of this prediction models allows us to interpolate and extrapolate the data for unexplored regions of RSW system input variables. In a real production line scenario, to obtain a targeted strength for the joints, this predictor equation provides several permutations of input variables which can play a critical role in selecting a preferred set of input parameters such as choosing low cycle time for the benefit of increased production rate, reducing the current magnitude for the benefit of increased electrode life-time or energy savings and reducing the external load for the benefit of reduction in component distortion. Therefore additional unexplored data could be achieved by predicting non-tested conditions in both interpolation (dual pulse of 75ms) and extrapolation (dual pulse of 200ms) conditions as shown in Figure 139, Figure 140 and Figure 141 for weld diameter, tensile strength and cross tension strength. The interpolated weld diameter, for the dual pulse of 75ms (Figure 139.a), as a function of current and electrode force shows no obvious abnormal values, also this dataset is within region of experimentally validated data and therefore most behaviours are controlled within the model. Contrastingly the extrapolated data for the dual pulse of 200ms (Figure 139.b) exhibits some behaviours that require additional investigation. A large area of yellow colour with weld size over 8.5mm which is larger than the electrode diameter of 8mm. This is due to R^2 having an accuracy of only 85% which again reiterates that additional parameters such as porosity and weld splashes etc needs to be considered in the model. Experimental data of the 200ms single pulse, indicated this region tend to be associated with an increased electrode indentation, weld porosity and splash region. Therefore we could anticipate that experimental values for the weld size to be between 8 and 9 mm. The simulated weld sizes of >9mm are unlikely to be experimentally achievable as material expulsion is inevitable and the electrode size is of 8mm, therefore the molten Al can spread beyond 8mm where the electrode force level is sufficient to constrain it. Moreover, to practically achieve a weld size over 9mm a considerable amount of heat will be required, which can have a considerable detrimental effect on the electrode life.

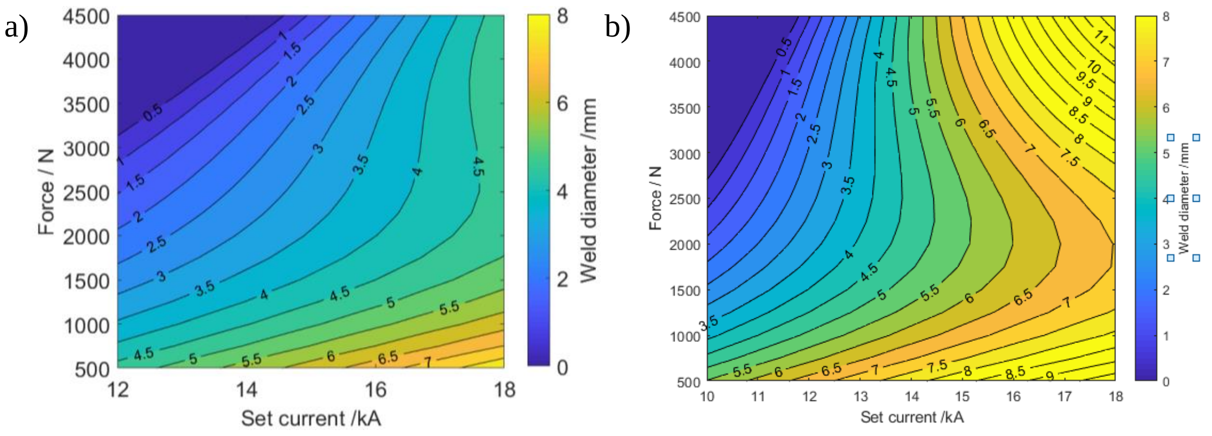

Figure 139 – Simulated weld diameter for dual pulse welding of 75ms (a) and 200ms (b) which is beyond experimental set parameters.

Correlated with this factor is high tensile performance observed in Figure 140 (b) for the simulated double pulse of 200ms. The failure load values situated in the yellow region, for low electrode force, greatly surpasses previous experimental joint expectations. This again reinforces the impact of R^2 for this model and indicates that the impact of unexplored variables and assumptions that need to be considered in the model. For this particular case one needs to consider the impact of the growth of the IMC layer, as this higher amount of heat input is expected to promote thicker (much higher than 2μm) intermetallic layer. This is in agreement of the literature that the behaviour will be affected by the brittle IMC [9], [24], as the layer is now surpassing the 2μm limit [122]. Therefore this indicates that this predicted values need to be validated and include additional variables in the model. It is also can be seen in Figure 139.b that the joints with higher electrode force exhibits negligible joint performance, again this can be attributed to the influence from the unexplored variables. The low TSS values at high electrode forces could be explained by reaching the end of weldability lobe, due to formation of the thick IMC layer as well as a high amount of weld volume loss and high amount of joint distortion. In the case of 75ms dual pulse the interpolated results for shear performance (Figure 140a) of the joints exhibit a holistic appearance similar to previews results. Simulated TSS data for dual pulse of 75ms is higher than that of experimentally observed values for dual pulse of 100ms which suggest that the simulated data overestimates reinforcing that that introducing a porosity parameter in the prediction model is necessary to predict more accurately. On the overall the semi-empirical model exhibits some potential for indicative behaviours for process exploration and indicates new pathways for further development. This allow to expand the exploration work without the need to generate a full indicative matrix for data testing, instead selected regions or points can be carried out to both perform system validation and improvement for model.

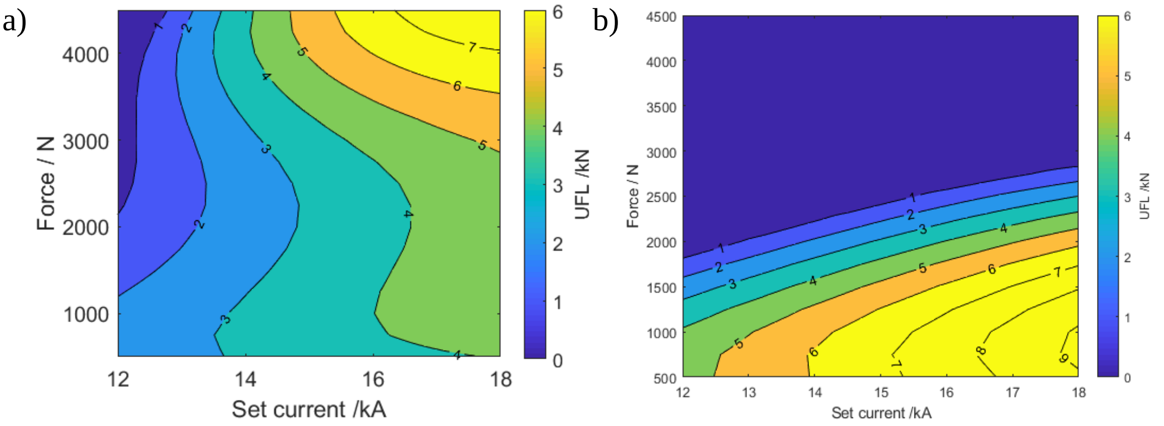

Figure 140 – Simulated tensile shear performance for dual pulse welding of 75ms (a) and 200ms (b)

The results for the CTS prediction are to be used as indicative only as the system predictor accuracy corresponds to a value of R^2 of only 60%, requiring for additional variables for improvement of predictor capability. This can be especially observed on the dual 75ms welding schedule (Figure 141.a), at high electrode forces and at low current, where the predicted performance is much higher which is unphysical and is an artefact from the model as these superior joint strength values are non-existent due the weld size being below 0.5mm (Figure 139.a). Small sized welds aren't capable of achieving high failure loads due to the high stresses over a small area. To improvise the prediction accuracy, since the weld diameters lower than 2mm will not achieve sufficient strength properties, the data corresponding to weld sizes <2mm has been omitted. The new normalized and cross validated results are now shown in Figure 142 and this resembles the behaviour observed experimentally.

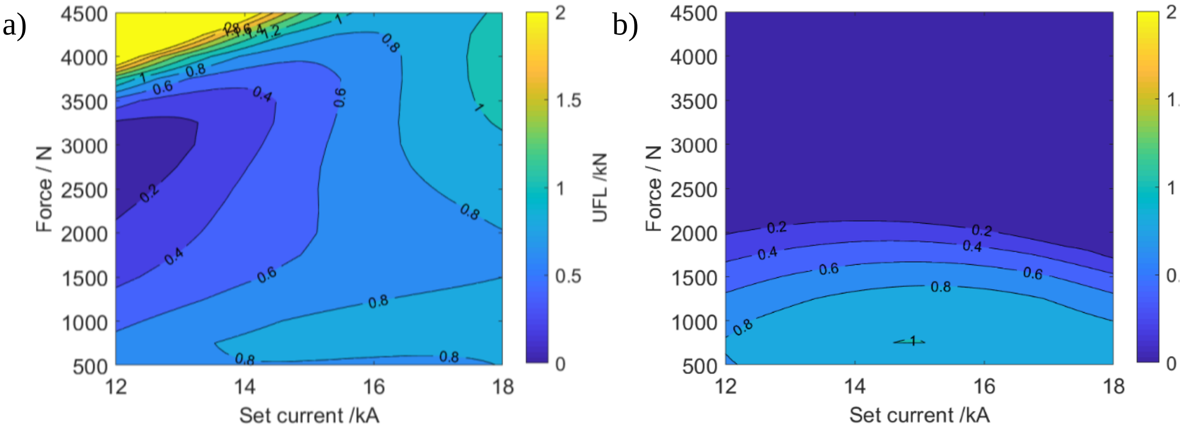

Figure 141 – Simulated cross tension performance for dual pulse welding of 75ms (a) and 200ms (b)

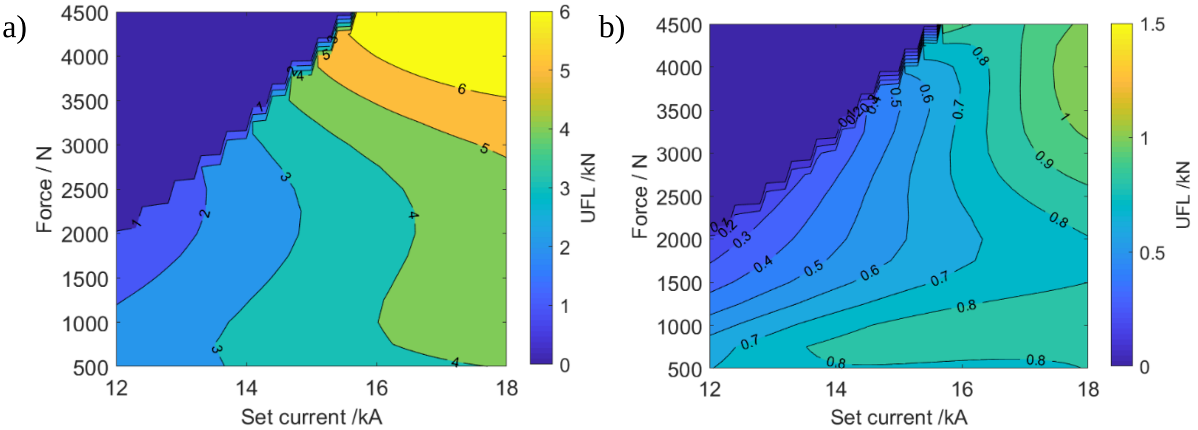

Figure 142 – Correlated results for TSS (a) and CTS (b) results adjusted for a weld size over 2mm

In order to achieve reliable results, which are close to experimental results, it is necessary to impose the following system constrains:

$$\begin{cases} 2mm < WD < 9\,mm \therefore\ TSS, CTS > 0 \\ p > 0 \\ 0 < t < 1s \\ 250\ < F < 5000\,N \\ 0 < I < 18\,kA \end{cases}$$

Where *p* is the number of pulses and needs whole counting numbers, *t* is the time and if it above 1s it would completely destroy the electrode and the system due to excess heat generation and enhanced Al diffusion into Cu electrode, *F* is the electrode force which should not exceed the 5kN as this is the maximum force that the electrodes are able to sustain, and *I* is the welding current which should be < 18kA to avoid severe contamination of electrode from the molten materials. The welding diameter, WD, range is 2 mm and 9mm which corresponds to the minimum diameter to hold two sheets together and the 9mm is the expected maximum achievable weld diameter for the electrodes of 8mm diameter. In a classical resistance welding of similar materials, it is expected that the weld diameter is lower than electrode size, which is associated with the uniform heating in both materials as well as the uniform local melting between the sheets. However this dissimilar joint has a non-uniform heating distribution from the disparity of materials resistance and melting points. As previously stated, the heat generation is predominantly caused by the high electric resistance of steel and the Al/steel interface and this then transferred to the aluminium to form the molten pool and subsequent welding after solidification.

4.2.2. Impact of galvanneal coating

Just like in the case of the GI steel the same experimental approach and 3D data representation is used to visualise the impact of the variations of the different parameters in the Joule heating equation on the joint characteristics/properties. The experimental data for the single pulse and dual pulses of welding of GA steel with Al sheet are presented in Figure 143, Figure 144, Figure 145 As described in previous section, increased time translates into an increased heat input and decreased average resistance, which in turn results in a bigger weld diameter.

Key differences between GA steel -Al joint characteristics compared to GI steel-Al joints are:

- Weldability lobe are larger for GA steel welded with Al.
- The weld diameter is smaller.
- The average measured resistance of the joint assembly is slightly higher than GI steel – Al joint due to thicker Fe-Zn layer in galvanneal steel which induces higher contact resistance. However, this small variation is not sufficient to influence the generated heat significantly at interface as it is not the dominant variable in joule heating when compared to the current.
- Higher electrode indentation (loss of weld thickness) in GA steel – Al joints due to the increased splash associated with brittle Fe-Zn layer.
- Weld sizes for 2x50ms dual pulse joints, shown in Figure 144, lie between their single pulse counterparts of 50ms and 100ms pulses, which is similar to GI steel.
- Weld sizes for 2x100ms dual pulse joints, shown in Figure 145, lie between their single pulse counterparts of 100ms and 200ms pulses, which is again similar to GI steel joints.
- 2x50ms pulse has led to reduced amount of indentation compared with the single pulse counterpart of 100ms. However, for the welding schedule of 2x100ms the observed indentation is very similar to the single pulse of 200ms.

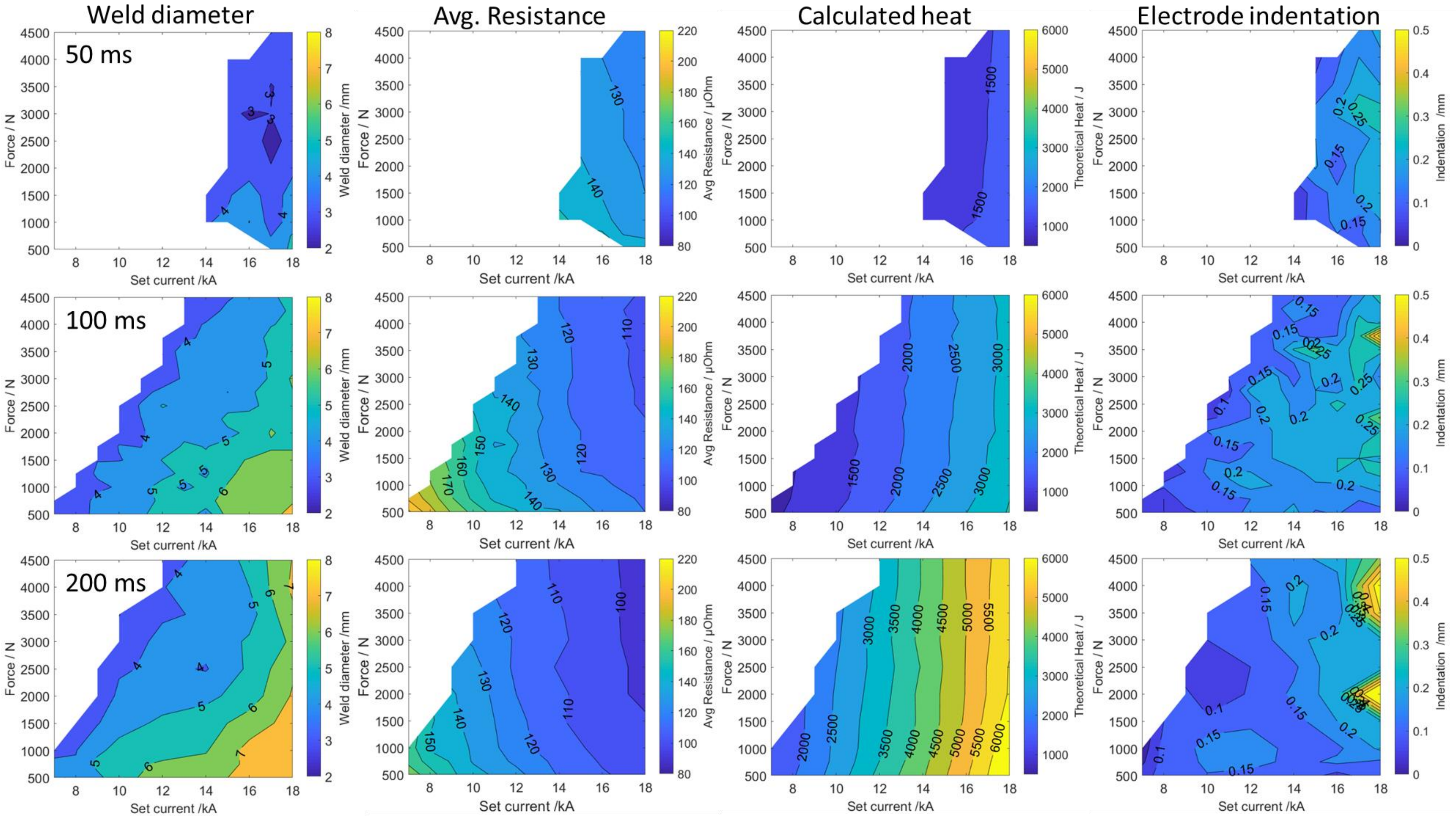

Figure 143 – Comparison of weld diameter, average resistance, calculated heat and electrode indentation for a single pulse of 50ms, 100ms and 200ms for GA steel

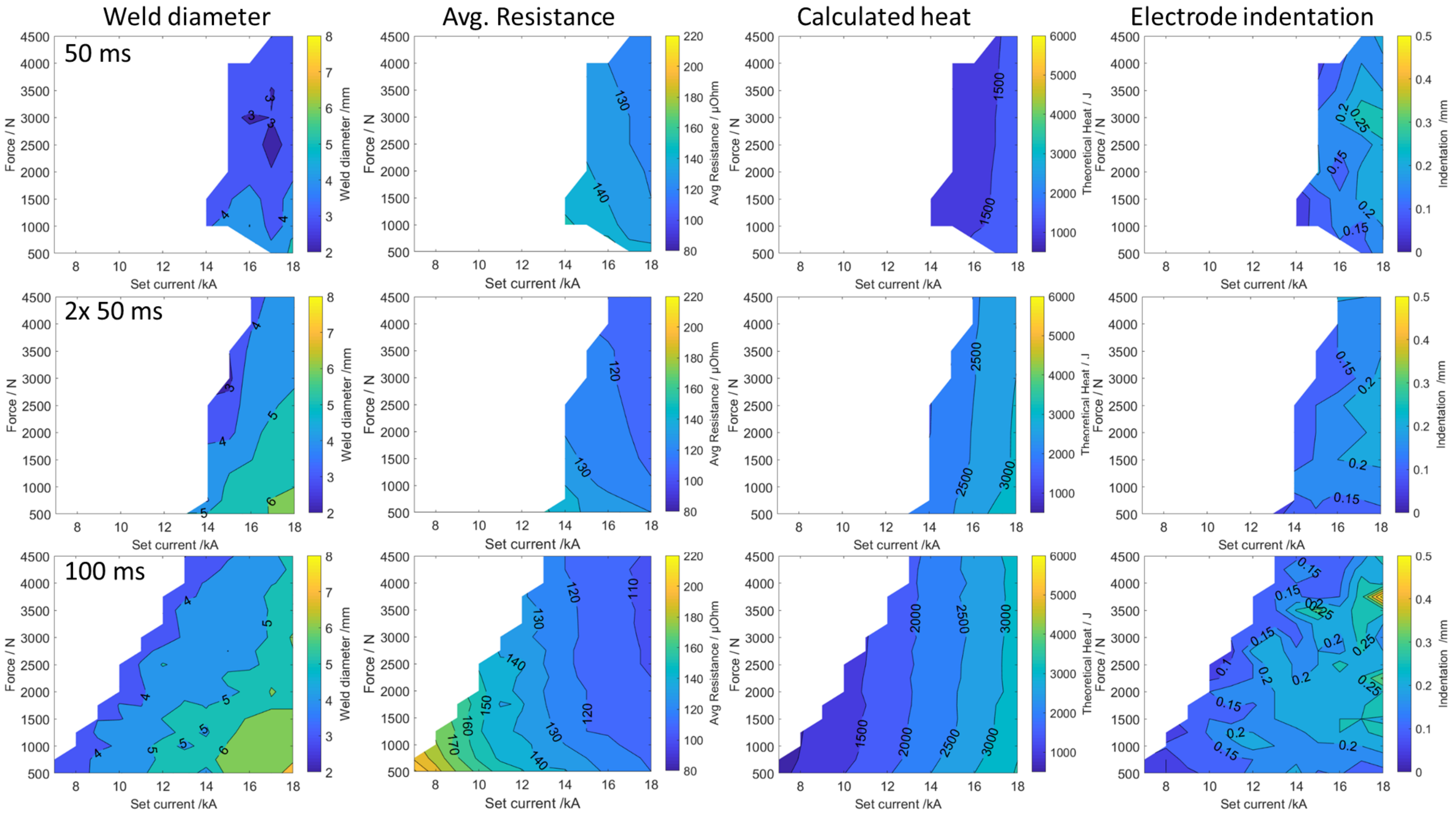

Figure 144 – Comparison of weld diameter, average resistance, calculated heat and electrode indentation for a single pulse of 50ms, 2x50 ms and 100ms for GA steel

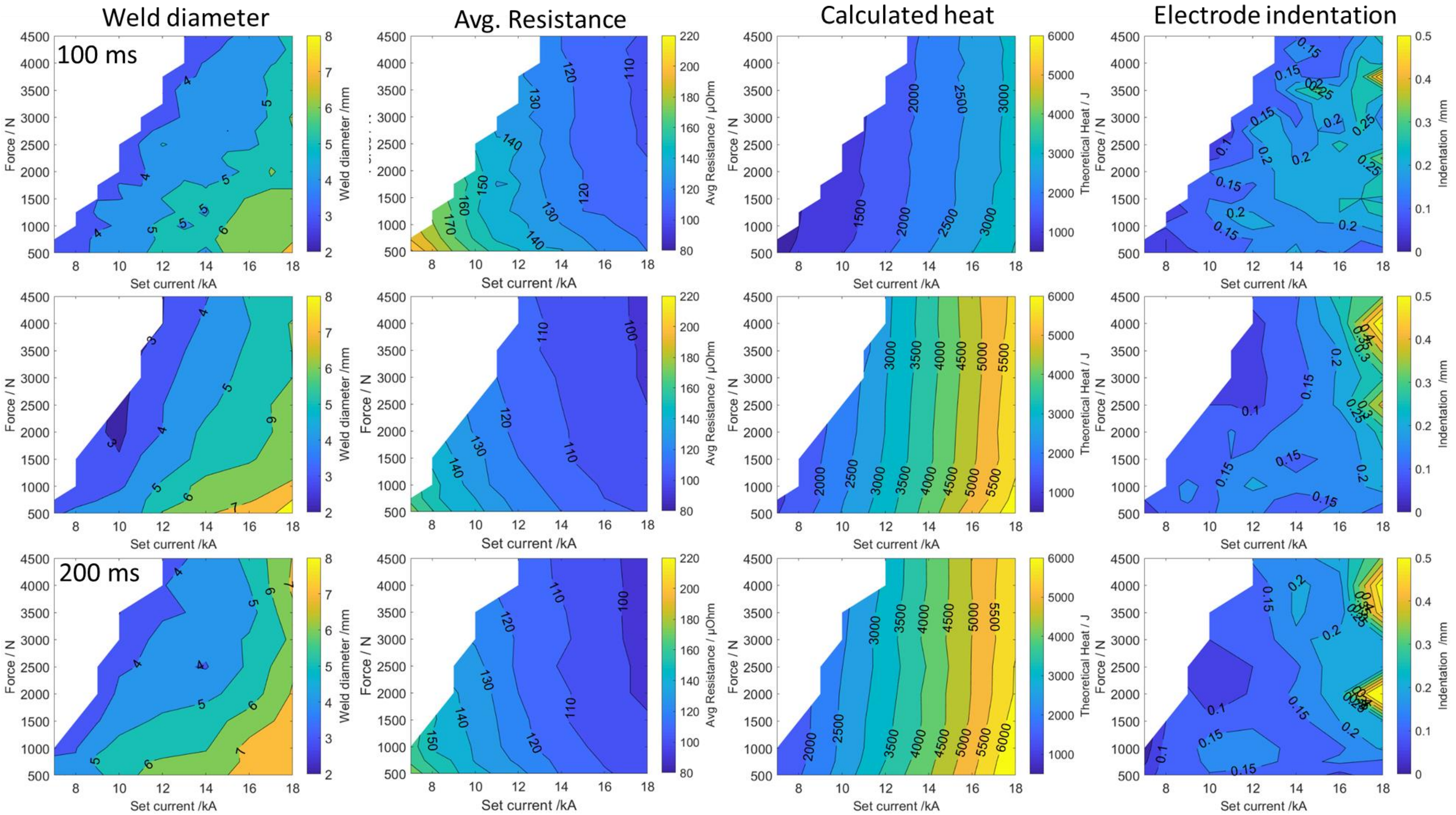

Figure 145 – Comparison of weld diameter, average resistance, calculated heat and electrode indentation for a single pulse of 100ms, 2x100 ms and 200ms for GA steel

Figure 146 is a cross- section of a DP600GA to 2mm AA6061 joint and it is evident that the joint based on GA steel is prone to higher amount of cracking across the cross sections during sample preparation, which is evidenced by the dark in contrast region alongside the joint interface. Additionally, porosity is evident in the joint vicinity which severely affects the weld performance by acting as crack initiation. The crack propagation follows closely, as shown in Fig. 147, alongside the IMC layer but not through the IMC layer itself despite the thicker layer with the thickness of 9µm. This factor is associated with the shrinkage cracks and porosity having a higher impact of the failure mechanism than the IMC layer for this sample.

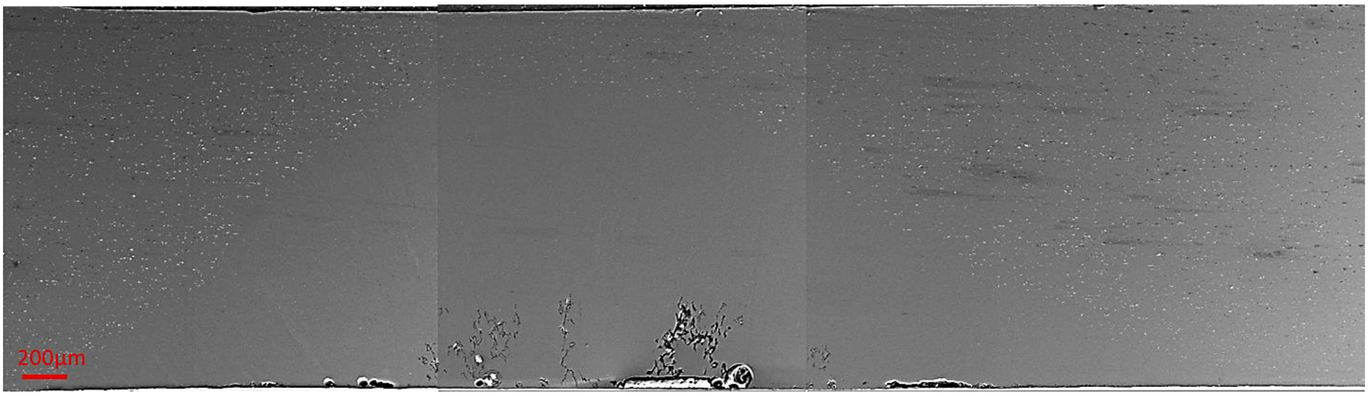

Figure 146 - Cross section of a DP600 GA – 2AA6061 joint for 2x100ms pulse 2 kN electrode force and 14 kA with porosity and weld porosity induced crack. The bottom part of the images is the interface between the AA6061 sheet and DP600 GA joint. Note that DP600 GA steel part of the joint assembly is not shown here.

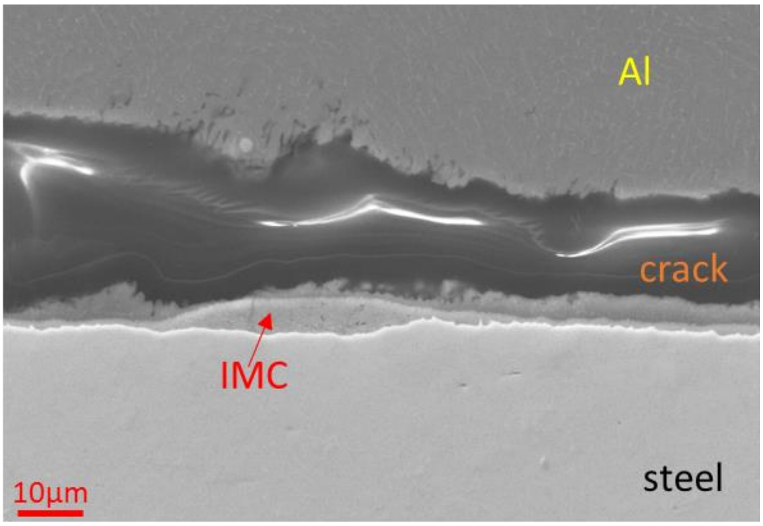

Figure 147 – Close up cross section of a DP600 GA – 2AA6061 joint for 2x100ms pulse with 2 kN electrode force and 14 kA. Crack propagation alongside IMC

The joint performance of the welds were characterized under tensile shear loading and cross-tension loading. To ensure a comparable matrix the same intervals for tensile shear and cross tension specimens were selected. Therefore, testing was performed for current ranging between 12 kA and 18 kA in 2 kA intervals. At each condition, the reported failure loads are the average values of 3 specimens along with the standard deviation. During the specimen preparation for mechanical performance tests, it was observed that joints are much more brittle than those of GI steel-Al joints and several samples broke thus leading to limited results for TSS and CTS conditions. This problem was severe for the specimens of 50ms pulse and therefore the results (Figure 148) are shown only for two conditions (18kA at electrode forces of 500 N and 750 N). The test results clearly show that joint strength is much lower than that of GI steel – Al joint. The standard deviation is higher for 500N load which indicates different levels of porosity in each of three tested samples.

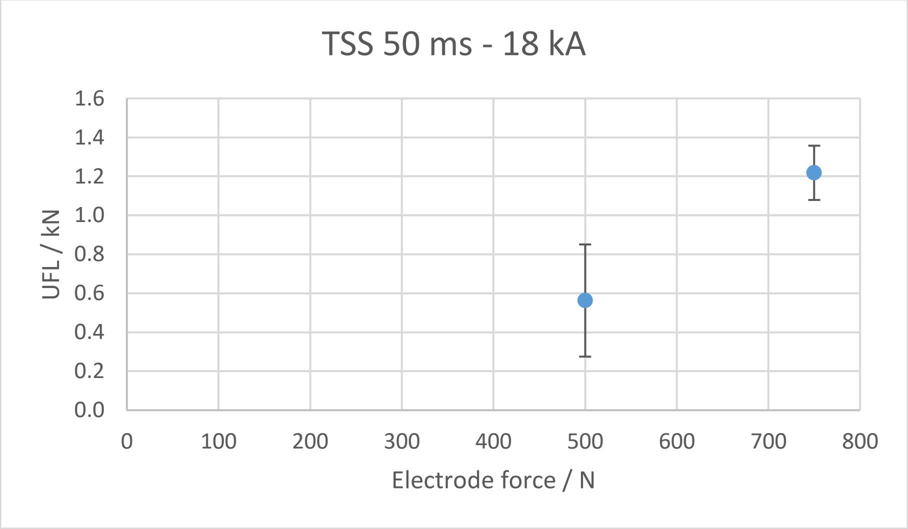

Figure 148 – Tensile failure load of the joints at 18kA and 50ms welding.

The tensile shear data for the remaining welding schedules is presented in Figure 149. These graphs reinforce previous conclusions as smaller welds are associated with the reduced joint performance, which continues to be associated with the high stress concentration over a small area. In addition, the strength performance for joints with dual pulse is similar to that of single pulse. 200ms single pulse weld exhibited a low standard deviation error for electrode forces higher than 1500N. However, this is not indicative of a good reproducibly of results due to a reduced number of samples. The welding schedules of the 100ms single and 50ms dual pulse mirror previous conclusions as the dual pulse promotes higher weld cohesion with lower standard deviation. Since the joints are brittle, it is important to note that additional testing of samples is necessary to make conclusive remarks.

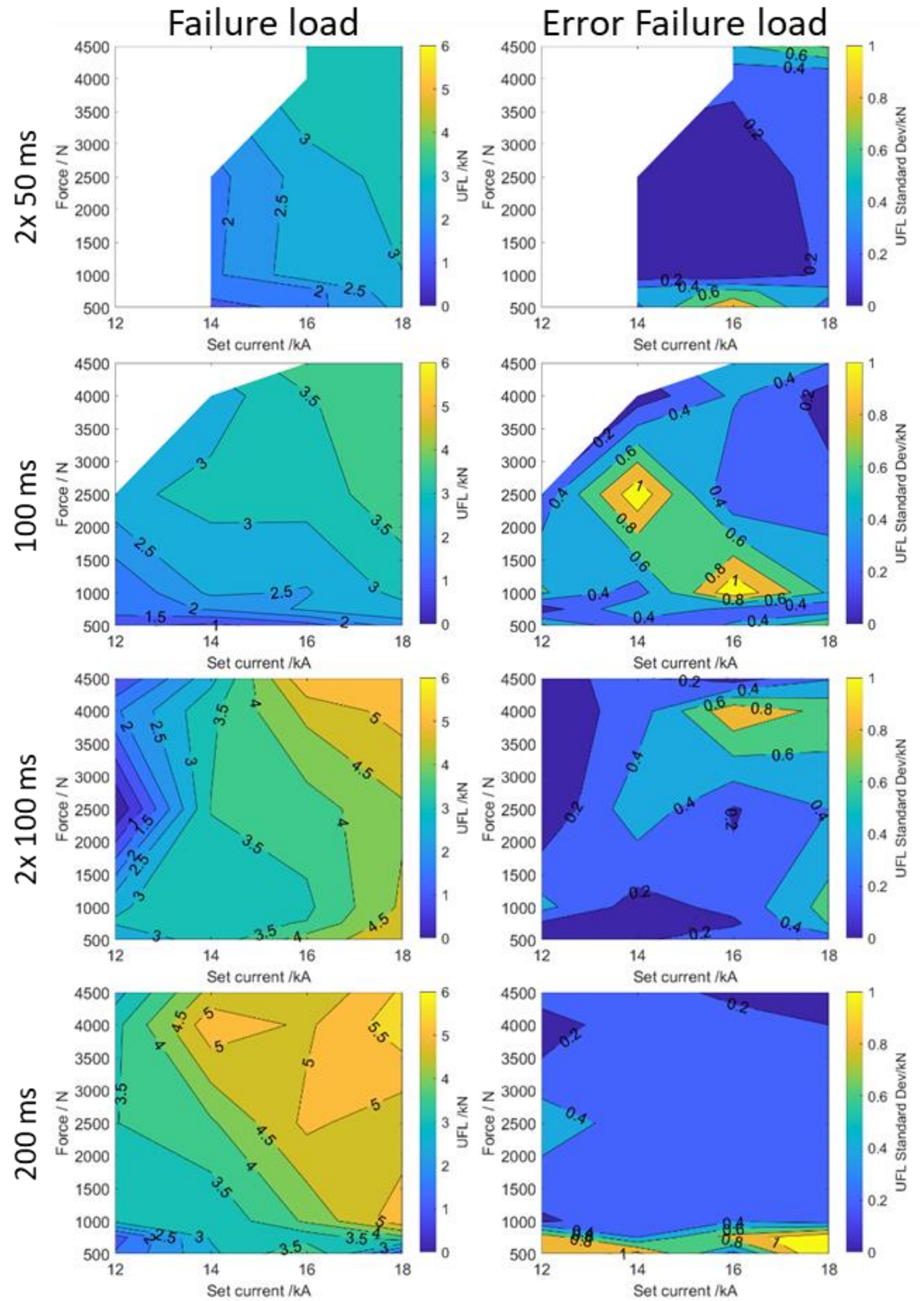

Figure 149 – Tensile shear failure loads and associated error for the joints with the GA steel

Just like the specimens for the TSS failure load, the 50ms welding schedule was only able to produce joints for 18kA and electrode forces of 500 and 750 N as can be seen in Figure 150 under CTS load condition. It is possible to observe how low the achieved performance is, bringing further evidence on the brittleness of these joints. Additionally these results are much lower compared with their GI steel counterparts.

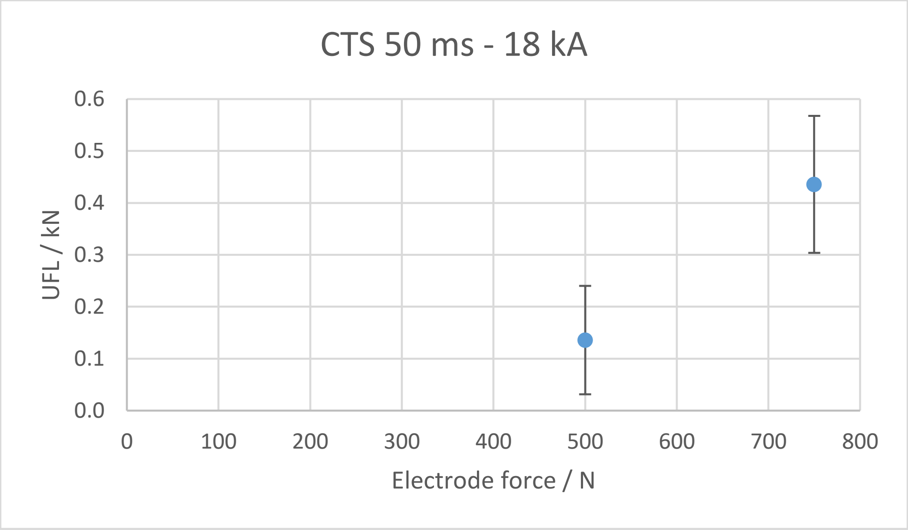

Figure 150 – Cross tension failure load of the joints at 18kA and 50ms welding.

The CTS data are presented in Figure 151. None of the joints of the GA steel exceeded more than 1.5 kN in failure load under cross-tension loading and also results are inconsistent with increased standard deviation and therefore have low reliability. Unlike in GI steel, GA steel surface has thicker Fe-Zn intermetallic layer which promotes thicker Al-Fe based intermetallics in the joint sections, thus leading to cracking at lower cross-tension loads and therefore joint fails at lower loads compared to GI-Al joints.

- The low observed values of TSS and CTS, as well as, the high stand deviations are associated with the increased percentage of Fe in the coating and the thicker IMC layer that results during welding. The low strength performance is in agreement with the literature where it is commonly established knowledge that brittle intermetallic layer >2µm plays a major factor determining failure loads.

- Comparable to previous observations, bigger welds are associated with higher performing joints where the load can be distributed over a larger joint area. Again, areas of higher porosity are associated with the higher standard deviation.

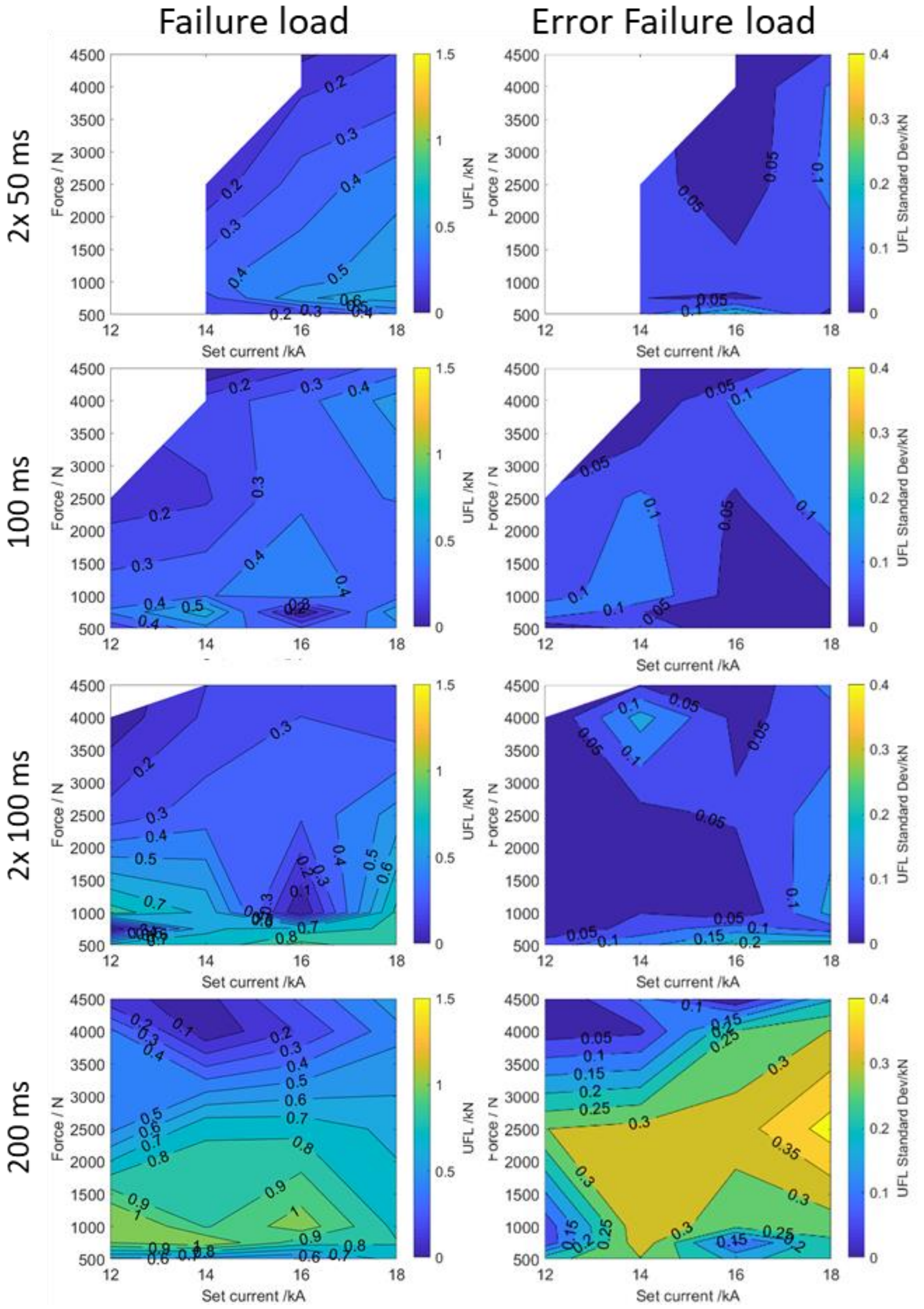

Figure 151 – Cross tension failure loads and associated standard deviation for the GA-Al joints

Similar to data analysis for GI steel – Al joints, Multivariate Polynomial Regression analysis has been performed for GA steel-Al joints by adopting the predictor variables (numbers of pulses; welding time, welding current; electrode force). The data was used to predict different outcomes (weld diameter (WD), Tensile Shear Strength (TSS) and Cross Tension Strength (CTS)). Multiple regressions were performed for all data in order to achieve optimised regression variables by considering the different polynomial orders as it can be observed in Table 17. However, due to a reduced number of specimens most fittings did not pass the cross-validation matrix for the polynomial regression and these data set are denoted with "*" in Table 17.

Even though the dataset for GA-Al joints is relatively small, the Multivariate Polynomial Regression analysis for WD yields higher R^2 with 3rd order polynomial which is similar to GI-Al steel joints. Although the TSS and CTS data could be expressed well with 3rd or 4th order polynomials, but this data did not pass cross-validation matrix and therefore the best fit is considered to be 2nd order polynomial.

Table 17 – Evaluation of model regression for the different polynomial orders by the value of R^2 and Mean Absolute Error (MAE) for the WD, TSS and CTS regressions

Regression	WD		TSS		CTS	
	R^2	**MAE**	**R^2**	**MAE**	**R^2**	**MAE**
Polynomial order 2	**0.898**	**0.066**	**0.826**	**0.159**	**0.752**	**0.551**
Polynomial order 3	**0.909**	**0.063**	**0.877***	**0.123***	**0.804***	**0.561***
Polynomial order 4	**0.876**	**0.070**	**0.899***	**0.113***	**0.855***	**0.497***

*-denotes failed cross-validation matrix

The simplified version of the 3rd order polynomial predictor equation to estimate the weld diameter size (WD) is presented below.

$$WD = 2.70 \times 10^{-3} \times F - 2.65 \times 10^{-7} \times F^2 + 4.57 \times 10^{-5} \times I - 2.05 \times 10^{-7} \times I \times F + 1.40 \times 10^{-11} \times I \times F^2 - 1.28 \times 10^{-8} \times I^2 + 2.41 \times 10^{-12} \times I^2 \times F - 2.50 \times 10^{-2} \times t \times F + 9.69 \times 10^{-7} \times t \times F^2 + 8.41 \times 10^{-3} \times t \times I + 4.88 \times 10^{-7} \times t \times I \times F - 9.08 \times 10^{-8} \times t \times I^2 + 3.10 \times 10^{-2} \times t^2 \times F - 1.69 \times 10^{-2} \times t^2 \times I + 9.37 \times 10^{-8} \times p \times F^2 + 1.87 \times 10^{-8} \times p \times I \times F + 1.08 \times 10^{-9} \times p \times I^2 + 3.42 \times 10^{-3} \times p \times t \times F - 1.23 \times 10^{-3} \times p \times t \times I - 3.89 \times 10^{-4} \times p^2 \times F + 5.83 \times 10^{-5} \times p^2 \times I - 1.76 \times 10^{-2} \times p^3 + 4.96 \times 10^{-13} \times I^3 - 6.91 \times 10^{-12} \times F^3$$

where p is the number of pulses, t is the welding time, I is the current and F is the electrode force. For weld diameter prediction, this semi-empirical model was obtained with an $R^2 = 0.909$ and a Mean Absolute Error (MAE) of 0.063 mm. The higher R^2 can be explained by the increased Fe content within the GA coated layer which allows formation of Al-Fe intermetallic region sooner and faster, allowing a reduced scatter variation of the joints. This can be observed in the goodness fit scatter plot (Figure 152) where it can be seen less scatter in data points between predicted and observed values. Since R^2 values are less than 1, similar to GI steel-Al joint, the semi-empirical model is still not accurate enough to completely describe the system behaviour with various variables, which indicates that there are unaddressed factors (porosity, intermetallic layer thickness etc) which needs to be considered.

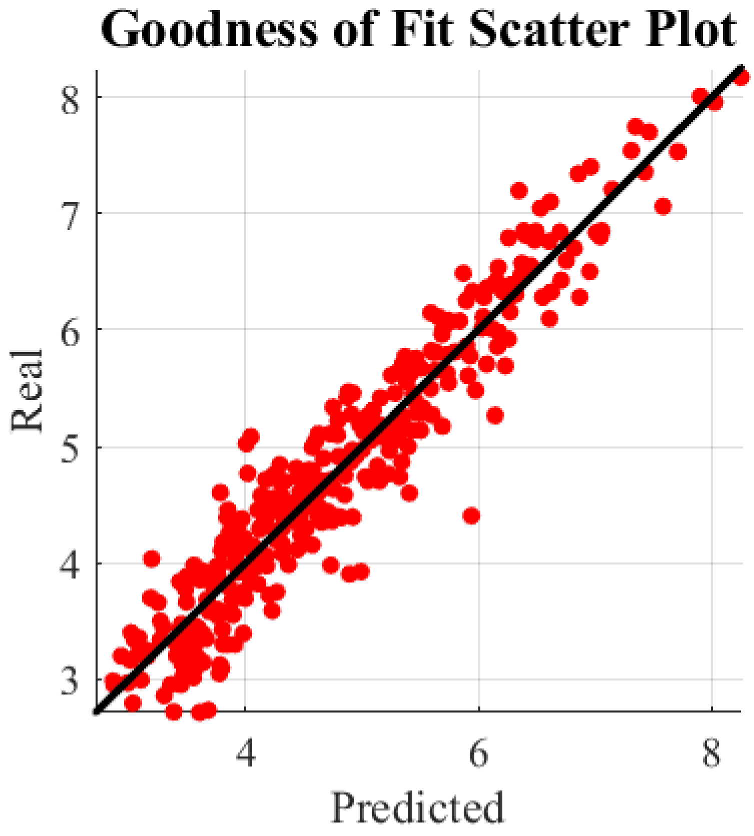

Figure 152 – Goodness of Fit Scatter Plot between Real and Predicted data for weld diameter.

The TSS data could be described well with 2nd order polynomial with R^2 of 0.826 and MAE of 0.159. The semi-empirical predictor equation for tensile failure load given below:

$TSS = 5.39 \times 10^{-4} \times F + 6.69 \times 10^{-4} \times I + 5.20 \times 10^{-8} \times I \times F + 18.2 \times t + 3.98 \times 10^{-4} \times t \times F + 7.69 \times 10^{-4} \times t \times I - 3.05 \times 10^{-4} \times p \times F + 1.99 \times 10^{-4} \times p \times I + 7.21 \times p \times t - 0.66 \times p^2 - 86.2 \times t^2 - 2.78 \times 10^{-8} \times I^2 - 1.37 \times 10^{-7} \times F^2 - 7.52$

The predicated values and the measured values are presented in Figure 153. As can be seen in this figure there are relatively few points with high variation and therefore this model should only be used for indicative purposes

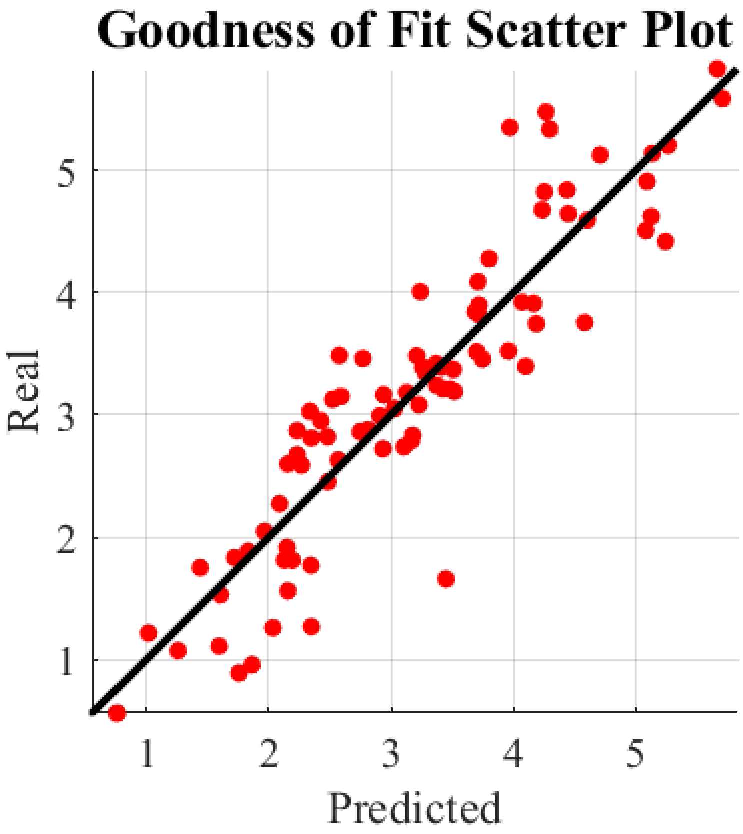

Figure 153 – Goodness of Fit Scatter Plot between Real and Predicted data for the prediction of tensile shear performance

For the cross tension data the prediction equation has been summarized below.

$CTS = 7.03 \times 10^{-6} \times F + 4.27 \times 10^{-6} \times I + 1.52 \times 10^{-8} \times I \times F + 9.43 \times t - 9.46 \times 10^{-4} \times t \times F - 3.80 \times 10^{-4} \times t \times I - 1.03 \times 10^{-4} \times p \times F - 7.61 \times 10^{-6} \times p \times I + 2.13 \times p \times t + 0.10 \times p^2 - 2.81 \times t^2 + 1.73 \times 10^{-9} \times I^2 - 1.92 \times 10^{-8} \times F^2 - 0.62$

Where the obtained R^2 was of 0.752 with a MAE of 0.551 and the analysis presented in Figure 154. Just like for the TSS model equation, this CTS predictor model is not able to achieve high reliable data despite the high R^2 due to the small dataset as well as the high amount of scatter on the goodness fit plot, as expected from an high MAE. Again this model can only be used for indicative purposes only.

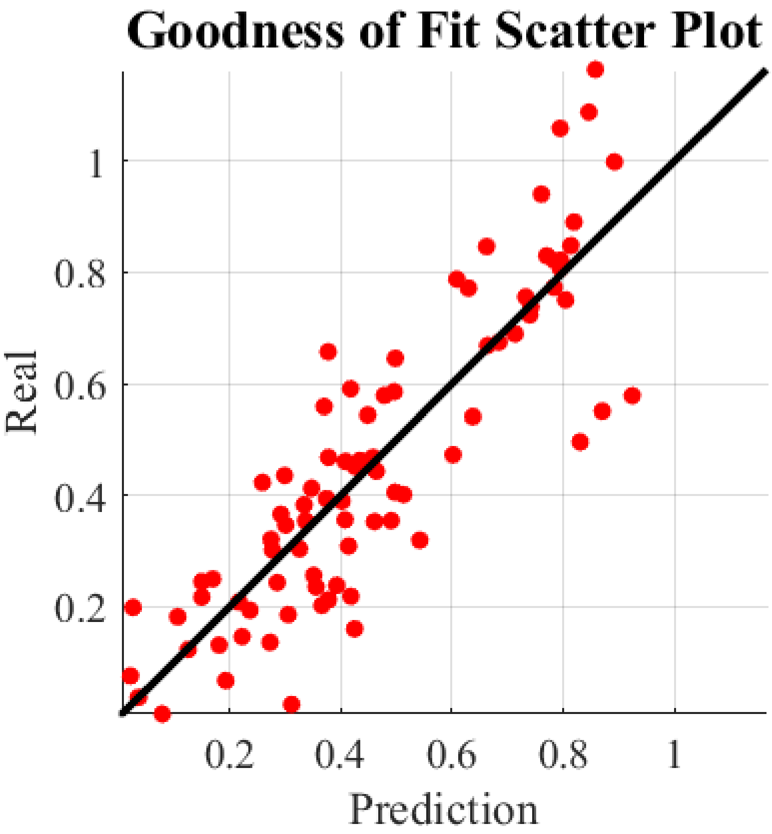

Figure 154 – Goodness of Fit Scatter Plot between Real and Predicted data for the prediction of cross tension performance

In order to confirm the predictor model conclusions, their applicability for the simulation of a single pulse and a welding time of 100ms was performed by varying the two remaining variables. The 3D contour plots for WD, TSS and CTS properties as a function of both the welding current and clamping are shown in Figure 155, Figure 156, Figure 157 respectively. As expected, the fitted equation for WD data is in good agreement with the measured data, which is consistent with the GI steel- Al data set. Although it is possible to observe in Figure 155 a small amount of disparity between real data and simulated data, the model can still provide a good description of the system.

Since the data for TSS and CTS is relatively limited and also there is a need for introducing parameters such as porosity and Al-Fe intermetallic layer kinetics, the data generated by current semi-empirical model should be considered as an indicative data that represents the observed experimental trend rather an accurate representation.

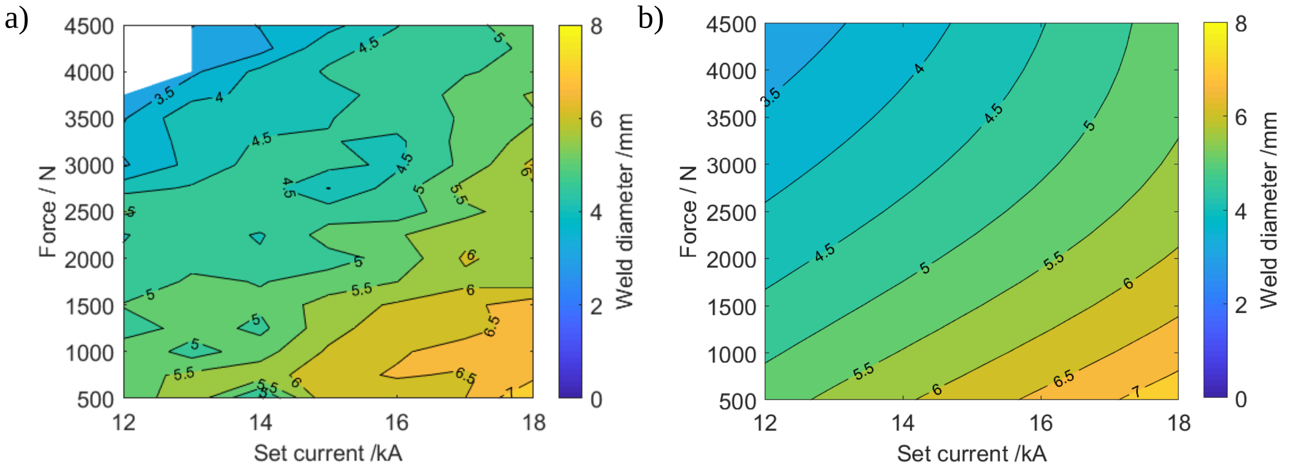

Figure 155 – Difference between real data (a) and simulation (b) of weld diameter size for a single pulse welding of 100 ms

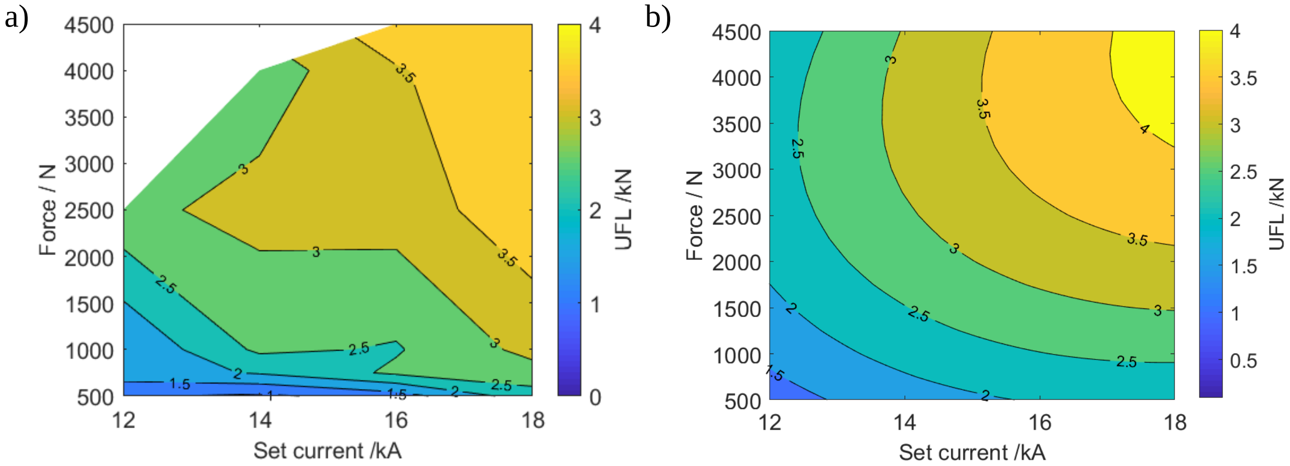

Figure 156 – Difference between real data (a) and simulation (b) of tensile shear strength for a single pulse welding of 100 ms

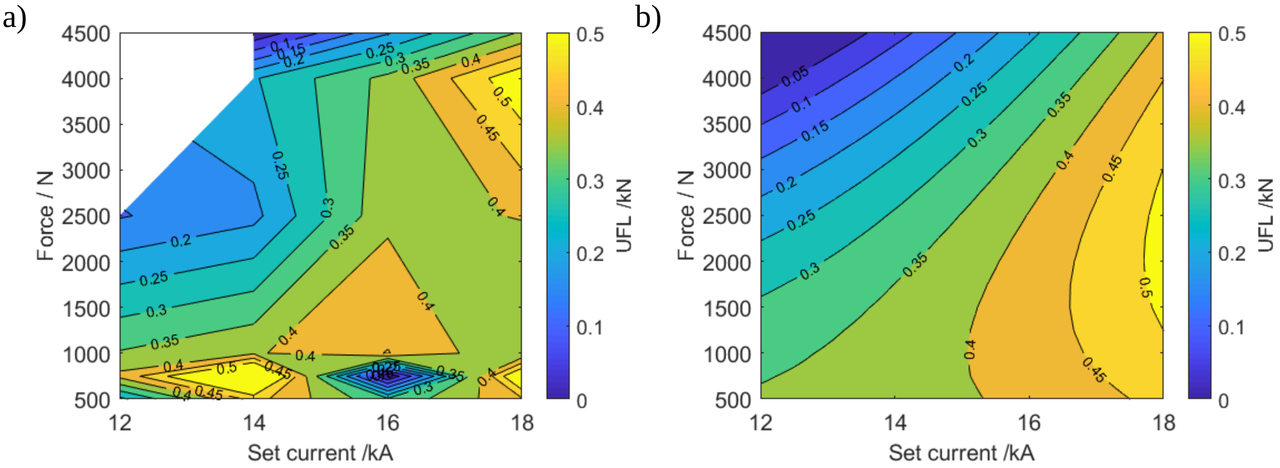

Figure 157 – Difference between real data (a) and simulation (b) of tensile shear strength for a single pulse welding of 100 ms

4.2.3. **Effect of the intermetallic layer**

One of the points highlighted in the thesis is the unavoidable formation of the intermetallic layer which is extremely brittle [9], [24]. The IMC layer is composed of several phases, which due to their different properties and crystal structures will lead to a brittle joint. According to most authors, the main dominant phases are Fe_2Al_5 and Fe_4Al_{13} which can be identified by SEM, as it can be seen in Figure 158. It is evident of the figure the columnar structures of the Fe_2Al_5 followed by the granular Fe_4Al_{13} layer.

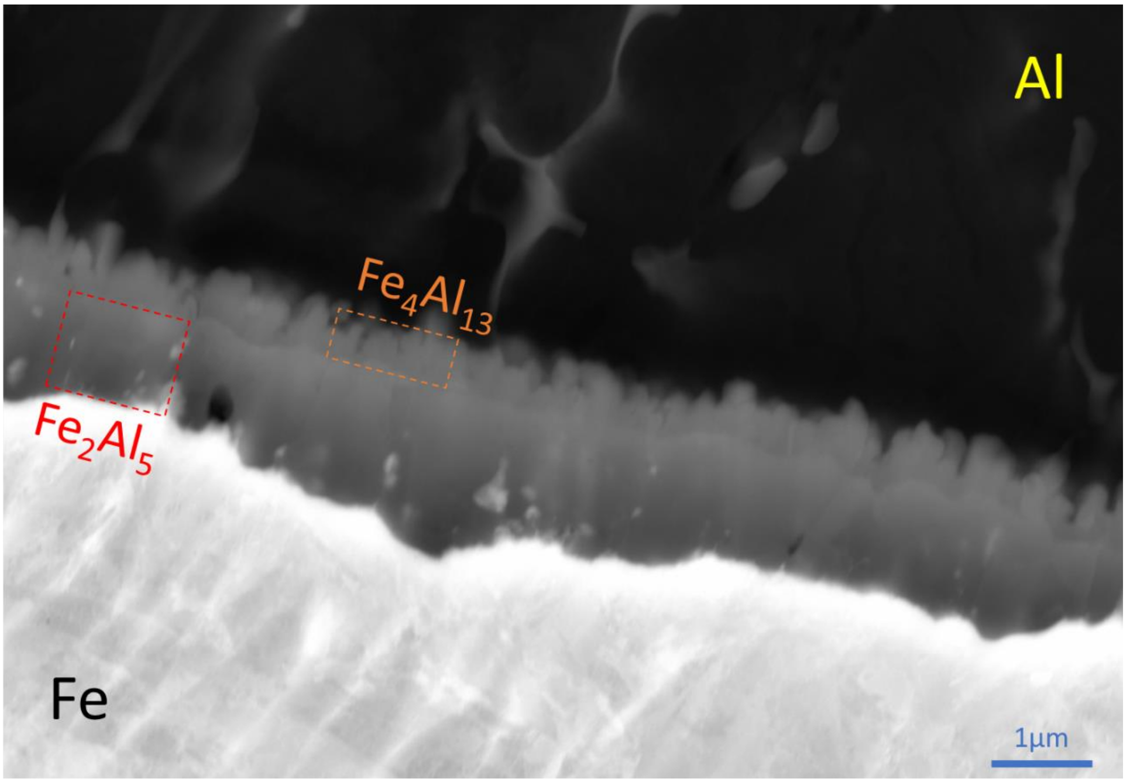

Figure 158 – SEM of a DP600GI-2AA6061 interface for a welding schedule of 100ms

Samples follow the growth mechanism presented by Ding *et al* [36] where the phase formation is initiated by the columnar Fe_2Al_5 becoming the dominant IMC layer. This is subsequently followed by the formation of the Fe_4Al_{13} phase which is Al rich. These three interfaces Fe/Fe_2Al_5; Fe_2Al_5 / Fe_4Al_{13}; Fe_4Al_{13}/Al are described by Bouche [37] and their formation is controlled by Fe diffusion. From the SEM picture, in Figure 158, no additional structures are visually identifiable, however according to Cheng et al [32] under equilibrium conditions there is the formation of $FeAl_2$ and FeAl at the interface between the Fe_2Al_5 and the steel. The $FeAl_2$ and FeAl phase is formed by solid state diffusion of Fe into the Fe_2Al_5. In Figure 158 there is a white in contrast region between Fe and Fe_2Al_5, which is normally associated with charging effects of the topographical profile. To investigate if there are any other phases apart from Fe_2Al_5 and Fe_4Al_{13} present, EDX composition analysis for different elements across the joint was performed as a line scan. Figure 159 presents both the image of the interface and the chemical constituents (at.%) across bulk steel and bulk aluminium. In the image, both Fe_2Al_5 and Fe_4Al_{13} intermetallic layers are clearly visually identifiable based on colour contrast, which is associated with average local atomic mass. Al and Fe rich regions are characterised by dark and bright in contrast respectively. However, compositional analysis allows the identification of 3 zones of interest, characterised by three different slopes, where Zones b and c can unequivocally be identified as Fe_2Al_5 and Fe_4Al_{13} respectively. In Zone a, between Fe and Fe_2Al_5 interfaces, another intermetallic layer consisting of $FeAl_2$ and FeAl phases is identified which is in agreement with Cheng *et al* [32].

The thickness of $FeAl_2$ and FeAl is of 0.8 μm, which is of sub-micron order as described by Springer *et al* [33], whilst the thicknesses of both Fe_2Al_5 and Fe_4Al_{13} are of 1.2 μm and 0.4 μm respectively. It is important to note that the thickness measurement for middle layer is highly accurate, whereas the measure thickness is an over estimation due to wider electron beam envelope.

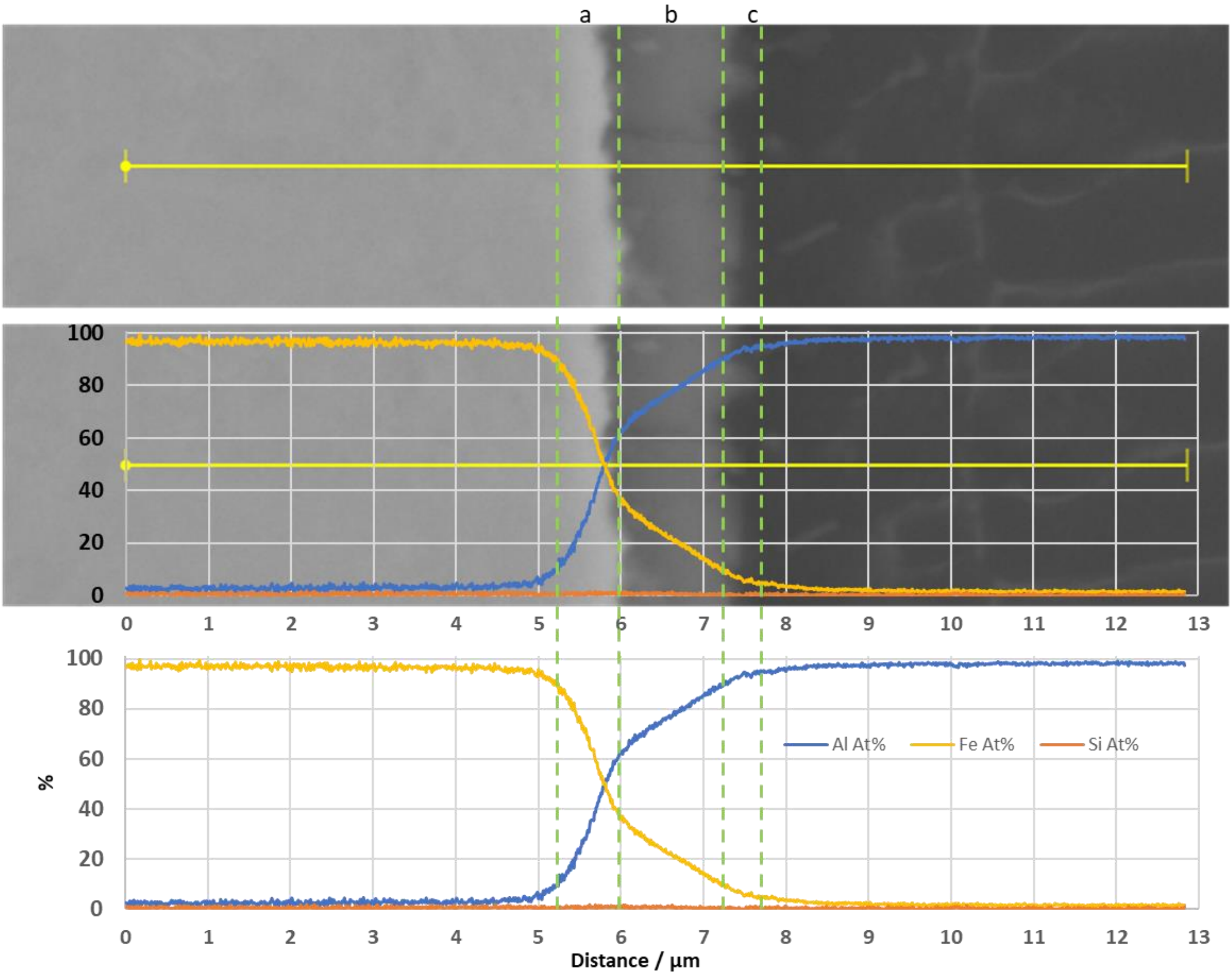

Figure 159 – SEM of a DP600GI-2AA6061 interface for a welding schedule of a dual pulse of 100ms with EDS analysis and layer identification. a) FeAl and $FeAl_2$ b) Fe_2Al_5 and c) Fe_4Al_{13}.

Additionally literature states the impact of Si plays an important role in the Fe-Al intermetallic formation system not only due to the formation of the ternary Al-Fe-Si phases but also for the apparent barrier effect. Joint shown in Figure 159 is also analysed for composition of Si, however is possible to identify that this composition of very close to 0%, as the Si composition does not exceed 2% in the base steel and also Al. On close inspection of the silicon content, as shown in Figure 160, where it is possible to observe an increase in Zone *a* and the transition of the depletion of Si in zone b and further depletion in Zone *c*. This agrees with Lemmens *et al* [44] where Si is observed to segregate at the interface between Fe_2Al_5/Fe_4Al_{13} under equilibrium conditions. It is also suggested that Si may act as a diffusion barrier, then controlling the growth of the intermetallic Fe-Al phases. Lemmens *et al* [45] also proven that Si influences the equilibrium parabolic growth rate of Fe_2Al_5.

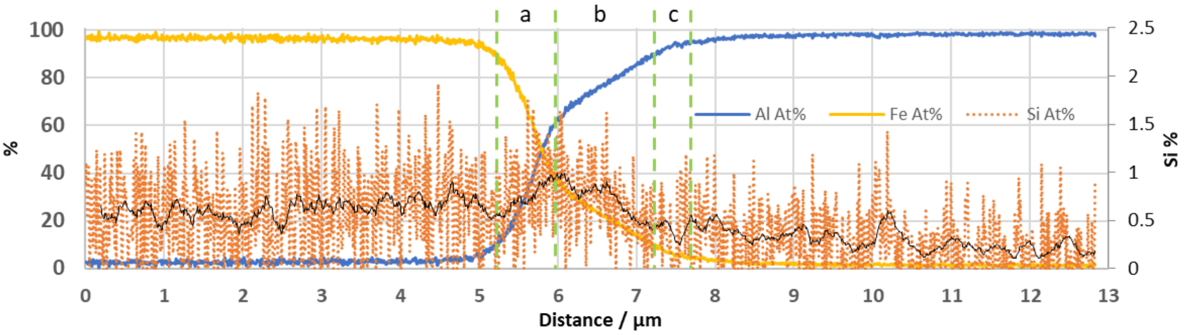

Figure 160 – EDX element analysis of DP600GI-2AA6061 interface for a welding schedule of a dual pulse of 100ms with layer identification. a) FeAl2 and FeAl; b) Fe_2Al_5; c) Fe_4Al_{13}

In sum, in this study the IMC thickness is very small therefore minimising the stress concentration points. Under tensile shear loading since the load is along the IMC thin layer, both ductile Al and Steel parent materials carry the load until deformation, after which crack formation occurs at the porous region between Al and Al_4Fe_{13}. As a result, the joint exhibits higher strength than in cross-tension loading. Contrastingly the low observed cross tension loads again reiterate that the geometrical orientation of intermetallic layer with respect to loading direction plays a critical role in determining the strength. Therefore the joints in CTS loading condition are not able to achieve high failure loads due to crack formation and growth across the joint via brittle intermetallic layer. Once the crack initiates, if it follows the IMC layer, then the local loading mode at the crack tip is cleavage. This has the highest local stress concentration of all loading modes and consequently the lowest joint strengths occur. If it were possible to direct the crack away from the IMC layer (or re-orientate the IMC layer its self), local cleavage loading would be avoided and greater joint strength would be achieved.

It is suggested [127] that it is possible to adapt the Arrhenius equation with a parabolic growth of Fe_2Al_5 phase to predict the thickness of the Fe_2Al_5 intermetallic layer.

$$dZ_{Fe_2Al_5} = \sqrt{\left(\frac{k_0 e^{-\frac{Q}{RT}}}{2t}\right)} dt \tag{3}$$

where K_0 = 0.001 m^2/s and Q = 146.8 kJ/mol are given by Wang *et al* [127] for AA6022 alloy and for aluminium alloy with 0.5% Si addition, K_0 = 0.0321 m^2/s and Q = 186 kJ/mol are given by Yin *et al* [46]. Rearranging equation (3) allows predicting what would be the local temperature for the measured Fe_2Al_5 thickness of 1.2 μm.

$$T = -\frac{Q}{R\,ln\left(\frac{2t\,Z^2}{k_0}\right)} \tag{4}$$

Therefore this would account for the local temperature of 557 ^{o}C according to the constants of Wang *et al* [127] and 631 ^{o}C according to the constants of Yin *et al* [46]. It should be noted that this temperatures are below the melting points of AA6061 which is of 654 ^{o}C. Although solid state formation of Fe-Al IMC is possible >500 ^{o}C and below melting temperature, this is not what is accounting in this process. It is important to note that these constants were obtained under equilibrium conditions and the obtained fit parameters of K_0 and Q are based on the assumption that the measured data follows parabolic behaviour over entire exposure time (1s to 3600s) which is much higher than the maximum current pulse time of 0.2s used in this study.

These conclusions are further supported by the observation of Bouche [37] where parabolic growth kinetics are observed above 30s and much faster kinetics are observed below 30s. Rong *et al* [40] justified that Fe_2Al_5 layer was associated with different governing growth kinetics, where the base of the finger (closer to the Fe) was governed by the interfacial reaction and diffusion, while the tip of the finger (closer to the Al) was only governed by the interfacial reaction. Investigated growth period by Rong *et al* [40] is between 1 s and 9 s and obtained K_0 of 0.084 and Q of 290.1 kJ/mol, which are significantly different from previous constants obtained by Wang *et al* and Yin *et al*. The new constants indicate that the required temperature for the formation of 1.2 μm thick Fe_2Al_5 require is of 1087^{o}C, which now correlate with the temperatures simulated from Wang *et al* [127]. Although the constants obtained from Rong *et al* [40] are for an interaction with pure Al (99.99%) and therefore will have a different kinetics compared with the AA6061 used in this work. The small additions of Si will have a barrier effect which hinders the growth of the IMC layer [49] and decreases the activation energy Q value [45]. Therefore K_0 and Q values for the alloy systems studied here requires in depth investigation.

For the weld shown in Figure 159, for I = 14 kA and time = 200 ms, the joule heat generate is 3.6 kJ by taking into account the contribution of the average system resistance experienced during the welding process. Under these welding conditions, the Al weld nugget volume is measured to be 17.1

mm^3. Therefore on an adiabatic system the weld formation would require 44.2 J to heat the system up to the estimated 1087^oC, from the defined initial temperature of 20^oC, with another 49.3 J for the melting of Al. The total 93.5 J would be consumed for the weld nugget formation, which is 2.6% of total heat calculated in the system. Although the system simulation is different for Wang *et al* [127], homologous conclusions can be obtained, as most of the energy will be used to heat the highest resistance in the system, which is the steel in steel-aluminium dissimilar joint. The amount of heat necessary to heat up the steel is 201.2 J which is much lower than the total heat generated across the joint assembly. Although there is a surplus energy sufficient to melt steel, microstructural investigation shown that there is no evidence of steel melting. This is caused by the heat dissipation via copper contact on the steel and the heat sink behaviour of Al sheet coupled with copper contact that is able to extract most of the heat generated. This is much higher than the indicative 30% heat dissipation from similar steel welding. The differences in thermal conductivity between the two dissimilar materials and the high thermal dissipation properties justify why most of the heat gets dissipated and does not contribute to the weld formation. This is in accordance with the ISO 18595 weld parameter recommendations for similar Al-Al welding, where short high current pulses should be used to minimize the heat loss by dissipation.

4.3. Conclusions

This work has shown that by understanding and controlling the system variables it is possible to improve both size and performance of dissimilar Steel-Al welds. It was experimentally proven that direct control of the electrode force impacts on the heat input of the system therefore controlling the weld size. To enable interpretation of results effectively, a new 3D approach for multivariable representation has been developed and presented in this thesis. This new approach allowed improved data visualisation and analysis by the ease of identifying areas of interest, e.g. improved weld size, for further analysis. All parameters that govern joule heating are shown to strongly influence the weld size and performance. Increased welding time either in single pulse or dual pulse increased the heat input and therefore increased the weld size. For a given pulse duration multiple pulses produced a larger weld size compared to its single pulse counterpart. Under optimal system parameters this work has shown that the weld size can be larger (8.8 mm) than the size of the electrode tip (8 mm).

Similar strengths were obtained in tensile shear strength for single pulse weld, however, the analysis of the standard error deviation show that a multi-pulse approach exhibits higher weld cohesion and stability by exhibiting a lower error, especially for the process windows of high heat inputs. The zones of high heat input correlate with greater amounts of porosity, evidencing the hypothesis that the second pulse would redistribute the melt locally leading to reduced porosity as a result of uniform shrinkage of melt which in turn leads to a more stable weld performance. The welding schedules totalling a welding time of 200 ms further confirm this, as at lower electrode forces the process is consistent with the higher heat input and therefore associated with greater amount of porosity and the standard deviation in strength values is much higher for the single pulse schedule. For the dual pulse of 200 ms (2x100ms) it is possible to observe a lower standard deviation combined with a better performing joint.

Due to the nature of loading in the cross-tension tests, none of the joints exceeded more than 1.5 kN in max failure load. Similar to conclusions obtained for tensile testing, bigger welds are associated with better performing joints where the load can be distributed over a larger area. Again, areas of higher porosity are associated with the higher standard deviation. Also as observed in tensile data, standard deviation for joints with dual pulses is lower, evidencing a greater reproducibility of results. The observed best performing joints are associated with the 200ms single pulse, however the 200ms dual pulse (2x100ms) show similar performance but with improved reproducibility which is of a practical importance for obtaining a BIW structure with uniform weld performance.

During the system exploration and optimization of weld quality a comprehensive data-set was compiled for system parameters and related improvements in weld performance, which enabled us to develop semi-empirical relations between system parameters and weld performance with acceptable reliability for weld size and tensile shear strength. These semi-empirical predictor models play a key role on the prediction of input parameters for the RSW system to achieve a desirable weld size and targeted strength. They also allow the identification of new areas of interest without the need for process exploration, reducing the amount of resources required. This allows the expansion of exploration work without the need to generate a full data set, instead selected regions or points can be carried out to both perform system validation and improvement for the model. Additional factors need to be considered and properly quantified to improve the model reliability and predictor capacities, e.g. weld porosity and IMC layer thickness.

In a real production line scenario, to obtain a targeted strength for the joints, this predictor equation provides several permutations of input variables, which can play a critical role in selecting a preferred set of input parameters such as choosing low cycle time for the benefit of increased production rate, reducing the current magnitude for the benefit of increased electrode life-time or energy savings and reducing the external load (electrode force) for the benefit of reduction in component distortion.

This work has shown, and proven, that by proper control of input parameters, it is possible to achieve a prediction of both weld size and tensile performance, without the need to perform additional destructive analysis (e.g. cross-sections inspection and weld porosity measurement).

The above conclusions are primarily for joints fabricated from galvanised steel and Al alloys sheets. The investigation of the impact of changing the coating of the materials from galvanised to galvanneal steel has shown that the small difference in the composition can impact negatively on the weld size as well as the material properties. The low observed values of TSS and CTS, as well as the high standard deviations in GA steel are associated with the increased percentage of Fe in the coating and the thicker IMC layer that result during welding. The low strength performance is in agreement with the literature where it is commonly established knowledge that brittle intermetallic layer with a thickness of >2μm plays a major factor determining failure loads. Comparable to previous observations, bigger welds are associated with higher performing joints where the load can be distributed over a larger joint area. Again, similar to GI steel, the areas of greater porosity are associated with the larger standard deviations in joints fabricated with GA steel. Since the semi-empirical relations obtained in GA steel joints are based on limited experimental data caused by brittleness of thicker intermetallic layers, the generated empirical equation could be improved with additional work.

Development of a manufacturing process that produces highly reliable joints with sufficient strength is of paramount importance as it will attest the applicability of this process on critical components such as BIW structures. Comparatively a joint of similar AA6061-AA6061 has a TSS and CTS strength of 3.7 kN and 3.3 kN respectively. This work successfully surpasses the TSS strength compared to a similar weld of Al-Al, however the same was not achieved in CTS. The meaning of this is that these joints should be therefore preferentially applied in areas predominantly loaded in shear. Although the CTS value still needs additional improvement, joints exhibiting a CTS strength value greater than around 1kN are generally considered to be of sufficient strength to hold the component together until the adhesive cures during BIW assembly. The CTS values reported in this thesis lie within the expected range of CTS performance, as shown by Hirose *et al* [122] where CTS strength was never able to exceed 2 kN performance.

Therefore this work allows the integration of dissimilar Steel-Aluminium into targeted applications within the BIW. Moreover, the correct combination of RSW with mechanical joining technologies promotes improved component performance by adopting multi-technology joint that minimizes the added weight. In this sense, for crash critical components mechanical fastened technologies are preferable as they would offer higher strength and for the remaining assembly RSW provides lightweight solution together with integrity.

5. Key Summary

This work expands the knowledge associated with challenge of Fe-Al joining by analysing and improving present available technologies in addition to proving a technological milestone on the enablement of Fe-Al RSW spot welding. Similarly these conclusions are divided by the bilateral approach of this work.

- **This work successfully identifies the capabilities and limitations of the individual joining technologies for different material combinations, establishing the necessary guidelines for technology selection culminating in a detailed guidance manual for technology selection.**

Currently no single joining process solution that is able to provide all the requirements to cover all joints in a car body. As highlighted there is a significant trade-off between joint properties, lightweighting, application and cost that need to be considered to secure a decision. Solutions are proposed where minimising the weight or cost of a joint are the main goals, but in these cases often joint strength is inferior. Where joint strength or capability to join a broad range of material combinations is the goal, other technology options are proposed, however disadvantages also need to be considered such as added weight or the requirement to have pre-formed holes within the materials.

- **The impact of hybrid joining (adhesive + joining technology) has also been identified and characterized again establishing the necessary guidelines for technology selection.**

Within the hybrid joining processes, the most lightweight technology is the adhesive alone with the huge concern that of the adhesive properties are only valid after curing, creating an impracticality in the high-volume manufacturing scenario (as the structure would simply fall apart without mechanical joints holding parts in place until the adhesive cures). By use of the multi variable approach this work helps a design engineer with the selection of the most appropriate hybrid solution to achieve the performance targets.

- **This work provides a technological milestone by enabling Fe-Al resistance spot welding by providing a basis for continuation of the understanding how to control the process in order to target the necessary properties, and the development of preliminary semi-empirical models to achieve the targeted properties**

This work has shown that by understanding and controlling the system variables it is possible to improve both size and performance of dissimilar Fe-Al welds. It was experimentally proven that direct control of the electrode force impacts on the heat input of the system therefore controlling the weld size. The new 3D approach for multivariable representation allowed improved data visualisation and analysis by the ease of identifying areas of interest, e.g. improved weld size, for further analysis. All parameters that govern joule heating are shown to strongly influence the weld size and performance.

This work has shown and proven that by proper control of input parameters, it is possible to predict both weld size and tensile performance, without the need to perform additional destructive analysis (e.g. cross-sections inspection and weld porosity measurement).

In a real production line scenario, to obtain a targeted strength for the joints, property predictor equation provides several permutations of input variables, which can play a critical role in selecting a preferred set of input parameters such as choosing low cycle time for the benefit of increased production rate, reducing the current magnitude for the benefit of increased electrode life-time or energy savings and reducing the external load (electrode force) for the benefit of reduction in component distortion.

Development of a manufacturing process that produces highly reliable joints with sufficient strength is of paramount importance as it will attest the applicability of this process on critical components such as BIW structures.

- **This work allows a design engineer to maximise component performance by selecting a multi process joining solution, to maximise the required properties at each point.**

This work allows the integration of dissimilar Steel-Aluminium into targeted applications within the BIW. Moreover, it would be possible to achieve improved component performance by adapting a multi-technology joint whilst minimizing the added weight. In this sense, for crash critical components mechanical fastened technologies are preferable as they would offer higher strength and for the remaining assembly RSW provides lightweight solution together with integrity.

6. Future work

This work offers a vast amount of high level, top view and in-depth know-how for the both the improvement and expansion of material integration into production lines. Due to the reduced amount of both time and resources during PhD, a large range of possibilities for future work have been identified.

In the work related to the mechanical fastening, the comparison of technologies was able to create a guide for technology selection based on cost, accessibility and joint mechanical performance. Nevertheless, this work would benefit from FEA simulation analysis for the different technologies during mechanical testing. This would allow improved interpretation of the force dissipation during loading conditions, trace relation between the different locking mechanisms and possibly propose additional improvements to the different locking mechanisms.

The RSW of dissimilar joints presented the most possibilities for future work in order to expand both the knowledge of the process and the impact on the IMC layer, weld size and weld performance. Therefore, the proposed future work is as follows:

- Increase the number of pulses - This would allow increasing the weld size and improving the weld reliability by reducing the weld porosity. In addition, the impact on the heat affected area could be analysed in relation to the number of pulses.
- For multi-pulse welds, analyse the impact of varying the duration of pulses and waiting interval on the weld properties.
- Perform temperature measurements in order to correlate with calculated heat with the generated temperature in the vicinity of the weld. Subsequently this data could be correlated with the IMC layer.
- Expand the analysis for the weld porosity and IMC layers thickness by using the 3D map representation of data. With these additional parameters, the new dataset would allow to improve quality of the semi-empirical models.
- The analysis of IMC layer thickness as a function of current, time and electro force can be used to derive the growth kinetics of IMC layers formation for temperature cycles <1s. It is important to note that, in the literature, the growth kinetics information such as the activation energy and pre-exponential coefficients are available only for temperature exposure times of > 1s.
- Correlate the IMC layer thickness with the weld performance

- Combine the generated models with FEA analysis for the system in order to perform a holistic model that would correlate the expected size, porosity, IMC layer thickness and weld performance.
- Expand the IMC layer thickness analysis performed on GI steel to GA steel to enable to understand IMC layer characteristics in this system.
- Produce and characterise the interface and performance of RSW joints with a structural adhesive.
- Perform electrode life time analysis to establish how many welds could be achieved prior to electrode cleaning and how many welds an electrode could be used before replacing it with a new one.
- The influence of the thickness of sheets to be joined on weld performance.

7. Bibliography

[1] E. Georgina, “2016 UK Greenhouse Gas Emissions,” 2018.

[2] E. Georgina, “2016 UK GREENHOUSE GAS EMISSIONS, FINAL FIGURES Statistical Release: National Statistics,” 2018.

[3] C. U. Automotive, “Lightweight Vehicles And Powertrain Structures : Uk Opportunities.,” 2013.

[4] Office for Low Emission Vehicles, “Driving the Future Today - A strategy for ultra low emission vehicles in the UK,” 2015.

[5] Z. L. Kowalewski, “Dynamic Properties of Aluminium Alloys,” 2012.

[6] Association Europian Aluminium, “CO 2 & Road Transport,” 2007.

[7] J. V. Ryabov, “Fusion Welding of Aluminium to Steel,” 1969.

[8] M. M. Atabaki, M. Nikodinovski, P. Chenier, J. Ma, M. Harooni, and R. Kovacevic, “Welding of Aluminum Alloys to Steels: An Overview,” *J. Manuf. Sci. Prod.*, vol. 14, no. 2, pp. 59–78, Jan. 2014, doi: 10.1515/jmsp-2014-0007.

[9] L. Shao, Y. Shi, J. K. Huang, and S. J. Wu, “Effect of joining parameters on microstructure of dissimilar metal joints between aluminum and galvanized steel,” *Mater. Des.*, vol. 66, pp. 453–458, 2015, doi: 10.1016/j.matdes.2014.06.026.

[10] Y. Yang *et al.*, “Microstructure, growth kinetics and mechanical properties of interface layer for roll bonded aluminum-steel clad sheet annealed under argon gas protection,” *Vacuum*, vol. 151, pp. 189–196, 2018, doi: 10.1016/j.vacuum.2018.02.018.

[11] M. Pervaiz *et al.*, “Emerging Trends in Automotive Lightweighting through Novel Composite Materials,” *Mater. Sci. Appl.*, vol. 07, no. 01, pp. 26–38, Jan. 2016, doi: 10.4236/msa.2016.71004.

[12] A. I. Taub and A. A. Luo, “Advanced lightweight materials and manufacturing processes for automotive applications,” *MRS Bull.*, vol. 40, no. 12, pp. 1045–1054, Dec. 2015, doi: 10.1557/mrs.2015.268.

[13] A. Rogozhin, M. Gallaher, G. Helfand, and W. McManus, “Using indirect cost multipliers to estimate the total cost of adding new technology in the automobile industry,” *Int. J. Prod. Econ.*, vol. 124, no. 2, pp. 360–368, Apr. 2010, doi: 10.1016/J.IJPE.2009.11.031.

[14] worldautosteel, “ADVANCED HIGH STRENGTH STEEL (AHSS)APPLICATION GUIDELINES,” *Http://Www.Worldautosteel.Org/Projects/Ahssguidelines/Ahss-Application-Guidelines-Version-4.Aspx*, 2009.

[15] J. Shaw, B. Engl, C. Espina, E. C. Oren, and Y. Kawamoto, “ULSAB-Advanced Vehicle Concepts - Materials,” in *SAE Technical Paper Series*, 2010, doi: 10.4271/2002-01-0044.

[16] M. D. Thorpe and H. Adam, “ULSAB-AVC - Overview and Design,” in *SAE Technical Paper Series*, 2010, doi: 10.4271/2002-01-0036.

[17] P. G. Schurter, “ULSAB-Advanced Vehicle Concepts – Manufacturing and Processes,” in *SAE Technical Paper Series*, 2010, doi: 10.4271/2002-01-0039.

[18] J. K. Shin, K. H. Lee, S. I. Song, and G. J. Park, “Automotive door design with the ULSAB concept using structural optimization,” *Struct. Multidiscip. Optim.*, 2002, doi: 10.1007/s00158-002-0189-z.

[19] K. H. Lee, J. K. Shin, S. Il Song, Y. M. Yoo, and G. J. Park, “Automotive door design using structural optimization and design of experiments,” *Proc. Inst. Mech. Eng. Part D J. Automob. Eng.*, 2003, doi: 10.1243/095440703769683261.

[20] P. Furrer, “Aluminium applications in the automotive industry,” in *Joints in Aluminium - INALCO 2007. Proceedings, 10th International Conference, Osaka, Japan, 24-26 Oct.2007*, 2007, pp. 45–52.

[21] F. Henriksson and K. Johansen, “On Material Substitution in Automotive BIWs – From Steel to Aluminum Body Sides,” *Procedia CIRP*, vol. 50, pp. 683–688, Jan. 2016, doi: 10.1016/J.PROCIR.2016.05.028.

[22] M. Tisza and I. Czinege, “Comparative study of the application of steels and aluminium in lightweight production of automotive parts,” *Int. J. Light. Mater. Manuf.*, vol. 1, no. 4, pp. 229–238, Dec. 2018, doi: 10.1016/J.IJLMM.2018.09.001.

[23] G. Meschut, O. Hahn, V. Janzen, and T. Olfermann, “Innovative joining technologies for multi-material structures,” *Weld. World*, vol. 58, no. 1, pp. 65–75, Jan. 2014, doi: https://doi.org/10.1007/s40194-013-0098-3.

[24] L. Agudo *et al.*, “Intermetallic Fe x Al y -phases in a steel/Al-alloy fusion weld,” *J. Mater. Sci.*, vol. 42, no. 12, pp. 4205–4214, Jun. 2007, doi: 10.1007/s10853-006-0644-0.

[25] S. Kobayashi and T. Yakou, “Control of intermetallic compound layers at interface between steel and aluminum by diffusion-treatment,” *Mater. Sci. Eng. A*, vol. 338, no. 1–2, pp. 44–53, Dec. 2002, doi: 10.1016/S0921-5093(02)00053-9.

[26] P. J. Karditsas and M.-J. Baptiste, “Aluminium oxide,” *Therm. Struct. Prop. Fusion Relat. Mater.*, 2012.

[27] T. B. Massalski, H. Okamoto, P. R. Subramanian, and L. Kacprzak, *Binary Alloy Phase Diagrams*, vol. 2. 1990.

[28] A. Van Alboom, B. Lemmens, B. Breitbach, E. De Grave, S. Cottenier, and K. Verbeken,

"Multi-method identification and characterization of the intermetallic surface layers of hot-dip Al-coated steel: FeAl3or Fe4Al13and Fe2Al5or Fe2Al5+x," *Surf. Coatings Technol.*, vol. 324, pp. 419–428, 2017, doi: 10.1016/j.surfcoat.2017.05.091.

[29] C. H. Zhang, S. Huang, J. Shen, and N. X. Chen, "Structural and mechanical properties of Fe-Al compounds: An atomistic study by EAM simulation," *Intermetallics*, vol. 52, pp. 86–91, 2014, doi: 10.1016/j.intermet.2014.04.002.

[30] Y. H. Liu, X. Y. Chong, Y. H. Jiang, R. Zhou, and J. Feng, "Mechanical properties and electronic structures of Fe-Al intermetallic," *Phys. B Condens. Matter*, vol. 506, no. October 2016, pp. 1–11, 2017, doi: 10.1016/j.physb.2016.10.032.

[31] G. Mathers, *The Welding of Aluminium and its Alloys*. 2002.

[32] W. J. Cheng and C. J. Wang, "Study of microstructure and phase evolution of hot-dipped aluminide mild steel during high-temperature diffusion using electron backscatter diffraction," *Appl. Surf. Sci.*, vol. 257, no. 10, pp. 4663–4668, 2011, doi: 10.1016/j.apsusc.2010.12.118.

[33] H. Springer, A. Kostka, E. J. Payton, D. Raabe, A. Kaysser-Pyzalla, and G. Eggeler, "On the formation and growth of intermetallic phases during interdiffusion between low-carbon steel and aluminum alloys," *Acta Mater.*, vol. 59, no. 4, pp. 1586–1600, Feb. 2011, doi: 10.1016/j.actamat.2010.11.023.

[34] M. Rank, P. Gotcu, P. Franke, and H. J. Seifert, "Thermodynamic investigations in the Al-Fe system: Heat capacity measurements of three intermetallic phases," *Intermetallics*, vol. 94, no. January, pp. 73–82, 2018, doi: 10.1016/j.intermet.2017.12.015.

[35] F. Haidara, M. C. Record, B. Duployer, and D. Mangelinck, "Phase formation in Al-Fe thin film systems," *Intermetallics*, vol. 23, pp. 143–147, 2012, doi: 10.1016/j.intermet.2011.11.017.

[36] Z. Ding *et al.*, "Microstructural evolution and growth behavior of intermetallic compounds at the liquid Al/solid Fe interface by synchrotron X-ray radiography," *Mater. Charact.*, vol. 136, no. November 2017, pp. 157–164, 2018, doi: 10.1016/j.matchar.2017.12.024.

[37] K. Bouché, F. Barbier, and A. Coulet, "Intermetallic compound layer growth between solid iron and molten aluminium," *Mater. Sci. Eng. A*, vol. 249, no. 1–2, pp. 167–175, Jun. 1998, doi: 10.1016/S0921-5093(98)00573-5.

[38] A. Coulet, K. Bouche, F. Marinelli, and F. Barbier, "Growth kinetics of intermediate compounds at a planar solid-solid or solid-liquid interface by diffusion mechanisms," *J. Appl. Phys.*, vol. 82, no. 12, pp. 6001–6007, Dec. 1997, doi: 10.1063/1.366465.

[39] A. Bouayad, C. Gerometta, A. Belkebir, and A. Ambari, "Kinetic interactions between solid iron and molten aluminium," *Mater. Sci. Eng. A*, vol. 363, no. 1–2, pp. 53–61, Dec. 2003, doi: 10.1016/S0921-5093(03)00469-6.

[40] J. Rong, Z. Kang, S. Chen, D. Yang, J. Huang, and J. Yang, “Growth kinetics and thickness prediction of interfacial intermetallic compounds between solid steel and molten aluminum based on thermophysical simulation in a few seconds,” *Mater. Charact.*, vol. 132, no. June, pp. 413–421, 2017, doi: 10.1016/j.matchar.2017.09.012.

[41] H. . Shahverdi, M. . Ghomashchi, S. Shabestari, and J. Hejazi, “Microstructural analysis of interfacial reaction between molten aluminium and solid iron,” *J. Mater. Process. Technol.*, vol. 124, no. 3, pp. 345–352, Jun. 2002, doi: 10.1016/S0924-0136(02)00225-X.

[42] S. Chen, D. Yang, M. Zhang, J. Huang, and X. Zhao, “Interaction Between the Growth and Dissolution of Intermetallic Compounds in the Interfacial Reaction Between Solid Iron and Liquid Aluminum,” *Metall. Mater. Trans. A*, vol. 47, no. 10, pp. 5088–5100, Oct. 2016, doi: 10.1007/s11661-016-3667-4.

[43] Z. Ding, Q. Hu, W. Lu, S. Sun, M. Xia, and J. Li, “In situ observation on the formation of intermetallics compounds at the interface of liquid Al/solid Ni,” *Scr. Mater.*, vol. 130, pp. 214–218, Mar. 2017, doi: 10.1016/J.SCRIPTAMAT.2016.12.010.

[44] B. Lemmens *et al.*, “Atom probe tomography of intermetallic phases and interfaces formed in dissimilar joining between Al alloys and steel,” *Mater. Charact.*, vol. 120, pp. 268–272, 2016, doi: 10.1016/j.matchar.2016.09.008.

[45] B. Lemmens, H. Springer, I. De Graeve, J. De Strycker, D. Raabe, and K. Verbeken, “Effect of silicon on the microstructure and growth kinetics of intermetallic phases formed during hot-dip aluminizing of ferritic steel,” *Surf. Coatings Technol.*, vol. 319, pp. 104–109, 2017, doi: 10.1016/j.surfcoat.2017.03.040.

[46] F. YIN, M. ZHAO, Y. LIU, W. HAN, and Z. LI, “Effect of Si on growth kinetics of intermetallic compounds during reaction between solid iron and molten aluminum,” *Trans. Nonferrous Met. Soc. China*, vol. 23, no. 2, pp. 556–561, Feb. 2013, doi: 10.1016/S1003-6326(13)62499-1.

[47] W. J. Cheng and C. J. Wang, “Effect of silicon on the formation of intermetallic phases in aluminide coating on mild steel,” *Intermetallics*, vol. 19, no. 10, pp. 1455–1460, 2011, doi: 10.1016/j.intermet.2011.05.013.

[48] W. Jiang, Z. Fan, G. Li, X. Liu, and F. Liu, “Effects of hot-dip galvanizing and aluminizing on interfacial microstructures and mechanical properties of aluminum/iron bimetallic composites,” *J. Alloys Compd.*, vol. 688, pp. 742–751, 2016, doi: 10.1016/j.jallcom.2016.07.085.

[49] N. Takata, M. Nishimoto, S. Kobayashi, and M. Takeyama, “Morphology and formation of Fe-Al intermetallic layers on iron hot-dipped in Al-Mg-Si alloy melt,” *Intermetallics*, vol. 54, pp. 136–142, 2014, doi: 10.1016/j.intermet.2014.06.003.

[50] H. Springer, A. Szczepaniak, and D. Raabe, “On the role of zinc on the formation and growth

of intermetallic phases during interdiffusion between steel and aluminium alloys," *Acta Mater.*, vol. 96, no. 4, pp. 203–211, 2015, doi: 10.1016/j.actamat.2015.06.028.

[51] J. Yang, Y. L. Li, H. Zhang, W. Guo, and Y. Zhou, "Control of interfacial intermetallic compounds in Fe-Al joining by Zn addition," *Mater. Sci. Eng. A,* vol. 645, pp. 323–327, 2015, doi: 10.1016/j.msea.2015.08.036.

[52] M. Yousaf, J. Iqbal, and M. Ajmal, "Variables affecting growth and morphology of the intermetallic layer (Fe2Al5)," *Mater. Charact.*, vol. 62, no. 5, pp. 517–525, 2011, doi: 10.1016/j.matchar.2011.03.004.

[53] Y. Zheng, F. Wang, T. Ai, and C. Li, "Structural, elastic and electronic properties of B2-type modified by ternary additions FeAl-based intermetallics: First-principles study," *J. Alloys Compd.*, vol. 710, pp. 581–588, 2017, doi: 10.1016/j.jallcom.2017.03.308.

[54] M. Israel, M. Israel, R. Mauermann, and J. Schellnock, "Thick sheet clinching," *Adv. Shipp. Ocean Eng. ASOE,* vol. 2, no. Nr.1, pp. 1–10, 2013.

[55] C.-J. Lee, J.-Y. Kim, S.-K. Lee, D.-C. Ko, and B.-M. Kim, "Design of mechanical clinching tools for joining of aluminium alloy sheets," *Mater. Des.*, vol. 31, no. 4, pp. 1854–1861, 2010, doi: 10.1016/j.matdes.2009.10.064.

[56] K. I. Mori, N. Bay, L. Fratini, F. Micari, and A. E. Tekkaya, "Joining by plastic deformation," *CIRP Ann. - Manuf. Technol.*, vol. 62, no. 2, pp. 673–694, Jan. 2013, doi: 10.1016/j.cirp.2013.05.004.

[57] S. Coppieters, P. Lava, S. Baes, H. Sol, P. Van Houtte, and D. Debruyne, "Analytical method to predict the pull-out strength of clinched connections," *Thin-Walled Struct.*, vol. 52, pp. 42–52, 2012, doi: 10.1016/j.tws.2011.12.002.

[58] J. MUCHA, L. KAŠČÁK, and E. SPIŠÁK, "Joining the car-body sheets using clinching process with various thickness and mechanical property arrangements," *Arch. Civ. Mech. Eng.*, vol. 11, no. 1, pp. 135–148, Jan. 2011, doi: 10.1016/S1644-9665(12)60179-4.

[59] K. Mori, Y. Abe, and T. Kato, "Mechanism of superiority of fatigue strength for aluminium alloy sheets joined by mechanical clinching and self-pierce riveting," *J. Mater. Process. Technol.*, vol. 212, no. 9, pp. 1900–1905, Sep. 2012, doi: 10.1016/j.jmatprotec.2012.04.017.

[60] M. Oudjene, L. Ben-Ayed, A. Delamézière, and J.-L. L. Batoz, *Shape optimization of clinching tools using the response surface methodology with Moving Least-Square approximation*, vol. 209, no. 1. 2009, pp. 289–296.

[61] X. He *et al.*, "Investigations of strength and energy absorption of clinched joints," *Comput. Mater. Sci.*, vol. 94, pp. 58–65, 2014, doi: 10.1016/j.commatsci.2014.01.056.

[62] F. Lambiase and A. Di Ilio, "An experimental study on clinched joints realized with different

dies," *Thin-Walled Struct.*, vol. 85, pp. 71–80, 2014, doi: 10.1016/j.tws.2014.08.004.

[63] C.-J. Lee, J.-Y. Kim, S.-K. Lee, D.-C. Ko, and B.-M. Kim, "Parametric study on mechanical clinching process for joining aluminum alloy and high-strength steel sheets," *J. Mech. Sci. Technol.*, vol. 24, pp. 123–126, 2010.

[64] Y. Abe, T. Kato, K. Mori, and S. Nishino, "Mechanical clinching of ultra-high strength steel sheets and strength of joints," *J. Mater. Process. Technol.*, vol. 214, no. 10, pp. 2112–2118, 2014, doi: 10.1016/j.jmatprotec.2014.03.003.

[65] C.-J. J. Lee, J.-M. M. Lee, H.-Y. Y. Ryu, K.-H. H. Lee, B.-M. M. Kim, and D.-C. C. Ko, "Design of hole-clinching process for joining of dissimilar materials - Al6061-T4 alloy with DP780 steel, hot-pressed 22MnB5 steel, and carbon fiber reinforced plastic," *J. Mater. Process. Technol.*, vol. 214, no. 10, pp. 2169–2178, 2014, doi: 10.1016/j.jmatprotec.2014.03.032.

[66] F. Lambiase, "Clinch joining of heat-treatable aluminum AA6082-T6 alloy under warm conditions," *J. Mater. Process. Technol.*, vol. 225, pp. 421–432, Nov. 2015, doi: 10.1016/J.JMATPROTEC.2015.06.022.

[67] Y. Zhang, H. Shan, Y. Li, J. Guo, Z. Luo, and C. Y. Ma, "Joining aluminum alloy 5052 sheets via novel hybrid resistance spot clinching process," *Mater. Des.*, vol. 118, pp. 36–43, 2017, doi: 10.1016/j.matdes.2017.01.017.

[68] J. Osten, P. Söllig, M. Reich, J. Kalich, U. Füssel, and O. Kessler, "Softening of High-Strength Steel for Laser Assisted Clinching," *Adv. Mater. Res.*, vol. 966–967, pp. 617–627, Jun. 2014, doi: 10.4028/www.scientific.net/AMR.966-967.617.

[69] H. G. Flory, "Rivetting into a blind hole," *J. Sci. Instrum.*, vol. 5, no. 7, pp. 230–230, Jul. 1928, doi: 10.1088/0950-7671/5/7/409.

[70] H. G. Flory, "Rivetting into blind holes," *J. Sci. Instrum.*, vol. 5, no. 12, pp. 393–393, Dec. 1928, doi: 10.1088/0950-7671/5/12/410.

[71] R. D. Lacey, "The Avdel MBC Aerospace Blind Riveting System," *Aircr. Eng. Aerosp. Technol. https Aircr. Eng. Aerosp. Technol.*, vol. 54, no. 60, pp. 15–18, 1982.

[72] D. Ulbrich, R. Primke-Engel, C. Blunk, and R. Glienke, "Mechanische Verbindungen im Metallleichtbau," *Stahlbau*, vol. 82, no. 11, pp. 805–818, Nov. 2013, doi: 10.1002/stab.201310108.

[73] D. D. Bloch and C. F. Hanson, "Free Hand Robotic Installation of Blind Bolts," in *Aerofast Conference & Exposition*, 1992, doi: 10.4271/922409.

[74] C. Soehner and H. Mayländer, "Traveling Column Machines for Automated Drilling and Fastening Operations on Different Aircraft Structural Components," *SAE Int. J. Aerosp.*, vol. 1, no. 1, pp. 2008-01–2283, Sep. 2008, doi: 10.4271/2008-01-2283.

[75] J. Mucha and W. Witkowski, “The Structure of the Strength of Riveted Joints Determined in the Lap Joint Tensile Shear Test,” *Acta Mech. Autom.*, vol. 9, no. 1, pp. 5–10, 2015, doi: 10.1515/ama-2015-0009.

[76] J. Mucha and W. Witkowski, “Mechanical Behavior and Failure of Riveting Joints in Tensile and Shear Tests,” *Strength Mater.*, vol. 47, no. 5, pp. 755–769, 2015, doi: 10.1007/s11223-015-9712-5.

[77] B. S. Sanjaykumar and P. S. M. C, “Comparative study of Fatigue Analysis of Pop up (Blind) Riveted with Solid Riveted Lap joint,” *Int. J. Eng. Sci. Comput.*, vol. 6, no. 6, pp. 6955–6960, 2016, doi: 10.4010/2016.1661.

[78] G. Di Lorenzo and R. Landolfo, “Shear experimental response of new connecting systems for cold-formed structures,” *J. Constr. Steel Res.*, vol. 60, no. 3, pp. 561–579, 2004, doi: 10.1016/S0143-974X(03)00130-5.

[79] B. Kelly and C. Costello, “FEA modelling of setting and mechanical testing of aluminum blind rivets,” *J. Mater. Process. Technol.*, vol. 153154, pp. 74–79, 2004, doi: 10.1016/j.jmatprotec.2004.04.184.

[80] S. Han, Z. Li, Y. Gao, and Q. Zeng, “Numerical study on die design parameters of self-pierce riveting process based on orthogonal test,” *J. Shanghai Jiaotong Univ.*, vol. 19, no. 3, pp. 308–312, Jun. 2014, doi: 10.1007/s12204-014-1504-8.

[81] R. Neugebauer, F. Jesche, C. Kraus, and S. Hensel, “Mechanical joining with self piercing solid-rivets at elevated tool velocities,” in *AIP Conference Proceedings*, 2011, vol. 1353, pp. 1278–1283, doi: 10.1063/1.3589692.

[82] R. Porcaro, a G. Hanssen, A. Aalberg, and M. Langseth, “Joining of aluminium using self-piercing riveting: Testing, modelling and analysis,” *Int. J. Crashworthiness*, vol. 9, no. 917158159, pp. 141–154, Mar. 2004, doi: 10.1533/ijcr.2004.0279.

[83] N.-H. Hoang, O. S. Hopperstad, M. Langseth, and I. Westermann, “Failure of aluminium self-piercing rivets: An experimental and numerical study,” *Mater. Des.*, vol. 49, pp. 323–335, 2013, doi: 10.1016/j.matdes.2013.01.034.

[84] N.-H. Hoang, R. Porcaro, M. Langseth, and A.-G. Hanssen, “Self-piercing riveting connections using aluminium rivets,” *Int. J. Solids Struct.*, vol. 47, no. 3, pp. 427–439, 2010, doi: 10.1016/j.ijsolstr.2009.10.009.

[85] A. He, Xiaocong, Baoying, Xing1, Kai, Zeng, Gu, Fengshou and Ball, “Numerical and Experimental Investigations of Self-piercing Riveting,” 2013.

[86] Y. Abe, T. Kato, and K. Mori, “Joinability of aluminium alloy and mild steel sheets by self piercing rivet,” *J. Mater. Process. Technol.*, vol. 177, no. 1, pp. 417–421, 2006, doi:

10.1016/j.jmatprotec.2006.04.029.

[87] S. U. Nagare and A. D. Wable, “Review : Experimental and Numerical Analysis of Self Piercing Riveted Joint,” *Int. Res. J. Eng. Technol.*, pp. 2171–2174, 2015.

[88] H. Ali Khan, J. Li, and C. Shao, “Analyses of Friction Stir Riveting Processes: A Review,” *J. Manuf. Sci. Eng.*, vol. 139, no. 9, p. 090801, Jul. 2017, doi: 10.1115/1.4036909.

[89] H. T. Kang *et al.*, “A Fatigue Life Prediction Method of Laser Assisted Self-Piercing Rivet Joint for Magnesium Alloys,” *SAE International Journal of Materials and Manufacturing*, vol. 8. SAE International, pp. 789–794, 2015, doi: 10.2307/26268776.

[90] L. Deng, M. Lou, Y. Li, and B. E. Carlson, “Thermally Assisted Self-Piercing Riveting of Aluminum AA6061-T6 to Ultra-High Strength Steels,” in *Volume 2: Materials; Joint MSEC-NAMRC-Manufacturing USA*, 2018, p. V002T04A036, doi: 10.1115/MSEC2018-6367.

[91] O. Hahn, G. Meschut, M. Bergau, and M. Matzke, “Self-pierce Riveting and Hybrid Joining of Boron Steels in Multi-material and Multi-sheet Joints,” *Procedia CIRP*, vol. 18, pp. 192–196, 2014, doi: 10.1016/j.procir.2014.06.130.

[92] G. Meschut, V. Janzen, and T. Olfermann, “Innovative and highly productive joining technologies for multi-material lightweight car body structures,” in *Journal of Materials Engineering and Performance*, 2014, vol. 23, no. 5, pp. 1515–1523, doi: 10.1007/s11665-014-0962-3.

[93] J. Mucha, “The numerical analysis of the effect of the joining process parameters on self-piercing riveting using the solid rivet,” *Arch. Civ. Mech. Eng.*, vol. 14, no. 3, pp. 444–454, 2014, doi: 10.1016/j.acme.2013.11.002.

[94] M. Jäckel, C. Kraus, and T. Kropp, “Effects of Increased Tool Velocity on Mechanical Joining of Steel and Aluminum Sheet Metals,” *Procedia CIRP*, vol. 23, no. C, pp. 24–28, 2014, doi: 10.1016/j.procir.2014.10.062.

[95] J. Mucha, “The failure mechanics analysis of the solid self-piercing riveting joints,” *Eng. Fail. Anal.*, vol. 47, pp. 77–88, 2015, doi: 10.1016/j.engfailanal.2014.10.008.

[96] J. Mucha and W. Witkowski, “The clinching joints strength analysis in the aspects of changes in the forming technology and load conditions,” *Thin-Walled Struct.*, vol. 82, pp. 55–66, 2014, doi: 10.1016/j.tws.2014.04.001.

[97] Ľ. Kaščák and E. Spišák, “MECHANICAL JOINING M ETHODS IN CAR BODY C ONSTRUCTION,” 2013.

[98] C. Chen, S. Zhao, M. Cui, X. Han, and S. Fan, “Mechanical properties of the two-steps clinched joint with a clinch-rivet,” *J. Mater. Process. Technol.*, vol. 237, pp. 361–370, 2016, doi: 10.1016/j.jmatprotec.2016.06.024.

[99] C. Chen, S. Zhao, M. Cui, X. Han, S. Fan, and T. Ishida, "An experimental study on the compressing process for joining Al6061 sheets," *Thin-Walled Struct.*, vol. 108, pp. 56–63, 2016, doi: 10.1016/j.tws.2016.08.007.

[100] C. Chen, S. Zhao, X. Han, M. Cui, and S. Fan, "Optimization of a reshaping rivet to reduce the protrusion height and increase the strength of clinched joints," *J. Mater. Process. Technol.*, vol. 234, pp. 1–9, 2016, doi: 10.1016/j.jmatprotec.2016.03.006.

[101] C. Chen, S. Zhao, X. Han, M. Cui, and S. Fan, "Investigation of mechanical behavior of the reshaped joints realized with different reshaping forces," *Thin-Walled Struct.*, vol. 107, pp. 266–273, 2016, doi: 10.1016/j.tws.2016.06.020.

[102] S. F. Miller, R. Li, H. Wang, and A. J. Shih, "Experimental and Numerical Analysis of the Friction Drilling Process," *J. Manuf. Sci. Eng.*, vol. 128, no. 3, p. 802, 2006, doi: 10.1115/1.2193554.

[103] L. Claus and S. Weitzel, "Self-Tapping Fasteners for Lightweight Designs Lightweighting Topics Relative to Thread," *SAE Tech. Pap.*, Apr. 2014, doi: 10.4271/2014-01-0785.Copyright.

[104] R. Szlosarek *et al.*, "Mechanical testing of flow drill screw joints between fibre-reinforced plastics and metals," *Mater. Test.*, vol. 55, no. 10, pp. 737–742, Oct. 2013, doi: 10.3139/120.110495.

[105] D. H. Amundsen and J. U. Gustad, "Behaviour and Modelling of Flow-Drilling Screw Connections," NTNU - Norwegian University of Science and Technology MASTER, 2014.

[106] J. K. Sønstabø, D. Morin, and M. Langseth, "Macroscopic Modeling of Flow-Drill Screw Connections," 2015, pp. 2–3.

[107] J. K. Sønstabø, D. Morin, and M. Langseth, "Macroscopic modelling of flow-drill screw connections in thin-walled aluminium structures," *Thin-Walled Struct.*, vol. 105, pp. 185–206, 2016, doi: 10.1016/j.tws.2016.04.013.

[108] A. G. Hanssen, L. Olovsson, R. Porcaro, and M. Langseth, "A large-scale finite element point-connector model for self-piercing rivet connections," *Eur. J. Mech. - A/Solids*, vol. 29, no. 4, pp. 484–495, 2010, doi: 10.1016/j.euromechsol.2010.02.010.

[109] J. K. Sønstabø, P. H. Holmstrøm, D. Morin, and M. Langseth, "Macroscopic strength and failure properties of flow-drill screw connections," *J. Mater. Process. Technol.*, vol. 222, pp. 1–12, Aug. 2015, doi: 10.1016/j.jmatprotec.2015.02.031.

[110] S. H. Hong, F. Yan, S.-J. Sung, J. Pan, X. Su, and P. Friedman, "Investigation of Failure Mode and Fatigue Behavior of Flow Drill Screw Joints in Lap-Shear Specimens of Aluminum 6082-T6 Sheets," *SAE Int. J. Mater. Manuf.*, vol. 9, no. 3, pp. 2016-01–0501, Apr. 2016, doi: 10.4271/2016-01-0501.

[111] J. Skovron *et al.*, “Characterization of Flow Drill Screwdriving Process Parameters on Joint Quality,” *SAE Int. J. Mater. Manuf.*, vol. 8, no. 1, pp. 2014-01–2241, Sep. 2014, doi: 10.4271/2014-01-2241.

[112] J. D. Skovron *et al.*, “Effect of Thermal Assistance on the Joint Quality of Al6063-T5A During Flow Drill Screwdriving,” *J. Manuf. Sci. Eng.*, vol. 137, no. 5, p. 051019, Sep. 2015, doi: 10.1115/1.4031242.

[113] J. D. Skovron, B. J. Ruszkiewicz, L. Mears, and T. Abke, “Effect of Electrical Augmentation on the Joining of Al6063-T5 Using Flow Drill Screws,” in *Volume 1: Processing*, 2016, p. V001T02A010, doi: 10.1115/MSEC2016-8578.

[114] G. Meschut, M. Matzke, R. R. Hoerhold, and T. Olfermann, “Hybrid technologies for joining ultra-high-strength boron steels with aluminum alloys for lightweight car body structures,” in *Procedia CIRP*, 2014, vol. 23, no. C, pp. 19–23, doi: 10.1016/j.procir.2014.10.089.

[115] G. Meschut, D. Hein, and M. Gerkens, “Numerical simulation of high-speed joining of sheet metal structures,” *Procedia Manuf.*, vol. 29, pp. 280–287, Jan. 2019, doi: 10.1016/J.PROMFG.2019.02.173.

[116] N. B. Sankaran and A. F. Luscher, “High Speed Ridged Fasteners for Multi-Material Joining,” 2019, doi: 10.4271/2019-01-1117.

[117] D. Small and P. Courtney, “Fundamentals of Industrial Adhesives,” *Adv. Mater. Process.*, vol. 163, pp. 44–47, May 2005.

[118] R. A. Pethrick, “Design and ageing of adhesives for structural adhesive bonding – A review,” *Proc. Inst. Mech. Eng. Part L J. Mater. Des. Appl.*, vol. 229, no. 5, pp. 349–379, Oct. 2015, doi: 10.1177/1464420714522981.

[119] K. Martinsen, S. J. J. Hu, and B. E. E. Carlson, “Joining of dissimilar materials,” *CIRP Ann. - Manuf. Technol.*, vol. 64, no. 2, pp. 679–699, 2015, doi: 10.1016/j.cirp.2015.05.006.

[120] T. Sakayama *et al.*, “Dissimilar metal joining technologies for steel sheet and aluminum alloy sheet in auto body,” 2012.

[121] K. Mori and Y. Abe, “A review on mechanical joining of aluminium and high strength steel sheets by plastic deformation,” *Int. J. Light. Mater. Manuf.*, vol. 1, no. 1, pp. 1–11, Mar. 2018, doi: 10.1016/j.ijlmm.2018.02.002.

[122] K. Miyamoto, S. Nakagawa, C. Sugi, H. Sakurai, and A. Hirose, “Dissimilar Joining of Aluminum Alloy and Steel by Resistance Spot Welding,” *SAE Int. J. Mater. Manuf.*, vol. 2, no. 1, pp. 58–67, 2009, doi: 10.4271/2009-01-0034.

[123] J. Chen, X. Yuan, Z. Hu, T. Li, K. Wu, and C. Li, “Improvement of resistance-spot-welded joints for DP 600 steel and A5052 aluminum alloy with Zn slice interlayer,” *J. Manuf. Process.*,

vol. 30, pp. 396–405, 2017, doi: 10.1016/j.jmapro.2017.10.009.

[124] W. Zhang, D. Sun, L. Han, and D. Liu, “Interfacial microstructure and mechanical property of resistance spot welded joint of high strength steel and aluminium alloy with 4047 AlSi12 interlayer,” *Mater. Des.*, vol. 57, pp. 186–194, 2014, doi: 10.1016/j.matdes.2013.12.045.

[125] J. Chen, X. Yuan, Z. Hu, C. Sun, Y. Zhang, and Y. Zhang, “Microstructure and mechanical properties of resistance-spot-welded joints for A5052 aluminum alloy and DP 600 steel,” *Mater. Charact.*, vol. 120, pp. 45–52, 2016, doi: 10.1016/j.matchar.2016.08.015.

[126] M. R. Arghavani, M. Movahedi, and A. H. Kokabi, “Role of zinc layer in resistance spot welding of aluminium to steel,” *Mater. Des.*, vol. 102, pp. 106–114, 2016, doi: 10.1016/j.matdes.2016.04.033.

[127] J. Wang, H.-P. Wang, F. Lu, B. E. Carlson, and D. R. Sigler, “Analysis of Al-steel resistance spot welding process by developing a fully coupled multi-physics simulation model,” *Int. J. Heat Mass Transf.*, vol. 89, pp. 1061–1072, Oct. 2015, doi: 10.1016/j.ijheatmasstransfer.2015.05.086.

[128] Z. Wan, H.-P. Wang, M. Wang, B. E. Carlson, and D. R. Sigler, “Numerical simulation of resistance spot welding of Al to zinc-coated steel with improved representation of contact interactions,” *Int. J. Heat Mass Transf.*, vol. 101, pp. 749–763, Oct. 2016, doi: 10.1016/j.ijheatmasstransfer.2016.05.023.

[129] Z. Wan, H. P. Wang, N. Chen, M. Wang, and B. E. Carlson, “Characterization of intermetallic compound at the interfaces of Al-steel resistance spot welds,” *J. Mater. Process. Technol.*, vol. 242, pp. 12–23, 2017, doi: 10.1016/j.jmatprotec.2016.11.017.

[130] N. Chen, H. P. Wang, B. E. Carlson, D. R. Sigler, and M. Wang, “Fracture mechanisms of Al/steel resistance spot welds in lap shear test,” *J. Mater. Process. Technol.*, vol. 243, pp. 347–354, 2017, doi: 10.1016/j.jmatprotec.2016.12.015.

[131] N. Chen, H. P. Wang, B. E. Carlson, D. R. Sigler, and M. Wang, “Fracture mechanisms of Al/steel resistance spot welds in coach peel and cross tension testing,” *J. Mater. Process. Technol.*, vol. 252, no. July 2017, pp. 348–361, 2018, doi: 10.1016/j.jmatprotec.2017.09.035.

[132] N. Chen, M. Wang, H. P. Wang, Z. Wan, and B. E. Carlson, “Microstructural and mechanical evolution of Al/steel interface with Fe2Al5growth in resistance spot welding of aluminum to steel,” *J. Manuf. Process.*, vol. 34, no. June, pp. 424–434, 2018, doi: 10.1016/j.jmapro.2018.06.024.

[133] J. Chen, Z. Feng, H. P. Wang, B. E. Carlson, T. Brown, and D. Sigler, “Multi-scale mechanical modeling of Al-steel resistance spot welds,” *Mater. Sci. Eng. A*, vol. 735, no. January, pp. 145–153, 2018, doi: 10.1016/j.msea.2018.08.039.

[134] W. H. Zhang, X. M. Qiu, D. Q. Sun, and L. J. Han, “Effects of resistance spot welding parameters on microstructures and mechanical properties of dissimilar material joints of galvanised high strength steel and aluminium alloy,” *Sci. Technol. Weld. Join.*, vol. 16, no. 2, pp. 153–161, Feb. 2011, doi: 10.1179/1362171810Y.0000000009.

[135] W. Zhang, D. Sun, L. Han, W. Gao, and X. Qiu, “Characterization of Intermetallic Compounds in Dissimilar Material Resistance Spot Welded Joint of High Strength Steel and Aluminum Alloy,” *ISIJ Int.*, vol. 51, no. 11, pp. 1870–1877, 2011, doi: 10.2355/isijinternational.51.1870.